TECHNISCHE UNIVERSITÄT MÜNCHEN
Institut für Photogrammetrie und Kartographie
Lehrstuhl für Methodik der Fernerkundung

Uncertainty assessment of single-pass TanDEM-X DEMs in selected applications

Cristian Rossi

Vollständiger Abdruck der von der Ingenieurfakultät Bau Geo Umwelt der Technischen Universität München zur Erlangung des akademischen Grades eines
Doktor-Ingenieurs (Dr.-Ing.)
genehmigten Dissertation.

Vorsitzender: Univ.-Prof. Dr.-Ing. habil. Xiaoxiang Zhu

Prüfer der Dissertation:

1. Hon.-Prof. Dr. rer. nat. Michael Eineder
2. Univ.-Prof. Dr.-Ing. habil. Richard H.G. Bamler
3. Prof. Dr. Stefano Tebaldini,
   Politecnico di Milano, Mailand, Italien

Die Dissertation wurde am 18.01.2016 bei der Technischen Universität München eingereicht und durch die Ingenieurfakultät Bau Geo Umwelt am 01.03.2016 angenommen.

Abstract

SAR interferometry is a well-known technique for producing surface models. In the global scale, the quality of these models significantly increased with the use of bistatic systems such as the German TanDEM-X mission. Quality can be measured in two scales: a global and a local one. A global scale quality analysis involves measures for the complete scene, characterizing the whole correctness with a single parameter. A local scale investigates instead inside the single elevation model cell, discriminating the different quality obtained by the various terrains and media present in the scene. A coherence analysis is a typical measure for InSAR models. Globally, a simple average gives an overall quality measure hint. Locally, it provides a measure of the DEM pixel height error. Unfortunately, this measure lacks in several aspects as not considering unwrapping errors and not being valid for certain types of scattering. Objective of this research is to assess standard and alternative elevation accuracy methods and to inspect the different capabilities of the bistatic system possibly solving accuracy-related issues.

In the global scale, a novel algorithm is proposed to detect areas affected by unwrapping errors by employing the radargrammetric shifts generated during the coregistration stage of an interferometric processor. As additional benefit, the algorithm provides an estimate of the so called absolute phase offset, thus not requiring external models or ground control points for the geocoding step. The approach is well-suited for operational processing schemes, e.g. by detecting models affected by errors which compromise the overall TanDEM-X elevation accuracy.

A local scale quality analysis requires the knowledge of the complex mechanisms involved in the electromagnetic signal propagation and backscattering. In fact, different accuracy levels can be awaited depending on the actual terrain to model. In particular, limitations have to be expected depending on the terrain slope and the medium to image. To investigate the differences in accuracy levels, three opposite scenarios are considered: flat agricultural areas, moderate to complex terrain with various land covers and urban areas.

On the one side, it is demonstrated how the accuracy level is very high when mapping agricultural crops, even allowing volumetric change studies when employing temporal data stacks.

On the other side, larger limitations are measured for moderate terrains. Besides the inability to map certain slopes due to the side-looking sensor geometry and the inherent geometrical decorrelations, unwrapping errors are most probable to appear and can be detected with the aforementioned global indicator. A couple of investigations with two different uncertainty assessment strategies are provided. The first, over a subglacial volcano, goes in the same direction of the previous, by analyzing the temporal variations and keeping the electromagnetic framework. The second, over Mediterranean hills, exploits the geometrical domain and compares TanDEM-X with the optical system CartoSAT-1.

Finally, the study moves to urban areas. The first part of the research lies in the model accuracy improvement given by processing modifications. With the help of high-resolution spotlight data, the focus can be posed also on the single structure height reconstruction, so that the study is driven on the layover portion of buildings. It is shown how layover strongly affects the model accuracy, by creating artificial elevation ramps. Detection of layover is then a fundamental step. A novel technique is presented. It makes use of the behavior of the geocoding processing stage embedded

in an interferometric SAR processor for this particular case. The extracted map gives a good indication of inaccurate zones. To better understand how accurate the model for those areas is, the research moves in the spectral domain. Here, spectral estimation is intended as an additional instrument towards a better understanding of the physical phenomena behind the layover scattering decomposition in order to interpret the generated building model.

Zusammenfassung

Die SAR Interferometrie (InSAR) ist eine bekannte Technik, um topographische Modelle (*Digital Elevation Models, DEMs*) der Erdoberfläche zu erzeugen. Durch die Nutzung neuartiger bistatischer SAR-Satellitensysteme wie TanDEM-X konnte die Qualität solcher globalen Modelle signifikant verbessert werden. Qualität ist dabei auf zwei verschiedenen Skalen messbar: einer globalen und einer lokalen. Eine Qualitätsanalyse auf globaler Skala beinhaltet Messungen für Aufnahmen großer Gebiete, welche die Korrektheit des ganzen Datensatzes mit einzelnen Parametern charakterisieren. Auf lokaler Ebene werden hingegen verschieden Qualitätsmaßzahlen für die unterschiedlichen Regionen, Materialien und Objekte innerhalb einer solchen Aufnahme unterschieden und individuell bewertet. Eine Analyse der interferometrischen Kohärenz ist eine solche typische Maßzahl für InSAR-Höhenmodelle. Global betrachtet, gibt eine einfache Mittelung der Kohärenz einen Hinweis auf die großflächige Datenqualität. Lokal ist sie ein Maß für den statistisch erwarteten Höhenfehler der einzelnen DEM-Pixel. Leider spiegelt dieses Maß nur sehr unvollständig die tatsächliche Genauigkeit in einem DEM wider und berücksichtigt nicht die systematischen Fehler, die zum Beispiel durch den Prozess der Phasenabwicklung (*phase unwrapping*) bei der DEM-Erzeugung entstehen können. Auch repräsentiert sie für eine Vielzahl von Radar-Rückstreumechanismen nicht den tatsächlichen Höhenfehler und ist daher kein universell gültiger Qualitätsindikator. Ziel dieser Arbeit ist es nun, Strategien zu definieren, um mit alternativen Methoden die Höhengenauigkeit zu erfassen und die Fähigkeiten des bistatischen Systems TanDEM-X zur Lösung von Qualitätsproblemen zu demonstrieren.

Auf globaler Skala wird ein neuartiger Algorithmus vorgeschlagen, um Regionen mit Unwrapping-Fehlern zu detektieren. Er nutzt dazu die radargrammetrischen Bildverschiebungen, die während der Ko-registrierung der zwei interferometrischen Kanäle in der InSAR-Verarbeitungskette (dem "Prozessor") abgeleitet werden. Ein zusätzlicher Nutzen dieses Algorithmus ist dabei die Bestimmung des sogenannten absoluten Phasenversatzes, der letztlich die absolute Höhe und Lage des DEMs beeinflusst und so eine Geo-lokalisierung der DEM-Pixel ohne Referenzpunkte am Boden oder zusätzliche Modelle ermöglicht. Dieser Ansatz ist gut geeignet für die operationelle Verarbeitung des gesamten Datenbestandes und liefert Indikatoren, welche individuellen DEMs Fehler aufweisen und die Höhengenauigkeit des TanDEM-X-Endproduktes kompromittieren könnten, sofern sie nicht korrigiert werden können.

Eine Qualitätsanalyse auf lokaler Skala erfordert das Wissen um die komplexen Mechanismen der elektromagnetischen Signalausbreitung und Rückstreuung. In der Tat werden unterschiedliche Qualitätslevel für die verschiedenen abgebildeten Terrainarten erwartet. Insbesondere gibt es Limitierungen durch unterschiedliche lokale Steigungen und die verscheiden aufgenommenen Medien. Um die Unterschiede in den Genauigkeiten zu demonstrieren, werden drei gegensätzliche Szenarien betrachtet: Flache landwirtschaftlich genutzte Gebiete, moderate bis komplexe Topographien mit verschiedener Landbedeckung und schließlich urbane Räume.

Einerseits wird demonstriert, welch hohe Genauigkeiten erreicht werden können wenn Agrarflächen kartiert werden - sogar bis hin zur Möglichkeit, Volumenänderungen der Vegetation in multitemporalen Aufnahmestapeln zu untersuchen.

Auf der anderen Seite begegnet man starken Einschränkungen in der Genauigkeit für Gebiete selbst mit nur moderaten Höhenvariationen. Neben der technisch bedingten Limitierung gewisse Steigungen aufgrund der seitwärts abbildenden Sensor-Geometrie im SAR gar nicht - bzw. nur mit verminderter Signalqualität aufgrund geometrischer Dekorrelation - erfassen zu können, treten hier vermehrt Unwrapping-Fehler auf. Der zuvor genannte globale Indikator kann in diesen Fällen diese Fehler detektieren. Ergebnisse einiger Demonstrationen mit zwei unterschiedlichen Strategien zur Erfassung der Qualität werden hier vorgestellt. Die erste betrachtet den Fall eines subglazialen Vulkans ist vergleichbar mit obigem Ansatz; die temporalen Variationen innerhalb des Rahmens der der elektromagnetischen Streueigenschaften zu analysieren. Der zweite Fall untersucht mediterrane Hügelregionen unter Ausnutzung der geometrischen Abbildungs-Eigenschaften und vergleicht die Ergebnisse von TanDEM-X mit denen des optisch abbildenden Satellitensystems CartoSAT-1.

Schlussendlich wenden wir uns den urbanen Räumen zu. Der erste Teil dieser Arbeiten liegt in der Verbesserung der Modell-Genauigkeiten durch Modifikationen des Prozessors. Mit Hilfe von hochauflösenden "Spotlight" SAR Daten, wird der Fokus auf die Höhenrekonstruktion von individuellen Strukturen gelegt. Insofern ist die Arbeit hier getrieben von den sogenannten *Layover*-Arealen der Gebäude, in denen die entfernungsbasierte SAR-Abbildungstechnik uneindeutig ist. Es wird aufgezeigt, wie stark Layover die Höhengenauigkeit beeinflusst, indem es künstliche Höhenrampen in der Rekonstruktion verursacht. Die Detektion von Layover-Gebieten ist daher ein fundamentaler Schritt. Eine neuartige Technik wird dazu vorgestellt. Sie nutzt für das Verhalten der Geokodierungsalgorithmen in dem InSAR Prozessor in diesen speziellen Fällen. Die damit extrahiert Karte liefert einen guten Indikator für Zonen derartiger Ungenauigkeiten. Um besser zu verstehen, wie akkurat das Höhenmodel für solche Bereiche ist, wird die spektrale Domäne hinzugezogen. Hier ist die spektrale Schätzung als zusätzliches Instrument zu verstehen, um die physikalischen Phänomene hinter der Dekomposition der Layover-Rückstreuung besser zu verstehen. Damit kann dann das mit InSAR-Methoden Gebäudemodell besser interpretiert werden.

Acknowledgments

There are so many people which contributed to this work, with cooperations, advices and discussions.

Many thanks to Michael Eineder and Richard Bamler, who offered me to be part of their fabulous research institute and who guided me through this research with an invaluable support.

Many thanks to Thomas Fritz, who always gives me advices and assistance for everything related to my work. This research would not have been possible without him.

Many thanks to the TanDEM-X team. To be part of the processing team and to touch many complex tasks of this mission is really an amazing professional experience. In particular, many thanks to Helko Breit, who is my precious source of knowledge for many processing aspects, to Nestor Yague-Martinez and Nico Adam, who helped me in my early stages with the interferometric processor, to Marie Lachaise and Fernando Rodriguez-Gonzalez, who built with me the phase unwrapping control map and supported over several algorithmic issues, to Silke Kerkhoff and Birgit Schättler, who introduced me to the operational environment, to Paola Rizzoli and Michele Martone, who are my answer to quality and system questions, to Andreas Niedermeier and Ulrich Balss, who gave me informatic and focusing support.

Many thanks to Alessandro Parizzi, Sergi Duque, Daniele Cerra, Wael Abdel Jaber, Elisa Fagiolini, Francesco de Zan, Paolo Sica and Giorgio Gomba, who helped me with clarifications and discussions with a cup of coffee in my hand.

Many thanks to Esra Erten, who presented me the polarimetric world and had the idea to investigate over agricultural fields.

Many thanks to Christian Minet, who presented me the geophysics world and clarified a lot of its aspects.

Many thanks to Stefan Gernhardt, Stefan Auer and Xiao Xiang Zhu, who supported my urban-related researches.

Many thanks to Pablo d'Angelo and Peter Reinartz, who presented me the optical systems and supported me for the DEM fusion.

Many thanks to Stefano Tebaldini, who accepted to be a reviewer of this research and who explained me several statistical SAR aspects at the Politecnico di Milano during my master studies.

Many thanks to all the people that I love. *In dreams and in love there are no impossibilities.*

Contents

Outline of the Thesis

Part I: Introduction and Theory

CHAPTER 1: INTRODUCTION

This chapter presents an overview of the thesis and its purpose, motivation and novelties. The topic line and its scientific relevance are traced.

CHAPTER 2: ACCURACY EVALUATION OF INSAR DEMS: FUNDAMENTALS AND STATE-OF-THE-ART

Single-baseline bistatic interferometry aimed to DEM generation is introduced with an overview of the processing techniques and on the accuracy descriptors. TanDEM-X is assumed as reference. The standards for DEM evaluation are also introduced and discussed. A large focus is on the possible error sources affecting the DEM, from electromagnetic issues affecting the absolute accuracy to the processing and system impact in the DEM uncertainty. The error investigation strategies employed for the thesis demonstrations are outlined.

Reference A.1: Rossi, C., Gonzalez, F. R., Fritz, T., Yague-Martinez, N., and Eineder, M., TanDEM-X calibrated raw DEM generation. *ISPRS Journal of Photogrammetry and Remote Sensing*, 73, 12-20, 2012.

Part II: Investigations

CHAPTER 3: TANDEM-X UNCERTAINTY INVESTIGATION OVER SMOOTH TERRAINS: THE LAKE GALA CASE STUDY

The first accuracy study is for an optimal terrain configuration. Agricultural fields are analyzed, with an eye on the rice plants growth cycle. A test site in Turkey is considered. A temporal series is employed to study seasonal differences. An investigation on the elevation model accuracy depending on the local electromagnetic backscattering is provided. Impact of wave polarization is also addressed. A dedicated on-site campaign is used to validate the results on a field-by-field basis.

Reference A.2: Rossi, C., and Erten, E., Paddy-rice monitoring using TanDEM-X. *IEEE Transactions on Geoscience and Remote Sensing*, 53(2), 900-910, 2015.

Reference A.3: Erten, E., Rossi, C. and Yuzugullu, O., Polarization Impact in TanDEM-X Data Over Vertical-Oriented Vegetation: The Paddy-Rice Case Study. *IEEE Geoscience and Remote Sensing Letters*, 12(7), 1501-1505, 2015.

CHAPTER 4: TANDEM-X UNCERTAINTY INVESTIGATION OVER MODERATE TERRAINS: THE BARDARBUNGA AND SERRA DE COLLCARDUS CASE STUDIES

The second accuracy study is for two separate test cases with moderate terrain slopes. In the first one, covering the Bardarbunga caldera in Iceland, the focus is on the temporal changes caused by an ongoing volcanic activity. The assessment is done in the electromagnetic domain. Uncertainty coming from wave penetration into snow is reviewed and validated. In the second one, the attention is posed more on geometrical issues than on local backscattering. A test site in Spain is here analyzed. Error localization and inspection are addressed by comparison with a LiDAR reference. An accuracy study with slope and aspect angles as test variables is assessed. At the purpose, also

the complementary CartoSAT-1 model accuracy is studied.

Reference A.4: Rossi, C., Eineder, M., Fritz, T., D'Angelo, P., and Reinartz, P., Quality assessment of TanDEM-X raw DEMs oriented to a fusion with CartoSAT-1 DEMs, *Proc. 33rd EARSeL Symp.*, Matera, Italy, 2013.

CHAPTER 5: TANDEM-X UNCERTAINTY INVESTIGATION OVER COMPLEX TERRAINS: THE BERLIN CASE STUDY

Urban areas are the most complex scenario to image with SAR sensors due to the numerous local terrain discontinuities. High-resolution spotlight data is employed here with a test site over Berlin (Germany). The analysis is performed on several aspects. Accuracy is in this case strongly driven by processing strategies. A dedicated processing chain is therefore studied. Error investigation is examined for layover areas, with a study on the impact of the facet backscattering in the elevation model. Error localization is by consequence derived with a novel approach making use of the interferometric configuration. Error interpretation is approached in the spectral domain.

Reference A.5: Rossi, C., and Gernhardt, S., Urban DEM generation, analysis and enhancements using TanDEM-X. *ISPRS Journal of Photogrammetry and Remote Sensing*, 85, 120-131, 2013.

Reference A.6: Rossi, C., and Eineder, M., High-resolution InSAR building layovers detection and exploitation. *IEEE Transactions on Geoscience and Remote Sensing*, 53(12), 6457-6468, 2015.

Summary

CHAPTER 6: SUMMARY

This chapter presents the conclusions and opens to possible applications.

Appendix

A1-A5: APPENDIX

The five papers summarized in the thesis are in the appendix.

Part I.

Introduction and Theory

1. Introduction

TanDEM-X is an innovative mission, started in 2010 with the launch of a twin satellite (TDX-1) placed in close formation with the TerraSAR-X satellite (TSX-1) (Krieger et al., 2007). The main mission objective is the generation of a global Digital Elevation Model (DEM) with HRTI-3 accuracy standards (see Sec. 2.1.3). The mission acronym says just that: *TerraSAR-X add-on for Digital Elevation Measurement*. An artist's view of the mission is sketched in Fig. 1.1.

The generation of the DEM is based on the SAR interferometry technique. The operation mode is *bistatic*, i.e. established on the simultaneous reception of the transmitted signal by one satellite which is received by two satellites. By doing so, strong error sources such as different atmospheric conditions or temporal changes are avoided. The other operation mode is called *monostatic*, and is based on the use of two acquired images over the same area at different times. A detailed description of the DEM generation with SAR interferometry is described in Chapter 2.

A peculiarity of the TanDEM-X mission is the three years' timeline. The first two years are dedicated to global acquisitions of land portions of the Earth at two different baselines. These acquisitions can be combined for the DEM generation in a *dual-baseline* fashion. A single acquisition may not be sufficient to accomplish the accuracy standards, since phase unwrapping errors may manifest. A second acquisition with a different baseline serves to mitigate this source of error by properly combining the two acquisition together (Lachaise et al., 2014). This can still not be enough for very complex terrains. The third year is dedicated to that, by acquiring at different incidence angles and looking geometries in order to correct for shadow and layover. Antarctic data is also collected during this third phase.

An assessment of the shape of individual DEM, here called *single-pass DEM* (or also *single-baseline* or *raw DEM*), for various selected land covers, is the main objective of this dissertation. To accomplish that, an investigation of the uncertainty sources, including their detection into the DEM and their interpretation, is carried out.

1.1. Scientific motivation

Nowadays, plenty of researches still use the Shuttle Radar Topography Mission (SRTM) DEM as reference due to its free availability. SRTM DEMs are in fact not global, since they are only available in between $56°$ S and $60°$ N. Moreover, they suffer from artifacts, such as voids, modulations and offsets (Rodriguez et al., 2006). NASA is currently planning to improve the SRTM DEM by reprocessing the raw data and fuse information coming from various other more updated sources (JPL, 2014). TanDEM-X data is instead more recent (the time span between the two missions is 10-15 years), is globally defined and has a higher resolution. A private company is designated to the DEM sale for commercial purposes (Airbus Defence and Space). For scientific purposes, specific quotas and TanDEM-X coregistered image pairs (CoSSC) can be freely obtained directly through the German Aerospace Center (DLR) science service system. A reduced resolution version of the produced DEM will also be released to the public. According to that, TanDEM-X can become a solid reference for DEM users.

DEM data is always subject to uncertainty (Wright, 1977; Wechsler and Kroll, 2006). An interesting study performed by S. Wechsler (Wechsler, 2003) revealed that most of the DEM users rarely

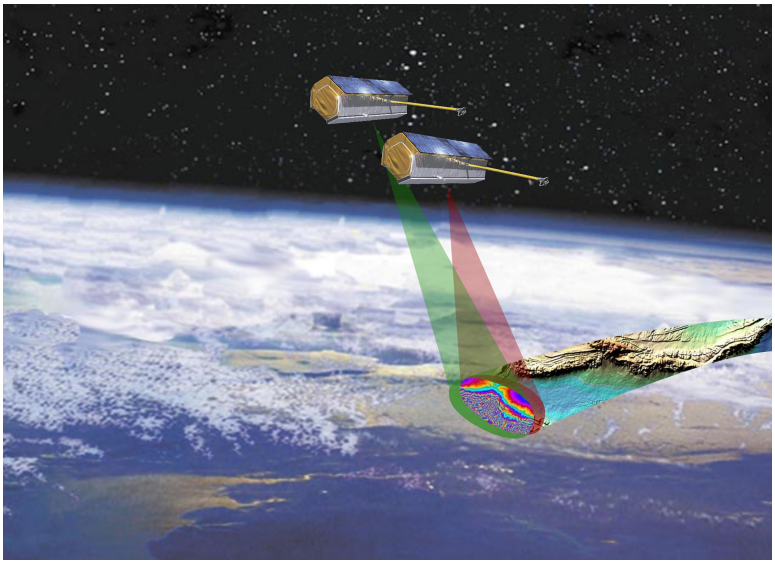

Figure 1.1.: Artist's view of the TanDEM-X mission (©DLR).

or never take into account for uncertainty, and about a quarter of the total is even not aware about that. Moreover, a consistent procedure to assess it is also not available. I personally think that it is important to comprehend the uncertainty of interferometric DEMs. My target is the single-baseline DEM, which can be easily generated with almost every interferometric software given a pair of SAR images. This DEM can be prone to errors. The understanding of their sources can help on the one side their corrections, and on the other side can allow the accuracy assessment of applications which are using the DEM as input. TanDEM-X is the first mission employing two satellites in close formation. Therefore, the uncertainty evaluation of raw DEMs is also valuable in the general bistatic interferometry framework.

1.2. Problem statement and thesis structure

Being a global mission, TanDEM-X is mapping every square meter of the Earth's land. Thus, all the possible land covers are included. As explained in the following chapters, Interferometric Synthetic Aperture Radar (InSAR) DEM accuracy is strongly terrain dependent, subject to both the cover type and the topography. This dissertation provides guidelines for assessing InSAR DEM accuracy in Part I and investigates them with four test cases in Part II. The inspections try to be as various as possible, with different land covers and slopes, starting from terrains which allow the generation of DEMs with good accuracy and concluding with terrains that yield DEMs with larger artifacts. A visual outline of the dissertation is given in Fig. 1.2.

More in detail, Part I (Chapter 2) gives the guidelines for the uncertainty assessment of InSAR DEMs in a general way. The InSAR system is introduced in Sec. 2.1.2, with a large focus on the generation algorithms, since a considerable fraction of DEM errors are caused by processing. In particular, the absolute phase offset derivation is examined in depth, since a novel algorithm has been developed and a new global accuracy indicator has been derived. The DEM standards, in terms of accuracy, are described in Sec. 2.1.3. Even though they are created for laser or optical systems, an extension to the InSAR system is given. The main InSAR error sources are summarized in Sec. 2.2. As aforementioned, sources are mainly originated from processing, system inaccuracies and the land cover. Finally, the theoretical part is concluded in Sec. 2.3 with the investigation

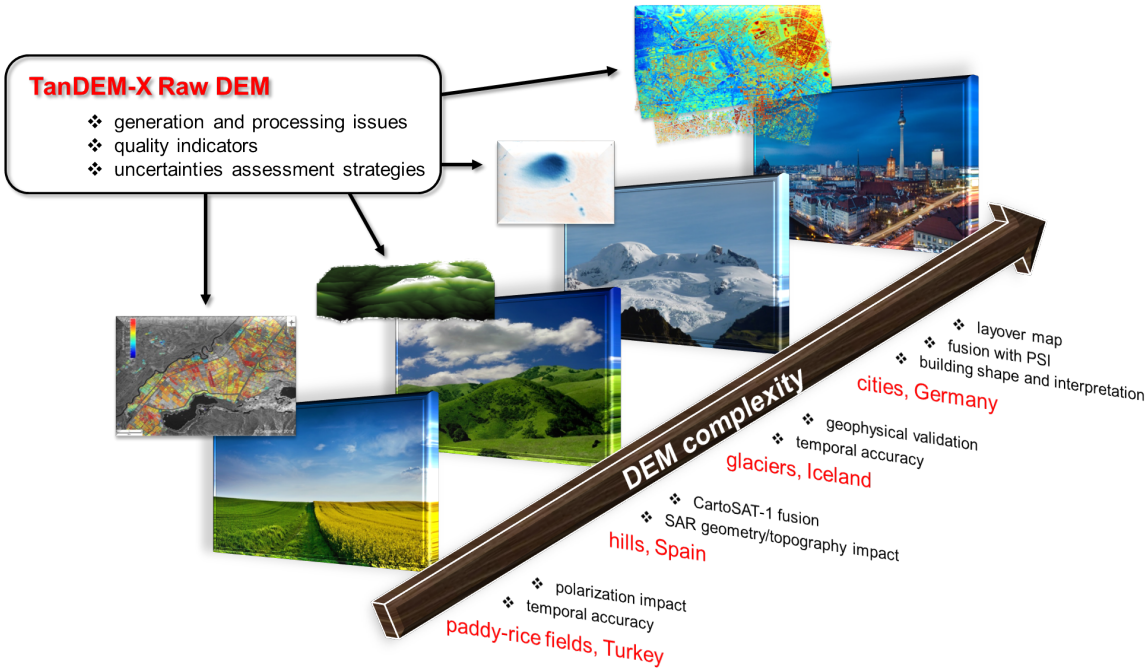

Figure 1.2.: Visual view of the dissertation's outline.

strategies adopted in the thesis.

In Part II, four uncertainty assessment tests are provided. The strategy is to build a path for the reader, starting from flat terrains and then moving to steeper and even vertical slopes. This path starts in Chapter 3 with the uncertainty assessment over agricultural areas. The analysis is made on the temporal dimension (Sec. 3.3), stressing how the uncertainty depends on the growing stage. The wave polarization impact in the assessment is an additional study and it is analyzed in Sec. 3.4. The electromagnetic and temporal assessment is a key analysis also for the next demonstration, over a subglacial volcano monitored during an ongoing activity (Sec. 4.2). Land cover type is in this case snow. The demonstration area has moderate slopes, as well as the following one, over Mediterranean hills (Sec. 4.3). In this case the assessment is performed in the geometrical domain, by exploring the accuracy dependency on slope and aspect angles. Complementary optical data serve as comparison. Finally, the path is concluded over the most complex terrain: urban area (Chapter 5). The complexity is originated by the frequent slope discontinuities. Since the InSAR DEM over buildings may be inaccurate due to the layover and shadow phenomena, its shape is estimated in Sec. 5.2.2. Next to the typical comparison with a reference, the accuracy assessment highlights are the derivation of a novel layover detector (Sec. 5.4.2) and the layover decomposition with a single InSAR pair (Sec. 5.4.3). For all the investigations a link with Part I is provided.

This dissertation resumes the work presented in five journal papers and one conference proceeding, attached as Appendix. The reader may choose whether to examine in depth the proposed topics by reading the papers or to have a more general but complete overview by just reading the dissertation. The main concepts and findings are present in both. To guide the reader through the dissertation, the relationship between the sections and the appendices is shown in Tab. 1.1. Sections not appearing in this table are written for the thesis purposes without being reported in the journal references. The study about the subglacial volcano monitoring in Chapter 4 summarizes a journal paper in preparation in the moment of writing this dissertation (Rossi et al., 2016).

chapter section	appendix section	topic
2.1.2	A.1., Sec. 2	ITP processing
2.1.2.3	A.5., Sec. III	InSAR geocoding
2.3.2	A.1., Sec. 4	ITP processing example
3.2	A.2., Sec. II	Paddy-rice dataset
3.3	A.2., Sec. III	Uncertainty investigation
3.4	A.3., Sec. III	Polarization impact
4.3.2	A.4., Sec. 2.2	Uncertainty investigation
5.2.1	A.5., Sec. 2	Urban processing issues
5.2.2	A.6., Sec. II, III	Building shape
5.3	A.5., Sec. 3.1	Urban dataset
5.4.1	A.5., Sec. 3.1	Uncertainty investigation
5.4.2	A.6, Sec. IV	Layover map
5.4.3	A.6., Sec. V	Principal slope estimation

Table 1.1.: Relationship between the thesis chapters and the journals in the appendix.

2. Accuracy evaluation of InSAR DEMs — fundamentals and state-of-the-art

This chapter gives the theoretical background to the overall study by describing the Digital Elevation Model (DEM) fundamentals and the uncertainty assessment. Sec. 2.1 focuses on the DEM production techniques for InSAR systems. The parameters characterizing the DEM are also described in this section. Sec. 2.2 inspects the error sources affecting the model accuracy. Finally, Sec. 2.3 deals with the uncertainty investigation methods used in this work and Sec. 2.4 draws the conclusions.

Part of this chapter (absolute phase determination in Sec. 2.1.2 and PUCM in Sec. 2.3.2) summarizes the paper in Appendix A.1: Rossi, C., Gonzalez, F. R., Fritz, T., Yague-Martinez, N., and Eineder, M., **TanDEM-X calibrated raw DEM generation**. *ISPRS Journal of Photogrammetry and Remote Sensing*, 73, 12-20, 2012 (Rossi et al., 2012).

2.1. Digital Elevation Models fundamentals

2.1.1. Definition

A Digital Elevation Model (DEM) is by definition a *model* describing the topographical variation of the Earth. Analyzing the single terms in the acronym:

- *Digital*. *Digital* implies a discretization process. Earth is composed by an infinite number of points. Each point on Earth is purely 0-D, i.e. without dimensions. Thus, it is in principle impossible to provide a true and complete representation. In practice, a set of points is considered sufficient to represent topographic variations. The generation of a gridded DEM from the set of points implies a digitizing process. To this end, a grid is set up and an elevation value per grid tile is provided. The final product is not 3-D, as it does not provide multiple elevations per DEM cell (e.g. no information for vertical features). Instead, it is stated to be 2.5-D, with a single elevation value per grid cell. Sampling issues are discussed in detail in Sec. 2.1.3.

- *Elevation*. Terrain height is the main information. Elevation is generally given above a certain level, e.g. a geodetic datum. For instance, TanDEM-X elevations are over the WGS84 ellipsoid. *DEM* is the general term and in this dissertation is used as synonym of DSM (Digital Surface Model), rendering the height of what lies on the Earth at a given position. Another acronym often used is DTM (Digital Terrain Model). DTM was the first acronym used for the purpose (Miller and Laflamme, 1958). *Terrain* may actually lead to some confusion, since, in the literature, it usually represents the bare ground, i.e. without objects or trees.

- *Model*. The term *model* generally implies a mathematical representation of the reality. In this geomorphological context, the term *model* can be seen as heritage of real, small scale miniatures of the Earth.

The original definition of Miller and Laflamme (Miller and Laflamme, 1958) is instructive: *"the digital terrain model (DTM) is simply a statistical representation of the continuous surface of the ground by a large number of selected points with known xyz coordinates in an arbitrary coordinate field."*.

2.1.2. InSAR processing

DEMs can be generated with various technologies, such as stereo photogrammetry, LiDAR and InSAR. Stereo photogrammetry refers to the technique of measuring the position of Earth points from a set of photographs - minimum two (Szeliski, 2010; d'Angelo et al., 2008). Although the use of photographs finalized to surface reconstruction is very old (the father of photogrammetry is historically recognized to be Aimé Laussedat with his first topographic map in 1861), photogrammetry is still the principal technique to produce elevation models. It is indeed estimated that 85% of all the available topographic maps has been produced through aerial images (Li et al., 2010). LiDAR (Light Detection and Ranging) is another popular system to produce DEMs (Wehr and Lohr, 1999; Baltsavias, 1999). It is an active system based on a pulse/CW laser employed to determine the distance between sensor and target. This technology reached its maturity in the nineteens and nowadays several companies offer laser surveys with airborne system. The InSAR system is analyzed in the following.

As for LiDAR, SAR is an active system, i.e. based on the transmission and reception of signals. The whole process is *coherent*, i.e. established on the use of both amplitude and phase information. In contrast with LiDAR, which determines a 3-D location from one range measurement and 2-D pointing angles, the InSAR 3-D positioning relies on two antenna locations and on the measure of the interferometric unwrapped phase. The processing from SAR raw data to DEM is in Fig. 2.1. In the next sections, the coregistration, the absolute phase determination and the geocoding processing stages are described since relevant for the uncertainty measures taken into consideration in the dissertation. Instead, the focusing and SAR image formation description can be found in several books, e.g. (Bamler and Schättler, 1993; Cumming and Wong, 2005), while general interferometric SAR processing details, including the processing stages not described in this dissertation, are given in (Bamler and Hartl, 1998; Hanssen, 2001).

2.1.2.1. Coregistration

Coregistration has the objective to obtain a precise sample-overlap between two SAR images. A typical algorithm employed for coregistering SAR data is the cross-correlation. First, it is helpful to depict the InSAR geometry.

In Fig. 2.2 an example of InSAR geometry is shown. The master satellite sees the point target P, lying at a terrain height h^P, with a look angle θ_1 at a range time $t^P_{\mathrm{ma}} = \frac{2|\mathbf{r}|}{c}$ (two-ways), while the slave one sees it for $(\theta_2, t^P_{\mathrm{sl}} = \frac{2|\mathbf{r_s}|}{c})$. $\mathbf{S_1}$, $\mathbf{S_2}$ and $\mathbf{T}$ are the master antenna, slave antenna and target vector coordinates, respectively. $\mathbf{B}$ is the baseline vector, and β the tilt angle, i.e. the angle between the baseline and the horizontal direction. In the SAR images, the point P is imaged at two different locations for the master and the slave channels, yielding a shift Δ^P. This shift is computed as

$$\Delta^P = \left(t^P_{\mathrm{sl}} - t^P_{\mathrm{ma}}\right) \cdot f^s_{\mathrm{rg}}, \tag{2.1}$$

where f^s_{rg} is the range sampling frequency. The measurement of Δ^P, in its range and azimuth components, is the key stage of any coregistration algorithm. As exemplary algorithm, the one operationally used for the TanDEM-X DEM generation is taken into consideration. The name of the processor carrying the InSAR chain is ITP (Integrated TanDEM-X Processor). In ITP, the azimuth and range shifts are computed for a set of patches arranged in a grid. A patch is composed by 1024 samples (32 by 32), experimentally proven to be a good compromise between accuracy, for the expected coherence, and computation time. The coregistration strategy is the following (Yague-Martinez et al., 2010):

1. *Geometrical shift derivation.* A geometrical computation of the azimuth and range shifts is firstly derived using orbit information and an external DEM (Sansosti et al., 2006).

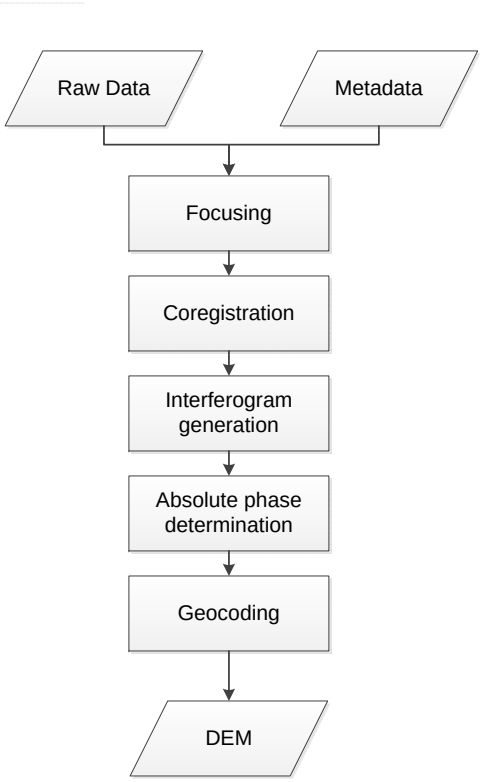

Figure 2.1.: Flowchart of a typical InSAR processing chain finalized to the DEM generation from SAR raw data.

2. *Cross-Correlation.* The geometrical estimate is used as an *a priori* to maximize the patches overlap. Firstly, a coherent-cross correlation on the complex data is performed. A peak test of the correlation function is used to compute the quality of the operation: if the test is not passed, then an incoherent cross-correlation (on the amplitude) is performed. If the quality is still bad, for example in areas with a very low SNR, then the geometrical shifts are used. An example is shown in Fig. 2.3.

3. *Outliers Rejection.* An outlier elimination procedure of the resampling matrices based on the correlation coefficient and on the shift values is performed.

Radargrammetric height retrieval The shifts derived in the coregistration stage are the basis for the generation of a stereo-radargrammetric DEM. Considering the system in Fig. 2.2, the height h^P can be geometrically derived solving an equation system (Franceschetti and Lanari, 1999):

$$\begin{aligned}(\mid \mathbf{r} \mid +\Delta^P)^2 &= \mid \mathbf{r} \mid^2 + \mid \mathbf{B} \mid^2 +2 \mid \mathbf{r} \mid\mid \mathbf{B} \mid \sin(\theta_1 - \beta) \\ \mathrm{h}^P &= H_{S_1} - \mid \mathbf{r} \mid \cos\theta_1,\end{aligned} \tag{2.2}$$

where H_{S_1} is the master satellite height on ground. The height accuracy depends on system parameters such as the SAR range resolution and the angular discrepancy between the two orbits and on the terrain features impacting in the shift accuracy (Méric et al., 2009). Several successful

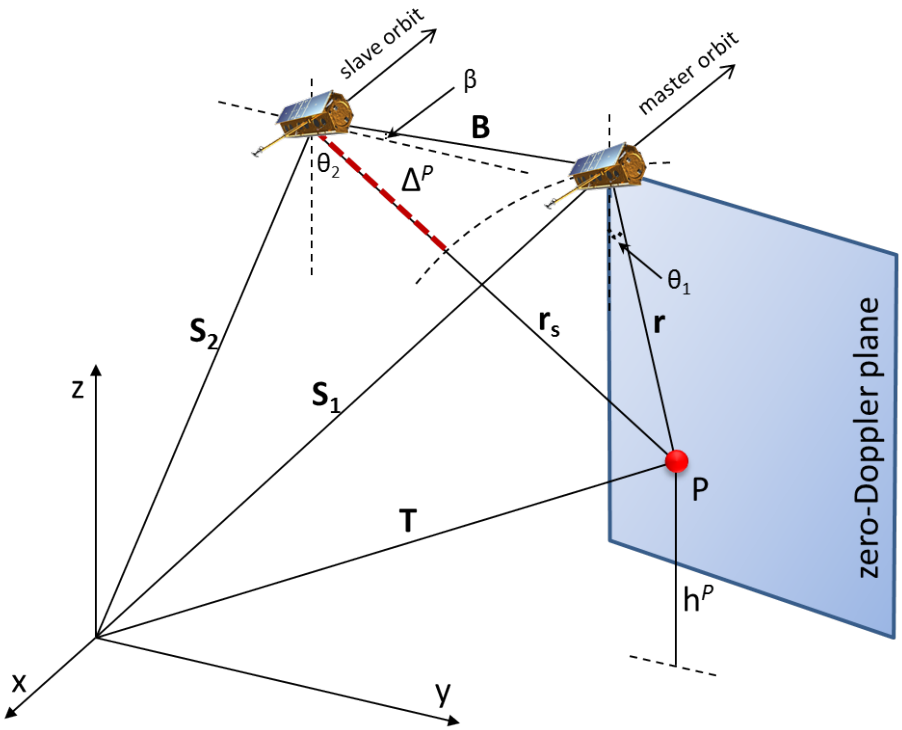

Figure 2.2.: Example of InSAR configuration. The master satellite sees the point P at the time $t^P_{\text{ma}} = \frac{2|\mathbf{r}|}{c}$, the slave satellite at the time $t^P_{\text{sl}} = \frac{2|\mathbf{r_s}|}{c}$. The stereo-radargrammetric shift for the target P between the two channels is Δ^P.

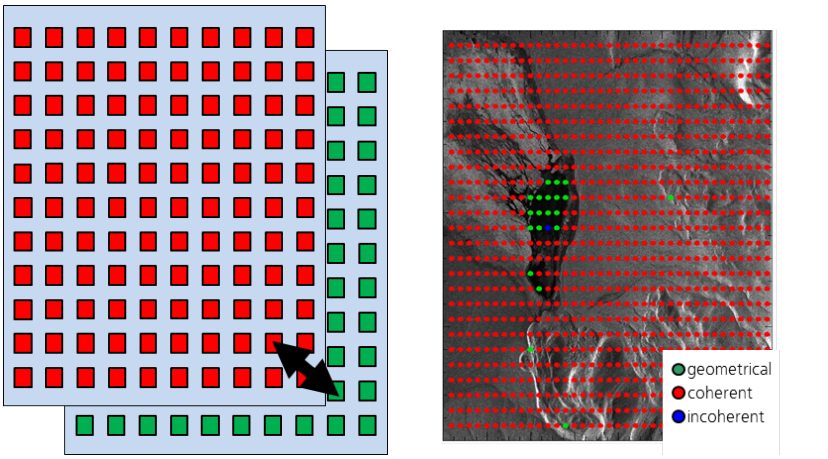

(a) strategy (b) example (Yague-Martinez et al., 2010)

Figure 2.3.: Coregistration processing stage. (a) Strategy. The shift between master and slave is computed for a regular set of patches. (b) Example. Coregistration type overlaid with SAR amplitude.

examples DEM generation with SAR radagrammetry have been reported. For instance, Capaldo et

al. (Capaldo et al., 2011), derived a radargrammetric DEM with an absolute height accuracy (Root Mean Square Error, RMSE) of 3.5 m with Cosmo-SkyMed in Spotlight mode.

2.1.2.2. Absolute phase determination

This essential step is here analyzed since a novel absolute phase offset estimation technique that brought to the derivation of a global DEM accuracy descriptor (see Sec. 2.3.2) is a the cornerstone of this work.

In contrast to the stereo-radargrammetric DEM retrieval described in the previous paragraph, a SAR interferometric technique is based on the exploitation of the complex interferogram. The interferogram is defined through phase principal values, with values ranging into the interval $(-\pi, +\pi]$. A critical stage of the interferometric chain is the absolute phase retrieval given the wrapped interferogram phase. This process, named *phase unwrapping*, is one of the most delicate of the whole processing chain. It consists, for every interferogram pixel, in the estimation of the number of phase cycles to be added to the wrapped value. A good reference with the various algorithms to solve this non-linear problem is (Ghiglia and Pritt, 1998).

The topographic phase ϕ_{top}, also called absolute unwrapped phase, is sensitive to the terrain height h through the relation

$$\frac{\partial \phi_{\text{top}}}{\partial h} = \frac{2\pi B_{\perp}}{\lambda \mid \mathbf{r} \mid \sin\theta_1} = \frac{2\pi}{h_{\text{amb}}}, \tag{2.3}$$

where $B_{\perp}$ is the perpendicular baseline between satellites (see also Sec. 2.2.7) and h_{amb} is a useful derived parameter called *height of ambiguity*. The phase unwrapping step defines the unwrapped phase from the (wrapped) interferometric phase ϕ as

$$\phi_{\text{unw}_i} = \phi_i + 2\pi k_i, \tag{2.4}$$

where k_i is the integer number of cycles estimated for the pixel i. Now, the estimation of the number of cycles is relative to a pixel, for which $k = 0$. This yields the definition of *absolute phase offset* ϕ_{off} as the missing number of cycles q for obtaining the topographic phase

$$\phi_{\text{top}_i} = \phi_i + 2\pi k_i + \phi_{\text{off}}, \tag{2.5}$$

$$\phi_{\text{off}} = 2\pi q. \tag{2.6}$$

In practice, two more terms must be added to this model. First, the approximately additive phase noise (Just and Bamler, 1994) ϕ_N. Second, to support the unwrapping process, a compensation for a known fringe field, i.e. ellipsoid, is typically performed to reduce the operation complexity. The topographic phase is finally

$$\phi_{\text{top}_i} = (\phi_i - \phi_{\text{flat}_i}) + 2\pi k_i^{\left(\phi_{\text{unw}_i} - \phi_{\text{flat}_i}\right)} + \phi_{\text{flat}_i} + 2\pi q + \phi_{N_i}. \tag{2.7}$$

In Eq. (2.7), $k_i^{\left(\phi_{\text{unw}_i} - \phi_{\text{flat}_i}\right)}$ refers to the number of cycles of the compensated phase.

The problem is its estimation. Basically, to estimate the offset, an absolute reference to be compared with the unwrapped field is needed. An external DEM would be the first solution. The availability of external DEMs may not be globally ensured, so that another solution must be foreseen. The proposed solution is to use the radargrammetric shifts in Eq. 2.1, transform them in phase, and use them in comparison to the unwrapped phase. The discrepancy is the estimation of the absolute phase offset. In particular, the coregistration shift transformed to phase is for the point P:

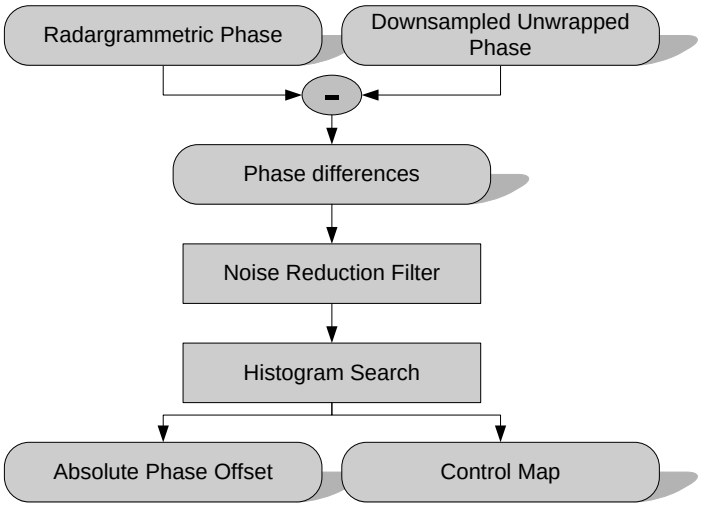

Figure 2.4.: Algorithm implemented for the retrieval of the absolute phase offset. The difference between the unwrapped phase and the stereo-radargrammetric estimates is used to derive the absolute phase offset and a control map.

$$\begin{aligned}\phi^P_{\text{radgr}} &= 2\pi f_0 \frac{\Delta^P}{f^s_{\text{rg}}} \\ &= 2\pi f_0 \left(t^P_{\text{sl}} - t^P_{\text{ma}}\right) \\ &= \phi^P_{top}.\end{aligned} \tag{2.8}$$

It is clear how the stereo-radargrammetric and the interferometric measures yield the same quantity, the absolute ranging, except for the phase offset, which is estimated with a difference between the two measures:

$$\Delta\phi = \phi^P_{\text{radgr}} - \phi^P_{\text{unw}} = -\phi^P_{\text{off}}. \tag{2.9}$$

The proposed algorithm is shown in Fig. 2.4. It is composed of four steps:

1. *Phase Difference Map Generation.* As explained in the previous paragraph, the stereo-radargrammetric shifts are computed for a set of scene patches, whereas the unwrapped phase is at the full interferogram resolution. It follows that the first step before evaluating the differences is a filtering and downsampling of ϕ_{unw} to the raster of ϕ_{radgr}.

2. *Noise Reduction Filter.* The global variance of the differences could be high due to the presence of patches for which an incoherent cross-correlation was performed, i.e. low coherence areas, affecting the stereo-radargrammetric phase, or to noise in the unwrapped phase caused by layover/shadow regions or general decorrelations. Therefore, when a histogram of the difference is built, it presents a wide main lobe. A filtering procedure over the phase difference map - the median filter is the easiest solution and it is the one operationally implemented - to reduce the sample standard deviation is then essential.

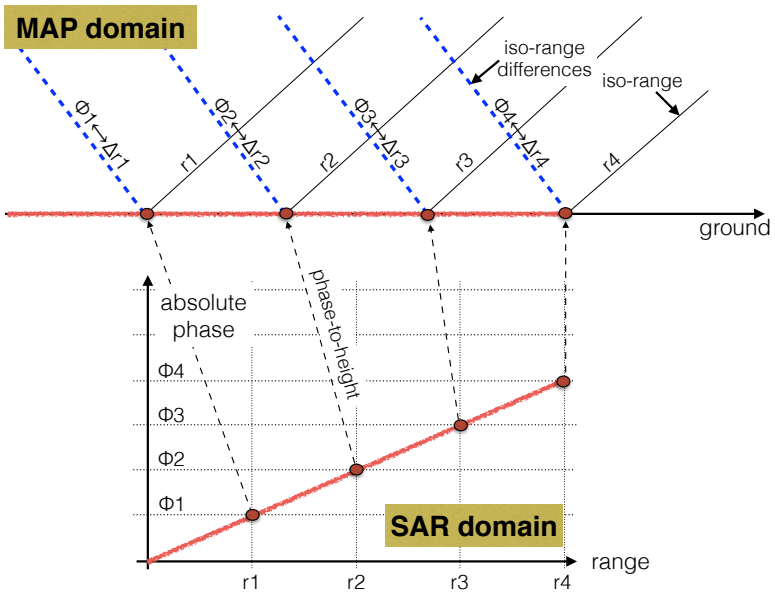

Figure 2.5.: SAR absolute phase mapping in a geographic domain considering flat terrain. Geographic points are determined at the intersection between iso-range circles and iso-range-differences hyperbolas, here drawn as straight lines.

3. *Histogram Search.* A phase unwrapping error creates a secondary lobe in the histogram. The taller the lobe is, the greater the area affected by the error. A peak detection is performed over the histogram of the filtered phase differences to detect possible phase unwrapping errors.

4. *Absolute Phase Offset Retrieval.* The mean value over the main lobe of the histogram of the differences provides the absolute phase offset ϕ_{off}. In this computation, only patches for which a coherent cross-correlation was performed are used. In case of a small number of coherent patches, less than the 10% of the total, also the incoherent ones are used.

The control map, a method to visualize unwrapping errors, is described in Sec. 2.3.2. Finally, this step is highly important since an absolute phase offset error would imply many distortions: height errors, displacements in line of sight and a stretching or a dilation of the DEM.

2.1.2.3. Geocoding

This processing step implies an absolute phase conversion in surface elevation and a georeference on a specific datum. The geometric principle of this operation is simple. A SAR sensor images a point on Earth at a particular range (see Fig. 2.2). On the Doppler plane, i.e. the plane defined with the smallest range in the synthetic aperture, all the points located on a circle with a ray centered at the sensor position are imaged at the same range, thus yielding infinite solutions. In an InSAR framework, this ambiguity is solved by imaging the same point with a second sensor. The locations of the two sensors represent the focal points of hyperbolas having equal range differences. The unwrapped phase is proportional to the range difference. Consequently, on the Doppler plane, a point on earth is located at the intersection between an *iso-range-difference* hyperbola and a *iso-range* circle. This relationship yields the generation of a digital interferometric elevation model. An

example of flat-Earth mapping is shown in Fig. 2.5.

3-D InSAR positioning Several methods were proposed for the geocoding processing stage (e.g. (Hellwich and Ebner, 2000; Schwäbisch, 1998)). They generally optimize the InSAR 3-D positioning issue, which requires the solution of a system of four equations for every target (Bamler and Hartl, 1998; Franceschetti and Lanari, 1999). Indeed, according to Fig. 2.2, the geocoding problem relies in finding the Cartesian coordinates of the target P: (x^P, y^P, z^P).

The first equation asserts that the target P is imaged on the zero-Doppler plane for the azimuth time t:

$$\dot{\mathbf{S}}_\mathbf{1}(t) \cdot (\mathbf{T} - \mathbf{S}_\mathbf{1}(t)) = 0, \tag{2.10}$$

where $\dot{\mathbf{S}}_\mathbf{1}$ represents the master satellite velocity vector. The second equation is the master range equation:

$$|\mathbf{T} - \mathbf{S}_\mathbf{1}(t)| = |r|\,. \tag{2.11}$$

Eq. 2.10 and 2.11 are not sufficient to solve for the three unknown (x^P, y^P, z^P) (the state vectors are assumed as known). The InSAR system solves the underdetermination with the slave channel. Similarly to the previous equations, the slave imaging in the zero-Doppler plane is

$$\dot{\mathbf{S}}_\mathbf{2}(t_s) \cdot (\mathbf{T} - \mathbf{S}_\mathbf{2}(t_s)) = 0, \tag{2.12}$$

where $\dot{\mathbf{S}}_\mathbf{2}$ represents the slave satellite velocity vector and t_s the slave azimuth imaging time, which is an additional unknown. The slave ranging equation is the following:

$$|\mathbf{T} - \mathbf{S}_\mathbf{2}(t_s)| = |\mathbf{r_s}|\,. \tag{2.13}$$

$|r_s|$ is related to the absolute unwrapped phase as

$$|\mathbf{r_s}| = |r| + \frac{\lambda \phi^P_{\text{top}}}{2\pi}. \tag{2.14}$$

Eq. 2.10-2.13 are now sufficient to obtain the target location.

2.1.3. Sampling and resolution

Grid sampling selection is a crucial point for the whole design of the DEM and its accuracy evaluation. Sampling often depends on the image resolution. *Horizontal resolution* is the capability to distinguish between two object heights separated by a certain distance. The minimum resolvable distance is what is called horizontal resolution. *Vertical resolution* is related to the single target height measurement accuracy.

2.1.3.1. System resolution

SAR resolution is varying on the two system dimensions: *range*, or across-track, and *azimuth*, or along-track. The capability of distinguishing two targets in range depends on the transmitted signal bandwidth B_w (Bamler and Hartl, 1998):

$$\Delta r_\text{gr} = \frac{c}{2B_\text{w}} \frac{1}{\sin\theta}, \tag{2.15}$$

where Δr_gr is the minimum separation between targets on ground, c the speed of light and θ the incidence angle. The minimum separation in along-track Δx just depends on the antenna size L_ant (stripmap mode):

$$\Delta x = \frac{L_{\text{ant}}}{2}. \tag{2.16}$$

This limit can actually be improved in the spotlight mode, by steering the antenna over a target during the flight. Typical resolution values are in the order of meters, with the exception of high-resolution sensors in X-band which can bring the resolution to decimeters for spotlight mode.

LiDAR resolution *DEMs generated with LiDAR are used as reference in several investigations presented in this dissertation. Laser scanner measures consist of sparse points, with footprints dependent on the system elevation and the laser beam divergence. The footprint can be approximated as the multiplication of the two parameters (Wehr and Lohr, 1999). As example, an aircraft flying at 500 m with a divergence of 1 mrad produces a footprint of 50 cm. The dismissed IceSAT satellite mission, carrying a laser altimeter at an orbit of about 600 km, produced footprint of 70 m (with shots every 170 m) (Schutz et al., 2005).*

Resolution has of course a big impact in the sampling of the generated elevation model. For instance, it makes no practical sense to produce a DEM with a sampling lower than the image resolution.

2.1.3.2. Optimal grid sampling and specifications

Optimal grid sampling must follow Shannon's sampling theorem: a continuous bandlimited function $f(x)$ can be reconstructed from a set of samples $f(n\Delta x)$ if $\Delta x \leqslant \frac{1}{2\nu}$, being ν the function bandwidth. The terrain shape has a bandwidth depending on its complexity. In principle, landforms are complex enough to be considered with unlimited bandwidth, thus making any terrain sampling ambiguous. In practice, landforms are approximated to reconstructible surfaces, having a minimum wavelength $\lambda_{min} < \lambda = 1/\nu$, therefore respecting the Nyquist criterion.

Sampling can be a sparse one, reducing the sampling distance for complex scenarios and increasing it for smooth terrain, or with a fixed spacing. The latter case is the most common one and it is the strategy adopted for the TanDEM-X mission. Since the considered digital elevation model is bidimensional, sampling is differentiated in the longitude and latitude dimensions. The minimum sampling distance in longitude and latitude directions are respectively $\Delta_{\text{LON}} \leqslant \lambda_{\text{LON}}/2$ and $\Delta_{\text{LAT}} \leqslant \lambda_{\text{LAT}}/2$. To encompass the sampling concept into the elevation model, one has to approximate terrain undulations with continuous functions like Fourier series. The function shall be then decomposed in harmonic functions of different wavelengths and the minimum wavelength shall be the one which determines the final model sampling (Pike and Rozema, 1975). This approach is valid for smooth terrains but it does not work for complex terrain like urban areas.

In operational DEM products, the employed technology triggers the sampling value. Two important and standardized requirements are *CE90*, circular error at 90% confidence level, and *LE90*, linear error at 90 % confidence level. They will be better analyzed in the following paragraphs. Depending on the requirements and the capability to accomplish them given the input data, one could decide for the final DEM sampling. For instance, the company DigitalGlobe is producing DEMs at a different post spacing and requirements exploiting optical WorldView data (DigitalGlobe, 2015): 8m, 4m, 2m posting at an absolute vertical accuracy of 8m, 4m, and 2m respectively. Also DEMs generated with LiDAR have a wide range of sampling possibilities depending on the number of points per square meter. In this case, it is not rare to encounter very-high-resolution DEMs with postings of few centimeters. DEMs generated with SAR data follow the same rule. In particular, a possible strategy to determine a reasonable output posting is to evaluate the relative height error given a desired coherence value and the number of looks used in the processing (Bamler and Hartl,

Product	Post Spacing	Absolute CE90 [m]	Absolute LE90 [m]	Relative LE90 [m]
DTED-1	3 arcsec (∼ 90m)	50	30	20
DTED-2	1 arcsec (∼ 30m)	23	18	12
HREGP	0.4 arcsec (∼ 12m)	15	12.4	6.2
HRE08	8 m	10	8	4
HRE04	4 m	5	4	2
HRE02	2 m	3	2	1
HRE01	1 m	2	1	0.5
HRE50	0.5 m	1	0.5	0.25
HRE25	0.25 m	0.5	0.25	0.12
HRE12	0.125 m	0.25	0.12	0.06

Table 2.1.: NGA standards for digital elevation models. DTED stands for Digital Terrain Elevation Data and was used for SRTM mission, HREGP stands for High Resolution Elevation geographic Projection and was adapted for the TanDEM-X mission, and HRE stands for High Resolution Elevation. Several level of HRE are defined and used for photogrammetric and laser DEMs.

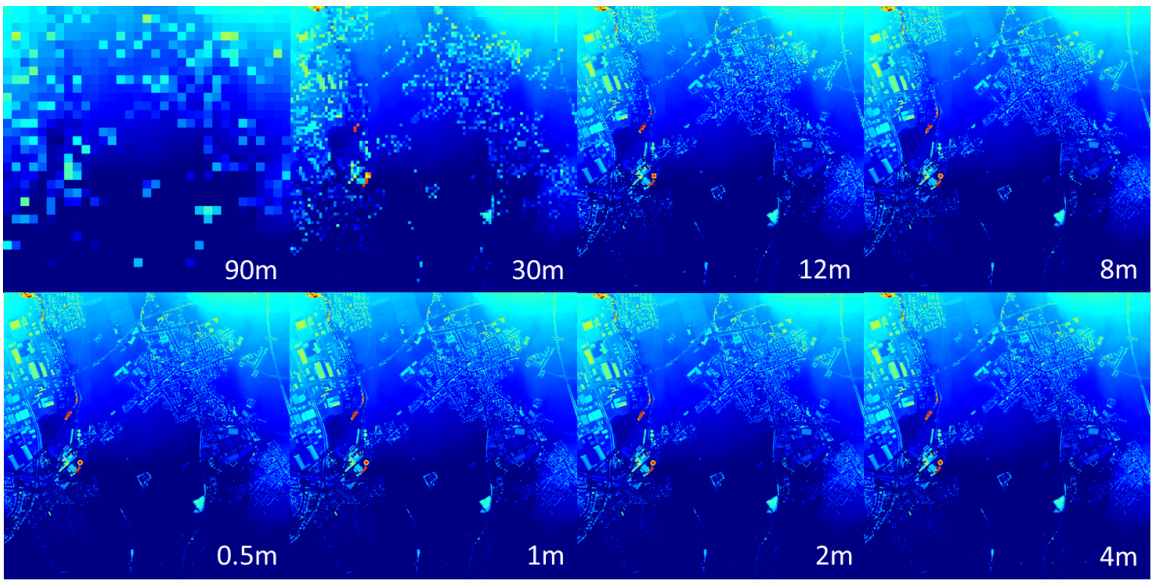

Figure 2.6.: DEMs at a different sampling obtained by interpolating a LiDAR DEM with 0.1 m sampling.

1998).

The USA military agency NGA (National Geospatial-Intelligence Agency) has standardized the specification for DEM at average to very-high resolutions (Heady et al., 2009). Next to file formatting, NGA has defined posting and accuracy parameters, as in Tab. 2.1. To see the impact of sampling in the DEM, the products in Tab. 2.1 are simulated in Fig. 2.6 by subsampling an input LiDAR DEM.

Absolute circular and linear height error Absolute height error is the major quality descriptor of every elevation model. It is generally provided in form of specification (see Tab.2.1). It refers to how close the elevation cell is to the real height. DEM standards usually define a confidence interval, e.g. 90%, in order to discard outlier values. The positional accuracy is defined in the horizontal and vertical dimensions. The horizontal dimension determines the *absolute circular error*, i.e. the radius of a circle in which a specific feature must lie. The vertical dimension determines instead the *absolute linear error*, i.e. the elevation discrepancy between measure and ground truth. The TanDEM-X specification states a 90% absolute circular error of 10 m and a 90% absolute linear error of 10 m (Krieger et al., 2007).

Relative height error Relative height error is the second major quality descriptor. In contrast to the absolute accuracy, it refers to the error between two defined points in the model. For that, it is sometimes specified as *point-to-point* error. As for the absolute specification, it is defined over a confidence interval and in both of the dimensions. The *relative circular error* describes how well the distance between to points in the model is represented. This horizontal error component has a 3 m specification for TanDEM-X at a 90% confidence. Similarly, the *relative linear error* describes the elevation error in between to points. For TanDEM-X, always at 90%, it must be smaller than 2 m for slopes smaller than 20 deg, and smaller than 4 m for larger slopes.

2.1.3.3. InSAR DEM horizontal and vertical resolutions

In the InSAR case, the interferogram generation determines the raw DEM horizontal resolution Ω_r through the independent number of looks used in the processing:

$$\Omega_r = \frac{n_{\text{az}}\delta_{\text{az}}^{gr} + n_{\text{rg}}\delta_{\text{rg}}^{gr}}{2}[m], \tag{2.17}$$

where n_{az} and n_{rg} are the azimuth and range independent number of looks and δ_{az}^{gr} and δ_{rg}^{gr} represent the single SAR pixel azimuth and range ground resolution. The estimation of the independent number of range and azimuth looks is performed considering the common bandwidth after the spectral filtering (see Sec. 2.2.8). Ω_r represents the average of the range and azimuth interferogram resolutions.

The horizontal resolution can also be measured with spectral techniques when an external ground truth DEM is available. Smith and Sandwell (Smith and Sandwell, 2003) and Pierce et al. (Pierce et al., 2006) evaluated the SRTM horizontal resolution by inspecting the spectral coherence between the SRTM DEM and a reference DEM. Their studies reported an horizontal resolution of 1.0-1.6 DEM pixels, i.e. 30-47 m, depending on the local terrain; with higher resolution near sharp edges and corners, and lower resolution in smoother area. More in detail, the spectral coherence is computed as

$$\gamma_{xy}^2(f) = \frac{|S_{xy}(f)|^2}{S_{xx}(f)S_{yy}(f)}, \tag{2.18}$$

where $S_{xx}(f)$, $S_{yy}(f)$ and $S_{xy}(f)$ are the autospectral density of the reference DEM, the autospectral density of the DEM under test and their cross-spectral density, respectively. Eq. 2.18 can be expressed in terms of Signal-to-Noise-Ratio (SNR) as

$$\gamma_{xy}^2(f) = \frac{SNR}{1+SNR}. \tag{2.19}$$

In case of no noise, $SNR = \infty$ and $\gamma_{xy}^2(f) = 1$. Instead, the condition $SNR = 1$ is used to determine the cutoff frequency for which $S_{yy}(f)$ is no longer correlated with $S_{xx}(f)$. This brings

to $\gamma^2_{xy}(f) = 1/2$. The cutoff frequency is represented by $f_{1/2}$. Thus, the estimate of the horizontal DEM resolution with a spectral coherence analysis is[1]

$$\widehat{\Omega}_r = 1/f_{1/2}. \tag{2.20}$$

An additional technique to measure Ω_r is the evaluation of the step response generated by a sharp edge in the DEM. A convolution of a step function (*terrain*) with a boxcar filter of width w (*system impulse response*) generates a ramp with same width of the filter. The horizontal resolution is than the measure of the ramp width. This method requires the presence of edges in the DEM. Pierce et al. (Pierce et al., 2006) tested this technique over the SRTM dataset employed also for the spectral coherence analysis and reported a slightly better resolution, 1.0-1.3 pixels, suggesting that this measure provides a more local estimate of the horizontal resolution. Actually, as described in Sec. 5.2.2, a topographical vertical step yields SAR layover, which is mapped in the DEM with a ramp depending on the layover backscattering components. The relationship between DEM ramp and horizontal resolution is then not straightforward and may bring to high biases in the estimation of Ω_r.

In case of a horizontal resolution higher than the grid sampling, i.e. the resolution numerical value is smaller, the DEM is composed by spatially independent pixels. In the other case, the DEM is composed by spatially dependent pixels, thus encompassing redundant information. The TanDEM-X raw DEM is operationally generated at a grid sampling of about 6 m and has a typical horizontal resolution of about 8-12 m, depending on the local InSAR geometrical configuration.

The vertical resolution depends on the phase noise of SAR data. The phase noise yields a surface random height error, which is also measured with the coherence parameter described in Sec. 2.2.8. Empirical measures of the phase noise impact into the generated DEM can be performed by measuring the surface noise over flat areas. A simple surface noise evaluation is a plane fitting to the surface, or a line fitting for a transect, and a measure of statistical parameters. The surface noise measure for a transect over the flat area of the salty lake Salar de Uyuni, Bolivia, is shown in Fig. 2.7. In this case, the TanDEM-X raw DEM shows a standard deviation of about 40 cm. This test site, composed by a very large and flat surface, is ideal for calibration campaigns and has been extensively used in the commissioning phase of the TanDEM-X mission.

2.2. InSAR DEM error sources

InSAR DEM errors can have several sources, from the system, to the processing chain, up to the environment to be imaged. They affect the interferometric phase ϕ with a component ϕ_{err}, and they can be expressed as height error h_{err}:

$$h_{\text{err}} = \frac{h_{\text{amb}}}{2\pi}\phi_{\text{err}}. \tag{2.21}$$

In this section, the main sources of error for InSAR DEMs are reviewed.

2.2.1. Material property

The terrain to be imaged has a strong impact in the DEM accuracy. Being SAR an active system, i.e. transmitting and receiving energy, it is affected by wave propagation phenomena. Indeed, the wave propagates into the terrain depending on the material property. The measured height, i.e.

[1] The cutoff frequency actually depends on the SNR of the reference DEM. For instance, in case of a DEM with the same noise level than the reference, the cutoff frequency is the frequency for which $\gamma^2_{xy}(f) = 1/4$ (Smith and Sandwell, 2003).

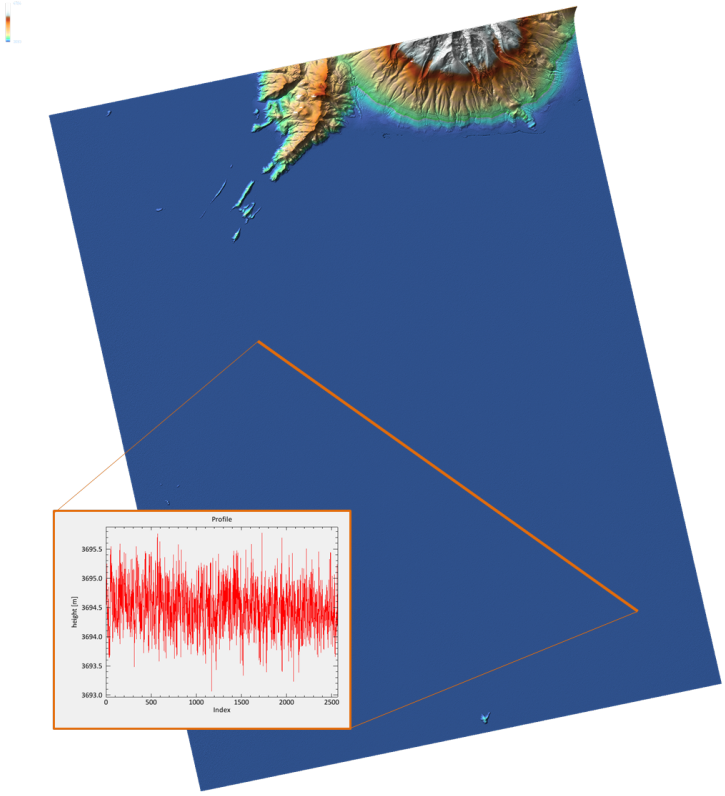

Figure 2.7.: Salar de Uyuni (Bolivia) TanDEM-x raw DEM. At the bottom, a randomly chosen transect shows a standard deviation of about 0.4 m.

the measured scattering phase center, depends on this property and in particular on the complex dielectric constant $\epsilon_r = \epsilon_r' - j\epsilon_r''$.

With more detail, the wave propagates as an electromagnetic field (Richards, 2009):

$$E(r) = E_0 \exp(-\Gamma r) = E_0 \exp(-\alpha_a r - j\beta_a r), \tag{2.22}$$

where E_0 is the magnitude of the field, r is the wave propagation distance and $\Gamma = \alpha_a + j\beta_a$ is the *complex propagation constant*, whose real part α_a describes the field losses due to the medium. It is also called *attenuation constant* and can be approximated as

$$\alpha_a = \frac{\pi}{\lambda} \frac{\epsilon_r''}{\sqrt{\epsilon_r'}}, \tag{2.23}$$

where λ is the wavelength. The approximation is valid when $\epsilon_r'' << \epsilon_r'$. Thus, ϵ_r is the key parameter, since it describes the medium characteristics in relationship to the electric field, i.e. how its power decreases in the medium where it travels. The loss of power density is described by the *penetration depth*

$$\delta = \frac{\lambda}{2\pi} \frac{\sqrt{\epsilon_r'}}{\epsilon_r''}, \tag{2.24}$$

i.e. the value of r for which is power is reduced to $1/e$. Deeper penetration is measured for low bandwidths and low moisture contents (ϵ'' is proportional to moisture).

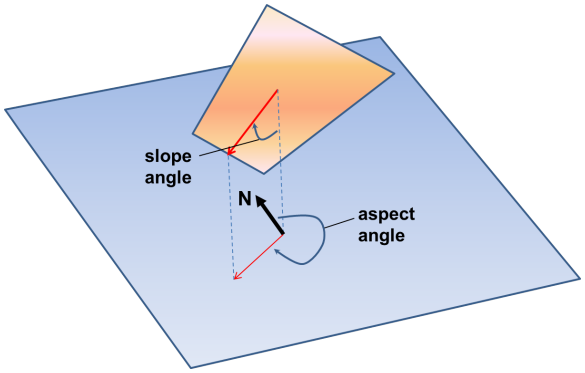

Figure 2.8.: Definition of slope and aspect angles.

δ approximates the measured elevation from the radar system:

$$\widehat{\mathrm{h}} = \mathrm{h_{sup}} - \delta \cos(\theta), \tag{2.25}$$

where $\mathrm{h_{sup}}$ is the terrain elevation and θ is the view angle.
Another meaningful parameter is the *extinction coefficient* κ_e:

$$\kappa_\mathrm{e} = \kappa_\mathrm{a} + \kappa_\mathrm{s}. \tag{2.26}$$

This coefficient describes the total power density loss as the sum of the loss by absorption and the loss by scattering κ_s. Loss by scatter implies inhomogeneities in the medium, i.e. particles of different ϵ, which reduce the backscattered power. Thus, Eq. 2.25 is valid only when $\kappa_\mathrm{a} >> \kappa_\mathrm{s}$. Deeper description about the radio wave propagation can be found in several dedicated books, e.g. (Ishimaru, 1978).

This analysis is particularly relevant for assessing the absolute DEM accuracy. A digital elevation model shall represent the top of the surface, and a penetration into it, thus underestimating the height, can be a major factor in the absolute error.

Investigations and examples of the impact of the material to be imaged into the DEM are provided for agricultural fields and frozen environments in Chapter 3 and 4, respectively.

2.2.2. Geometrical distortions

The understanding of the geometrical distorsions firstly requires the description of the slope and aspect angles.

Slope describes the ratio between vertical and horizontal height changes, or, in other words, the ratio between *rise* and *run* in direction of aspect angle (see Fig. 2.8). It is usually expressed in degree or percentage. Mathematically, it is the magnitude of the first derivative of the terrain, which is modeled with a surface function $S(x, y)$:

$$\alpha = \arctan \sqrt{\left(\frac{\partial S(x,y)}{\partial x}\right)^2 + \left(\frac{\partial S(x,y)}{\partial y}\right)^2}. \tag{2.27}$$

There are various techniques for estimating slopes from Eq. 2.27 (Weih Jr., 2004). The most simple approach is to compute the horizontal and vertical gradients of a DEM cell by employing 4 adjacent cells.

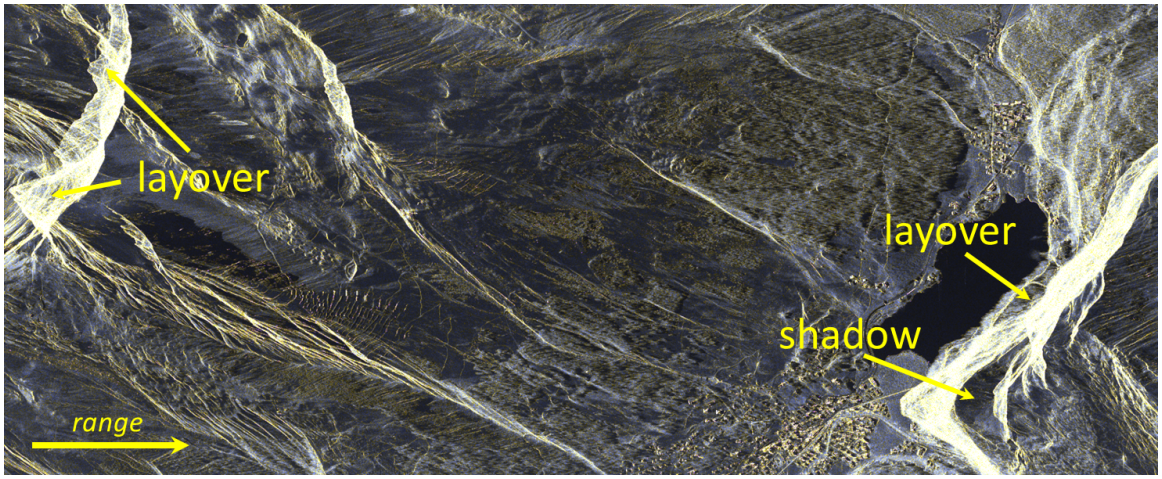

Figure 2.9.: TerraSAR-X composite view of Davos, Switzerland.

Slope is a crucial factor in the evaluation of InSAR DEMs. In fact, SAR has a side-looking view, thus being affected by geometrical distortions like shadow and layover. Shadow occurs in regions not visible by the radar, while layover occurs where multiple terrain portions are imaged in the same cell. Due to the oblique view, in layover areas, higher objects appear at early ranges, thus flipping the normal perspective, e.g. a mountain peak is imaged before its slopes. These distortions are visible in Fig. 2.9, a TerraSAR-X staring spotlight acquisition over the town of Davos in Switzerland. Terrain slope is related to the distortions: layover takes place for slopes larger than the SAR look angle, while shadow for counter-slopes smaller than the complementary of the SAR look angle. The impact of terrain slope in the DEM is studied in detail in the following chapters. In summary, DEM accuracy degrades with slope angle. For instance, TanDEM-X specifications have two different requirements for the relative height error depending on the slope. The TanDEM-X single-pass DEM over Davos is shown in Fig. 2.10. In the layover part of mountains, a slope trend is clearly visible (see the portion at the bottom). This trend is studied in detail in Sec. 5.2.2.

A spaceborne SAR system flies along orbits having a certain heading angle, i.e. the angle between the geographical north and the orbit. Geometrical distortions have their maximum impact for terrain facets oriented towards the sensor. Therefore, aspect angle is also relevant in studying DEM uncertainties. As shown in Fig. 2.8, aspect is a circular variable (0°-360°) describing the orientation of a slope angle:

$$\alpha_{aspect} = \arctan\left(\frac{\frac{\partial S(x,y)}{\partial x}}{\frac{\partial S(x,y)}{\partial y}}\right). \tag{2.28}$$

Also the simplest aspect angle estimation for a DEM pixel employs the four nearest cells.

Layover and shadow impact in the absolute and relative components of the DEM error. Being layover a composition of different terrain patches, its effect requires the decomposition of the signal and the evaluation of the individual components. The analysis of the geocoding stage of the InSAR processor is particularly relevant at the purpose. This evaluation is provided in Chapter 5.2.2. The shadow trend in the DEM is instead difficult to predict, since shadow areas are characterized by system noise.

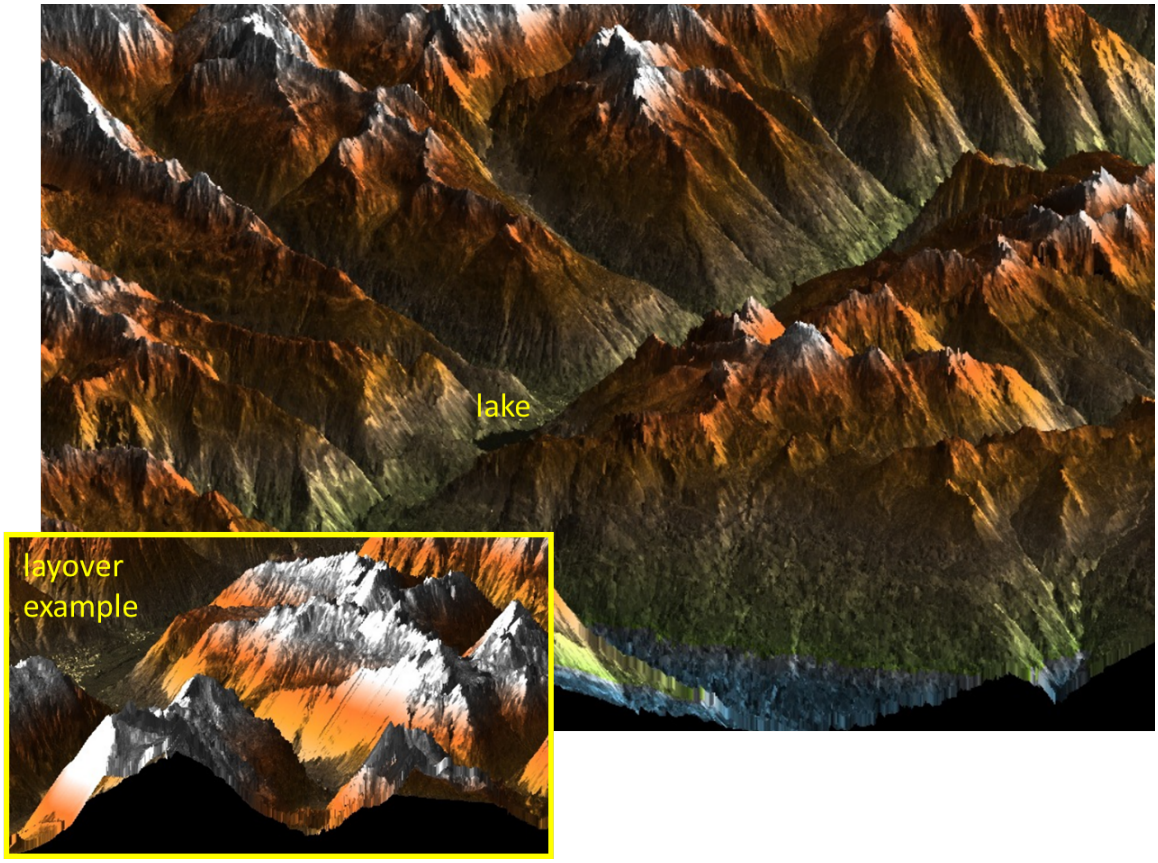

Figure 2.10.: TanDEM-X raw DEM over the region of Davos, Switzerland. Lake well visible in Fig. 2.9 is highlighted here. In the spotlight, an exemplary DEM portion with layover dominance.

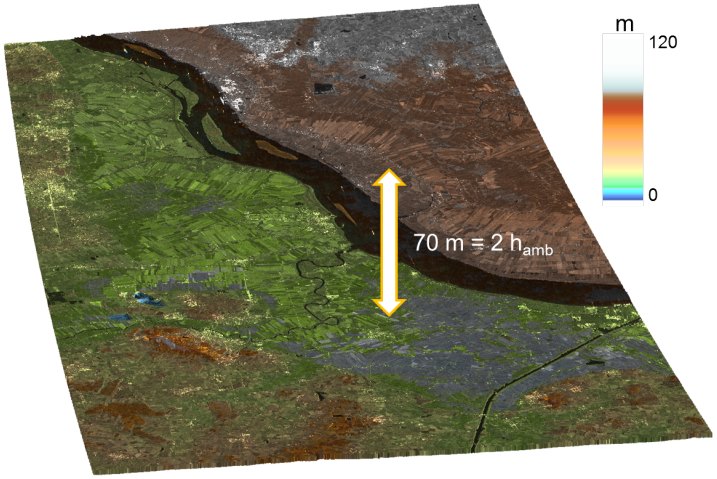

Figure 2.11.: 3-D view of a TanDEM-X raw DEM over the Elbe estuary (Germany). The two sides of the river are mapped with two different heights due to an unwrapping error.

2.2.3. Processing: phase unwrapping

Interferometric phase is wrapped, i.e. defined in the interval $[-\pi, \pi)$. As in Eq. 2.5, the absolute phase must be derived from the wrapped phase with the phase unwrapping operation. Unwrapping is a complex task since it is ill-posed and with multiple solutions. Its operation is based on the integration of the phase gradient estimate along paths (Ghiglia and Pritt, 1998). The basic constraint states that a closed path must start and end at the same topographic height, or, in other words, the estimated gradient field must be conservative. This constraint is not met when the path crosses *branch cuts*, i.e. lines connecting singular points in the phase, also called *residues* or vortex. A residue can be generated by topographical features or phase noise. The first source of residues can be tackled by reducing the system baseline (reducing the number of fringes), while the second by properly smoothing the phase field.

An error in the unwrapping stage may bring dramatic consequences in the produced DEM. Indeed, errors of multiple of height of ambiguities (Eq. 2.3) may be present in the DEM, strongly affecting the absolute error measure (both circular and linear). An example is displayed in Fig. 2.11, where a river separates two flat land regions. Here, the two regions present two different heights, with a discrepancy of 70 m, equal to two heights of ambiguity, due to wrong gradient estimates. Being a major DEM artefact, this error source requires an appropriate detection and post-processing in order to correct for it. A detection technique is presented in Sec. 2.3.2. Phase unwrapping correction requires additional acquisitions at different baselines. The multi-baseline TanDEM-X processing chain, and the TanDEM-X mission itself, are based on multiple InSAR acquisitions (Lachaise et al., 2014).

2.2.4. Processing: phase offset

The absolute phase offset, introduced in Sec. 2.1.2, is a crucial parameter. Indeed, it triggers the geocoding algorithm to a solution for the phase-to-height transformation as part of the estimated topographic phase. An error in its estimation brings biases, stretches and geolocations artifacts in the generated DEM. Even though these errors can be calibrated afterwards with proper references, it is meaningful to provide a correct estimation. An example of estimation impact is represented in Fig. 2.12. The InSAR geometry in the figure has been illustrated in Sec. 2.1.2. An offset in the absolute phase moves the real point on Earth $P1$ to the position $P2$, implying a geolocation error in both the horizontal and the vertical dimensions, and increasing the absolute circular and linear error measures.

2.2.5. Processing: atmosphere

Atmospheric propagation must be considered in the geolocalization. The microwave signal is delayed though the ionosphere and the troposphere, and this delay must be taken into account for a proper geocoding. More in detail, the ionospheric delay, which has a small impact on the geolocation accuracy at X-band, is modeled with a constant delay over the whole scene corresponding to 5 [TECU] (Breit et al., 2010), whereas the tropospheric delay, which is the dominant source of geolocation errors, is parameterized with an hight-dependent model. The model used for the TanDEM-X tropospheric delay is:

$$\Delta R_{\text{tropo}} = \frac{\text{ZPD}}{\cos(\theta)} \cdot \exp\left\{-\frac{h}{H}\right\}, \tag{2.29}$$

where ZPD is the Zenith Path Delay, set to 2.3 m at sea level, h is the height, locally adapted for the DEM pixel, and H is a scale factor of 6000 m.

The incidence angle θ is slightly varying for the master and slave channels: this variation must be taken into account and the correction in Eq. 2.29 must be transformed into a differential one (Krieger et al., 2012). In (Breit et al., 2012) it is reported that in a typical TanDEM-X scenario, for a height of ambiguity of 40 meters and a point on ground at the sea level, the differential slant range

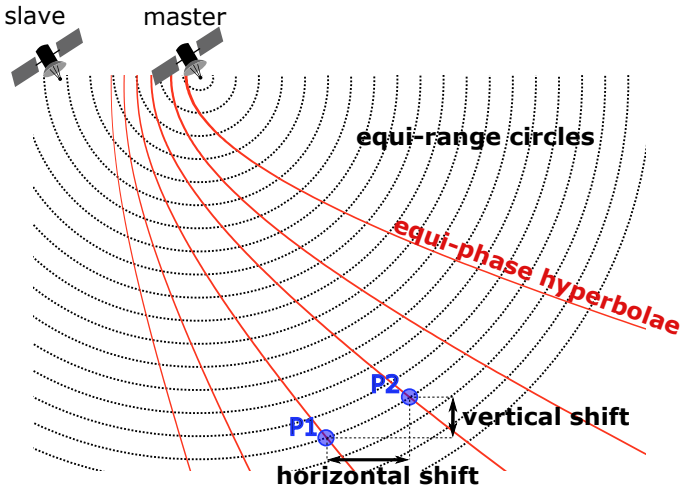

Figure 2.12.: Impact of a wrongly estimated absolute phase offset in the DEM. The point P1 is estimated through the intersection between the interferometric absolute phase, represented in red with iso-curves, and the actual range, represented in black with circles. A change in the phase offset brings the estimation for that specific range to P2.

correction is varying between about 0.5 and 1.5 millimetres for incidence angles varying between 30 and 45 degrees, yielding an absolute height correction varying between 0.7 and 2 meters.

2.2.6. Processing: synchronization

System synchronization is a fundamental operation in bistatic interferometry and it is briefly introduced for the TanDEM-X system. It is based on the use of two independent ultra-stable oscillators (USO). Phase and frequency differential deviations could strongly affect the DEM quality, even yielding a non-producible DEM. The correction must be performed during the SAR screening and directly to the raw data. In (Breit et al., 2011) it has been reported how the TanDEM-X mission well tackles the synchronization through the use of dedicated sync-horns, which are exchanging calibration pulses between satellites, and with a dedicated processing chain which produces no residual phase (and DEM) errors.

2.2.7. Baseline error

Another fundamental system parameter affecting the DEM quality is the baseline between satellites. In the interferometric chain, orbital information is used in every stage which is based on geolocalizations, such as the phase simulation, the geometrical coregistration and, most important, the final geocoding processing step.

The typical baseline trigonometric decomposition is shown in Fig. 2.13. Following the analysis in (Krieger et al., 2007), an error in the perpendicular baseline estimation brings to a DEM error

$$h_{\text{err}} = h\frac{\Delta B_{\perp}}{B_{\perp}}. \tag{2.30}$$

An error $\Delta B_{\perp}$ equal to 1 mm (TanDEM-X baseline specification precision), yields a DEM error h_{err} of a few centimeters for nominal geometries. For instance, a perpendicular baseline of 439 m at an incidence angle of 45 deg yields an height error of ± 2.1 cm. A larger contribution is expected for inaccuracies in the parallel component, yielding height errors of some meters. In this case,

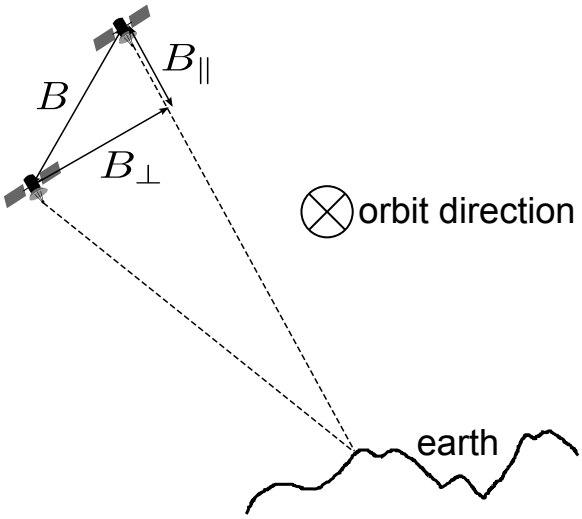

Figure 2.13.: Definition of baseline (B), perpendicular baseline ($B_{\perp}$) and parallel baseline ($B_{||}$). The represented plane is the one perpendicular to the orbits.

$$h_{\text{err}} = \frac{h_{\text{amb}}}{\lambda} \Delta B_{||} \tag{2.31}$$

Moreover, a tilt of a few millimeters per km is also caused by inaccuracies in the parallel component of the baseline.

2.2.8. Coherence decomposition

In InSAR processors, the random error is measured by the coherence parameter. Coherence assesses the quantity of decorrelation that occurs between the two SAR signals. It is defined as the cross-correlation between the two complex SAR images x_1 and x_2 and can be estimated as:

$$\gamma = \left| \frac{\sum x_1 x_2^* \exp\{-j\phi_{\text{known}}\}}{\sqrt{\sum |x_1|^2 \sum |x_2|^2}} \right| \tag{2.32}$$

In Eq. 2.32, ϕ_{known} is a deterministic phase value representing the topography and other known phase trends in the estimation window. This factor must be compensated to accomplish stationarity (Touzi et al., 1999). Given the coherence, the marginal probability density function for the interferometric phase ϕ is derived using *gamma* Γ and *hypergeometric* F functions (Just and Bamler, 1994)

$$\begin{aligned} pdf(\phi;\gamma,L) = & \frac{\Gamma(L+1/2)(1-\gamma^2)^L \mid \gamma \mid \cos(\phi-\phi_0)}{2\sqrt{\pi}\Gamma(L)(1-\gamma^2\cos^2(\phi-\phi_0))^{L+1/2}} \\ & + \frac{(1-\gamma^2)^L}{2\pi} {}_2\text{F}_1(L,1;\frac{1}{2};\phi^2\cos^2(\phi-\phi_0)), \end{aligned} \tag{2.33}$$

where L is the independent number of looks and ϕ_0 is the coherence argument. The standard deviation of the interferometric phase $\sigma_\phi(x,y)$ is derived by integrating Eq. 2.33. The DEM standard error for every range and azimuth samples (r,a) is then calculated, according to Eq. 2.21, as:

$$h_{\text{err}}(r,a) = \sigma_\phi(r,a)\frac{h_{\text{amb}}}{2\pi}. \tag{2.34}$$

The error is proportional with the height of ambiguity: higher heights of ambiguity yield higher errors. There is actually a limit for the height of ambiguity, since lower ambiguities yet yield low standard errors, but the unwrapping stage may be very complex, producing errors well above the theoretical standard ones.

Coherence can be decomposed in several factors (Zebker et al., 1992; Krieger et al., 2007; Martone et al., 2012):

$$\gamma_{\text{tot}} = \gamma_{\text{ss}} \cdot \gamma_{\text{proc}} \cdot \gamma_{\text{system}} \cdot \gamma_{\text{vol}} \cdot \gamma_{\text{temp}} \tag{2.35}$$

Analyzing them one by one:

Spectral shift (γ_{ss}). This term can be further decomposed in the range and azimuth components.

For the range component, the spectral shift theory shall be introduced. The basic concept is that the range spectra of a SAR image is varying depending on the look angle. A look angle discrepancy, as in the cross-track InSAR case, yields a shift in the range spectra, measured as (Gatelli et al., 1994)

$$\Delta f = \frac{f}{\tan(\theta - \alpha)} \Delta\theta, \tag{2.36}$$

where α is the terrain slope and $\Delta\theta$ the look angle difference between slave and master channels. Eq. 2.36 can be rewritten with system parameters:

$$\Delta f = \frac{cB_{\perp}}{\lambda R \tan(\theta - \alpha)}, \tag{2.37}$$

The shift produces spatial decorrelation (also called *baseline decorrelation*):

$$\gamma_{\text{ss}_{rg}} = 1 - \left| \frac{\Delta f}{B_{\text{w}}} \right|. \tag{2.38}$$

This decorrelation can be then expressed as height error by making use of Eq. 2.33 and Eq. 2.34.

An analysis of the decorrelation induced by range spectral shift in a nominal TanDEM-X scenario is shown in Fig. 2.14. The coherence loss is very limited, contained between 0.03 and 0.05. Considering the simulations represented in Fig. 2.14, a coherence loss of 0.03 and 0.05 corresponds to a relative height error of 22 cm and 30 cm for $h_{\text{amb}} = 40$ m and an equivalent number of looks of 25. This error component can be filtered out, but one could even think not to perform this processing step considering the high computational cost, thus taking into account to slightly increase the overall relative height error.

Also for the azimuth component, the common band should be preserved and the non-overlapping parts discarded. Here, the band variations depend on the Doppler Centroid oscillations caused by the satellite's attitude control loop. Similarly to Eq. 2.38,

$$\gamma_{\text{ss}_{az}} = 1 - \left| \frac{\Delta f_{\text{DC}}}{B_{\text{az}}} \right|, \tag{2.39}$$

where Δf_{DC} is the Doppler centroid variation between channels and B_{az} refers to the system azimuth bandwidth. TerraSAR-X and TanDEM-X satellites implement the *total zero Doppler steering* (Fiedler et al., 2005), so that their Doppler discrepancy should be contained within 200 Hz. With this value, and assuming a nominal bandwidth of 2800 Hz, the coherence loss results of about 0.07, i.e. a relative height error of 36 cm for $h_{\text{amb}} = 40$ m and an equivalent number of looks of 25.

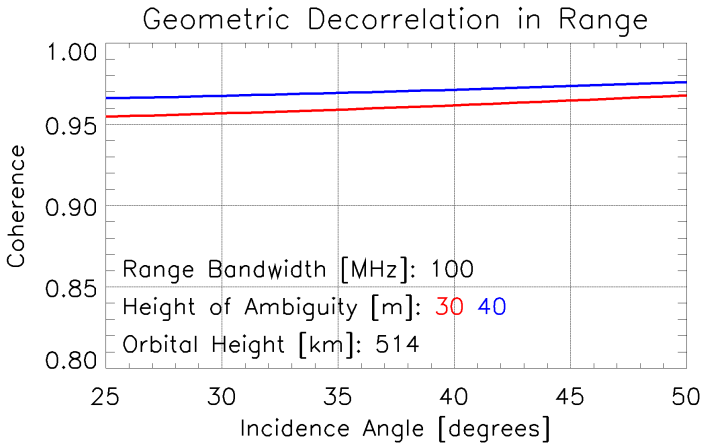

Figure 2.14.: Simulation of coherence loss due to range spectral shift for two nominal TanDEM-X scenarios at height of ambiguities equal to 30 m and 40 m and flat terrain.

Processing (γ_{proc}). The two channels must be coregistered in order to form a coherent interferogram. It is self-evident that a 1-resolution cell-shift brings complete decorrelation, so that the coregistration impact in the coherence shall be considered only for fractions of the resolution cell. For distributed scatterers, a mis-registration of μ_{misr} as a fraction of range or azimuth resolution (the following equation holds for both cases) brings to a coherence:

$$\gamma_{\text{proc}} = \begin{cases} \text{sinc}(\mu_{\text{misr}}), & \text{if } 0 \leq \mu_{\text{misr}} \leq 1 \\ 0, & \text{if } \mu_{\text{misr}} > 1 \end{cases} \tag{2.40}$$

The TanDEM-X cogitation processing stage is built to ensure errors well below the tenth of a pixel (Yague-Martinez et al., 2010). Assuming this error, the coherence loss results in about 0.02.

System noise (γ_{system}). In this component, the characteristics of the system, such as gain factors, quantization, ambiguities and antenna characteristics are included. Encompassing all the noise sources in the Signal-to-Noise-Ratio (SNR), the decorrelation results (Zebker et al., 1992):

$$\gamma_{\text{system}} = \frac{1}{\sqrt{(1 + \text{SNR}_{\text{TSX}}^{-1}) \cdot (1 + \text{SNR}_{\text{TDX}}^{-1})}} \tag{2.41}$$

In (Krieger et al., 2007) it is reported how the TanDEM-X mission is built to keep all the coherence losses in minimal terms, in order of 0.02-0.03.

Volume decorrelation (γ_{vol}). This component is particularly relevant for vegetated areas, and it is related to the penetration in the scattering medium. It is the relative (random) part of the phenomenon studied in Sec. 2.2.1. Its modeling depends on the medium and on the system parameters. A demonstration for agricultural fields and for subglacial volcanoes is presented in Chapter 3 and 4, respectively.

Temporal decorrelation (γ_{temp}). This component, related to the temporal variations of the scattering phase center, is not relevant for bistatic missions. It is only relevant for water surfaces, which decorrelate in milliseconds and for which a DEM generation with nominal TanDEM-X configurations is not feasible.

2.3. DEM uncertainty investigation

Unique and universally recognized standards for InSAR-DEM error investigation do not exist. The American Federal Geographic Data Committee (FGDC) compiled in 1998 a document (Federal Geographic Data Committee, 1998) with error investigation guidelines for the evaluation of photogrammetric DEMs given external references. With the advent of LiDAR technology, the American Society for Photogrammetry and Remote Sensing (ASPRS) compiled in 2004 a version for LiDAR DEMs (Flood, 2004).

InSAR-DEM accuracy strongly depends on the terrain to be imaged. It is senselessness to define investigation standards without taking into account the various issues coming from the complex InSAR system. An unique investigation strategy, e.g. a difference with reference points (Sec. 2.3.1), could be non sufficient to clarify the type of error present in the DEM. The purpose of this section is to revise several novel and well-established methods that will be employed for the investigations in the next chapters.

2.3.1. Difference with reference

The most straightforward way to evaluate the DEM quality is a direct comparison with references, in form of another DEM or in form of ground control points. Although the comparison is made by a simple difference, some question like: *which reference must be used? how many points are needed for a consistent analysis? where must they lie? which descriptor is more appropriate?* arise. The aforementioned specifications (Federal Geographic Data Committee, 1998; Flood, 2004) answer to these questions. A summary can be also found in (Russell and Congalton, 1998). In the following, they are briefly described with an extension to the InSAR case.

Reference independency and sources. It is clear that the reference must be originated from a different acquisition than the one under test. The chosen reference system (ALS, SAR, camera) can be the same. Nevertheless, calibration sources should not be considered as reference. For instance, ICESat points or GPS measures used in DEM calibration process should not be employed as reference. The reference accuracy is also an issue. Whereas the FGDC specifications generally state that the highest accurate reference shall be employed, the ASPRS specifications state that reference accuracy must be one to three times better than the one under test. This second specification is reasonable. In the final TanDEM-X DEM case, a corrected version of SRTM with ICESat has been employed for calibration. Thus, neither SRTM (which has also a lower accuracy, and must be then discarded) nor ICESat should be employed for comparison. In the following chapters, the references employed for the TanDEM-X verification are LiDAR and GPS measures.

Number and location of reference points. In case the reference is another DEM at a higher accuracy, the number of points is not an issue since the comparison is done one-to-one after resampling the reference in the same grid of the DEM under study. Contrariwise, in case the reference is composed by sparse ground truth points (also called Ground Control Points (GCPs)), then their number is a statistical issue. In presence of normally distributed errors, a valid Root Mean Square Error estimate (see next paragraph) requires a minimum of 100 samples to estimate the error distribution close to its exact solution, with its standard deviation within 5% of its truth (Chai and Draxler, 2014). To be noticed, the DEM accuracy is often varying depending on the land cover class. A proper comparison should then comprise a certain number of points per class. Since collecting 100 elevations per class can be a hard and expensive job, especially taking into account that the points should be coherently distributed in the area under test, in many cases a fewer number is often accepted. For instance, in the FGDC specification, a minimum number of 20 points per class is accepted, even if this number is not statistical consistent. In the InSAR case, it is important to avoid

to place GCPs in geometrical distortion areas (layover, shadow), where the DEM is inaccurate and the difference result would result strongly biased.

Root mean square error. The reference discrepancy needs a quantification. In the mapping field, the standardized value for the vertical and horizontal positional accuracy is the root mean square error. RMSE is defined as:

$$\text{RMSE} = \sqrt{\frac{\sum_i^n \left(x_i - x_{\text{ref}_i}\right)^2}{n}}, \tag{2.42}$$

where x_i and x_{ref_i} are the i-th sample of the DEM and the reference, respectively. RMSE is of particular interest since it fully characterize the error distribution, but just in case of normally distributed errors with zero-mean. Another used statistical descriptor of the DEM error is the standard deviation, which describes about the 68% of the normal population:

$$\widehat{\sigma}_{\text{err}} = \sqrt{\frac{\sum_i^n \left(x_i - x_{\text{ref}_i} - \overline{e}\right)^2}{n-1}}, \tag{2.43}$$

where $\overline{e}$ is the mean error. In DEM specifications, a confidence interval is often defined for the error. Keeping the Gaussian case, the 90% probability level is defined as $(1.645 \cdot \widehat{\sigma}_{\text{err}})$ and the 95% as $(1.960 \cdot \widehat{\sigma}_{\text{err}})$.

The FGDC standards created several scientific discussions among mapping researchers. First, it is stated that RMSE is a measure of the mean vertical error $\overline{e}$, so that in Eq. 2.43 RMSE is used instead of $\overline{e}$ (Russell and Congalton, 1998; Federal Geographic Data Committee, 1998). Second, RMSE is also used in defining the 95% confidence interval as $(1.960 \cdot \text{RMSE})$. Consequently, several modification suggestions have been proposed. In particular, Zandbergen (Zandbergen, 2008) recommended that:

1. DEM error specifications should not use a single descriptor, such as RMSE, to characterize the error in spatial data. This over simplifies the complexity and distribution of common spatial data types.

2. The assumption of normality of DEM errors is not valid for most of the spatial types and must be reconsidered. For instance, this is also the case of the urban SAR case investigated in Chapter 5. Also the confidence interval defined as $(1.960 \cdot \text{RMSE})$ must be corrected.

3. Measures characterizing other error distributions should be taken into account. For instance, Chai and Draxler (Chai and Draxler, 2014) compared RMSE and the simple mean absolute value, which is more suitable for Laplacian distributions:

$$\text{MAE} = \frac{1}{n}\sum_i^n \left|x_i - x_{\text{ref}_i}\right|. \tag{2.44}$$

   A difference between MAE and RMSE is that MAE uniformly weights the errors, while RMSE penalizes errors with high absolute value due to the quadratic exponent.

4. A number of GCPs of 20 is insufficient to characterize the error.

2.3.1.1. State-of-the-art

Being a difference with a reference an easy and standard operation, hundreds of studies report about DEM uncertainty investigations by employing this technique. Most of them are linked to specific applications which are using the DEM, like for forest mapping with TanDEM-X by Solberg et al. (Solberg et al., 2013) and for urban areas mapping with TanDEM-X by Rossi and Gernhardt (Rossi and Gernhardt, 2013) (see Chapter 5), both using laser scanning as reference. Some studies have been performed to validate SRTM DEMs, independently of the chosen application. The use of external references for the inspection of the SRTM DEM horizontal resolution has been performed by Smith and Sandwell (Smith and Sandwell, 2003) and Pierce et al. (Pierce et al., 2006). SRTM vertical accuracy has been investigated by Sun et al. (Sun et al., 2003) and Carabajal and Harding (Carabajal and Harding, 2005), who used LiDAR data to validate SRTM heights.

2.3.2. Phase unwrapping control map

In Sec. 2.2.3, the phase unwrapping stage has been briefly introduced and found as possible source of relevant errors in the DEM. The *Phase Unwrapping Control Map* (PUCM) (Rossi et al., 2012) gives a visual overview of the phase unwrapping errors.

This map is generated using the histogram computed for the absolute phase offset estimation. As described in Sec. 2.1.2, in presence of one or more phase unwrapping errors, the histogram is composed of several lobes. The PUCM is generated by masking the lobes not used for the phase offset estimation, through a local minima search. A standard Red-Green-Blue (RGB) color table is then imposed to the map, centered on the estimation value. Therefore, by visually inspecting the map, one can have a visual impression of the quality of the InSAR DEM: if this map is green in its entirety, then the phase unwrapping operation worked well and the final DEM is expected to have no unwrapping errors. The presence of red/blue color is also meaningful, as the main lobe shape can be visually comprehended: a strong presence of these colors stands for a large estimate variance (wide lobe). Additionally, the lobe structure can be also derived since the color map is linear. A PUCM derivation example is presented in the next paragraph.

Finally, a quality parameter, derived exploiting the comparison of the interferometric and the stereo-radargrammetric measurements, is derived. It is named *quality ratio* (q_{ratio})

$$q_{\text{ratio}} = \frac{p_{\text{tot}} - p_{\text{out}}}{p_{\text{tot}}}, \tag{2.45}$$

where p_{tot} is the total number of pixels of the radargrammetric control map and p_{out} is the number of masked pixel outside the main lobe. The q_{ratio} is a novel and useful parameter for performance assessment as it gives to the ground segment, i.e. the facilities competent for the acquisition, processing, distribution and archiving of the satellite data, the percentage of false heights to be corrected in a second stage. It has been and it is currently extensively used in the TanDEM-X DEM production chain.

Processing example. An operational processing example helps to better understand the algorithms presented in Sec. 2.1.2. The considered acquisition was taken on April 11, 2011, over the Cordillera Central Mountains, Peru. The main parameters are outlined in Tab. 2.2.

The SAR amplitude image of the master channel is shown in Fig. 2.15. The scene is mountainous, composed of several peaks and valleys, presenting all the typical SAR geometric phenomena due to the side looking geometry: layover, shadow and foreshortening. The interferometric average coherence is 0.65. It is a mean over all the scene, including the problematic areas affected by geometrical distortions.

The SAR coregistration processing step can be performed in three ways, as outlined in Sec. 2.1.2.1. In Fig. 2.16(a) the three different areas are represented in violet (coherent cross-correlation), blue (incoherent cross-correlation) and yellow (geometric registration). The percentage of the three

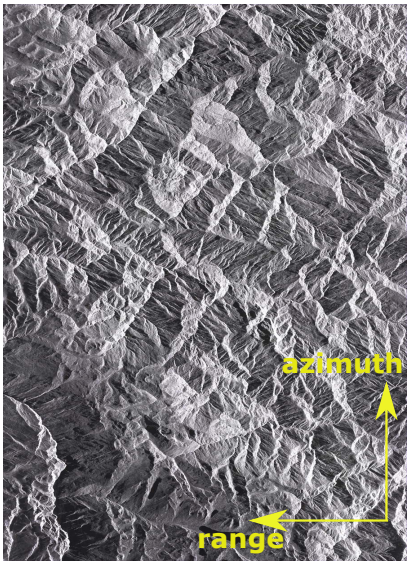

Figure 2.15.: Processing example: SAR amplitude image of the master channel.

methods is respectively 76%, 21% and 3%, or, expressing in number of patches, 86000, 24000 and 3300. At a first sight, the incoherent estimates are located in the problematic areas and the geometric ones where the backscattering is very low. The stereo-radargrammetric shifts computed at this stage are shown in slant range coordinates in Fig. 2.16(b). They are the basis for the generation of the *radargrammetric DEM*. The parallax effect is clear through the range ramp, spanning about two pixels.

The processing continues with the interferogram generation and the phase unwrapping stages. The difference between the unwrapped phase and the stereo-radargrammetric one (Eq. 2.9), generated exploiting Eq. 2.8 with the shifts in Fig. 2.16(b), is shown in Fig. 2.16(c). This map is the foundation for the absolute phase offset estimation through its histogram exploitation (Fig. 2.17). Although from the map it is possible to visually see two homogeneous areas which are different from the mean at the bottom left and right, in the histogram those regions are masked by noise. Moreover, the standard deviation of the histogram is considerably high: 28.6 radians. From the difference's histogram it is thus not possible to find any phase unwrapping error directly. When a median filtering of size 5x5 is iteratively applied for noise reduction, the histogram main lobe is highly compressed, reaching a variance of 2.24 rad. The filtering operation allows the detection of two secondary peaks, whose underlying area is colored in yellow in Fig. 2.17. These small peaks correspond to the regions at the bottom left and bottom right affected by the PU errors, caused by the shadow area surrounding them. The peak detection is performed with a local minima/maxima search.

Parameter	**Value**
Central Incidence Angle	47 deg
Perpendicular Baseline	140 m
Height of Ambiguity	60 m
Average Coherence	0.65
q_{ratio}	94.2

Table 2.2.: Main parameters of the Cordillera Central Mountains acquisition used as test site.

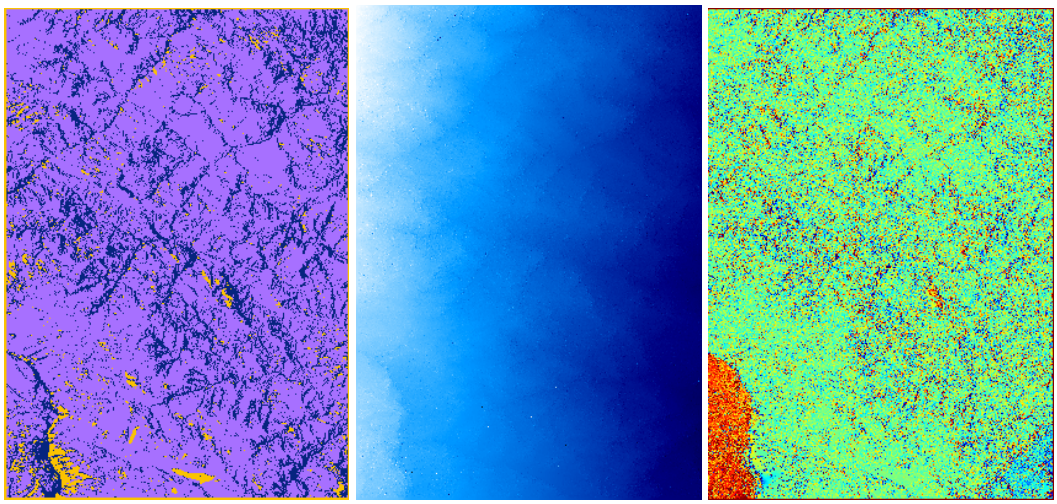

(a) coregistration map (b) radargrammetric shifts (c) phase difference

Figure 2.16.: Processing example: (a) ITP SAR Coregistration Map. The purple, blue and yellow colors represent respectively the estimate from coherent cross-correlation, incoherent cross-correlation and orbital information. (b) Stereo-radargrammetric shifts derived from the coregistration processing step. The color scale is saturated between -1 [pixel] (blue) and +1 [pixel] (white). (c) Stereo-radargrammetric and unwrapped phase difference. The color scale is a linear RGB saturated between -200 and 0 radians.

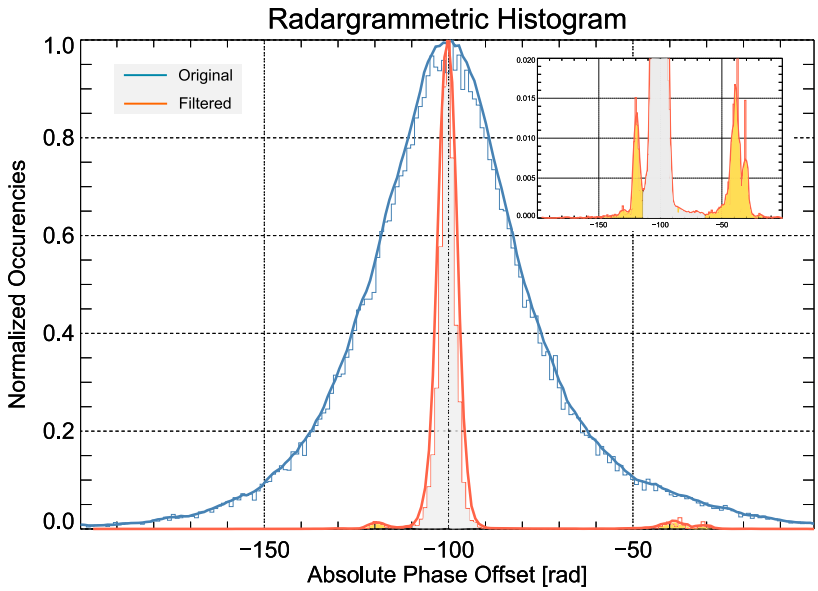

Figure 2.17.: Processing example: Histogram of the phase difference (blue) and its filtered version (orange). In grey the area corresponding to main unwrapped region, in yellow the area corresponding to phase unwrapping errors. In the top right window, a zoom over the secondary peaks is highlighted.

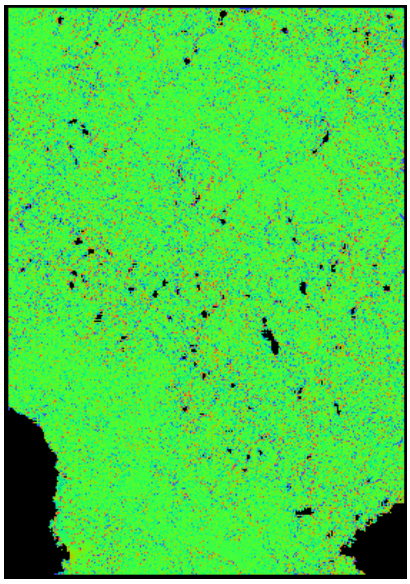

Figure 2.18.: Processing example: PUCM. The unmasked area has a RGB color scale centered at the maximum of the histogram main lobe.

The detection of false heights is visually represented in the radargrammetric control map in Fig. 2.18. Two local minima were found for $m_1 = -111.8$ and $m_2 = -87.7$ radians; values outside the range $[m_1, m_2]$ are masked in black. The q_{ratio}, computed as in Eq. 2.45, is 0.942, meaning that about the 6 % of the scene has a wrong terrain height (the masked areas). Looking the blue and the red spots in Fig. 2.18, it is possible to see how these noisy estimates, lying at the extreme parts of the main lobe of the histogram in Fig. 2.17, correspond in fact to regions for which incoherent or geometric methods were used in the coregistration operation, as shown in Fig. 2.16(b). Beside the two areas located at the south-west and south-east of the acquisition, also some small regions are outside the main lobe range. Comparing this small black patches with the map in Fig. 2.16(c), it is noticeable their matching with geometrical coregistration shift estimates. The portion of the scene used for the absolute offset estimation is the unmasked area for which a coherent cross-correlation operation was used in the coregistration processing step.

The final Raw DEM is represented in a three dimensional view in Fig. 2.19. The detected phase unwrapping errors are regularly geocoded, i.e. no voids are generated, and will be corrected in a second stage with the help of additional acquisitions (Lachaise et al., 2014).

2.3.2.1. State-of-the-art

The phase unwrapping control map and the quality ratio are novel instruments, created for the TanDEM-X ground segment with the purpose to control in real-time, i.e. not in a post-production stage, the height accuracy of the single-baseline DEM and to calculate the absolute phase offset in order to exclude from its computation wrongly unwrapped areas. The only comparable processing chain is the one used for the SRTM mission, the first dedicated to the DEM production on a semi-global scale. The SRTM data processing has been performed by JPL (Farr and al., 2007) for C-band data and by DLR (Rabus et al., 2003) for X-band data. Both of the interferometric processors do not consider an in-processing check of possible phase unwrapping errors prior to the geocoding stage. This has actually an impact in the phase offset estimation, since the consideration of unwrapping artifacts in the offset estimation yields phase offset biases. These biases bring to a generation of DEMs with geolocation errors depending on the unwrapping error extension. In the SRTM pro-

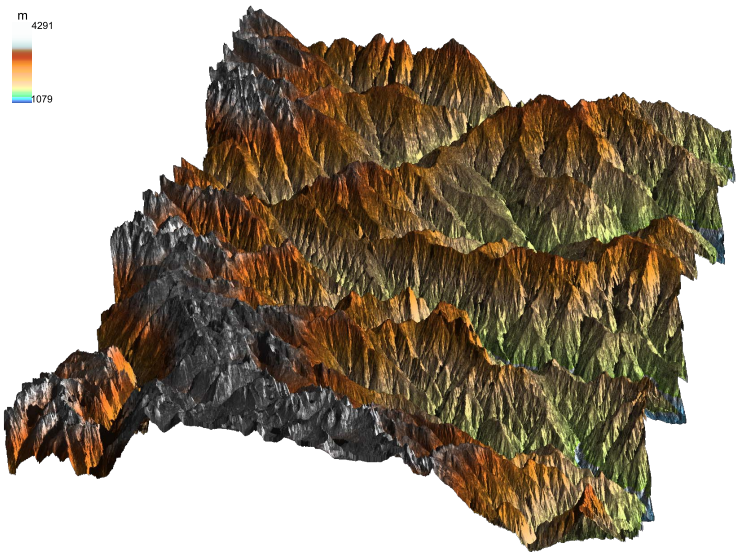

Figure 2.19.: Processing example: three dimensional view of the Raw DEM generated with the acquisition taken on the 11th April, 2011, over the Cordillera Central Mountains in Peru.

cessing, these geolocation errors have been corrected in a second stage, during the post-calibration and tile mosaicking. Remaining unwrapping errors have been detected in the DEM with thresholding techniques and filled with invalid data. Nevertheless, not all the artifacts have been corrected and phase unwrapping height jumps are still present in the database. For that, NGA initiated a search of unwrapping artifacts in the DEM (Ham, 2005) and JPL is currently enhancing the overall elevation model (JPL, 2014).

2.3.3. Slope and aspect 2-D PDF plot

SAR systems cannot map all possible terrain slopes due to the intrinsic side looking view. As outlined in Sec. 2.2.2, shadow and layover zones strongly affect the output DEM, making it unreliable at these positions. The key factor to identify geometrical distortions is the local incidence angle θ_{inc}. This angle is defined as the angle between the SAR antenna pointing vector and the normal to the terrain surface. Shadow is defined for $\theta_{\text{inc}} > 90°$, whereas layover for $\theta_{\text{inc}} < 0°$ (in the aforementioned vector ordering). The terrain descriptors impacting in this geometrical evaluation are slope and aspect. Eineder (Eineder, 2003b) reported about a way to represent the SAR visibility given all the possible slope/aspect combinations by using a plot in cylindrical coordinates. The circle spans all the possible aspect angles while the ray module represents a slope, with the null slope being the center of the plot. When plotting the SAR visibility in that plot, an eye shape is forming up. This plot takes than the name *slope and aspect eye plot* or more generally *slope and aspect 2-D Probability Density Function (PDF) plot*. An example is shown in Fig. 2.20. The inclination of the *red eye* is given by the system heading angle.

The slope and aspect eye plot is particularly useful in the DEM inspection. An external DEM reference can be represented in terms of slope and aspect for every DEM pixel. Given the SAR geometry, the eye borders can be easily depicted by exploiting the relationships described above. After coregistering the reference with the DEM under test, pixels lying outside the eye shape can be considered poorly accurate since lying in shadow or layover regions. This simple method to tag

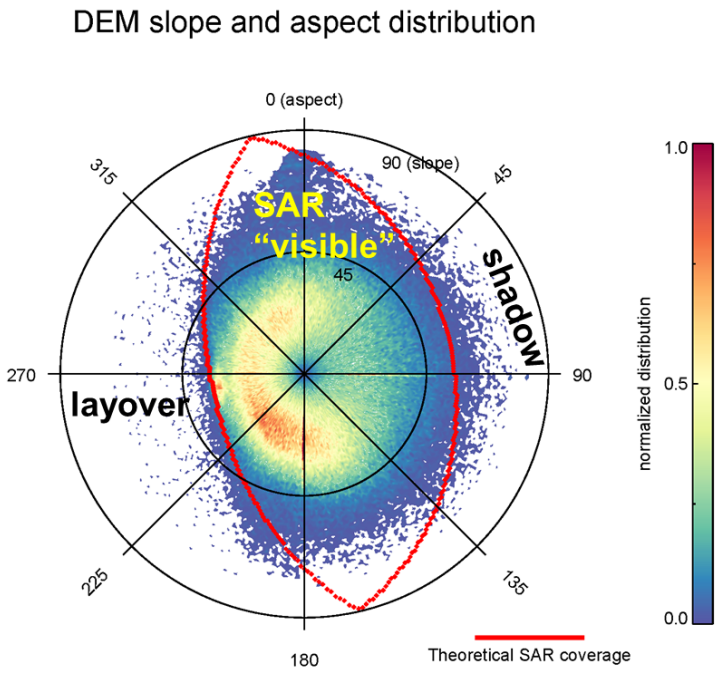

Figure 2.20.: Slope and aspect eye plot example.

inaccurate pixels actually takes into consideration just slopes responsible for the layover (and not the passively lay-over ones), and does not take into account passive shadow slopes (Kropatsch and Strobl, 1990).

When an external DEM is not available, also the produced DEM can be inspected in the same way. In this case, the inspection is more qualitative than quantitative, for instance to check the DEM pixel distribution (to be stressed: layover and shadow areas are not well imaged in the generated DEM, which misrepresents slope and aspect estimations). Pixels situated outside the SAR visibility eye can always be considered as inaccurate and this plot can then be seen as an additional instrument of DEM accuracy inspection. In Fig. 2.20 an example of InSAR DEM distribution is shown. DEM noisy pixels located outside the theoretical SAR coverage. Other usage examples are described in Chapter 4.

2.3.3.1. State-of-the-art

The impact of terrain slope and aspect in DEM accuracy is a recurrent research topic for every kind of DEM source (e.g. (Bolstad, 1994; Gorokhovich and Voustianiouk, 2006; Toutin, 2002)). Also the impact of DEM accuracy in slope and aspect estimation is a studied topic (e.g. (Zhou, 2004; Chang and Tsai, 1991)). Analysis of slope and aspect impact in InSAR DEM accuracy have been performed for instance by Ludwig and Schneider (Ludwig and Schneider, 2006), who used a reference DEM for the evaluation. The slope and aspect 2-D PDF function has been used by Deo et al. (Deo et al., 2015) to test the accuracy of a fusion of two TanDEM-X raw DEMs acquired in different geometries.

2.3.4. Geometrical distortions map

Strictly linked to the previous section, shadow and layover can be identified during the InSAR processing. Classical estimation techniques employ an external DEM for that purpose (Kropatsch

and Strobl, 1990). A reliable estimation must be performed by using a similar or higher resolution DEM than the one under generation. This is obviously against the sense of DEM production. Thus, very often a freely available reference is employed for that purpose. This is the case of the TanDEM-X DEM production (Rossi et al., 2010; Rossi et al., 2012), where STRM is employed to tag geometrical distortions. Being SRTM a lower-resolution source, layover and shadow zones result underestimated. In particular, in ITP, shadow is estimated during the synthetic fringes computation. A change of sign for the gradient of the synthetic phase in range direction implies a direct shadow area; the indirect shadow is detected with a local phase search considering as boundary the phase value of the near direct shadow pixel. This information is then geocoded. The layover computation is made in the geocoding processing stage, analyzing the lack of monotony of the slant-range function through the exploitation of the mapping matrices relating a SAR coordinate to a geographic coordinate.

The exploitation of the geocoding mapping matrices brought to a novel layover detection technique, valid just for urban DEMs (Rossi and Eineder, 2015). This technique is of particular interest since it identifies non-accurate portion of DEMs - building layovers - without the use of external supports. A complete description of the algorithm is in Chapter 5.4.2.

2.3.4.1. State-of-the-art

The impact of layover and shadow into the interferogram, and thus into the DEM, has been studied by Eineder (Eineder, 2003a), who simulated the geometrical distortions through geometrical relationships. In this dissertation, a special focus is for the detection of layover generated by buildings. There are a few studies on this topic, since the quality of urban DEMs is strongly related to the sensor resolution, and still single-pass InSAR data is not reaching accuracy levels of optical and laser scanning data, for which a much larger number of research studies have been reported. The first study of layover detection has been proposed by Bickel et al. (Bickel et al., 1997), who modelled the building SAR layover backscattering into the interferometric coherence. A general modelling of layover into the coherence has also been reported by Wilkinson (Wilkinson, 1998). Multi-pass InSAR can not only allow the detection of layover areas, but also the layover solution and decomposition (e.g., (Gini et al., 2002; Zhu and Bamler, 2010)). Only with the availability of spotlight TanDEM-X data some more study has been reported. Thiele et al. (Thiele et al., 2013) built a detector based on the phase trend in layover areas, i.e. a phase ramp, while Guo and Zhu (Guo and Zhu, 2014) reported about a detector based on coherence thresholding.

2.3.5. Temporal analysis

In some cases, a couple of DEMs from the same source, or even more, are available for a specific area. Being acquired with the same instrument, they cannot be used for absolute error studies, but they can be exploited for relative error assessments. For instance, in (Rizzoli et al., 2012), a couple of TanDEM-X DEMs is employed to demonstrate the successful accomplishment of the relative height error specification with an inspection of the histogram of the difference among them.

DEM calibration is probably the most important processing step of any multi-temporal elevation study. Uncalibrated data provides misinterpretations of the geophysical outcomes. Calibration can be performed as an in-processing or as a post-processing step. Although the novel method proposed in Sec. 2.1.2 is a feasible solution for a single DEM calibration, it should be applied with precautions for a temporal stack of DEMs over the same area. This is because every single DEM absolute phase offset is independent and based on the local InSAR geometry, and baseline inaccuracies may vary between geometries, thus producing absolute height differences between DEMs. For this reason, the calibration using a common reference is a more favorable solution. On the one side, if the purpose is to check topographical changes relative to one of the acquisitions in the data stack, then the quality of the reference is not important and a simple ellipsoidal model at a certain height can be employed. On the other side, if multiple sources are employed and the

absolute elevation of the data is an issue, then a reliable source shall be taken for calibration, as SRTM or TanDEM-X elevation models.

A peculiar use of temporally acquired InSAR acquisitions stands for the investigation of dynamical Earth changes. These changes may be generated from hazards, from human interventions or simply from natural life cycles. In all the cases the uncertainty investigation goes, in a certain sense, towards an inspection of change detections by analyzing differences, which requires absolutely calibrated DEMs. In particular, in the first case, for natural hazards, the uncertainty investigation can be locally adapted to the hazard under test, with cross-checks on the impact of the hazards with other sources or with temporal geophysical models. In the second case, the human intervention is well suitable for change detection algorithms in the DEM and their quality assessment. The third case relies on the growth of plants. Also here, the uncertainty analysis is based on the temporal inspection of geophysical models and external ground truth measures. The temporal reliability of DEMs is a principal contribution of this dissertation and is largely analyzed in the following chapters.

2.3.5.1. State-of-the-art

Temporal DEM accuracy analysis with TanDEM-X is quite a new topic due to the recent availability of data. Next to the studies reported in this dissertation, the work in (Antropov et al., 2015) is similar in purposes and results to the inspection in Chapter 3, with an inspection of the potential of dual-pol TanDEM-X for boreal forest height estimation. Also temporal volcano shape changes have been reported with TanDEM-X. Lava discharge rates at Kilauea Volcano in Hawai'i (USA), volumetric changes at the lava dome of Merapi volcano in Indonesia and lava flow volumes at Nyamulagira volcano in D.R. of Congo have been investigated in (Poland, 2014), (Kubanek et al., 2015) and (Albino et al., 2015), respectively.

2.4. Discussion and conclusions

This chapter presented the fundamentals of the uncertainty evaluation of InSAR DEMs.

First, the focus has been posed on the production InSAR processing chain and in particular on the coregistration, absolute phase determination and geocoding algorithms. The coregistration stage is a processing step in common with stereo-photogrammetric and stereo-radargrammetric DEM productions. On a certain sense, InSAR processing continues where the stereo processing finishes. Indeed, the coregistration shifts are the basic input for a photo/radargrammetric DEM generation. The largest contrast is made by the shift resolution. Whereas photogrammetric shifts allows the definition of a high-resolution DEM, the InSAR ones permit the delineation of a coarse-to-medium-resolution DEM, since they are generated by averaging a consistent number of pixels. Nevertheless, this coarse DEM has been found to be a very useful instrument during the processing: it allows the estimation of the absolute phase offset, a crucial parameter in the InSAR processing, and is the primary input for a novel accuracy-check instrument named Phase Unwrapping Control Map (PUCM). PUCM has been operationally integrated in the TanDEM-X processor at the DLR processing facilities. Another common processing stage, for all the systems, is the orthorectification/geocoding. Although this stage may seem a standard one and not particularly relevant, its exploitation reveals the source of possible DEM artifacts. For instance, for urban scenarios, the geocoding exploitation allows the definition of a layover detector.

Second, general considerations about the DEM grid sampling and DEM resolution have been provided. DEM grid sampling is a common issue in DEM production and various format specifications exist. Optimal sampling must follow the sampling theorem, thus being dependent on the local terrain undulations. However, a common sampling strategy is to define a grid with a specific

pixel sizes and to provide one elevation value per pixel. The grid is defined according to the sensor resolution and the desired specifications. In the TanDEM-X case, the grid sampling is 12 m for the final product. This grid allows the accomplishment of the relative height error specification for a coherence of about 0.5 and a nominal baseline configuration.

The DEM resolution evaluation is also an important assessment. Resolution depends on the system processing parameters and can be estimated for its horizontal component with spectral techniques, given a ground truth reference. The vertical component depends on the intrinsic SAR phase noise. The investigations in the following chapters reveal an horizontal resolution of about 9-10 m and a vertical one in the decimetric order for the best scenario.

Third, posing the focus just on InSAR systems, the error sources have been investigated. This investigation settles the foundation for the inspections presented in this dissertation. Electromagnetic wave propagation into the material is a major source for absolute discrepancies with references at the surface top. TanDEM-X investigations over rice fields and glaciers in Part II will demonstrate just that. Geometrical distortions strongly impact high terrain slopes, such as mountainous terrains and buildings. InSAR processing can affect over many faces the produced DEM. Sensible system settings, as the synchronization link, may have larger impacts, even bringing to blank DEMs for every terrain configuration. Also the system baseline has a fundamental importance, on the one side by triggering the sensibility to possible unwrapping errors, and on the other side by affecting the generated DEM in case of an inaccurate estimation. A popular parameter for the uncertainty assessment remains the interferometric coherence. Dozens of studies have been performed about decomposing it in several error sources.

Finally, the uncertainty assessment techniques employed in the next chapters are introduced. The classical technique is a direct comparison with higher-resolution references. The reference choice and distribution (in case of sparse points) have been subject of study with an extension of the ASPRS LiDAR specification to the InSAR case. Every study tends to provide the RMSE as the only DEM quality parameter. Actually, RMSE provides a sufficient error characterization just in case of Gaussian distributed DEM errors. In the thesis framework, also the geometrical distortions detection, yielding inaccurate DEM portions, plays a big role and it is further investigated. In particular, layover and shadow areas present large artifacts in the generated DEM. They can be predicted by inspecting the terrain slope and aspect. The specific case of building layover will be analyzed in depth. Last but not least, temporal localization is also of fundamental importance. The uncertainty measure of dynamically changing terrains must be located in time to properly characterize it due to the varying electromagnetic properties of the medium. Here, it will be shown that the uncertainty measure can also be validated with geophysical parameters, next to the standard validation technique which exploits ground truth data.

Part II.

Investigations

3. TanDEM-X uncertainty investigation over smooth terrains: the Lake Gala case study

This chapter summarizes the paper in Appendix A.2: Rossi, C., and Erten, E., **Paddy-rice monitoring using TanDEM-X**. *IEEE Transactions on Geoscience and Remote Sensing*, 53(2), 900-910, 2015 (Rossi and Erten, 2015).

The polarization study in Sec. 3.4 is summarized from the coauthored paper in appendix A.3: Erten, E., Rossi, C., Yuzugullu, O., **Polarization Impact in TanDEM-X Data Over Vertical-Oriented Vegetation: The Paddy-Rice Case Study**, *IEEE Geoscience and Remote Sensing Letters*, 12(7), 1501-1505, 2015 (Erten et al., 2015).

3.1. Inspection placement in the thesis framework and relevance

The investigation presented in this chapter deals with smooth terrains, and in particular with the capability of TanDEM-X to represent agricultural fields. Smooth terrains are intended as composed by flat terrains or slowly varying and small slopes. They are generally not affected by geometrical distortions or phase unwrapping errors, therefore their elevation accuracy is usually very high. The uncertainty assessment is addressed by checking the material impact in the absolute height (Sec. 2.2.1) and inspecting system and processing parameters (Sec. 2.2.8). The estimated height is validated with ground truth references (Sec. 2.3.1) coming from a dedicated campaign and is geophysically related to the temporal tracking of plant growth (Sec. 2.3.5). Moreover, a special analysis is performed on the impact of system polarization on the elevation accuracy.

Investigation relevance The investigation is performed for paddy-rice fields, even though in principle it can be generalized for other vertical-oriented vegetation crops. The relevance of the study comes from economical and geo-political aspects. According to a recent Food and Agricultural Organization (FAO) study, rice is the most valuable livestock product in the world, with a total value of about 190 billion US dollars in 2012. As a consequence, a big interest of international agencies, insurance companies and governments is posed on this staple food. For instance, politicians and governments are particularly interested in the monitoring of farming practices and land control, e.g. to check for hidden and/or spoofed markets. Insurance companies are interested in forecasting coverage costs by knowing the status of crops at the moment of possible flooding. Agencies would like to regulate the product import/export based on the yield estimation and the current demand. It is self-evident how the TanDEM-X possibility to globally monitor paddies by providing the growth status and field borders is then particularly relevant. Growth status is directly linked with plant elevation, as explained in Sec. 3.2, while field borders are derived with the special processing described in Sec. 3.3.

3.2. Dataset description

The test site chosen for the demonstration is the Lake Gala National Park, at the border of Greece and Turkey. The park is a unique wetland environment consisting of lakes, rivers and agricultural fields (see Fig. 3.1). In the last 50 years, changes in topography due to debris flow and heavy rain affecting the regional ecosystem were measured. Recently, the region is controlled by the

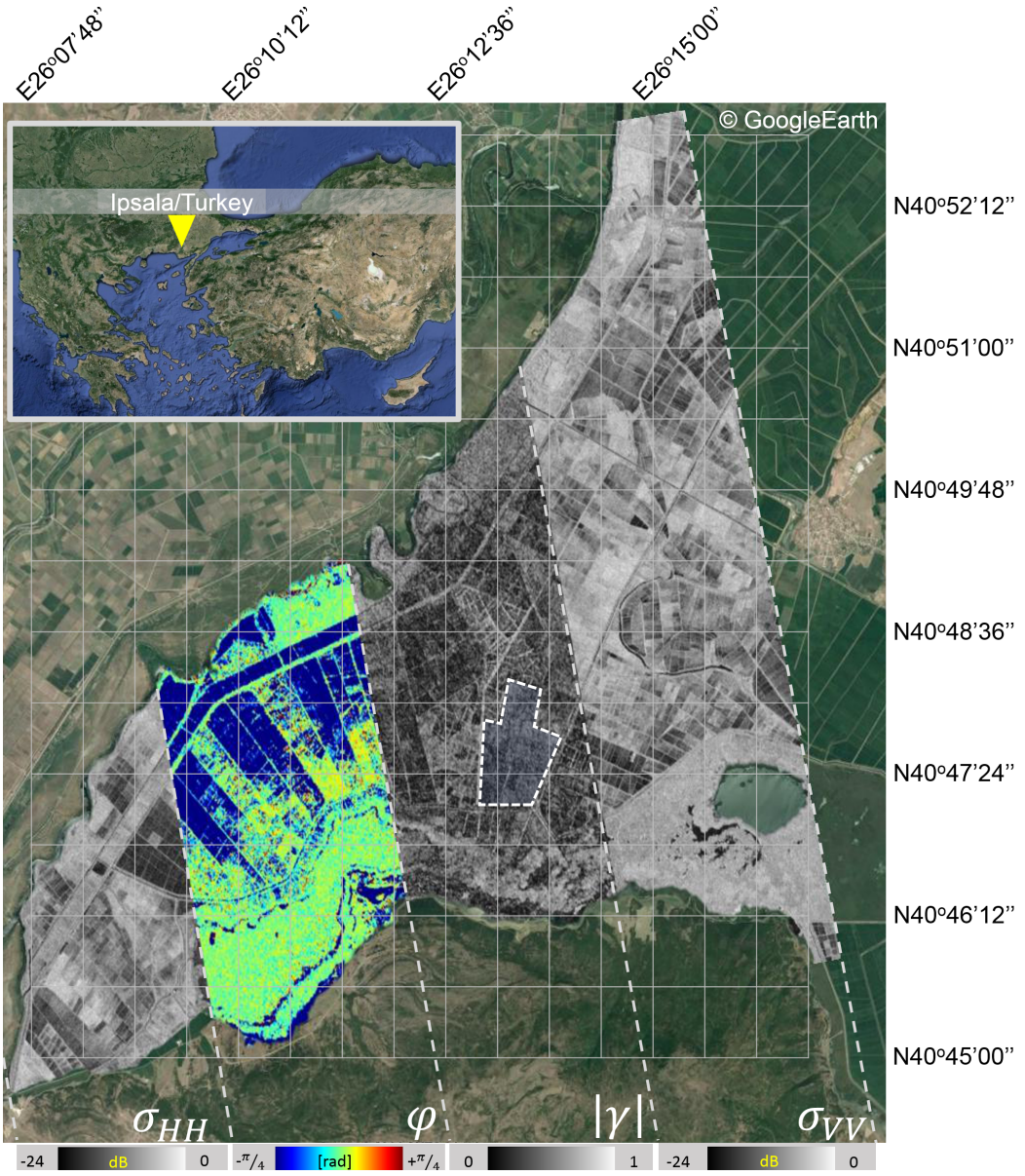

Figure 3.1.: Agricultural study area in Ipsala, Turkey. The co-polar images acquired on June 21, 2014 in HH and VV polarization, and their coherence and phase difference measurements are placed over the Google-Earth image. The selected fields for the polarization study performed in Sec. 3.4 are highlighted over the coherence portion.

government and made available for agricultural practice, mainly for paddy-rice. Considering the regional risk of debris flow, agricultural fields have to be monitored, controlling by this way the effect of flow. For instance, if the seeding has been affected from flow and irrigation, farmers can do transplanting again before it is too late for seeding. TanDEM-X monitoring is then particularly appealing for this test site.

Before describing the TanDEM-X dataset employed for the analysis and the ground campaign performed for the demonstration, a concise overview of rice growing cycle, necessary to interpret

Major Stage	BBCH	Description
Vegetative	00	Germination
	10	Leafing
	20	Tillering
	30	Stem elongation
	40	Booting
Reproductive	50	Heading
	60	Flowering
	70	Fruiting
Maturation	80	Ripening
	90	Senescence

Table 3.1.: BBCH Scale of Rice

TanDEM-X results, is provided in the following section.

3.2.1. Rice growth cycle

A rice growth cycle from panicle initiation to maturing, takes about 110-250 days. Throughout this cycle, roots and bottom part of the stem stay submerged in water for approximately 90 days. The rice growth cycle mainly consists of three stages: *vegetative*, *reproductive* and *maturation*. In these phenological stages, rice plants exhibit distinct structural differences. These differences are described by using a scale called *Biologische Bundesanstalt, bundessortenamt und CHemische industrie* (BBCH) (Lancashire et al., 1991). All growing stages can be associated with the BBCH-scale, as shown in Table 3.1.

3.2.2. TanDEM-X dataset

16 dual-pol TanDEM-X acquisitions have been acquired over the Lake Gala region in 2012 and 2013. Specifically, nine acquisitions have been commanded in 2012 and eight in 2013 at the same incidence angle. As shown in Tab. 3.2, only the 2012 acquisitions are covering all the rice growing stages (May to October), whereas the 2013 acquisitions are missing the maturation stage (August to October). For this reason, even though the GPS campaign has been conducted in 2013 (Sec. 3.2.3), the sole 2012 acquisitions are employed in the demonstration. An additional reason relies to the height sensitivity of the different bistatic configurations. The height of ambiguity (h_{amb}) is ranging between about 20 and 30 meters for the 2012 acquisitions and between about 40 and 50 meters for the 2013 ones. To give a quantitative idea, assuming a Gaussian distributed phase error, a coherence value of 0.8 yields a standard error of 0.36 meters for the 12.05.2012 processed configuration (h_{amb}: 23.1 m) and a standard error of 0.84 meters for the 26.07.2013 one (h_{amb}: 52.8 m) (see Sec. 2.2.8).

The data stack is processed with the Integrated TanDEM-X Processor. The processor is commanded to generate HH and VV DEMs, for a total of 32 DEMs, with an output raster of 6 meters. As in Table 3.2, the interferogram resolution is triggered to be around 10 meters by multi-looking the input co-registered data, yielding height errors at a coherence value of 0.8 specified in the last column of the table (Eq. 2.34). Considering the purpose of tracking crop height in all the growing stages, multi-looking is a necessary step to reduce the phase noise and the resulting standard error to a decimetric level. As aforementioned, due to the relatively smooth topography of the scenes, phase unwrapping is not an issue (even for small height of ambiguities) and no unwrapping errors have been detected. To ensure a straightforward analysis, all the DEMs have been generated at the same output grid and have been equally calibrated jointly using SRTM and ICESat data.

Figure 3.2.: The first line shows portions of agricultural fields acquired on the 30^{th} of May, 2013, illustrating the differences in agricultural practice. The second line shows the temporal pictures of field 8.

3.2.3. Reference dataset

Reference data has been collected in cooperation with the Istanbul Technical University (ITU). In particular, the state organization Trakya Agricultural Research Institute collected detailed ground truth in 8 fields with 4 independent samples per field during the growth cycle (May to October) of paddy-rice in 2013. Among the various gathered physical parameters, *height above ground and water* is the one of interest for the demonstration. The fieldwork dates are illustrated in Fig. 3.2 with the pictures taken during these studies. To highlight the spatial variation in response to changes in agricultural practice, the first line in Fig. 3.2 shows the pictures taken from different fields on the same day. In this region different fields are cultivated variously depending on the field owner's decision. In the study area, the sowing method is direct seeding by broadcasting, implying a random seeding instead of a regular straight-row one. This is a rather important point, since it highlights the expected randomness of the scattering.

Fig. 3.3 shows the plots of the relationship between canopy height and day of the year obtained during the field works. Most fields were homogeneous and crops reached maximum height after flowering. Plant height ranges in between 0 cm and 140 cm.

acquisition date (DOY)		center incidence angle [deg]	perpendicular baseline [m]	height of ambiguity [m]	interferogram resolution [m]	standard error* [m]
12.05.2012	(133)	36.8	253.7	23.1	10.2	0.36
14.06.2012	(166)	36.8	242.3	24.2	10.3	0.38
06.07.2012	(188)	36.8	234.3	25.1	10.2	0.40
17.07.2012	(199)	36.8	227.2	25.8	10.2	0.41
28.07.2012	(210)	36.8	222.7	26.3	10.3	0.42
19.08.2012	(232)	36.8	213.4	27.4	10.2	0.43
10.09.2012	(254)	36.8	204.4	28.7	10.3	0.46
13.10.2012	(297)	36.8	187.1	31.3	10.3	0.50
26.11.2012	(331)	36.8	181.3	32.3	10.3	0.51
05.03.2013	(64)	36.8	112.0	52.8	10.4	0.83
16.03.2013	(75)	36.8	111.5	53.1	10.4	0.84
10.05.2013	(130)	36.8	139.7	42.1	10.4	0.67
21.05.2013	(141)	36.8	141.1	41.6	10.3	0.66
01.06.2013	(152)	36.8	146.6	40.2	10.3	0.63
23.06.2013	(174)	36.8	144.3	40.7	10.4	0.64
26.07.2013	(207)	36.8	111.6	52.8	10.3	0.84

*Standard error computed at a coherence value of 0.8 for an equivalent number of looks of about 30.

Table 3.2.: Main parameters of the interferometric data set

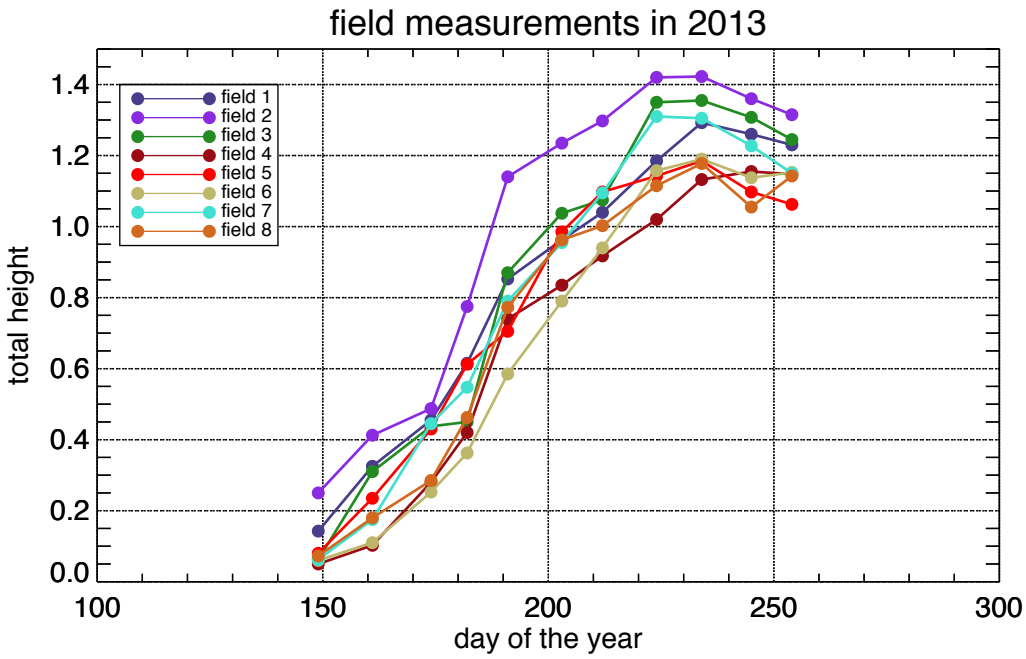

Figure 3.3.: Relationship between the day of the year and the canopy total height for the 8 fields under test.

3.3. Uncertainty assessment strategy and results

The uncertainty assessment is performed in the temporal domain. Objective of the assessment is the comprehension of the TanDEM-X mapping capability through the cultivation period and the relationship with physical and system parameters. DEMs are generated as described in Sec. 3.2.2. A technique to extract field borders in order to perform the assessment on a field-by-field basis is described in the next section. The analysis based on the temporal interpretation is explained in the following one.

3.3.1. Field segmentation

In the context of precise farming it is substantial to define field borders which are usually changing every cultivation period. Water management pattern is a further asset useful to suppliers. Thus, crop segmentation is mandatory for a field-by-field uncertainty assessment, reasonably assuming a consistent growing within single fields. An important sub-product to exploit, generated during the interferometric processing, is the coherence. By describing the similarity of the coregistered complex master and slave data, the coherence is a considerable input for the analysis, supporting the segmentation algorithm. The adopted strategy is to relate the field segmentation in a water detection problem. Indeed, flooded parcels of land characterize the early vegetative state. During this state, fields are covered by water and separated by a path network composed by soil or rare grass, as visible also in Fig. 3.4, representing the May 2012 acquisition. A gravel road network is also in the test site separating parcel groups. This natural segmentation is well visible by inspecting the interferometric coherence in Fig. 3.4(b), as good as inspecting the master channel amplitude in Fig. 3.4(a). This visibility relies on the water body dielectric properties. Non-moving water behaves like a mirror, reflecting the incident signal wave in a specular direction, yielding a very low return to the SAR antenna. This phenomenon brings also a low interferometric coherence. Moreover, it

(a) amplitude

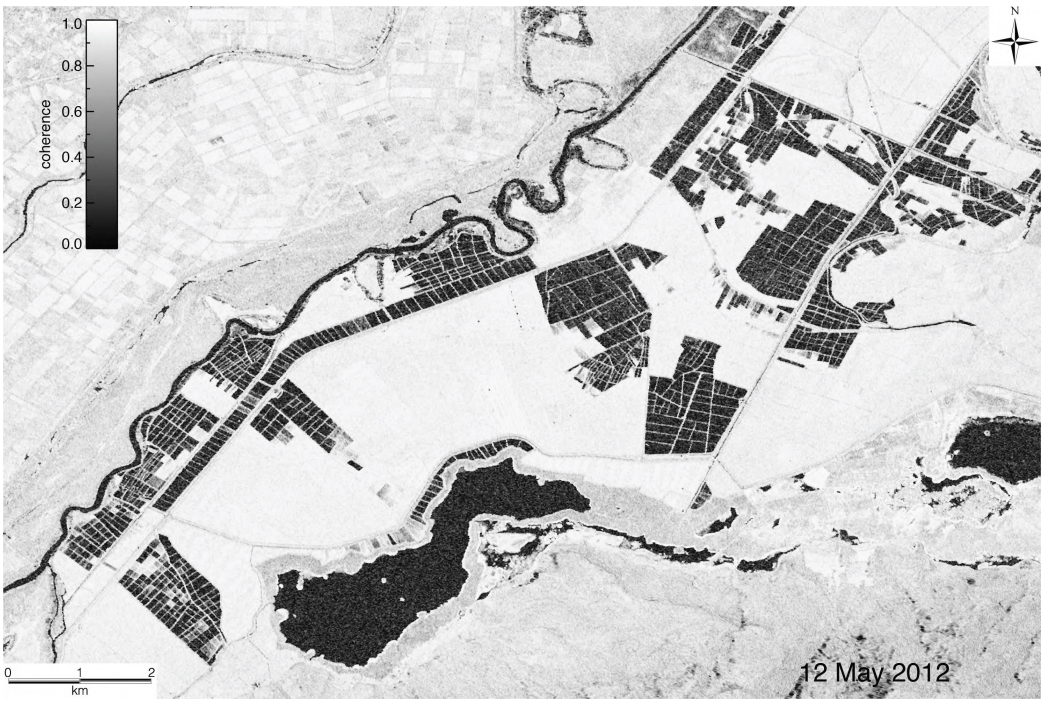

(b) coherence

Figure 3.4.: SAR master channel amplitude (a) and interferometric coherence (b) of the 12.05.2012 TanDEM-X acquisition, used to extract field shapes.

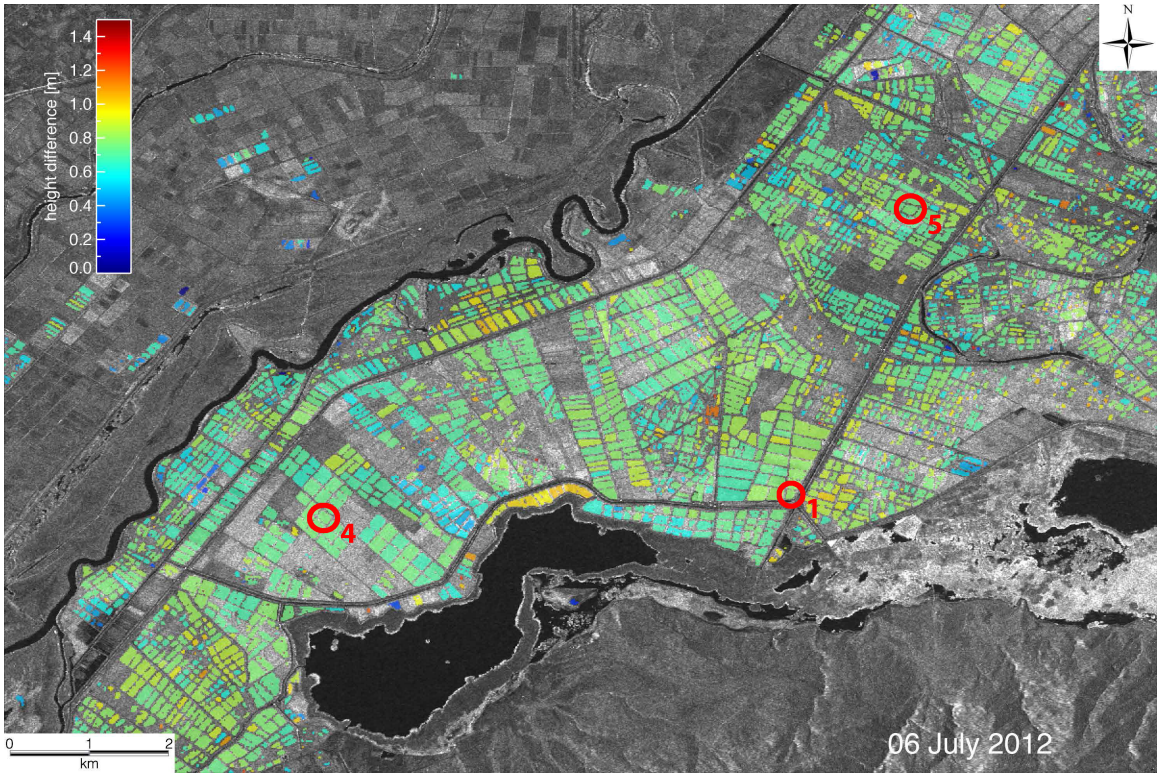

Figure 3.5.: Temporal 2012 height change analysis. Difference between the July acquisition and the reference one in November. The changes are shown in a field-by-field basis, for fields having coherence higher than 0.8 for both the analyzed and reference acquisitions. The three fields under analysis are marked.

is also known that a water body decorrelates within tens of milliseconds (Bamler and Hartl, 1998) (TanDEM-X small along-track time lags varying between 50 ms (equator) and 0 ms (poles)). The technique proposed by Wendeler et al. (Wendleder et al., 2013), operationally employed for the generation of water body mask as an auxiliary product of the official TanDEM-X DEM, is adopted. Specifically, a threshold value of 40 for the amplitude digital number (corresponding to -20 dB in Sigma-Nought) and 0.23 for the coherence were selected. In this study, this strategy is applied for scenes having flooded crops. In Fig. 3.4, the 12.05.2012 amplitude and coherence data show the flooded parcels for that date with low values. As visible, not all the fields were already flooded (see also Fig. 3.2). To better cover the test site, additional information is retrieved by using also the 21.05.2013 and 01.06.2013 acquisitions.

Straight after the water detection, a binary morphological erosion with a 3x3 rectangular structuring element is performed to remove isolated artifacts and a binary shape fill is performed to remove possibly remaining holes within shapes. The final mask is then segmented and the fields numbered. A total of more than 2000 fields are detected. The detection and the segmentation are performed in the geocoded domain, in order to easily compare them with ground truth data.

3.3.2. Temporal analysis

Since the analysis is on the plant elevation, and the generated DEM is defined over the WGS84, a reference height corresponding to the plant base elevation must be considered. For that purpose, the last 2012 acquisition, in November, is taken as reference. Figs. 3.5, 3.6 and 3.7 show the plant

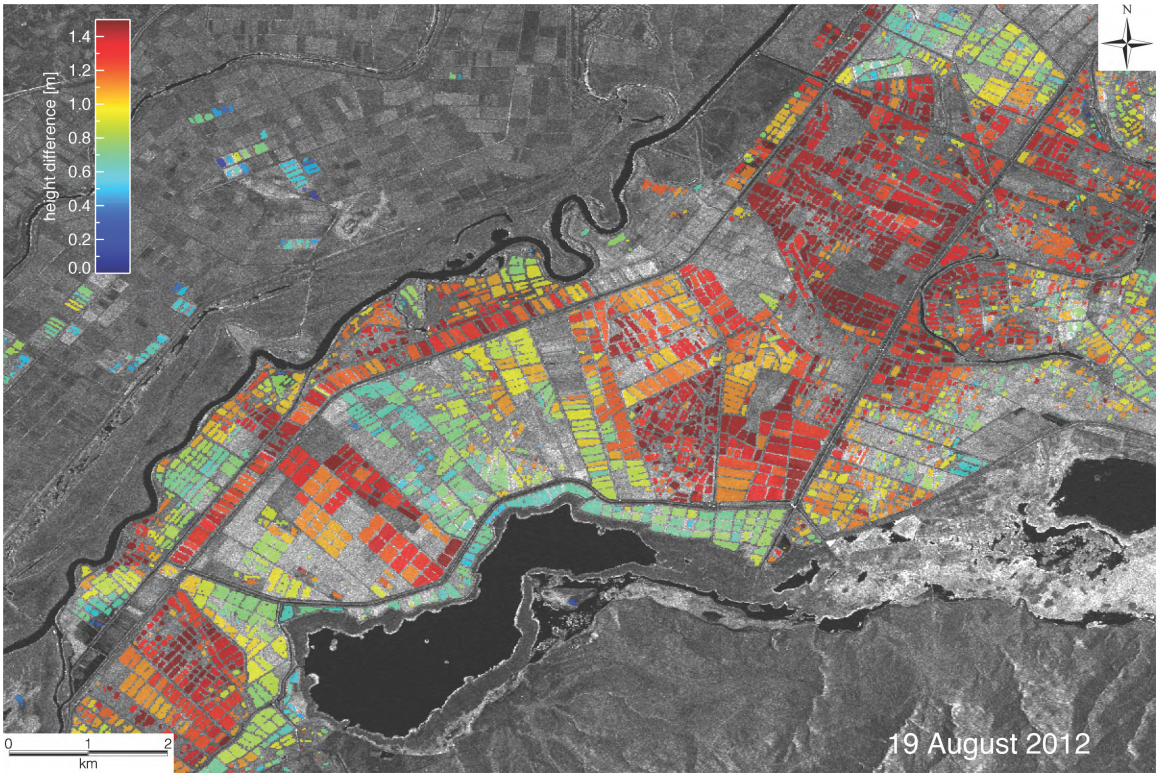

Figure 3.6.: Temporal 2012 height change analysis. Difference between the August acquisition and the reference one in November. The changes are shown in a field-by-field basis, for fields having coherence higher than 0.8 for both the analyzed and reference acquisitions.

growth of July 06, August 19 and September 10, 2012, respectively. The differences with the reference height of November 2012 are here represented with an overlay between the amplitude and the mean height difference for detected fields which have an average coherence above 0.8 in both the analyzed and the reference acquisitions. Inspecting these maps, one could check the growing trend on a field-by-field basis. For instance, the July map in Fig. 3.5 shows a quite homogeneous result with plant heights around 70 cm. The August map in Fig. 3.6 reveals the growing of most of the plants, with doubled heights compared to Fig. 3.5. For some of the fields, the higher maturation level is reached about a month later, as visible in Fig. 3.7. In general, these maps can be used for the agricultural planning, in terms of production volume and outcomes.

This qualitative inspection already demonstrates the capability to reach the centimetric accuracy necessary to track rice plants. To further highlight it, in Fig. 3.8 the mean height for the 2012 detected fields (flooded in Fig. 3.4) is shown in black and the standard deviation highlighted in purple. The reference temporal elevation is over-plotted. The mean trend exhibits a good accordance with the reference. The height deviation for the late July acquisitions has to be linked to the different growing periods of the detected fields.

The quantitative inspection is performed for three out of eight fields (marked in Fig. 3.5). The analysis shall link the obtained accuracy derived through a comparison with reference data with the physical characteristics of the plant. The framework is the one delineated in Sec. 2.2.1. In particular, considering the interferometric analysis, the smaller the extinction, the lower the scattering center (Eq. 2.23-2.25). Consequently, the retrieved plant elevation will be equal or smaller than the plant

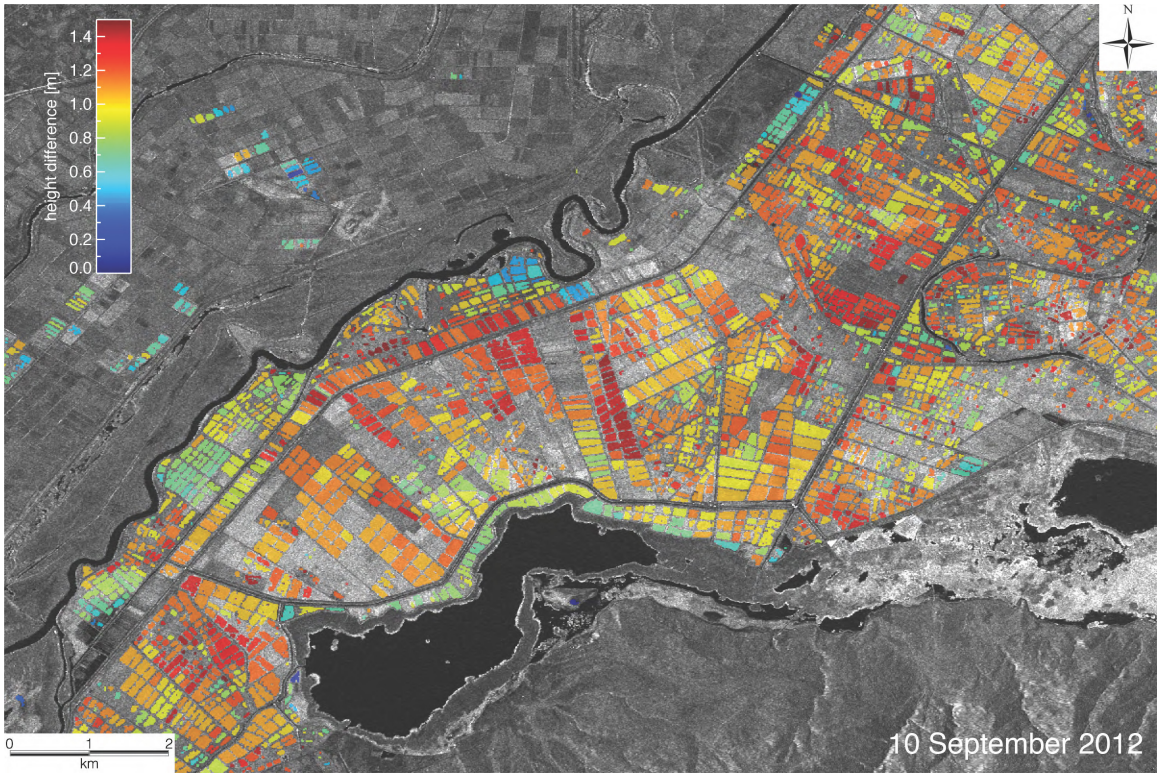

Figure 3.7.: Temporal 2012 height change analysis. Difference between the September acquisition and the reference one in November. The changes are shown in a field-by-field basis, for fields having coherence higher than 0.8 for both the analyzed and reference acquisitions.

top depending on the actual effective dielectric constant of the canopy and the ground, since in the proposed approach the canopy height is retrieved with a difference between a plant growing phase and bare soil.

An important remark for the comparison between interferometric heights and ground truth data relies on the different years of the two data sources. As beforehand underlined, the sole 2012 TanDEM-X data fully covers the growing stages and is used for validation despite the campaign has been performed in 2013. In practice, validation inaccuracies could take place depending on the seeding date decided by the field owner. For the fields under analysis the seeding date discrepancy between the two years has been stated to be less than a week, thus strongly limiting this error source. A second inaccuracy source resides in changes in plant moisture variations between the two years, manifesting in a root mean square error increase due to the different penetration into the canopy.

The differential-InSAR-based and the field-measurement-based canopy height is shown in Fig. 3.9 in form of scatterplot for three fields. Due to the growing height trend in time, this plot can be easily interpreted. Generally, the elevation trend is well detected by the interferometric measure for the late vegetative phase, reproductive and maturation stages. Instead, the early vegetative phase represented by the May 2012 acquisition yields strongly biased elevation values and is not considered.

The June acquisition corresponds to the central vegetative stage (tillering, Tab. 3.1). At this phase, plants emerge from water (see the second and the third picture in the second row in Fig.

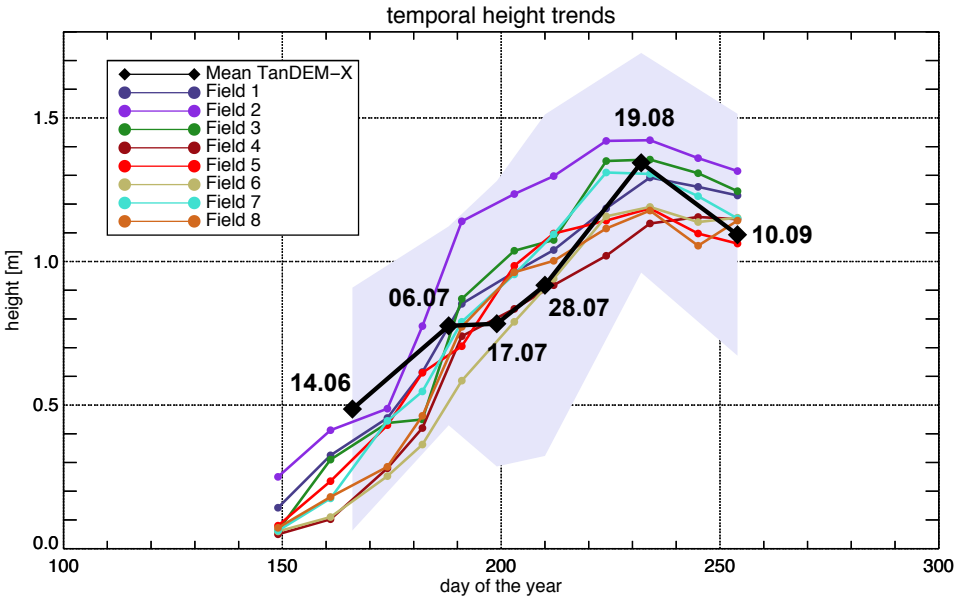

Figure 3.8.: Mean temporal TanDEM-X elevation trend for all the 2012 detected fields over the specific date marked in the plot (black) and corresponding standard deviation (purple). The reference fields are overplotted with colors in the legend.

3.2). In the SAR resolution cell different phenomena such as double scattering, water reflection and surface reflections combine together. The interferometric elevation results underestimated, showing a mean difference with reference data of 7.7 cm for all the eight fields under study. A singular exception is measured for the field 5, with an overestimation of about 10 cm, to be attributed to a lower coherence value and a higher phase noise. For this take, double bounces between growing vegetation and standing water should be the dominant part of the radar return. The scattering phase center is located at the water elevation for the cardinal effect on corners - in this case represented by quasi-vertical stems on calm water. However, the small measured height difference suggests the partial presence of the phenomenon due to the use of a short wavelength (3.1 cm) at a relatively high incidence angle (about 37 deg) yielding a limited penetration of the echo inside the fresh vegetated volume. For the three July measurements the elevation is largely underestimated, with a mean difference of 26.5 cm. Also this discrepancy, at the end of the vegetative stage and beginning of the reproduction (booting-heading, Tab. 3.1), can be explained with the radar wave interaction with the inner part of fresh canopy (see fourth picture in the second row in Fig. 3.2). The August acquisition exhibits instead a generally good matching, with a mean underestimation of 4.8 cm. Being at the beginning of the maturation stage (fifth picture in the second row in Fig. 3.2), plants start to densely produce milky grains at their surface which reflect the signal at X-band. The last considered acquisition, in September, falls at the end of the maturation (seventh picture in the second row in Fig. 3.2). The grain is dry and mature, with a maximum height slightly smaller than the previous stage. On this date the interferometric elevations result again underestimated on average, with a mean difference of 16 cm. In principle, at this stage, plant elements are more randomly oriented and drier than in previous ones, hence making more similar the propagation for all polarizations. The best fit analysis in the form of $y = ax + b$ in Fig. 3.9 is used for calculating the offset between the two measurements. As the data time sampling is not overlapping, a linear interpolation for the reference at the InSAR locations is performed. The two sources result highly correlated, with a correlation coefficient R equal to 0.88, 0.96 and 0.84 for the three fields

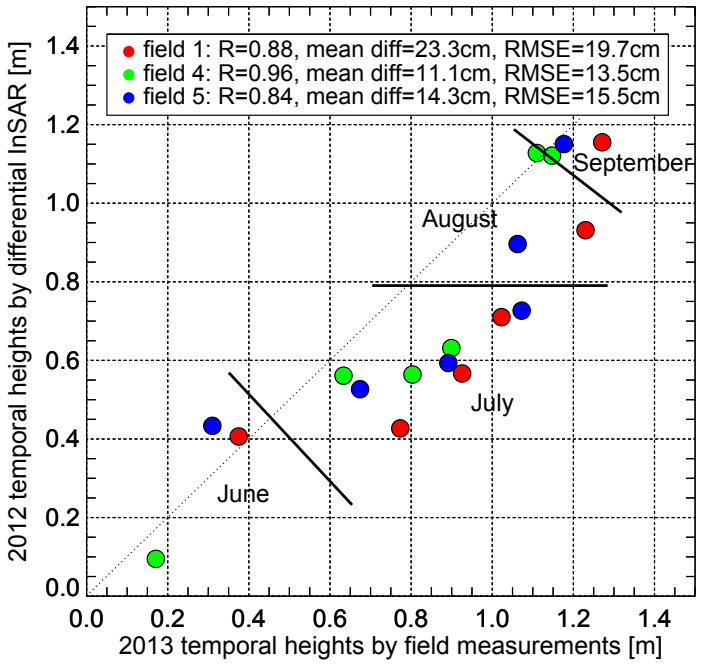

Figure 3.9.: Comparison of height measurements, superimposed over temporal BBCH scales, between the ground measurements (purple circles) held in 2013 and the one from bistatic interferometry ((a) red, (b) green, (d) blue circles) in 2012 over the 3 different fields shown in Fig. 3.5. (d) the corresponding scatter plot with quantitative analysis at the top.

under analysis. The mean differences and root mean square errors are in the decimetric level. In detail, the mean differences between reference and InSAR result 23.3, 11.1 and 14.3 cm and the root mean square error 19.7, 13.5 and 15.5 cm. Even though the scattering analysis and the quantitative evaluation performed on this section are useful to understand the overall process, the focus shall be on the centimeter accuracy of the system for this application, and its capability of temporarily tracking the elevation through most of all the growing stages of paddy-rice fields.

3.4. Polarization impact

The results and discussion provided in the previous section have been derived using the horizontal (HH) polarization and demonstrated the possibility of estimating the height (and consequently the phenological stage) of the fields from TanDEM-X data with no additional ground measurements. In this section, the vertical (VV) polarization is studied, with the purpose to study the differences and possibly recommend the *best polarization* for crop monitoring.

In Fig. 3.10 the interferometric coherence is plotted for the HH and VV channels for the 30 randomly selected fields marked in Fig. 3.1. An evident visual divergence appears for the late vegetative-early reproductive stage (around 17-Jul). Here, the HH elevation accuracy is larger than the VV one, as coherence values are higher (Eq. 2.34). Standard deviation is also smaller for the horizontal polarization. Thus, when considering to assess crop elevation with bistatic data for the central growing stage, it seems advantageous to privilege the HH channel. The two other stages perform similarly: early vegetative has very low coherence and poor elevation estimates for both channels, whereas late reproductive and maturation perform well.

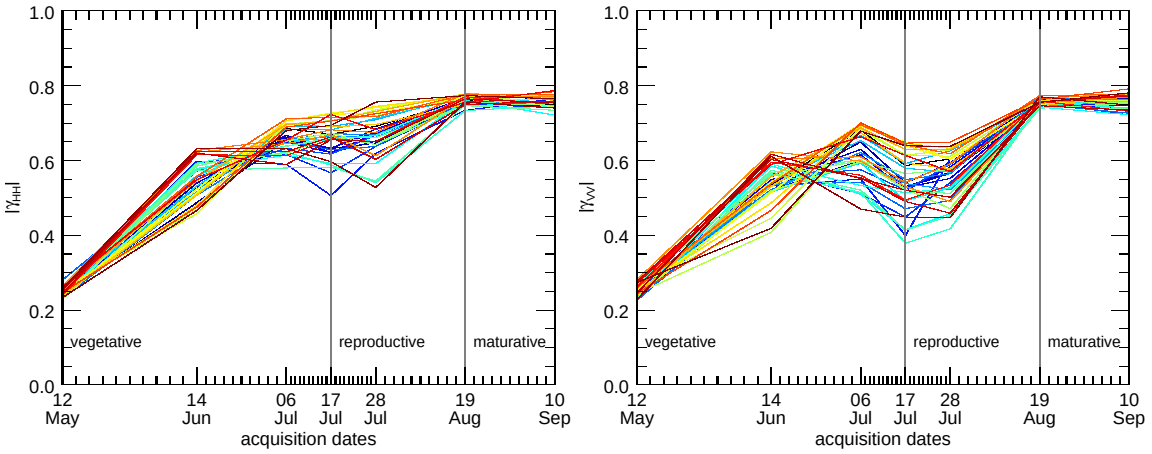

(a) HH coherence

(b) VV coherence

Figure 3.10.: Multi-temporal coherence measurements from TanDEM-X HH (a) and VV (b) channels along the plan growth cycle for 30 different fields.

To make polarization dissimilarity more clear, the Probability Density Functions (PDF) in terms of histogram of the elevation differences are temporally plotted in Fig. 3.11. Histograms of elevation differences from HH and VV polarized acquisitions were established among the selected fields for each acquisition day. On the one hand, for flooded fields, the co-polar elevation difference measurement is uniformly distributed because of the unreliable phase information. On the other hand, for the other acquisitions the elevation differences are more closely to the Gaussian distribution, being mean and variance strongly dependent on radar parameters and canopy properties.

It is interesting to see the effect of the extinction coefficient in the vertical channel through almost all the phenological stages. Excluding the first two dates, the temporal mean difference measurements increase monotonically until the acquisition date of 28^{th} of July. After, they decrease monotonically until when the plant starts to collapse and to lose its height -hence vertical structure-. For the PDF obtained from the agricultural fields acquired on the 25^{th} of November when the fields were already harvested, there is almost ($\sim mm$ level) no difference between polarimetric TanDEM-X measurements.

Dates	sample mean [m]	sample std [m]	Gaussian center [m]	Gaussian std [m]
12 May	0.84	2.04	-	-
14 Jun.	-0.01	0.23	0.00	0.07
06 Jul.	-0.03	0.08	-0.03	0.07
17 Jul.	-0.03	0.11	-0.02	0.09
28 Jul.	-0.09	0.19	-0.10	0.11
19 Aug.	-0.08	0.07	-0.08	0.09
10 Sep.	-0.05	0.10	-0.04	0.07
23 Oct.	0.02	0.07	0.01	0.05
26 Nov.	0.00	0.06	0.00	0.04

Table 3.3.: Sample and Gaussian-fit statistics of the difference between HH and VV elevations for the selected fields under analysis.

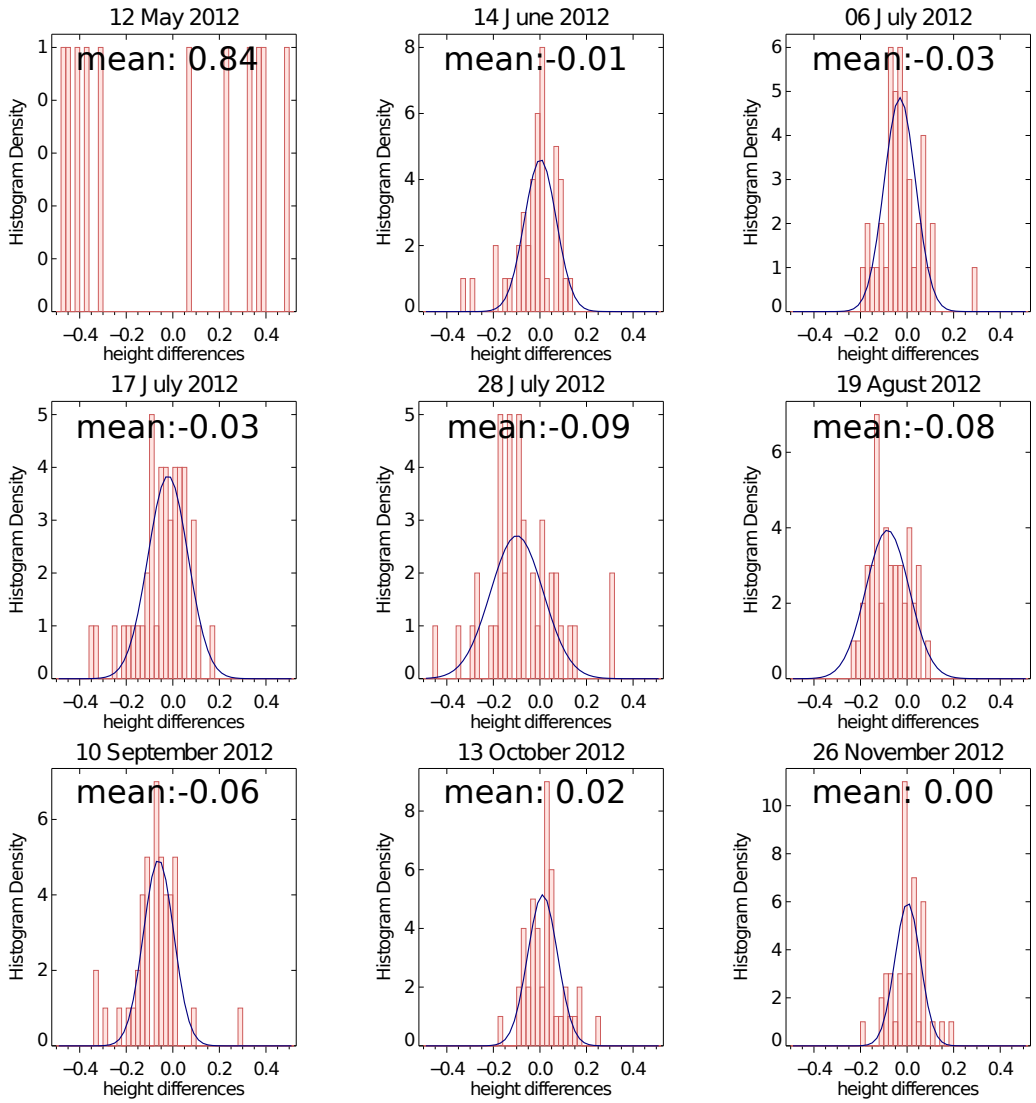

Figure 3.11.: Temporal histograms of the difference between elevation measurements from HH and VV polarized TanDEM-X images among the neighbor paddy fields. A Gaussian fit (blue line) is superimposed.

In this PDF based analysis, the estimate of the sample mean elevation differences (Eq. 2.44) is not the only interest. A consistency analysis among the neighbor paddy fields is also important, and it is given in Tab. 3.3. The sample standard deviations for each acquisition date show the variability of the outcomes for each phenological stage. Values are nearly stable through maturation stage, but in vegetative and reproductive stages they are relatively high considering also the differences in growing rate. As reported in Tab. 3.3, a Gaussian fit analysis is superimposed for each acquisition date histograms. Temporal Gaussian standard deviations are in accordance with the signature of sample standard deviations. Horizontal polarization yields digital elevation models with lower crop heights, up to about 10 cm differences. Vertical polarization yields higher elevation models, i.e. close to the true top canopy elevation. As aforementioned, horizontal polarization provides, on the average, more accurate elevation results for the central growing stage. So, what is the best polarization for crop elevation monitoring? Generally, if the objective is the determination of the crop elevation, local field coherence should be the final trigger. Nevertheless, for more reliable phenological stage estimation simply based on height, the VV channel can be preferred since it yields higher phase centers, therefore better modeling the top of the canopy.

3.5. Discussion and conclusions

This chapter underlined the potential of TanDEM-X in paddy-rice elevation mapping. The outcomes can also be an input for the production estimation in terms of volumetric changes. This is particularly remarkable, considering that the plant tracking requires a centimetric accuracy level and the TanDEM-X specifications are in the order of meters. The uncertainty study demonstrated three major points:

1. For the first time, plant growing was *directly* measured from a spaceborne SAR system. Previous demonstrations (e.g. ERS in TanDEM configuration) *indirectly* derived the elevation from coherence decomposition (Wegmüller and Werner, 1997).

2. For the first time, the impact of differential extinction on the crop height estimation by differential interferometry was experimentally studied with spaceborne SAR data.

3. As outlined in Sec. 2.3.5, it is important to carry out uncertainty studies in the temporal dimension. In particular, it was demonstrated how the accuracy level is varying depending on the plant phenological stage.

This investigation covered just one of the possible land cover classes for smooth terrains. A large interest is posed also on forest mapping. Several works on different algorithms (e.g. PolInSAR (Kugler et al., 2014), InSAR (Solberg et al., 2013), data fusion (Kellndorfer et al., 2010) and etc.) have been already performed with TanDEM-X over different kind of forests (e.g. tropical, boreal (Askne et al., 2013), mangrove (Lee and Fatoyinbo, 2015) and etc.). Among them, the work in (Antropov et al., 2015) is similar in purposes and results to the inspection in this chapter. Antropov et al. have tested the potential of dual-pol TanDEM-X in boreal forest height estimation. Measured coherence has been reported rather high (above 0.8), with higher penetration for the HH channel - as for paddy-rice - and a temporal variability depending on the season. The mean RMSE has been reported to be around 3 meters.

4. TanDEM-X uncertainty investigations over moderate terrains: the Bardarbunga and Serra de Collcardus case studies

The Bardarbunga test case presented in this chapter summarizes a paper under review in the moment of writing: Rossi, C., Minet, C., Fritz, T., Eineder, M., and Bamler, R., **Temporal monitoring of subglacial volcanoes with TanDEM-X - application to the 2014-2015 eruption within the Bardarbunga volcanic system, Iceland**. *Remote Sensing of Environment* (Rossi et al., 2016).

The Serra de Collcardus test case is partially taken from the conference paper in Appendix A.4: Rossi, C., Eineder, M., Fritz, T., D'Angelo, P., and Reinartz, P., **Quality assessment of TanDEM-X raw DEMs oriented to a fusion with CartoSAT-1 DEMs**, *Proc. 33rd EARSeL Symp.*, Matera, Italy, 2013 (Rossi et al., 2013).

4.1. Inspection placement in the thesis framework and relevance

Moderate terrains mainly represent hilly landscapes or mountains with gentle slopes. There is actually no definition or a specific slope threshold for categorizing these landscape. In this dissertation, they place in the middle between smooth terrains and cities. Two investigations are proposed.

The first one, over the Bardarbunga volcano, Iceland, exploits a particular case of a subglacial volcano in activity. The uncertainty assessment is performed in the temporal domain (Sec. 2.3.5), as done for the paddy-rice demonstration in the previous chapter. The dynamical variations of the terrain are compared here with altimeter data (Sec. 2.3.1). The absolute error is linked to the wave propagation in frozen environments for different seasons (Sec. 2.2.1). The system configuration impact in the produced DEM is assessed in Sec. 2.2.8.

The second inspection is for the hilly region named Serra de Collcardus, close to Barcelona (Spain). Here the uncertainty focus is based on the comparison between an optical DEM generated with CartoSAT-1, a LiDAR surface model and the TanDEM-X one. Differences linked to terrain topographical descriptors (Sec. 2.3.3) are introduced and the optical and SAR systems are tested according to their specifications. The LiDAR system is here used as the reference.

Investigation relevance The first demonstration is applicable in the geophysical field. Volcanic hazards take place with a certain regularity on our planet, and the understanding of their dynamics can help geophysicists in modelling and forecasting. They need the continuous monitoring of the environment in which they are located in order to ensure safety, when they take place in civilized areas, or more in general to control consequences like deviated air traffic, fast mud flows in frozen places, tsunamis in coastal places and etc. National governments are the primary interlocutors for that. The capability of TanDEM-X in assessing accurate surface changes is then relevant in understanding the possibility and the limits of its data usage in that context.

The second demonstration is suitable for the TanDEM-X mission itself, by checking the quality in a standard and not dynamic environment with various instruments and descriptors. Moreover, the comparison with DEM generated from other sources brings additional knowledge to potential customers and researchers interested in DEM products.

4.2. The Bardarbunga test case

The focus of the investigation is the Bardarbunga caldera, in the Vatnajökull National Park, Iceland. A small fissure opened up in the Holuhraun plain, situated 48 km north-east of the caldera, on August 29, 2014, and the eruption lasted a few hours. The main fissure eruption commenced on August 31, 2014, and lasted for 6 months. The unrest started nearly two weeks before with an intense seismic swarm. This was the largest effusive eruption to occur in Iceland since the 1783-1784 Laki eruption and was characterised by the extrusion of extensive lava flows. A total of 1.6 $\pm$ 0.3 km^3 of lava was produced and an area of 84.1 $\pm$ 0.6 km^2 was covered (Gislason and al., 2015). Through the combined use of InSAR and GPS measurements, the dyke propagation was also modelled and a magma flow rate of 260 m^3/s was reported (Sigmundsson et al., 2015). During these months the Bardarbunga caldera slowly collapsed, which is a rare event in Iceland (the previous caldera collapse in Iceland is dated 1875) (Riel et al., 2015). In this scenario, TanDEM-X remote sensing data is of particular interest. By producing medium-high resolution and accurate elevation models of the caldera, it is possible to evaluate volume losses and topographical changes and to increase the knowledge about the ongoing activity.

This test site is rather particular since Bardarbunga caldera is composed by a layer of 600-800 m thick ice above the caldera's surface. Here, SAR wave penetration into materials (Sec. 2.2.1) can play a big role since measured height depends on the penetration entity (Eq. 2.25). The dielectric proprieties of the caldera ice cap must be then taken into account, together with the various system parameters. This analysis and general considerations about the utilization of DEMs from different sources are presented in Sec. 4.2.1. The dataset is described in Sec. 4.2.2. The temporal uncertainty assessment, supported by radar altimeter data in C-band (Guðmundsson et al., 2007) for specific tracks over the caldera after the eruption is investigated in Sec. 4.2.3.

4.2.1. Snow impact in DEM uncertainty

The penetration of the radar wave into ice and snow is a well-studied topic. Empirical results in (Rignot et al., 2001) showed small penetration over exposed ice (1-2 m in C-band) and large penetration (up to 10 m in C-band) for dry firn. In the following analysis the penetration depth is quantified employing the models of Hallaikanen et al. (Hallikainen et al., 1986) for dry, wet snow and ice. The temperate Vatnajökull glacier has no dry snow facies (Williams Jr et al., 1991); nevertheless the freshwater ice and the dry snow modelling are considered in the following for completeness. These models depend on the system frequency and on several snow properties such as snow density, temperature, and volume water content. The analysis serves to trace a line regarding the absolute height accuracy of TanDEM-X DEMs and also of the radar altimeter used for comparison. The system bandwidth of the two systems is varying: while altimeter works in C-band (wavelength equal to 6.97 cm), TanDEM-X is acquired in X-band (wavelength equal to 3.12 cm). As a complement, also the SRTM mission and the future Tandem-L one (Krieger et al., 2009) are considered (SRTM is not covering Iceland). The penetration depths are given in Tab. 4.1. Pure water is not taken into account here, since water has a very high dielectric constant, making the approximation $\epsilon_r'' << \epsilon_r'$ and Eq. 2.23-2.24 not valid. It is in fact of few interest for the Vatnajökull monitoring since water areas of the DEMs, e.g. glacial lakes, exhibit low backscatter in the SAR image and yield therefore inaccurate elevation models.

Considering wet snow, the wave penetration dependency on the water content is depicted in Fig. 4.1 for the TanDEM-X and radar altimeter systems. According to the International Classification for Seasonal Snow on the Ground (Fierz and al., 2009), the water content x-axis in Fig. 4.1 is classified in three areas. The SAR wave penetration depth for *wet*[1] and *very wet* snow is limited to a few

[1]This classification name can create some confusion. The classification into dry and wet snow shown in Tab. 4.1 simply differentiates the snow in presence of liquid water volume (wet snow) and without it ($V_w = 0$, dry snow).

snow type	property	TanDEM-X	Altimeter	SRTM	Tandem-L	$\Delta h_{\text{Alt-TDX}}$
ice	T= $-5°$	4.6	13.9	10.9	28.8	9.3
	T= $-15°$	6.9	24.1	18.2	57.1	17.2
dry snow	$\rho_{ds} = 0.1$	69.4	208.8	163.7	433.2	145.4
	$\rho_{ds} = 0.3$	21.8	65.4	51.3	135.7	43.6
	$\rho_{ds} = 0.5$	11.6	35.0	10.9	75.6	23.4
wet snow	$V_w = 1$	0.17	0.5	0.36	4.9	0.33
	$V_w = 2$	0.07	0.21	0.15	2.1	0.14
	$V_w = 3$	0.04	0.12	0.09	1.3	0.08

Table 4.1.: Penetration depth in freshwater ice at two different temperatures, in dry snow at three different snow densities, and in wet snow at three different water contents and fixed snow density of 0.3 g/cm^3 for the two systems under study and the SRTM and Tandem-L missions. $\Delta h_{\text{Alt-TDX}}$ represents the difference between altimeter and TanDEM-X depth.

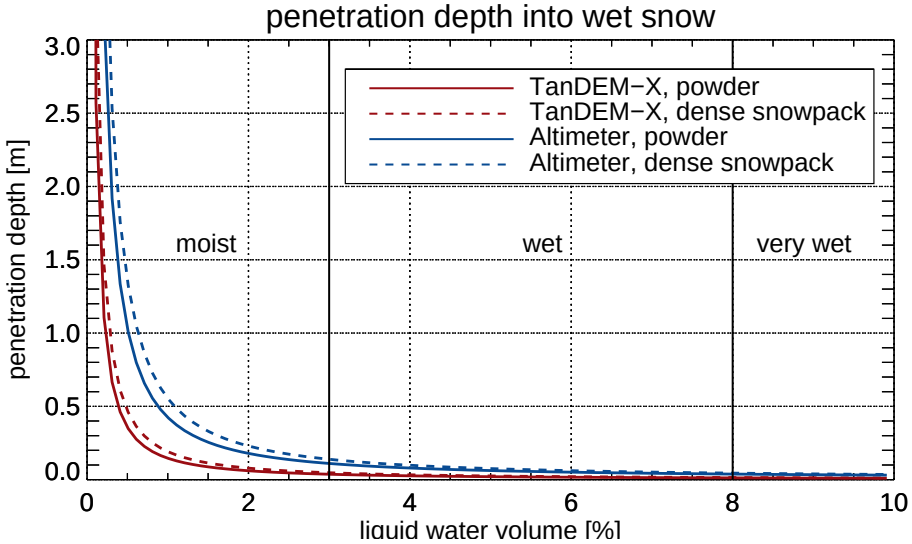

Figure 4.1.: Penetration depth in wet snow terrain type for TanDEM-X and the radar altimeter employed for validation. Two extreme snow densities are plotted for each system: newly fallen powder snow ($\rho_{ds} = 0.05$)and extremely dense old snowpack ($\rho_{ds} = 0.5$). Intermediate densities lie in between the two curves. Snow wetness is classified according to the *International Classification for Seasonal Snow on the Ground* in three categories: moist, wet and very wet.

decimeters. Instead, for very low levels of moisture, the penetration depth can also reach few meters. The snow density has a little impact in the penetration depth for wet snow cover. This analysis is relevant for the studied application since the Vatnajökull glacier can be considered of wet snow type with variable liquid water volume (Williams Jr et al., 1991). Thus, overall, the discrepancy between TanDEM-X and altimeter are expected to be very small, assuming the same snow conditions.

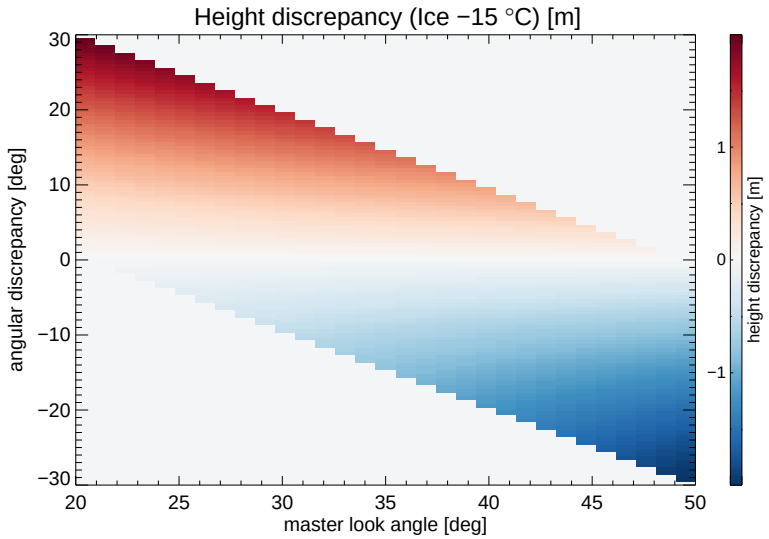

Figure 4.2.: Height discrepancy of two DEMs generated from two InSAR acquisitions at two different look angles (TanDEM-X case). Master looking angle (first DEM) and angular discrepancy (second DEM) are in the x and y coordinates respectively. The scale for dry snow ranges in between 12 m and for wet snow in between 10 cm.

4.2.1.1. Generalization to temporal InSAR DEMs

A temporal DEM series analysis is often used for scientific purposes to analyze topographical changes (Poland, 2014; Kubanek et al., 2015; Albino et al., 2015). A relevant issue is the relative calibration of the DEMs. Differently calibrated DEMs result in the misinterpretation of the obtained results. For glacial environments, the calibration can be a huge issue, since the terrain elevation is continuously changing according to local Earth dynamics. A reasonable approach is to calibrate DEMs with external references.

According to Eq. 2.25 and Tab. 4.1, the parameters affecting the final elevations are the physical snow proprieties, the sensor looking angle and sensor frequency. In the following, the impact of these parameters for a temporal analysis of elevations is provided.

Physical parameters Physical snow properties are have a large impact on the final elevation value. As shown in Tab. 4.1, the phase center variations can be very high (up to tens of meters) due to different parameters, such as water content and snow type. Thus, if the purpose is to track dynamical changes, the data stack should be characterized by the same snow properties. This is a very stringent constraint but should definitively be taken into account in the analysis.

Look angle Look angle enters in the interpretation in Eq. 2.25, as a weight to the penetration depth. Limit cases are flat look angle (90 deg), yielding no penetration, and vertical look angle (0 deg), bringing maximum penetration. Radar scenes acquired at different look angles then yield different elevations. The discrepancy depends again on the snow properties. In Fig. 4.2 the height discrepancy between two DEMs generated with two InSAR acquisitions at different look angles is depicted for freshwater ice at -15°C case. Other scenarios share the same trend but at a different scales.

Frequency System wavelength enters in all the models. Larger wavelengths yield larger penetrations. In Fig. 4.3 the comparison between TanDEM-X and another DEM acquired with an InSAR

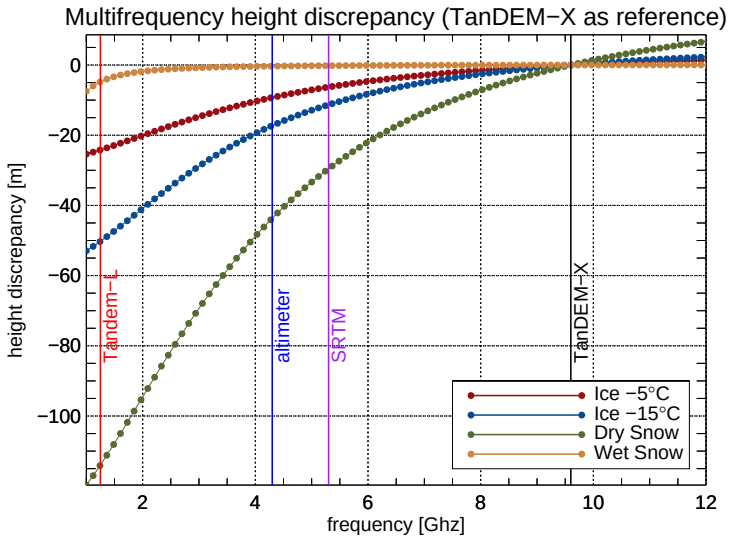

Figure 4.3.: Height discrepancy of two DEMs generated from two InSAR acquisitions at two different look angles. One of the two DEM is acquired with TanDEM-X. In the x axis, the frequency is spanning from L-band to X-band. Four different terrain types are considered; dry snow is assumed with a fixed density of 0.3 g/cm^3 and wet snow is assumed with the same density and a volumetric water content of 1 $\%^{vol}$.

acquisitions at a different frequency is depicted. Distinct bands provide deviating elevation values. For instance, SRTM and Tandem-L deviate with TanDEM-X of more than 100 and about 30 meters for dry snow, respectively.

Resuming, a temporal analysis of frozen environment with InSAR DEMs is very sensible to the system parameters and to the snow status. The comparison of DEMs over specific areas shall be performed in the same time of year (and even same time of the day) to ensure similar snow dielectric properties. Moreover, the same weather conditions should also be assured. Additionally, it makes no sense to use very different bands without re-calibration of the DEMs for the different penetrations.

4.2.2. Dataset description

The TanDEM-X dataset is composed of five bistatic acquisitions covering the caldera. The main system parameters are given in Tab. 4.2. The height of ambiguity is high enough to ensure a phase unwrapping with no errors. The mean scene coherence γ brings small height errors h_{err} (Eq. 2.34). To calibrate the TanDEM-X data stack, the operationally calibrated and mosaicked TanDEM-X DEM has been employed (Gruber et al., 2015). This model is generated using several acquisitions and IceSAT points as reference. A single tile is spanning 1 square degree, and it is sufficient to cover the scenes in the stack. It is depicted in Fig. 4.4. The acquisitions are fully covering the Bardarbunga caldera and the southern part of this volcanic system. The footprint of the data stack and the caldera outline are represented in Fig. 4.4.

4.2.3. Uncertainty assessment and results

Expectation The absolute TanDEM-X height error w.r.t. the real superficial ice cap height can be estimated given a ground truth. This is not available due to the ongoing hazard. Nevertheless, for

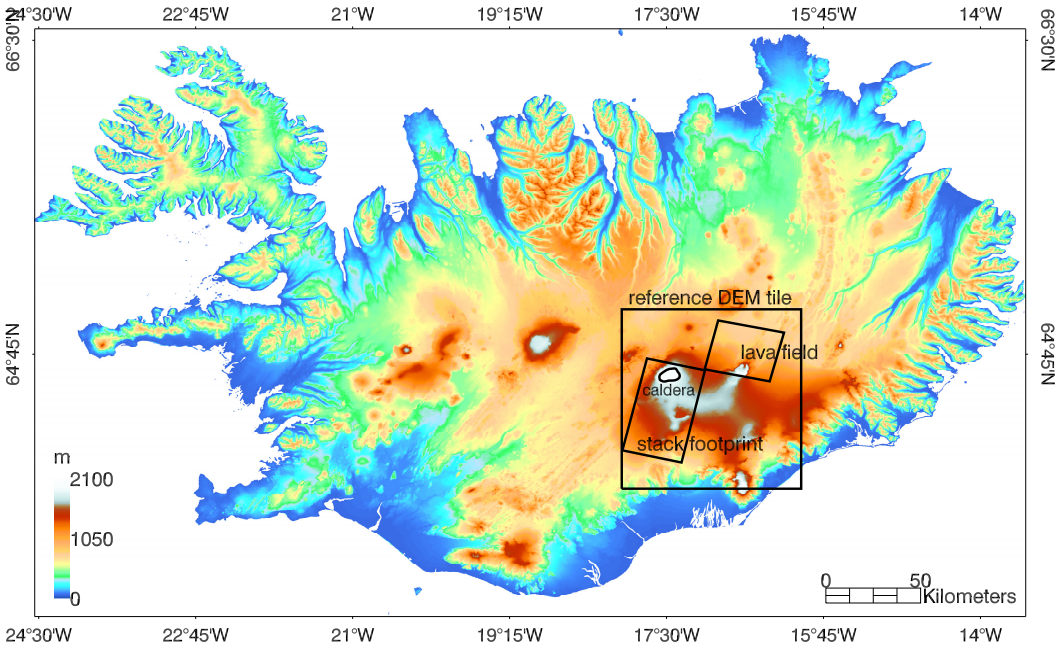

Figure 4.4.: Footprints of the TanDEM-X acquisitions over the Bardarbunga caldera and the Holuhraun lava field. This figure shows the topography of Iceland and is generated by mosaicking TanDEM-X DEM tiles. The reference TanDEM-X DEM tile used for calibration purposes is also highlighted.

Data	$B_\perp$ **[m]**	h_a **[m]**	θ **[deg]**	γ	$h_{\mathbf{err}}$	$q_{\mathbf{ratio}}$
01.08.2014	29.7	163.3	31.4	0.86	2.3	99.9
12.08.2014	31.1	156.2	31.4	0.80	2.8	99.9
17.10.2014	50.2	96.6	31.4	0.92	0.94	99.9
28.10.2014	38.2	126.8	31.4	0.92	1.2	99.9
08.11.2014	57.8	84.2	31.4	0.91	0.89	100.0

Table 4.2.: Geometrical and processing parameters of the TanDEM-X test site under study.

the paper purposes, i.e. the caldera subsidence monitoring, a constant absolute error over the stack is tolerated since the interest is on the relative height difference. Thus, it is important to ensure a consistent phase center location for the data in the stack. According to the considerations in Sec. 4.2.1.1, uniform snow conditions and a constant incidence angle are the requirements. While the stack incidence angle is not changing (see Tab. 4.2), a uniform snow condition is more difficult to assess, since different periods of the year may have a strong impact. However, the high elevation of the caldera, about 2000 m above sea level, the constant SAR early acquisition time, 07:49 a.m., and the consequent low temperature, always below 0°C, prevent melting issues. Assuming then the absence of freshwater ice at the surface top, the discussion should move on the wetness of the snow at the moment of the acquisition. SAR backscatter can be used for the purpose. The work of Stiles and Ulaby (Stiles and Ulaby, 1980) helps to clarify several aspects. First of all, the backscattering coefficient decreases with snow wetness. According to the analysis in (Stiles and Ulaby, 1980), the summer backscatter corresponds to a liquid water volume larger than 1 [$\%^{vol}$], making the TanDEM-X height measure very close to the surface top (see Tab. 4.1). In contrary, autumn

acquisitions exhibit a backscatter yielding a lower liquid water volume, therefore prone to more substantial penetration issues. An empirical analysis over the large glacier area at the south-east of the caldera, chosen in order to avoid evident topographical changes and marked in Fig. 4.7(d), reveals a mean difference of 1.26 m. This difference , according to Fig. 4.1, corresponds to a liquid water content smaller than 0.5 [$\%^{vol}$].

Regarding the system impact on the relative height accuracy, the variation of the height error depending on the local coherence as in Eq. (2.34) is depicted in Fig. 4.5(a). The system heights of ambiguity yield error below 2 meters for coherence values below 0.9. 7 looks in the range dimension and 5 looks in the azimuth one are used in the processing; the independent number of looks is 25. Fig. 4.6(a) shows the error computed for one of the takes in the stack. Errors are strongly related with terrain slope, represented in Fig. 4.6(b). The error dependency with terrain slope is represented in Fig. 4.5(b). The theoretical trend does not apply for shadow and layover areas, where the measured elevation is not reliable (Rossi and Eineder, 2015; Deo et al., 2015); the two regions are marked in the plot. It is interesting to notice that flat slopes, as over the Bardarbunga caldera, yield errors of about 10-20 cm for the TanDEM-X InSAR configuration under analysis. The contribution of the spectral shift into the total coherence, i.e. total relative DEM error, is rather small, with coherence losses of about 0.05-0.1, corresponding to height errors of about 1 meter, for slopes up to about 25 degrees for the heights of ambiguity of the current dataset. Larger contributions shall be expected from volume decorrelation and system noise (SNR) (Martone et al., 2012).

Height differences and geophysical validation To evaluate the topographical changes, the DEMs are generated over a fixed geographical grid with spacing of about 6 m in latitude and longitude. The original interferogram resolution, computed taking into account the independent number of looks and the SAR cell resolution, is about 9 meters.

The DEM differences between the first DEM in the stack (01.08.2014) and all the others are depicted in Fig. 4.7. The Bardarbunga caldera contour is traced according to the outline sketched in Sigmundsson et al. (Sigmundsson et al., 2015). Fig. 4.7(a) shows the differential height on the 12th of August. Here, no relevant changes are noticeable since this topographical map represents the elevation differences with a reference time lag of just 11 days and still before the main fissure opened up in the Holuhraun plain. The small-scale topographical changes are mainly due to system noise. Instead, the topographical maps in Figs. 4.7(b), 4.7(c) and 4.7(d) are relevant since respectively showing the topographical changes 47, 58 and 69 days after the main eruption started. The most prominent topographical change is the caldera subsidence, originated by the collapse of part of the ground above the magma chamber. The considerable depression left in the landscape, with subsidence peaks above 50 m for the largest time lag in Fig. 4.7(d), is well visible. The formation of icecap cauldrons at the south-eastern rim of the caldera is also noticeable. Moreover, the differential maps reveal the complete topographical changes over the imaged part of the Vatnajökull glacier. Among them, two accumulations at the eastern Skafta cauldron and at the Grimsvötn volcanic system are remarkable and tagged in Fig. 4.7(b).

The result of a quantitative study on the caldera subsidence is displayed in Table 4.3. SAR backscatter is measured by calibrating the amplitude signal and compensating for the local incidence angle. The reference DEM shown in Fig. 4.4 has been used for this purpose. The mean caldera backscatter is given in the second column of Table 4.3. The difference between summer and autumn backscatter has been already analyzed in the previous paragraph. The mean coherence over the caldera given in the third column is in general very high and the relative height error in the fourth column the considerably low.

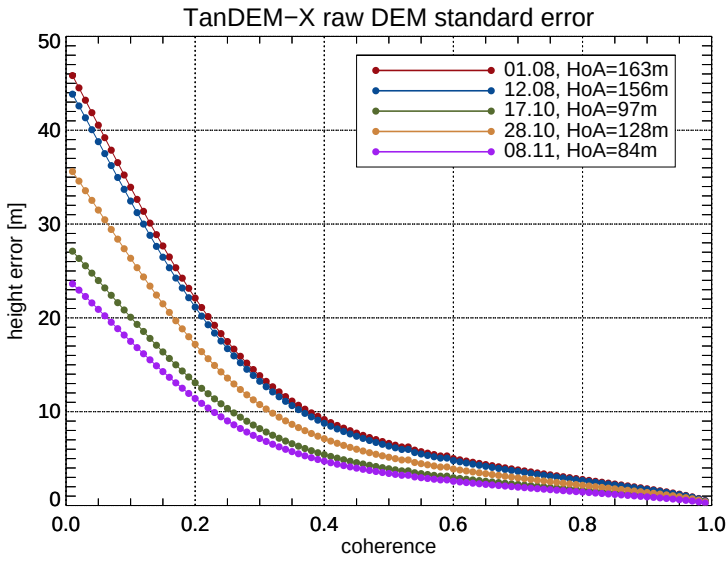

(a) height error vs coherence

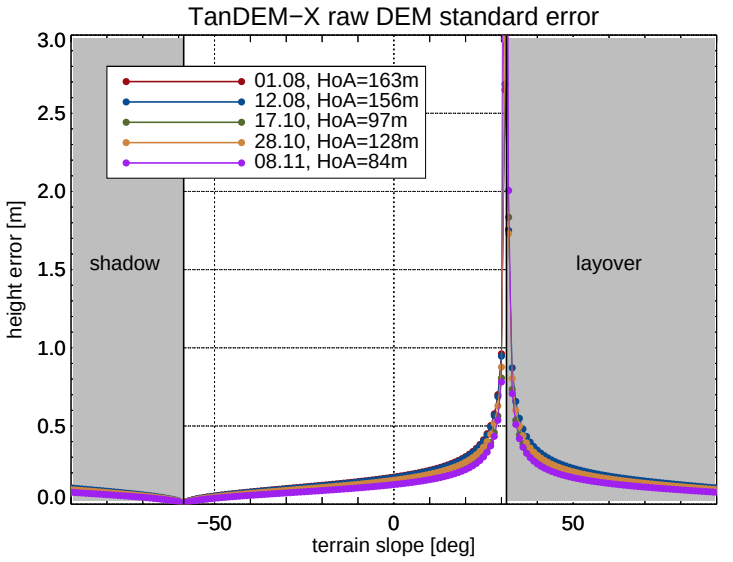

(b) height error vs terrain slope

Figure 4.5.: Standard height error trends of the five acquisitions under study. (a) Error dependency with the local coherence. (b) Error dependency with terrain slope. Shadow and layover areas do not provide accurate results and the marked curves are therefore not valid. Slopes are measured in range direction: positive slopes are the ones facing the radar, negative slopes the ones tilted away.

The caldera collapse is evaluated in terms of mean height and volume changes in the fifth and sixth column of Table 4.3 respectively. These mean values represent the average change over the caldera outline depicted in Fig. 4.7. For the last stack acquisition, thus 69 days after the main fissure opening, the caldera already sunk in average by 16 meters, with peaks of about 50 m in its north-eastern part (see next section), and with an impressive volume loss of about 1 billion cubic meters.

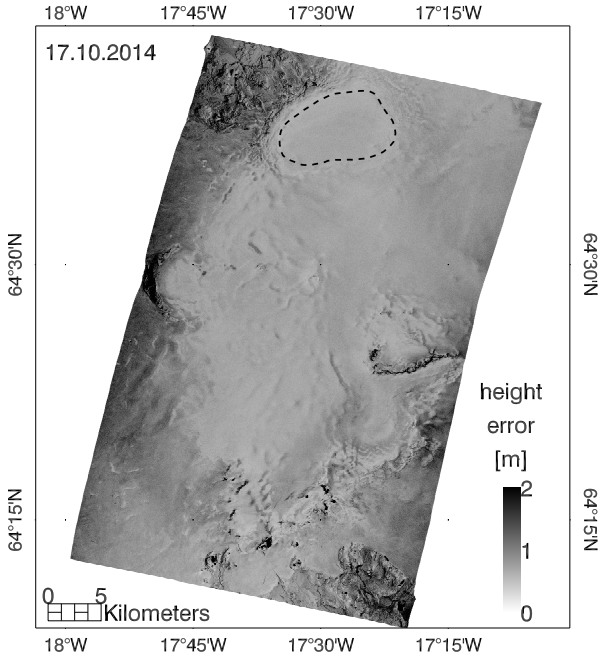

(a) height error map

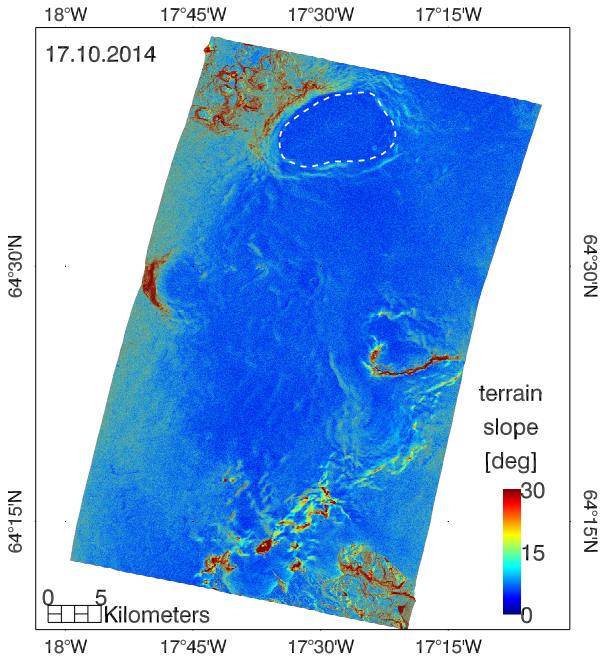

(b) terrain slope map

Figure 4.6.: (a) Height error map for the 17.10.2014 take computed with the local coherence. (b) Terrain slope computed from the 17.10.2014 take. The Bardarbunga caldera outline is highlighted.

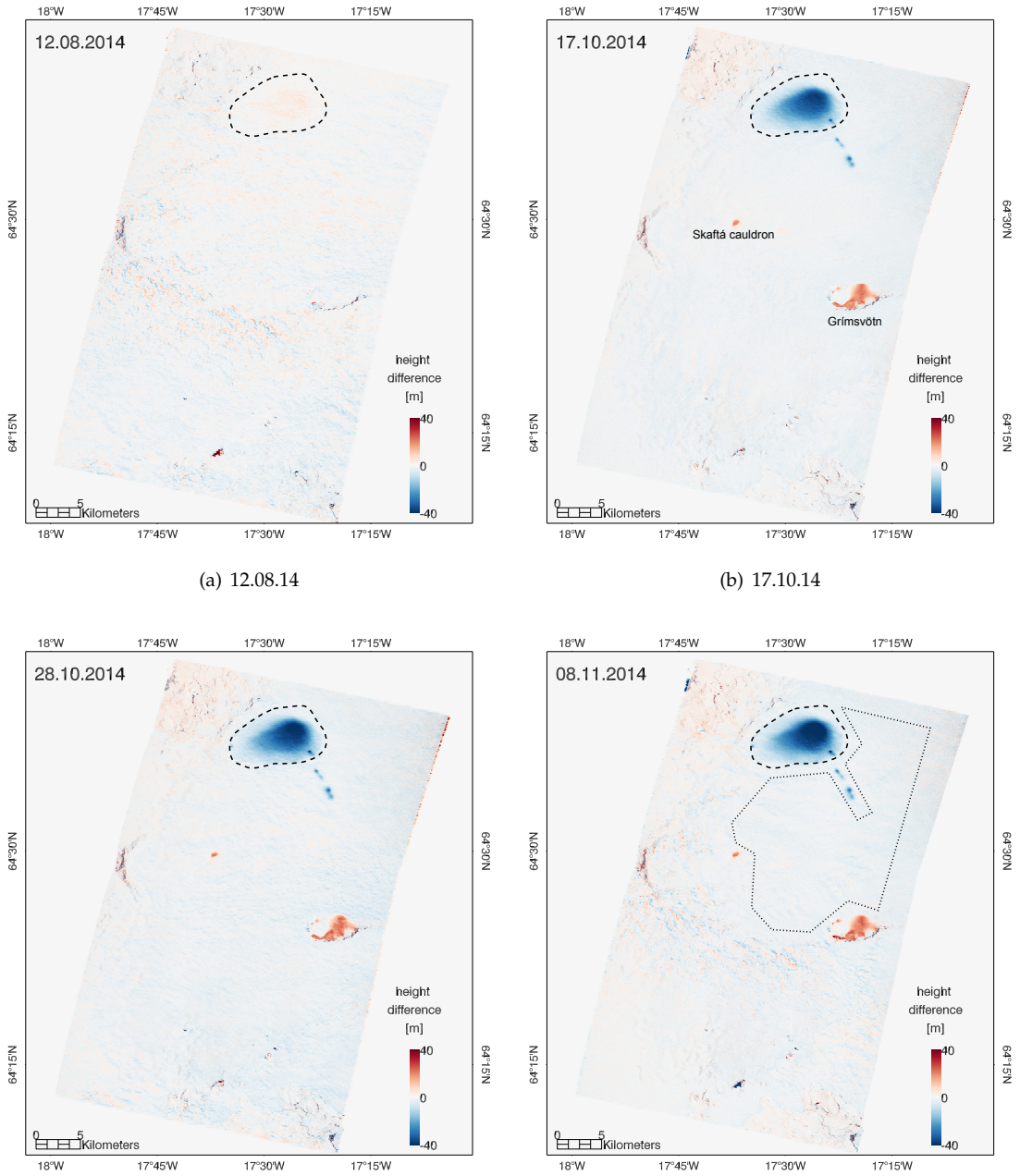

(a) 12.08.14

(b) 17.10.14

(c) 28.10.14

(d) 08.11.14

Figure 4.7.: DEM differences relative to the first DEM in the stack (01.08.2014). Bardarbunga caldera is highlighted in all the differences. The dashed area at the south-east of the caldera in (d) is the one used to evaluate the seasonal wave penetration difference.

This yields an average rate of change of about one meter per week.

For subglacial volcanoes such as Bardarbunga, the caldera subsidence does not refer just to the ground volume loss related to the eruption, but also to the melting of snow/ice because of heat-

Data	σ_0 *[dB]*	γ	h_{err} *[m]*	$\Delta\bar{h}_{1.8}$ *[m]*	$\Delta V_{1.8}$ *[m^3]*
01.08.2014	-15.23 $\pm$ 0.86	0.90 $\pm$ 0.03	1.34	-	-
12.08.2014	-15.31 $\pm$ 0.75	0.90 $\pm$ 0.03	1.70	0.52	0.33e8
17.10.2014	-9.86 $\pm$ 0.74	0.96 $\pm$ 0.01	0.63	-13.85	-8.81e8
28.10.2014	-9.75 $\pm$ 0.76	0.96 $\pm$ 0.01	0.55	-15.13	-9.62e8
08.11.2014	-9.60 $\pm$ 0.77	0.94 $\pm$ 0.01	0.69	-16.39	-10.4e8
Reference	-	-	0.67	-4.53	-2.88e8

Table 4.3.: Mean value of relevant parameters computed over the Bardarbunga caldera. The six columns represent, from left to right, acquisition date, mean calibrated SAR backscatter of the master acquisition, mean coherence, mean standard height error, mean DEM difference between and current data, mean volume difference between first stack acquisition and current data.

ing flux release from the magma intrusion. A peculiar aspect of this eruption is that jökulhlaups related to the cauldrons formation at the caldera rim, the south-east flank of the Bardarbunga, or above the dike intrusion north-west of Bardarbunga, where minor subglacial eruptions probably occurred, were never observed. The water location release is still unknown, and possibly most of it is drained into the groundwater system below the Vatnajökull glacier. A one-to-one comparison of the derived volume loss, for validation purposes, with external lava volume measurements is therefore not possible since one of the volume sources remains unknown. Nevertheless, it is meaningful to compare our caldera volume loss estimation, 1.08 km^3, with the lava volume extent measured on November 04, 2014 (Gislason and al., 2015), 1.0 $\pm$ 0.3 km^3, thus 4 days before our estimate. Considering the seasonal discrepancy of the phase scattering center, our caldera loss estimate is corrected to a volume of 0.963 km^3. The two estimates are very similar, although the caldera loss originated by the additional loss contribution created by the ice melting is not compensated. It should be noted that a consistent role in the volume comparison can arise from the newly formed cauldrons, which are not considered in the caldera volume loss and whose subsidence may be associated to the lava volume. Also other phenomena such as subglacial eruptions and dyke widening may impact in the comparison, since they affect the lava volume measure. In general, a ratio of one between the erupted volume and the subsidence volume indicates that the crust deformation is fully compensated by the compressibility of the magma (Johnson et al., 2000).

Comparison with radar altimeter data A huge campaign has been performed by the University of Iceland over the Bardarbunga caldera and surroundings. The system is a radar altimeter, with measures every 15-20 m and absolute accuracy of 2-3 m (Guđmundsson et al., 2007). Altimeter is in C-band at a frequency of 4.3 Ghz. As predicted in Fig. 4.3, the measured height compared with TanDEM-X should be generally lower.

In Fig. 4.8 the profile of the TanDEM-X acquisitions along the altimeter track which hits the highest change in the caldera is shown. Changes of more than 40 m in 3 months are revealed. The maximum rate of subsidence is of 49 cm/day, in accordance with (Riel et al., 2015), who reported a rate of 50 cm/day. The caldera structure is not symmetric, and its lowest depression lies at its north-east part. The fitting with altimetric data is evident, although morning phase center at X-band results lower than midday phase center at C-band, as shown in Fig. 4.9. To generate this plot, TanDEM-X data have been interpolated to match the exact time and date of the altimeter. Here, one notices a lower scattering center for the altimeter of 3-5 meters in the proximity of the caldera, and a lower scattering center of TanDEM-X data of about 1 meter in the caldera position. With the same snow conditions, one would always expect the phase center of the radar altimeter to be

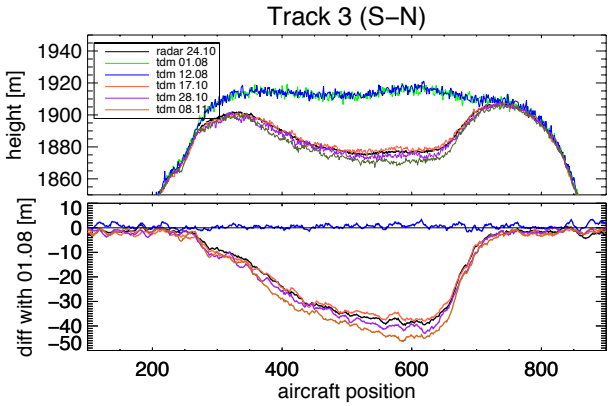

Figure 4.8.: Elevation measured for Track 3 for the 5 TanDEM-X acquisitions and the altimeter (top) and elevation differences with the first data in the stack (bottom).

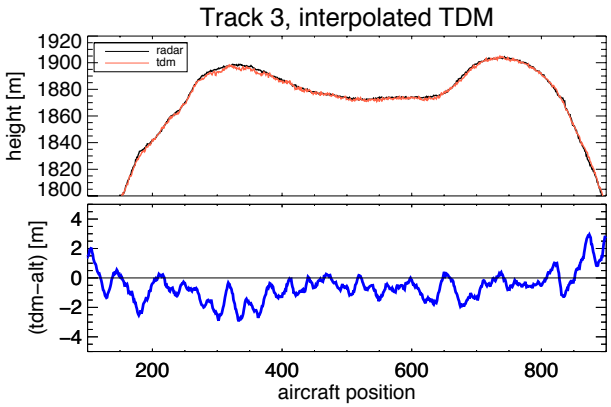

Figure 4.9.: Elevation measured for Track 3 of the altimeter and TanDEM-X interpolated at date and time of the radar measure (top). Difference between the two heights (bottom).

lower than the one of TanDEM-X (Tab. 4.1). The reason for the trend is the non-linearity of the phase center during the day (Stiles and Ulaby, 1980). Indeed, TanDEM-X data is taken for all the acquisitions at 07:49 a.m., so, in the early morning. Altimeter data is yet acquired around midday. In the interpolation process, it is silently assumed that the snow condition at the altimeter time and date is the same of TanDEM-X, but it is obviously not like that. At midday it is reasonable to assume that the snow water content is higher than early morning, due to the increasing temperature, thus causing a higher phase center, even very close to the surface top (Tab. 4.1). However, it is interesting to see how outside the caldera the altimeter signal penetrates more than X-band radar, even though the increasing temperature. Different snow dielectric properties are a possible explanation for this.

4.3. The Serra de Collcardus test case

This investigation takes place at the Serra de Collcardus, a hilly region close to Barcelona (Spain). This test site is chosen since it is part of the benchmark set of the ISPRS Commission 1. LiDAR and CartoSAT-1 data have been made available at the purpose (d'Angelo and Reinartz, 2011).

4.3.1. Dataset description

Two TanDEM-X takes over the Serra are analyzed. The first, acquired on February 22, 2013, has been taken in ascending orbit configuration and has a mean incidence angle equal to 34.7 deg and a height of ambiguity equal to 46.6 m. The second, acquired on January 5, 2014, has been taken in descending orbit configuration and has a mean incidence angle equal to 34.8 deg and a height of ambiguity of 48.6 m. The measured horizontal resolution Ω_r is 9 m (Eq. 2.17) and the DEMs are generated with a sampling of 6 m, thus with partially dependent samples (see Sec. 2.1.3). The patch is spanning over a squared area of 4 by 4 km.

Complementary data are a LiDAR surface model, assumed as ground truth, and a CartoSAT-1 one. The LiDAR DSM has been generated from a 3-D ALS point cloud with a mean of 0.5 points per square meter, which was acquired on November 27, 2007. The CartoSAT-1 DSM has been generated at a sampling of 5 m from a stereo pair having a ground resolution of 2.5 m and being acquired on March 5, 2008 (d'Angelo and Reinartz, 2011).

The four patches are resampled over the same grid with 5 m sampling. Their shaded versions is shown in Fig. 4.10.

4.3.2. Uncertainty assessment strategy and results

The assessment is performed for the TanDEM-X raw DEM. The availability of a CartoSAT-1 surface model makes a complementary assessment also appealing and it is therefore carried out. To be noticed, the CartoSAT-1 horizontal resolution is better than the TanDEM-X one (5 m vs. 9 m).

Visual inspection The first analysis is just a visual inspection of the DEMs in Fig. 4.10. The superior quality of the LiDAR DSM is apparent. In the CartoSAT-1 DSM a series of holes represent unmatched pixels, which are assigned to a dummy value. Both of the TanDEM-X DEMs do not have voids[2] but the surface noise (Sec. 2.1.3.3) is visibly higher than CartoSAT-1. Moreover, a clear layover artefact (as already seen in Fig. 2.10) is noticeable at western slopes for the ascending take and for eastern slopes in the descending one. Complementary slopes, where shadowing may occur, appear instead noisy.

Slope and aspect 2-D PDF plot The DEM geometrical distribution (Sec. 2.3.3) is shown in Fig. 4.11. LiDAR reveals the true distribution. Terrain slopes are distributed quite regularly over all the aspects (with a small predominance for southern slopes). The majorities are between 10 deg and 30 deg. Very few slopes exceed 30 deg. The CartoSAT-1 DSM slightly enlarges the slopes support, especially in the north-south direction. Compared to the LiDAR DSM, a concentration towards smaller slopes is also noticeable.

As expected, the TanDEM-X distribution is rather peculiar. The ascending distribution is mirrored with the descending one. Peaks of the distributions stand for aspect angles in layover areas. Instead, backward slopes are not as dominant as slopes facing the radar due to the random nature of shadow, which yields randomly oriented facets in the DEM. The eye-plot representing the

[2]The geocoding algorithm employed in ITP is set up to always assign an elevation value for every DEM pixel, even if originated from geometrical distortions.

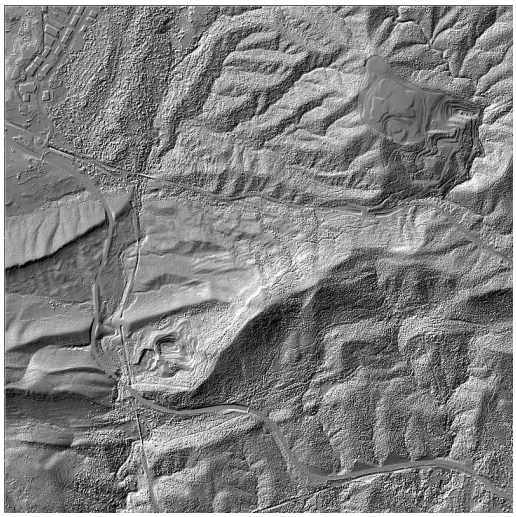

(a) LiDAR

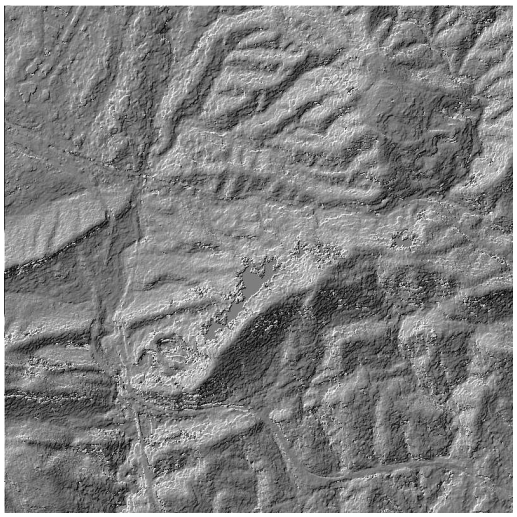

(b) CartoSAT-1

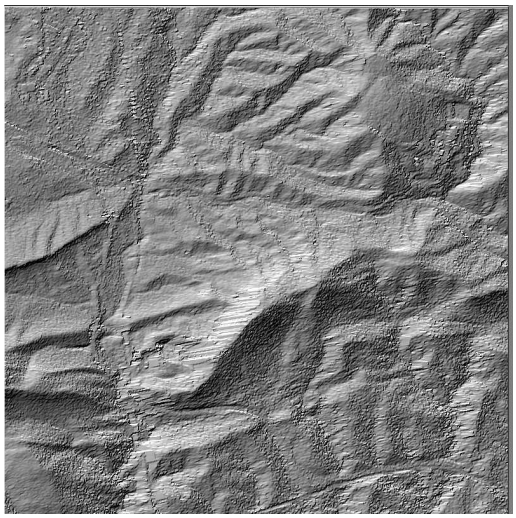

(c) TanDEM-X (ascending)

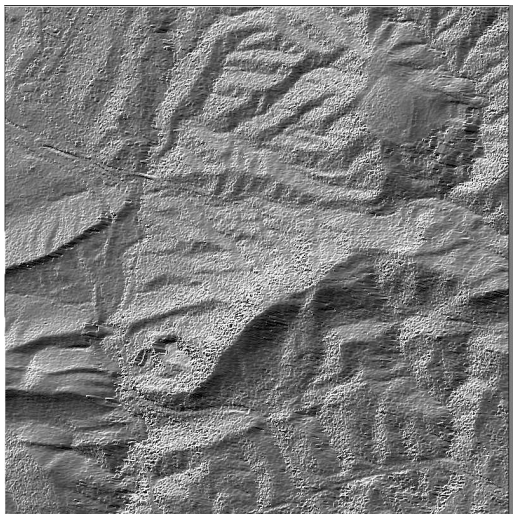

(d) TanDEM-X (descending)

Figure 4.10.: Shaded DEMs over the *Serra de Collcardus* (Spain).

theoretical SAR coverage includes the majority of the DEM pixels. Pixels lying outside should be considered as invalid pixels. They are mainly consequent to interpolation artifacts.

Slope and aspect error dependency The 2-D PDF plot can be employed to represent the geometrical dependency of the absolute error, computed with a difference with the LiDAR DSM. In Fig. 4.12(a) and Fig. 4.12(b) the TanDEM-X absolute error is represented for the ascending and the descending case, respectively. Higher errors lie at large slopes. The error distribution follows the theoretical bounds, so that it also has a sort of eye-shape. The CartoSAT-1 error distribution is depicted in Fig. 4.12(c). In contrast to the TanDEM-X one, the largest error is measured for north-

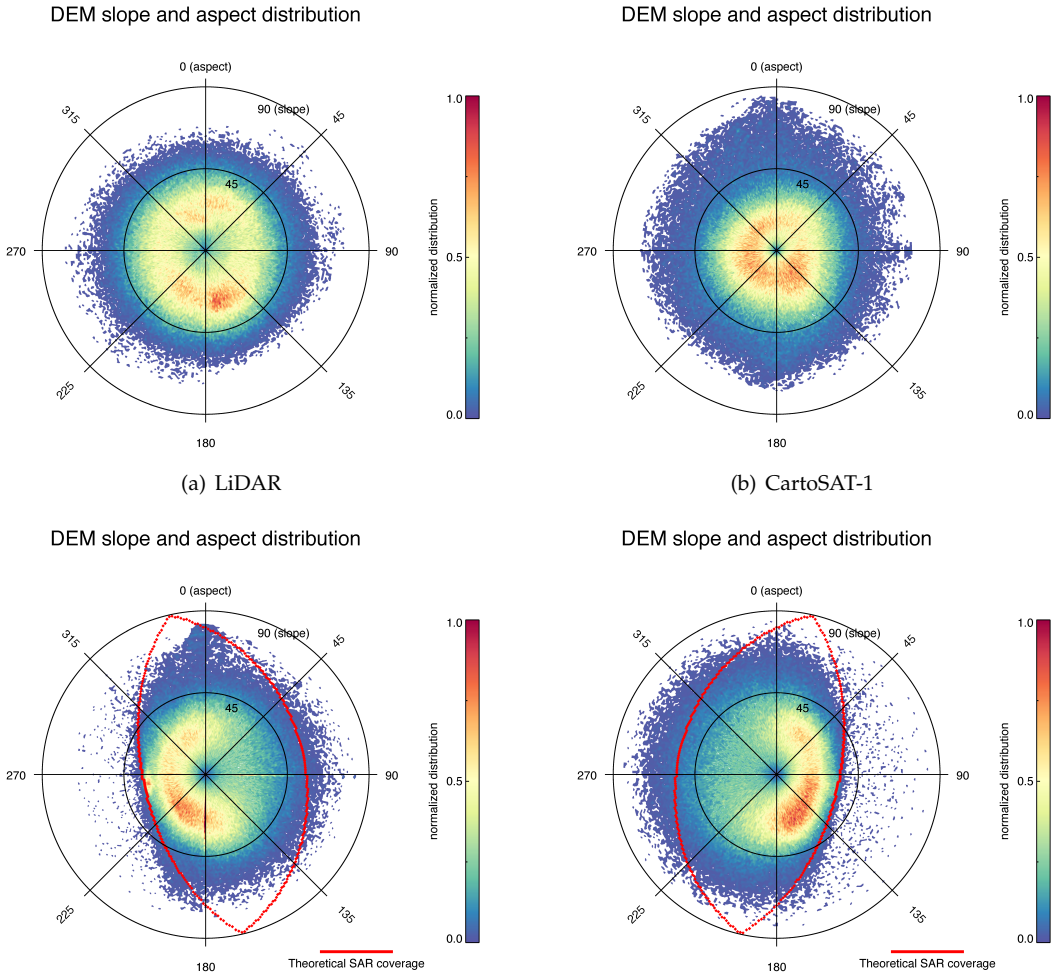

(a) LiDAR

(b) CartoSAT-1

(c) TanDEM-X (ascending)

(d) TanDEM-X (descending)

Figure 4.11.: Slope and aspects 2-D PDF plot representing the distribution of the DEMs over the *Serra de Collcardus* (Spain). Slope and aspect angles are computed from the LiDAR surface model.

western aspects. This is due to the CartoSAT-1 orbit and the two camera view (at $-5°$ and $26°$), creating foreshortening and a lower resolution for that set of aspects/slopes. This error distribution discrepancy makes the fusion between TanDEM-X and CartoSAT-1 quite appealing. Indeed, the simple fusion test in (Rossi et al., 2013) (Appendix A.4) reported a 25% RMSE drop for the fused DEM compared to the single TanDEM-X model.

The aspect and slope angles represented in Fig. 4.12 have been estimated using the LiDAR surface model, thus they are assumed unbiased. It is interesting to evaluate the absolute error difference when computing the geomorphological parameters directly from the models under test. This analysis is shown in Fig. 4.13. First, terrain slope and aspect angles are estimated from both the reference and the TanDEM-X elevation models. Then, the absolute error dependency with terrain slope/aspect is compared for the two estimations. When the terrain slope/aspect angles are equally estimated from the reference and the TanDEM-X DEMs, the differential absolute error is

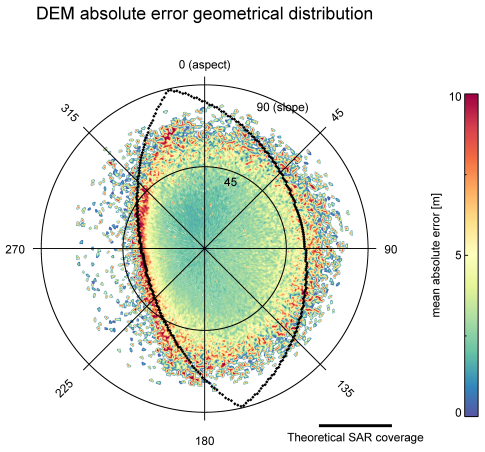

(a) TanDEM-X (ascending)

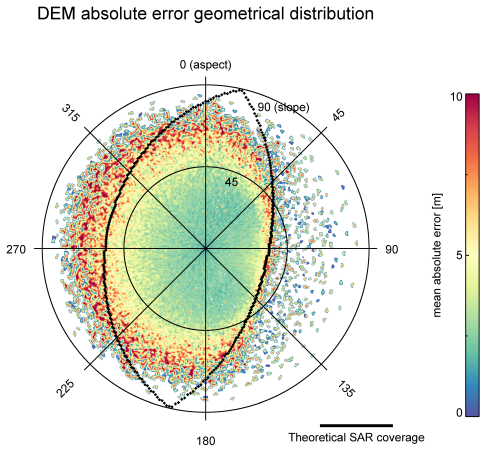

(b) TanDEM-X (descending)

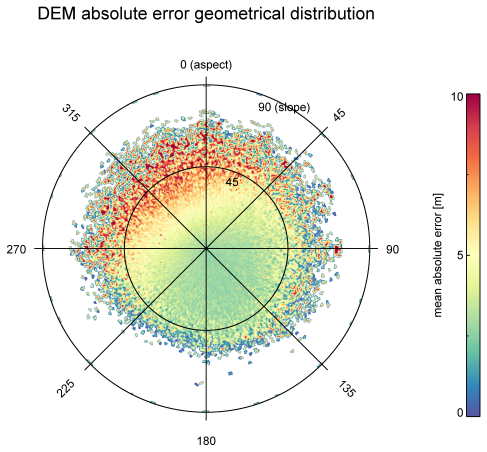

(c) CartoSAT-1

Figure 4.12.: Slope and aspects eye-plots representing the absolute error position over the *Serra de Collcardus* (Spain). Slope and aspect angles are computed from the LiDAR surface model.

equal to zero. Fig. 4.13(a) shows a differential error contained in a few meters up to about 20 deg. For larger slopes it consistently increases up to about 20 m. The explanation is outlined in Sec. 2.3.3. SAR cannot represent all the possible slopes, making then a terrain slope estimation from an InSAR-DEM a significant operation just until the maximum representable slopes.

The aspect differential error is shown in Fig. 4.13(b). It is below the meter for all the aspects.

CartoSAT-1 allows a more accurate estimate of terrain slopes (Fig. 4.13(c)), with a differential error contained in 2 m up to about 60 deg. This is a considerable gain in comparison with the TanDEM-X system. The aspect differential error is in the meter range (Fig. 4.13(d)), as for TanDEM-X.

Difference histograms The final analysis is on the general error distribution. In Fig. 4.14(a) and Fig. 4.14(b) the absolute error distributions for the TanDEM-X and CartoSAT-1 DEMs are shown. The distribution is centered around 1 m for TanDEM-X (general underestimation) and -3 m for

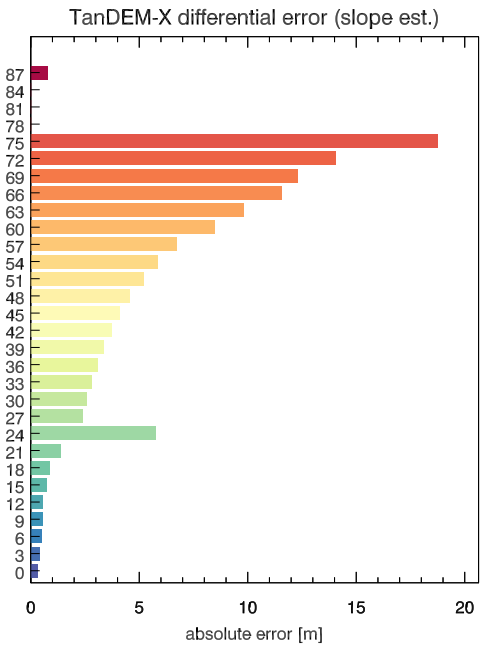

(a) TanDEM-X slope (asc.)

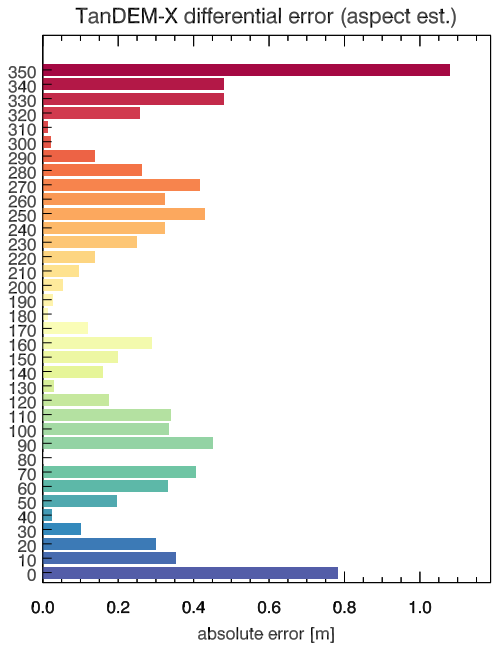

(b) TanDEM-X aspect (asc.)

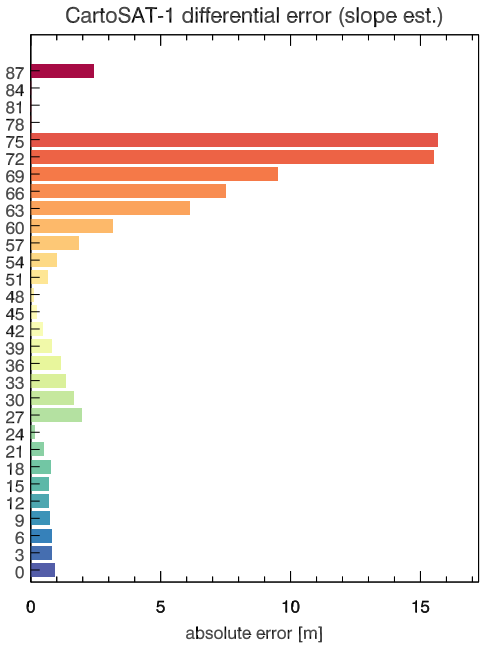

(c) CartoSAT-1 slope

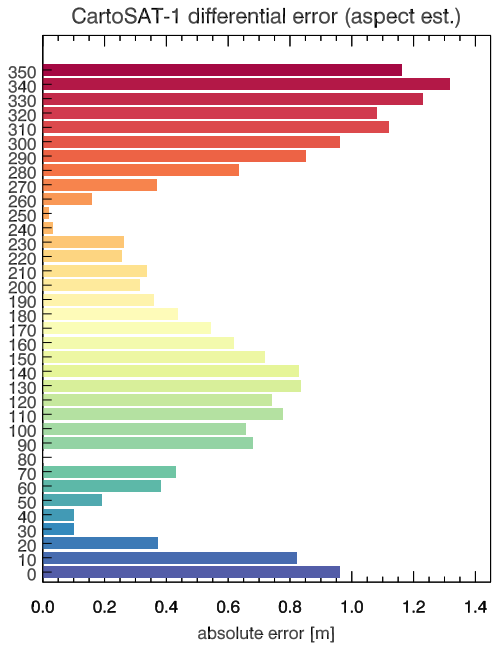

(d) CartoSAT-1 aspect

Figure 4.13.: Differential error caused by a slope and aspect estimation directly from TanDEM-X model (a) and (b) and CartoSAT-1 (c) and (d) instead of the true aspect and slope.

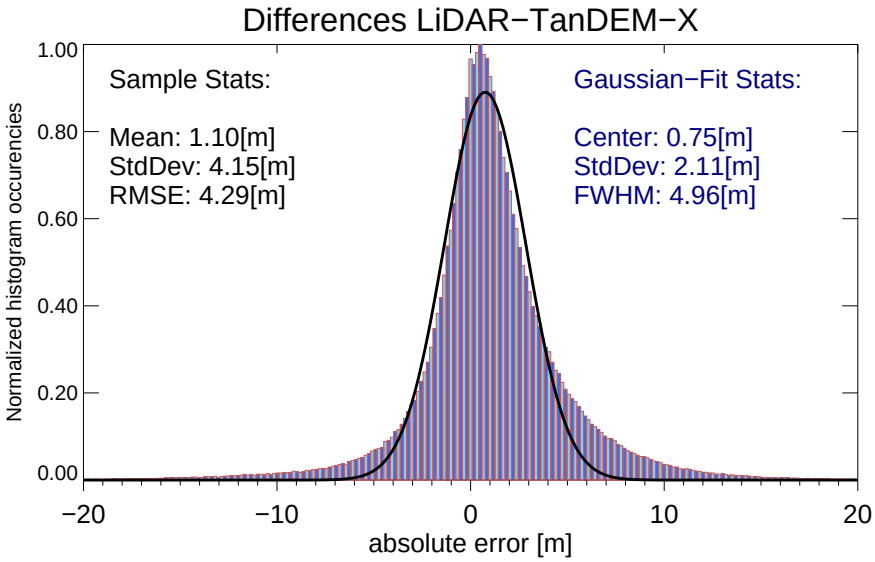

(a) TanDEM-X

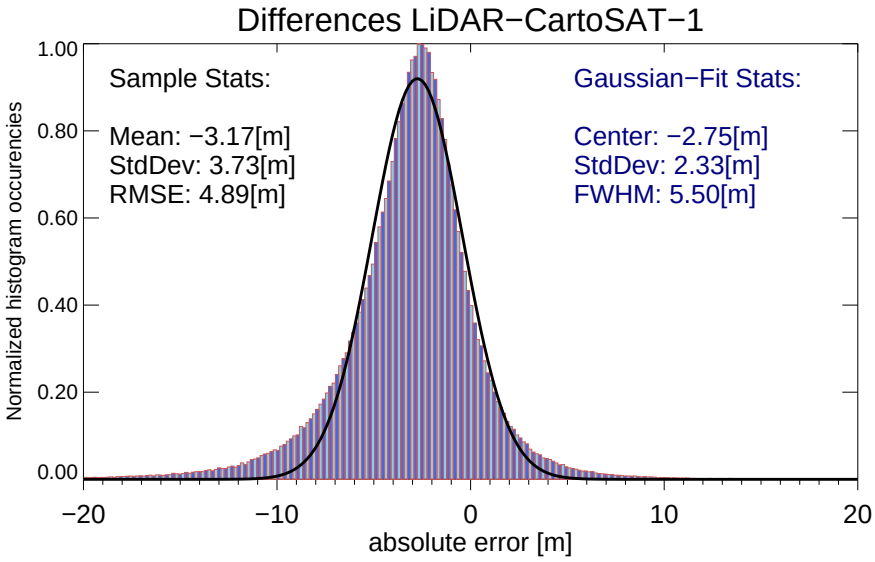

(b) CartoSAT-1

Figure 4.14.: Absolute error distribution for TanDEM-X (a) and CartoSAT-1 (b).

CartoSAT-1 (general overestimation). The TanDEM-X mean error depends on the local topographical features in layover areas, where the DEM takes the form of a ramp (the complete explanation is provided in Sec. 5.2.2) and in shadow areas, where the DEM results noisy. The CartoSAT-1 overestimation is instead explainable with inaccuracies of the reference SRTM DEM, used in this case for calibration. The TanDEM-X distribution presents a smaller Gaussian-fit Full Width at Half Maximum (FWHM) than the CartoSAT-1 one, although the error standard deviation is lower for the CartoSAT-1 DEM due to a less marked distribution tail. The RMSE, computed as in Eq. 2.42, is smaller for TanDEM-X. Both of the distributions are not close to a Gaussian one, resulting in

different mean and standard deviation values for sample and Gaussian-fit statistics. According to the considerations in Sec. 2.3.1, RMSE is then not fully characterizing the error distributions.

4.4. Discussion and conclusions

This chapter was dedicated to the TanDEM-X uncertainty assessment for moderate terrain. Two investigations were provided. For the first inspection, over the Bardarbunga volcanic system in Iceland, the assessment strategy employed also for smooth terrain was adopted. The focus has been posed on the electromagnetic framework, to assess the absolute error dependency on the imaged terrain (in this case snow) and on the temporal domain for different seasons. This investigation is geophysically relevant, since it describes the terrain variations of the Vatnajökull glacier consequent to the Bardarbunga eruption. For the second inspection, over the Serra de Collcardus in Spain, a more rigorous and geometrical approach was employed due to the presence of a reference fully covering the same area. Also an optical surface model was analyzed for completeness and comparison. The main conclusions for the investigations are the following:

1. It is fundamental to consider the acquisition time of the InSAR data employed to generate the DEM. In the first test case, it was demonstrated how the summer and autumn acquisitions over a glacier exhibit height changes of a few meters. Changes were measured also for night and day acquisitions, due to snow dielectric properties change.
2. Strictly liked to the previous point, in case multiple InSAR acquisitions are used for the uncertainty assessment, it is important to control the parameters affecting the generated height, such as incidence angle, polarization and carrier frequency.
3. For the first time, the Bardarbunga caldera was monitored in its entirety during the first period of the 2014-2015 eruption. An maximum subsidence of 50 cm/day was measured and confirmed by other researchers. A volume loss of about 1 billion cubic meters in about two months was also measured.
4. The uncertainty assessment can be performed with an indirect validation by using geophysical outcomes. More in detail, it was shown how the caldera volume loss measured with TanDEM-X can be directly related to the lava volume measured at the eruption site.
5. Terrain slope and aspect angles play an important role in uncertainty assessment. A demonstration over an hilly region showed how TanDEM-X absolute error is shaped by the theoretical SAR coverage defined by the layover and shadow boundaries.
6. The measured error distributions were not strictly Gaussian. The RMSE, fully characterizing normal distributions by definition, should not be the only considered parameter for the error assessment.
7. An estimation of terrain slope angles from TanDEM-X data has poor accuracy for angles larger than 20 deg. CartoSAT-1 provides a more accurate slope angle estimation.
8. Even though the CartoSAT-1 horizontal resolution is about two times better than the TanDEM-X one, the two models are comparable in terms of vertical accuracy.
9. A fusion of CartoSAT-1 and TanDEM-X could provide a significantly better model, since their errors are aspect-dependent and complementary. This is shown in Appendix A.4. The simple weighted average method proposed in A.4 shows a significant drop of the RMSE of about 25% for TanDEM-X and 30% for CartoSAT-1. Another improvement can be obtained by fusing the DEMs derived from ascending and descending geometries. In (Deo et al., 2015) a drop of the RMSE of about 5% is reported for the fused DEM.

5. Uncertainty investigation over complex terrains: the Berlin case study

This chapter summarizes the paper in Appendix A.5: Rossi, C., and Gernhardt, S., **Urban DEM generation, analysis and enhancements using TanDEM-X**. *ISPRS Journal of Photogrammetry and Remote Sensing*, 85, 120-131, 2013 (Rossi and Gernhardt, 2013),

and the paper in Appendix A.6: Rossi, C., and Eineder, M., **High-resolution InSAR building layovers detection and exploitation**. *IEEE Transactions on Geoscience and Remote Sensing*, 53(12), 6457-6468, 2015 (Rossi and Eineder, 2015)

5.1. Inspection placement in the thesis framework and relevance

Complex terrains are composed by steep slopes. Among them, an urban area is probably the most complex terrain to map with Synthetic Aperture Radar (SAR) sensors. Indeed, geometrical distortions such as layover and shadow always occur due to the SAR side looking viewing geometry on the frequent metropolitan slope discontinuities. Besides distortions, multiple scattering phenomena and building overlays make data interpretation difficult (Stilla et al., 2003). In this context, a height map generation is quite a challenging issue. The InSAR processing chain can be revised in order to provide an accurate urban DEM (Sec. 5.2.1). The uncertainty assessment should first analyze the appearance of the building in the DEM. This is provided in Sec. 5.2.2, by inspecting the geocoding algorithm. An analysis about what is really seen by the SAR sensors in building positions is provided in Sec. 5.4.3. As for all the other investigations, a difference with references (Sec. 2.3.1) is the primary inspection method. References are in this case a LiDAR model and a Permanent Scatterer (PS) point cloud. Additionally, verified that the inaccuracies are coming mainly from layover areas, a novel detector is proposed (Sec. 2.3.4 and 5.4.2).

Investigation relevance Optical and LiDAR remote sensing technologies are widely used in the generation of urban DEMs. Nowadays, this land cover class has been exclusively mapped by those sensors. Nevertheless, with the establishment of a new SAR mission dedicated to build elevation models as for TanDEM-X, it becomes interesting to understand the potentials of InSAR in mapping cities. To characterize fine structures like buildings, the horizontal resolution must be the highest as possible. Whereas the horizontal resolution Ω_r for stripmap data is around 8-12 m, for High-Resolution Spotlight (HRS) mode Ω_r is around 3.5 m (Rossi and Gernhardt, 2013) and Staring Spotlight data can even improve it to about 1.5 m. In this dissertation, the focus is on HRS-InSAR. The interest in city models is self-evident, since humans are living in there. Their mapping is then important for many management applications, such as urban development monitoring, urban climate studies and renewable energy surveys.

5.2. High-resolution urban DEM generation

As outlined in Sec. 2.1.3, the primary objective of the TanDEM-X mission is the generation of a global DEM following the high standard accuracy HRTI-3 (Krieger et al., 2007). To accomplish the specifications, stripmap data is used. Nevertheless, the stripmap horizontal resolution does not assure an accurate mapping of dense metropolitan areas, where the separation between buildings

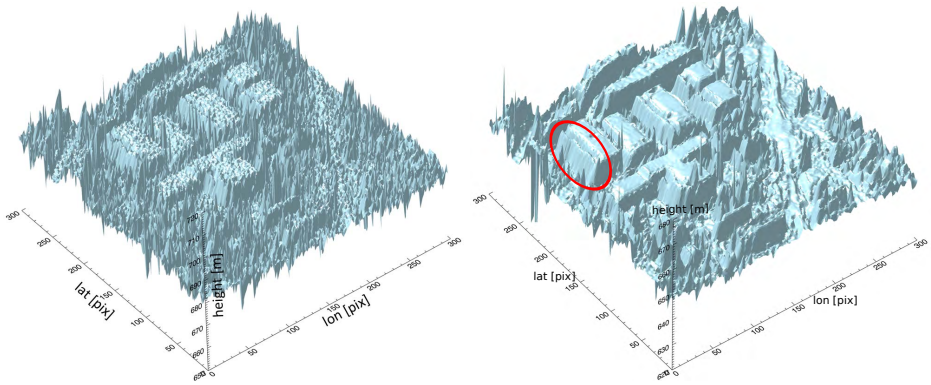

(a) boxcar (b) NL-InSAR

Figure 5.1.: Three dimensional shaded visualization of a HRS DEM over an industrial area generated using: (a) operational algorithms (b) adaptive filtering. The raw DEM sampling is 1.66 m, the patch extent is 500 by 500 meters.

is smaller than the resolution. The mission foresees however experimental spotlight acquisitions to generate higher resolution DEMs following the HRTI-4 standards with a grid sampling of 6 meters. With this sampling, a denser urban mapping is feasible. In this chapter the focus is on high resolution DEMs, for building reconstruction purposes. In this case, the ITP processing at DLR may be modified in order to generate solutions adapted for urban mapping. In the next section the main modifications and the urban limitations to the interferometric chain are introduced.

5.2.1. Processing issues

Spectral filtering The spectral shift stage can be switched off in case of purely urban areas. The statistical base which justifies it, namely distributed scattering, is generally not valid for municipal zones (Sec. 2.2.8).

Coregistration Matching is a complex issue in cities. The ITP algorithm described in Sec. 2.1.2 makes use of moving windows to estimate the radargrammetric shifts. The standard window size of 32 by 32 pixels corresponds, in spotlight mode, to 35 m in azimuth and 19 m in range. The estimation is not provided for every pixel of the SAR image, but just for a set of them disposed on a grid. The separation of the windows is 70 m and 30 m in azimuth and range respectively. Even if assuming the estimation performed for every pixel (with an enormous computational cost), the problem of multiple heights mapped inside the window is remaining. This creates a coregistration-mismatch, which depends on the baseline, incidence angle and height difference between scatterers in the window.

Multilooking For urban modelling purposes, the fast performing moving average window algorithm employed to reduce the phase noise in the ITP multilook stage can be changed. In particular, adaptive algorithms making use of amplitude statistics to fuse pixels with the same characteristics are particularly recommended. The one in (Deledalle et al., 2011), named Non-Local InSAR (NL-InSAR), connecting non-consecutive pixels inside a search window, can be used for this purpose. The need to employ adaptive methods is clear by looking at Fig. 5.2.1, showing portions of the operationally and adaptively processed (NL-InSAR) urban DEMs for a high resolution spotlight acquisition. The interferometric phase is processed to obtain a resolution Ω_r of 3.65 meters (Eq. 2.17). The phase noise mitigation is evident comparing the two raw DEM portions. The height

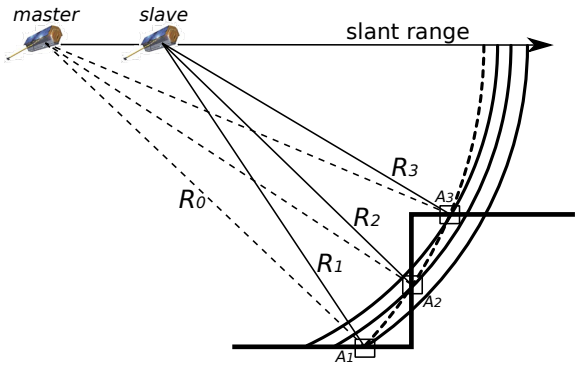

Figure 5.2.: Interferometric signal model for a building layover pixel. R_1 is the slant range distance between the satellite and the ground scatterer A_1, similarly for the wall scatterer (R_2, A_2) and the roof scatterer (R_3,A_3). R_0 is the master distance between the satellite and the three scatterers.

variance of the flat roof of the four buildings - about 5000 DEM samples - in the middle of the area is 4.72 meters for the operational ITP software case and 0.68 meters for the experimental one.

Phase Unwrapping This a very delicate step in urban scenarios. Unwrapping can be avoided when the unwrapped phase is limited in between π and $-\pi$. To accomplish that, the height of ambiguity should be as large as the maximum building elevation, assuming flat terrain. If this is not the case, then the generated model will present height jumps (in form of *holes* or *steps*) with an intensity depending on the ratio between h_{amb} and the building height.

Geocoding This step is described in the next section.

5.2.2. Building shape in the DEM

To estimate the building shape in the interferometric DEM, its absolute phase must be derived. At the purpose, the simplest construction, a cuboid laying on flat terrain, is considered and depicted in Fig. 5.2. It can be decomposed in four parts: ground, layover, roof and shadow. For the first and third part the mapping is assumed accurate. In contrast, the absolute phase in the shadow area is unpredictable. The layover phase trend can instead be predicted. Layover is a superposition of contributions from ground, wall and roof.

In the interferometric framework, for the master satellite, the slant range distance R_0 between the satellite and the three layover scatterers is not varying by definition. On the contrary, three different distances are measured between slave satellite and points on ground (R_1), wall (R_2) and roof (R_3). Thus, the master s_m and slave s_s focused signal at the range r and azimuth x in the layover area are (Bamler and Hartl, 1998):

$$\begin{aligned} s_m(r,x) &= \sum_{i=1}^{3} A_i(r,x)\exp\{-j2kR_0(r,x)\} \\ s_s(r,x) &= \sum_{i=1}^{3} A_i(r,x)\exp\{-j2kR_i(r,x)\}\,, \end{aligned} \tag{5.1}$$

where k is the wavenumber and A_i is a complex variable including the bidimensional system impulse response and the local backscatter, assumed equal in both geometries.

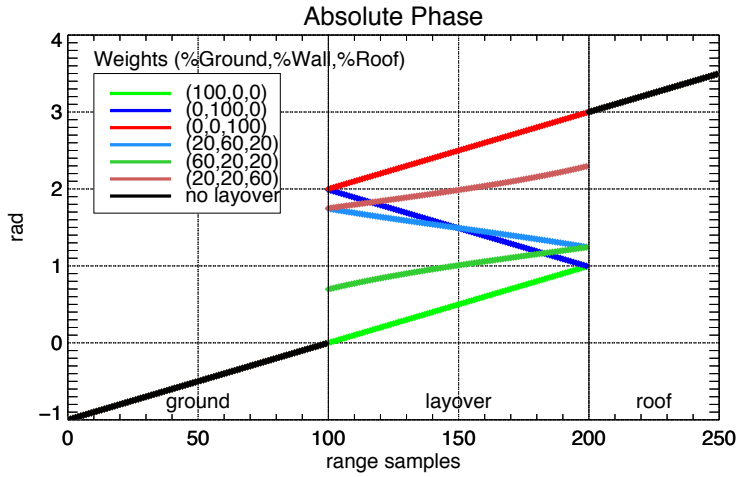

Figure 5.3.: Noise-free absolute phase simulation of a step function considering various exponential weights for the different segments composing the function. Ground, wall and roof represent the lower horizontal, the vertical and the higher horizontal segments respectively. In the layover area, 6 cases are considered with different colors.

The interferometric phase is the argument of a sum of nine complex terms:

$$\begin{aligned}\phi(r,x) &= \arg\left(s_m(r,x)s_s^*(r,x)\right)\\ &= \arg\left(\sum_{i=1}^{3}\left[\left(A_i^*\sum_{j=1}^{3}A_j\right)\cdot\right.\right.\\ &\qquad \left.\left.\exp\left\{-j2k\big(R_i(r,x)-R_0(r,x)\big)\right\}\right]\right)\end{aligned} \tag{5.2}$$

The analytic derivation of (5.2) without further approximations is not bringing to a compact expression. Instead, simulations and test on real data have been conducted (Thiele et al., 2007). Eq. (5.2) is plotted in Fig. 5.3 assuming A_i as a real constant for simplicity. The factors A_i are considered as weights to the exponential terms, i.e. they represent the impact of the single layover components in the signal. The interferometric phase is a decreasing function for increasing slant ranges in case of positive height of ambiguity. A noticeable phase gradient is at the layover beginning, with a singular exception for total ground dominance ($A_2 = A_3 = 0$). Total wall dominance ($A_1 = A_3 = 0$) yields the highest gradient. Mixed weights produce phase jumps with spreads depending on the actual backscattering configuration. The absolute phase layover trend is non-linear, with the exception of single component dominance.

In Fig. 5.4 the focus is on the mapping of such a trend, in case of total vertical dominance. The basics for the interpretation of this plot are in Sec. 2.1.2.3. In this circumstance, the mapping of the SAR domain in the cartographic one is sparse, i.e. with a variable distance between mapped points. As effect, a DEM derived with a bilinear interpolation between points presents artificial ramps. In this example, the derived DEM points are shown in blue. The generated elevation points from the absolute phase are in red. The height of the elevation points, and consequentially the artificial model slopes, depends on the layover contributors weighting in the returned signal. In this case, for total wall dominance, a couple of elevation ramps are expected in front of the building. A real example of interferometric urban elevation model with the highlighted effect is in Fig. 5.1(b). All the buildings imaged in this portion present the layover artifact, as underlined for one of them with

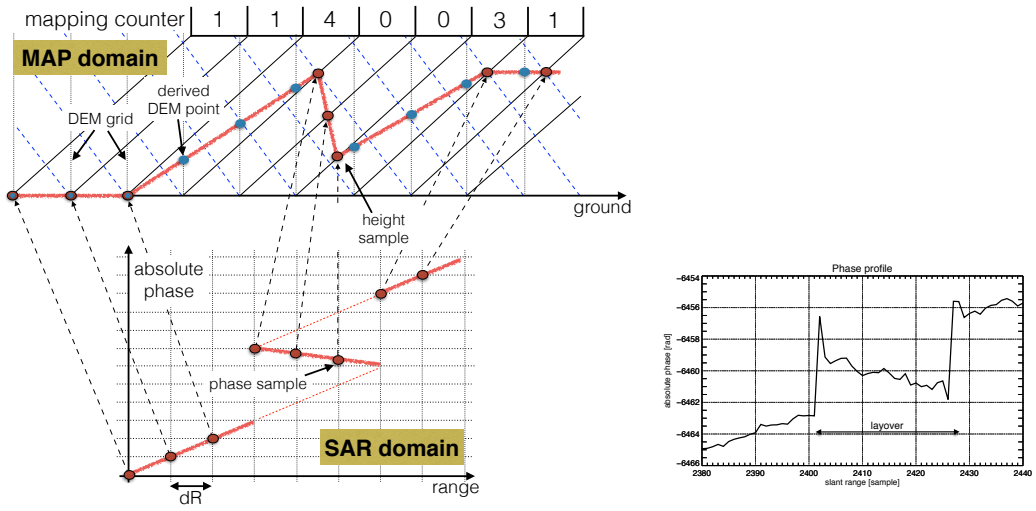

(a) mapping (b) real trend

Figure 5.4.: SAR absolute phase mapping in case of building layover. (a) A phase gradient yields an elevation model ramp when employing a bilinear interpolation for the derivation of DEM points. (b) Range section of the InSAR absolute phase for the highlighted building in Fig. 5.2.1.

a red circle. A range section of the corresponding absolute phase is in Fig. 5.4(b). The real trend fits well with the simulated one in Fig. 5.3. Evidently, accuracy is limited at layover locations.

5.3. Dataset description

The test site chosen for the analysis is Berlin (Germany). A bistatic HRS acquisition has been acquired on the January 4, 2012. The satellites had a normal baseline of about 110 meters yielding a height of ambiguity of 65 meters. The incidence angle at the center of the scene is 41.8 degrees. The geometrical and processing parameters are in Tab. 5.1.

This acquisition is used for the generation of the high resolution DEM. The upper part of Fig. 5.5 shows the produced DEM, generated at a raster of 2.5m by employing the Intensity-Driven Adaptive Neighborhood (IDAN) algorithm (Vasile et al., 2006) for the interferogram generation and the coherence computation. In the lower part of the figure a visual comparison for the boxed area between four different DEMs is provided. Besides the experimentally processed DEM (with adaptive filtering), an equal resolution raw DEM is generated with operational algorithms. Additionally, a standard 12m resolution DEM is generated from a stripmap acquisition, acquired on August 11, 2011, having a normal baseline of 135 m and a height of ambiguity of +50 m. Finally, a DLR SRTM X-SAR DEM with 30 m resolution and a LiDAR DEM at 1 m raster are also available. The latter is used as ground truth. These inputs and their public availability is in Tab. 5.2.

5.4. Uncertainty assessment strategy and results

A first visual inspection of the DEM in Fig. 5.5 resembles the considerations below:

- *Building shape.* The ramp on the side of the building facing the satellites, explained in Sec. 5.2.2, is quite evident throughout the DEM. The left side of the buildings is affected by layover.

Parameter	Value
range bandwidth	300 Mhz
PRF	8200 Hz
center incidence angle (master)	41.8 deg
effective baseline	108.1 m
height of ambiguity	+65.4 m
SSC pixel spacing (range)	0.45 m
SSC pixel spacing (azimuth)	0.86 m
spectral shift filtering	enabled
multi-look algorithm	IDAN
interferogram resolution	2.72 m
mean coherence	0.69

Table 5.1.: Processing parameters for the Berlin spotlight test site.

input data	acquisition date	availability
DLR SRTM X-SAR	23-02-2000	public
Spotlight TDM SSC	04-01-2012	TDM science users
Stripmap TDM SSC	11-08-2011	TDM science users
LiDAR	Jan-Mar 2009	internal

Table 5.2.: Input data acquisition dates and availability.

Buildings appear wrongly geolocated due to this issue. Buildings oriented in azimuth are more subject to this phenomenon.

- *Local phase unwrapping errors.* Phase unwrapping issues may manifest themselves in the DEM at two scales: a large error, as the one in Fig. 2.11, and a local or micro error, not detectable with the PUCM. These second ones can be caused by shadow/noise and appear in the DEM as holes (dark blue color in Fig. 5.5) or spikes (dark red). Their deviation from the real height is a multiple of the height of ambiguity. A smoother phase and an enhanced coherence, obtained by using adaptive fringe filters, have been demonstrated to reduce these errors. An example is shown in the lower part of Fig. 5.5. The rectangular building at the upper-left part of the image is the German parliament building. The building is not present at all, replaced by a *hole* instead, in the operational raw DEM (second bottom-left panel). When increasing the resolution, the building appears (second bottom-left panel), even though micro-errors are present, like its upper-left part. Only the use of a filter mitigates the errors. The parliament building is only one example, dozens are noticeable when comparing filtered and unfiltered DEMs.

- *Vegetated areas.* Tree heights are underestimated, as visible comparing TanDEM-X to LiDAR for the park at the southern part of the German parliament building. The underestimation can be related to the phenomena studied in Chapter 3.

- *DEM evolution.* The first DEM section, DLR SRTM X-SAR, has been added just to show the gain in detail when increasing the sensor resolution (left to right).

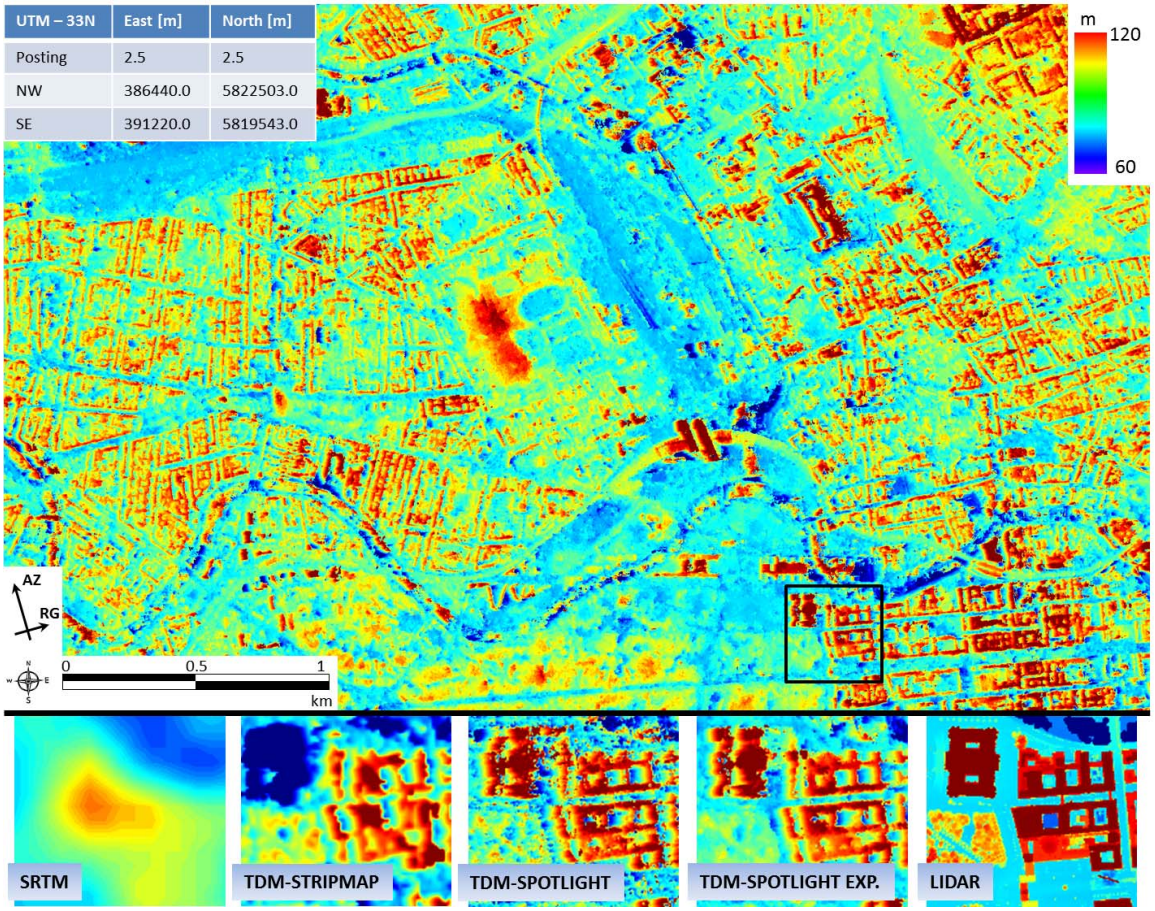

Figure 5.5.: Experimental 2.5m resolution TanDEM-X DEM of Berlin, Germany (top). In the lower part, a visual comparison of the highlighted portion is shown for DLR SRTM X-SAR DEM, operational TanDEM-X raw DEM, experimental high-resolution TanDEM-X raw DEM, experimental filtered high-resolution TanDEM-X raw DEM and LiDAR DEM (left to right). The DEMs are in UTM projection (coordinates at the top-left). The SAR angles are shown at the bottom-left.

5.4.1. Difference with reference

The LiDAR model is resampled to the TanDEM-X grid in order to evaluate the absolute error. A peculiarity of this research is to classify *buildings* (where there is the effective interest) and *non-buildings* in the uncertainty analysis. At the purpose, a complementary PS point cloud, generated as in (Gernhardt and Bamler, 2012), is used as input for the generation of the so called *PSI-DEM*. The PSI-DEM is a rasterized version of the point cloud, which is transformed to a 2.5-D DEM by adopting the algorithms described in Sec. 3.3 of Appendix A.4. Considering that PSs mainly appear at building locations in the scene, the PSI-DEM validity map can also be seen as a segmentation map between structures (valid/in PS cells) and non-structures (invalid/outside PS cells). Using this knowledge, and the reference DEM, two histograms representing the height differences for the whole tile are analysed in the following.

First, the error for non-structures (e.g. roads, vegetation) is shown in Fig. 5.6(a). The sample mean and standard deviation are respectively 0.32 and 7.64 meters and the Root Mean Square Error (RMSE) 7.65 meters. A Gaussian fit is superimposed. The Gaussian standard deviation and Full

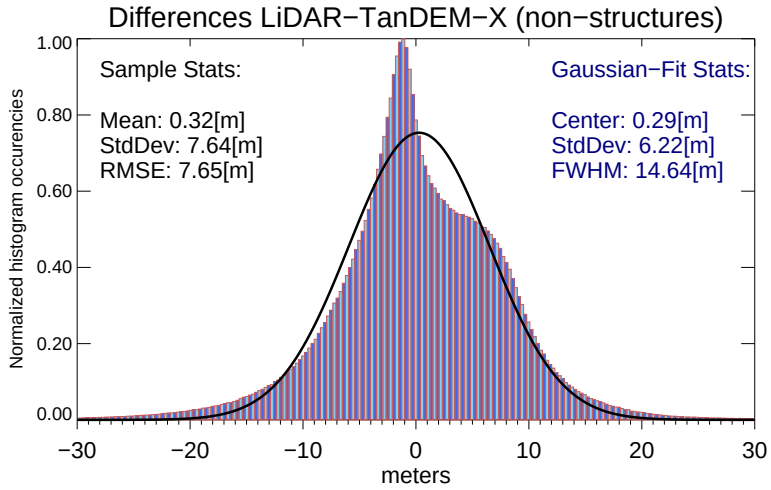

(a) PS-DEM cell undefined

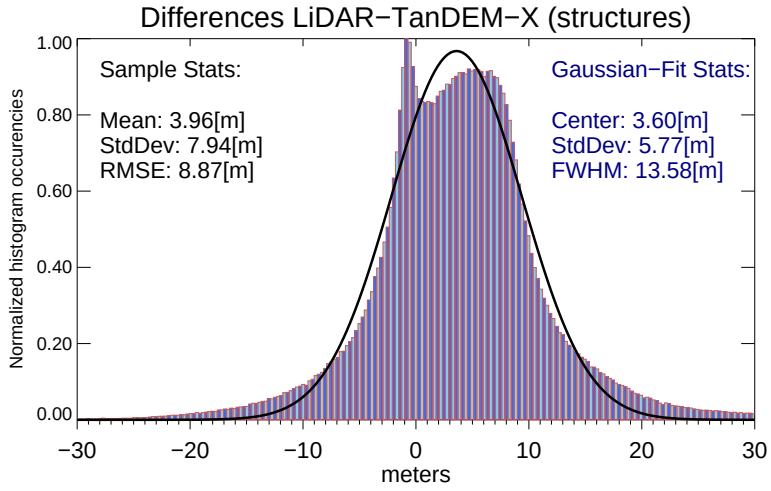

(b) PS-DEM cell defined

Figure 5.6.: Absolute error distribution for TanDEM-X in structure positions (a) and non-structure positions (b).

Width at Half Maximum (FWHM) are respectively 6.22 and 14.64 meters. Whereas the mean is centred around zero, meaning that the TanDEM-X raw DEM is well calibrated, the histogram appears bimodal. The first narrow lobe corresponds in fact to the ground areas next to every building for which TanDEM-X overestimates the heights, as explained in Sec. 5.2.2. The mean overestimation is around 2 meters.

Second, the error between the reference and TanDEM-X, considering the structures, is shown in Fig. 5.6(b). The histogram has statistics comparable with the previous one, with a slightly smaller Gaussian standard deviation. It is centred at around 4 meters. For other scenarios, this value may change depending on the current incidence angle, which triggers the height slope at the building layover positions. The small peak is caused by local occlusions.

The distributions are not following the Gaussian fit because of the DEM artifacts in layover po-

sitions. Thus, as seen in Sec. 4.3.2, and according to the considerations in Sec. 2.3.1, RMSE is then not a statistically significant parameter.

In Appendix A.4, a fusion between the PSI-DEM and TanDEM-X, simply filling the PSI-DEM invalid pixels with TanDEM-X, and thus improving the model at building locations, is reported. To visually better understand the improvements, and visually evaluate the building shape studied in the previous section, a 3D model of the parliament of Germany, already investigated in the bottom panels in Fig. 5.5, is shown in Fig. 5.7. The layover height slope is quite evident at the front façade of the structure (Fig. 5.7(a)). Moreover, a second ramp, caused by a height jump (internal atrium), is visible in the right part of the building from this perspective. A precise DSM reconstruction from LiDAR data can be seen in Fig. 5.7(c). The fused DEM TanDEM-X - PSI is shown in Fig. 5.7(b). The improvement in comparison to the sole TanDEM-X DEM is noticeable. At the building location the height slope is no longer present. The remaining slope next to the front façade is due to the fact that the PSI-DEM is not defined for the ground area adjacent to the parliament. The overall shape of the building also better fits with the reference. For this section, the absolute error for TanDEM-X is 4.17 ± 12.8 meters and for the Fused DEM is 0.87 ± 9.66 meters. To be noticed, the particular DEM shape in layover position in Fig. 5.7(a) is the same already encountered in the previous demonstrations in Fig. 2.10 and Fig. 4.10(c) and Fig. 4.10(d). The elevation scale is obviously different, but the shape is similar.

5.4.2. Layover map generation

In the previous sections, it has been demonstrated how the urban DEM is inaccurate at layover positions. A layover map is then significant for the uncertainty assessment (see also Sec. 2.3.4). In this context, a novel building layover detector has been implemented. The major advantages versus standard estimators are the absence of high-resolution external DEMs and the building segmentation. The major disadvantage is the suitability just in an interferometric scenario, which is actually the DEM generation case, and not for a single complex image.

The detection principle is based on the inspection of the geocoding step of the interferometric processor, and in particular on a special sub-product generated for the purpose and named *mapping counter*. The mapping counter is a map, in slant range coordinates, whose samples m_c describe the number of occurrences of a SAR interferogram pixel in the produced DEM. For flat terrain, the SAR mapping on the DEM raster depends on the DEM posting and the subsampling used in the interferometric processing. For simplicity, let's assume a *1:1* mapping, i.e. an InSAR pixel corresponds to a DEM pixel. In this situation, for an ideally flat terrain and noiseless interferogram, every SAR pixel is used just once and the mapping counter is a unit matrix. A divergence with this condition is an indicator of slopes. In the urban case, where the terrain is usually flat or locally flat, a divergence with this condition is an indication of layover. To better understand the mapping counter values in presence of layover, they are shown in the upper part of Fig. 5.4(a).

A phase gradient creates a *multiple-mapping* region, i.e. $m_c > 1$. A straightforward technique to extract layovers is then to detect pixels accomplishing this condition, for every slant range line of the mapping counter. This constraint identifies the beginning of a slope, or, in our case, a building layover zone. The following mapping counter pixels shall accomplish the condition $m_c = 0$. The detection implies a segmentation of the two regions and a mutual-link search. Flexibility in the mutual link must be introduced as phase noise - or a particular contributor weighting set - may disjoint them. A set of refinements finalizes the layover map. If the building is large, then the non-mapping region must be enclosed in between two multiple-mapping regions by cause of the phase gradient at the end of the layover zone (see Fig. 5.3). In contrary, if the building is totally under the layover effect, then also its shadow area can accomplish the condition $m_c = 0$, thus falsely enlarging the estimated layover patch. In the latter case, the interferometric coherence is exploited in order to define the layover ending point with a simple thresholding. This is the basic concept behind the mapping counter exploitation; fine refinements and the more general case of *n:m* map-

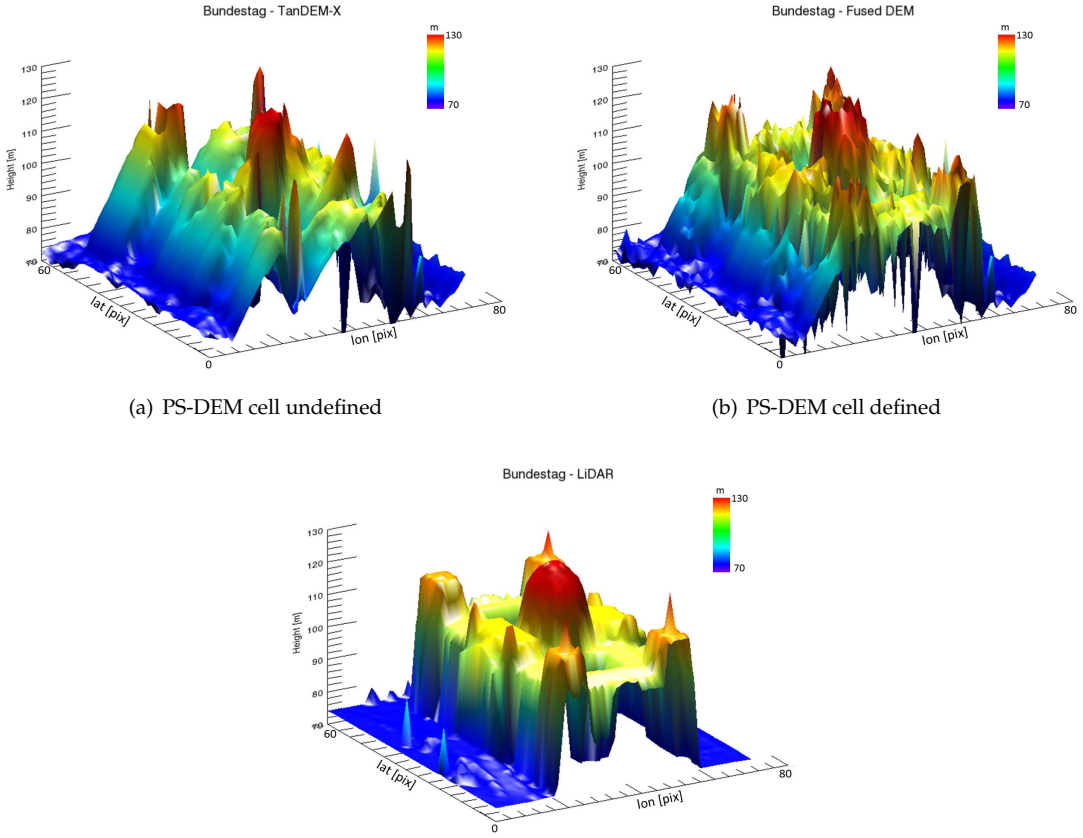

(a) PS-DEM cell undefined

(b) PS-DEM cell defined

(c) PS-DEM cell defined

Figure 5.7.: 3D model of the German parliament as seen by TanDEM-X (a), Fused DEM (b) and LiDAR (c). The model extent is 150 (northing) by 200 (easting) meters. Using LiDAR as reference, the absolute error for TanDEM-X is 4.17 ± 12.8 m and for the Fused DEM is 0.87 ± 9.66 m.

ping is described in Appendix A.5.

The application to the current data set is shown in Fig. 5.8. The mapping counter of the full acquisition is shown at the top-left. The map is quantized on three levels: a null value, in black, a unit value, in grey, and higher values in white. These last values, representing multiple mappings, are extracted and shown in the center-left map. In addition to the paper purposes, they can be used to estimate the building orientation in case of rectangular shapes. At the bottom-left, the non-mapping ($m_c = 0$) patches are extracted and coded in white. Mainly representing building shapes, they contain the larger part of the desired information. The mutual link search, noise and shadow removal and segmentation bring to the result shown at the bottom-right. The geocoded version of the map is a direct indication of inaccurate zones of the urban DEM. No a-priori assumptions have been made about building shapes. The SAR amplitude of the master channel is also shown on top-right to highlight the difficulties encountered by algorithms based only on simple amplitude and coherence thresholds (e.g. the layover portion of a building may be smaller than the full building patch).

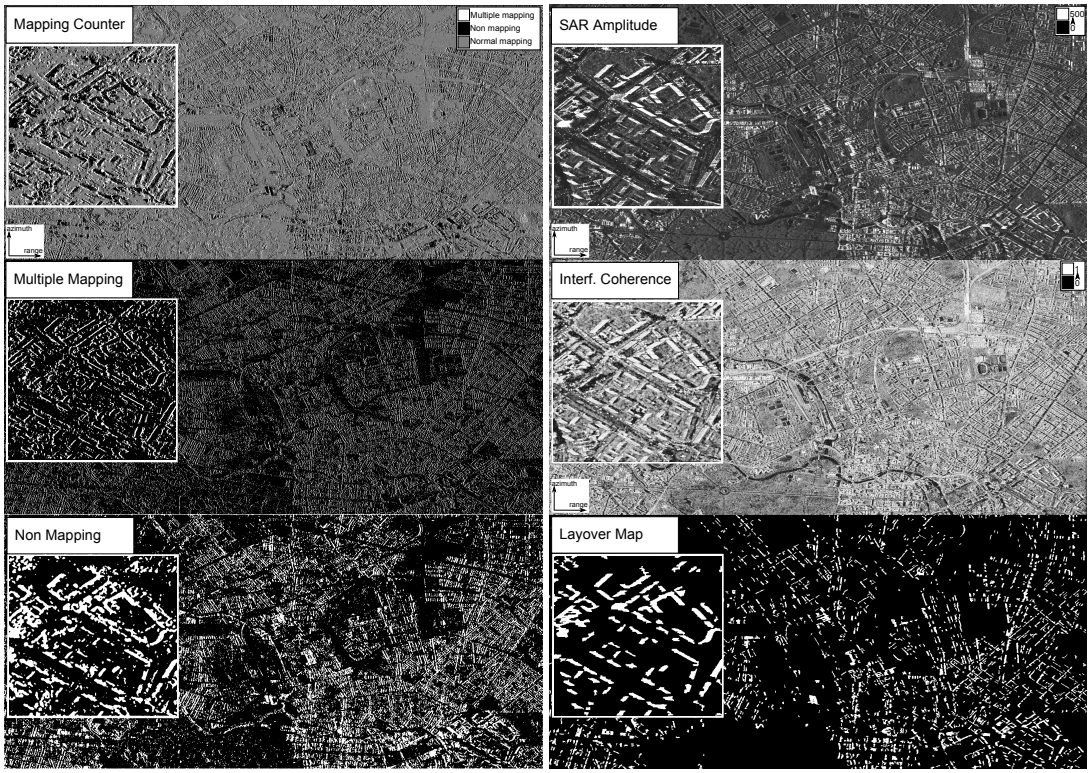

Figure 5.8.: Visual representation of the layover detection processing steps. (Top left) Mapping counter. In black the *non-mapping* areas having value $m_c = 0$, in gray the normal mapping areas having value $m_c = 1$ and in white the *multiple mapping* areas having value $m_c > 1$ are represented. (Middle left) *Multiple mapping* areas extracted from the mapping counter are in white. (Bottom left) *Non-mapping* area extracted from the mapping counter are in white. (Top right) SAR amplitude of the master channel in SAR coordinates. (Middle right) Interferometric coherence (Bottom right) Final building layover map. The detected and segmented buildings are white coded. For all the figures the highlighted portion is a zoom of the south-east part of the map.

5.4.3. Layover analysis

As seen in Sec. 5.2.2 and in Eq. 5.2, building layovers are composed of several contributors that mix up with certain weights. Profiting from the output of the layover map, each building layover can be exploited in order to *see* what the patch really contains. This is also called *layover decomposition*, i.e. the derivation of the number of contributors and their backscatter. It usually require techniques that use a stack of images such as tomography (Zhu and Bamler, 2010). In this research, the focus is on how much information one can derive with a single InSAR acquisition. The topic is very relevant in the uncertainty assessment framework. Indeed, approximating (5.2) at the first order, i.e. $\phi(r, x) \simeq \phi'_r dr + \phi'_x dx$, and solving for the local backscatter, layover heights can be determined by making use of the SAR phase-to-height conversion (Bamler and Hartl, 1998).

This problem is handled in the spectral domain, by estimating the fringe frequencies in the layover patch and relating them to the physical slopes included in the patch (Eq. 2.36). A detailed study has been performed (for the first time with this purpose) and it is reported in Appendix A.5 with simulations and test on real data. Here, just the main outcomes are resumed. The frequency estimation algorithms under test are MUltiple SIgnal Classification (MUSIC) and the periodogram

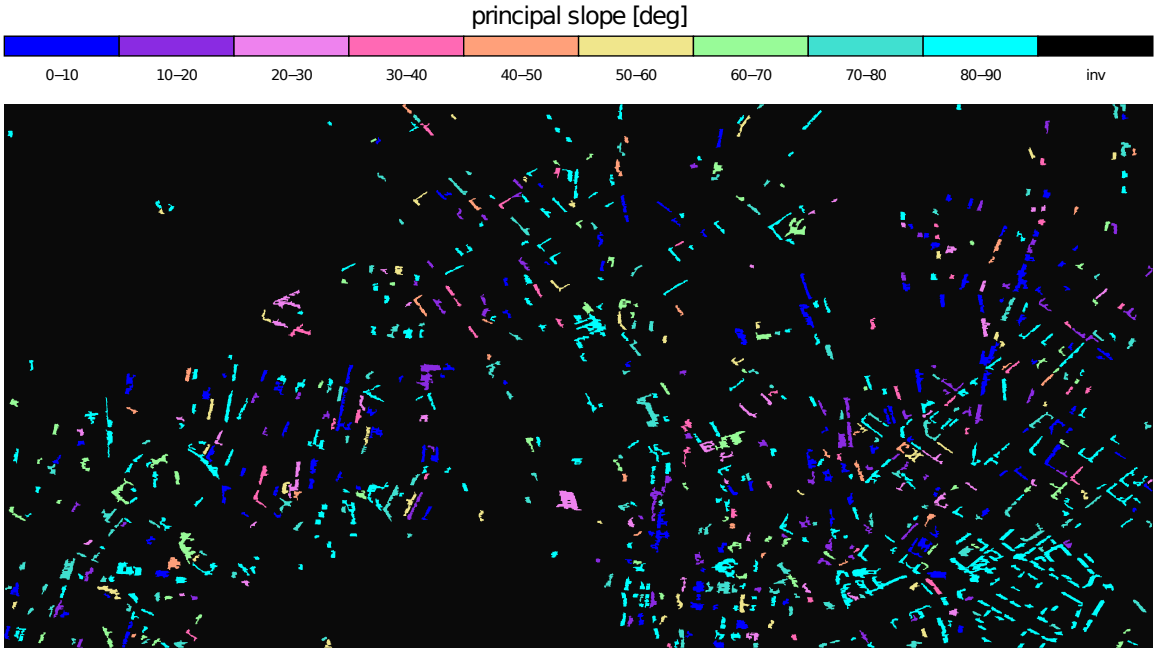

Figure 5.9.: Principal slope for the detected building layovers. A segmentation on the detected map and a conventional MUSIC algorithm is used to estimate the dominant frequency for layovers having a minimum range and azimuth support of 15 and 10 samples. Colour scale is at the top.

(Kay, 1988). The estimation is performed in the range dimension, with the azimuth dimension used to average the estimates. With the typical small layover support[1], only the MUSIC algorithm provides a reliable estimation, but just for a single contributor, when it dominates over others. In particular, the main layover component can be estimated with about 15 samples. Accurate secondary component estimation requires about a double number of samples, which makes a complete decomposition feasible only for high-rise and isolated buildings at X-band. Thus, only for the strongest component, i.e. the one with an higher backscatter, a single frequency slope is estimated and denoted *principal slope*.

Since MUSIC provides frequency locations, but not an estimate of signal backscatter, a further estimation technique is required to detect the dominant frequency. First of all, the number of components is required as MUSIC input. For that, the Minimum Description Length (MDL) (Kay, 1988) has been chosen as selection technique. Considering the particular case, a maximum number of 3 components is considered. After that, if a single contributor is detected, then obviously it is the dominant one, otherwise the dominant one is estimated by inverting the MUSIC model.

This framework is exploited to derive the principal slope of the layover portions derived for the current test site. The result is in Fig. 5.9. Estimated slopes are regularly quantized in 9 classes. Considering the simulations in Appendix A.5, the fringe frequency is estimated only for layover patches having a minimum range and azimuth support of 15 and 10 samples, respectively. Discarded buildings can be visually recognized by comparing Fig. 5.9 and the bottom-right map in Fig. 5.8.

[1]Building layovers extend for a number of pixels depending on the building height and the incidence angle. Smaller incidence angles and higher constructions provide larger supports. By definition, also higher sensor resolution increases

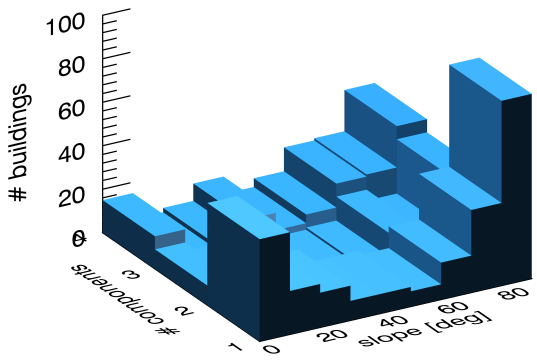

Figure 5.10.: Two dimensional histogram of the estimated slopes and number of layover components. Axis represent the number of building layovers (z), the number of components (y) and the estimated principal slope (x).

In Fig. 5.10 the model order, i.e. the estimated number of layover components, is shown for the 9 slope classes. An analysis of the result indicates that for about 60% of the analyzed buildings (in total 866) wall has the dominance in the signal return. Flat roofs (or ground) dominate for about 25% and other slopes, as tilted roofs, for the remaining 15%. A first consideration is about the generally larger wall support at the acquisition incidence angle (Tab. 5.1) considering the buildings conformation of the city under analysis. In fact, excluding wall portions not visible by the radar due to local occlusion (e.g. trees or close buildings), wall is generally totally included in the portion whereas roofs are only summing up for a section of the total layover support. A second consideration is about the balconies-windows configuration, which creates a set of strong reflectors at the vertical slope. For these configurations, the facade layover contribution dominates over the others. An example is provided in Fig. 5.4.3. The mentioned buildings conformation is evident for this portion, representing the southern-eastern part of the derived map and already taken as reference in the zoom panels of Fig. 5.8. The derived spectrum and MUSIC pseudo-spectrum for a benchmark structure are plotted at the bottom of the figure. A first degree model is detected. The estimated principal slope is close to 90 degrees.

Strong reflectors at the roof tops make the roof slope dominate. An example is in Fig. 5.4.3. The orange and the connected yellow building are belonging to a single layover patch. The adjacent red building is instead differently segmented due to a low coherence area which disjoins it. The horizontal slope is found as dominant, because of the set of solar panels and chimneys on the flat roof. The spectra are here more complex: in the layover patch also adjacent trees superimpose and the vertical slope is not estimated. The other two slopes are not accurately estimated, once again demonstrating the inability to completely reconstruct the layover signal with a single interferogram. Nevertheless, the principal component provides useful information, e.g. the facet in which strong scatterers are lying. This information is not easy to retrieve by inspecting the single amplitude, coherence and absolute phase. On the whole, it has been experimentally verified that when various scatterers at a specific facet exhibit a high backscattered signal return, their facet slope is measured and a single slope is estimated. Fig. 5.10 demonstrates that for the majority of the detected layovers a single contributor is estimated.

the number of layover pixels.

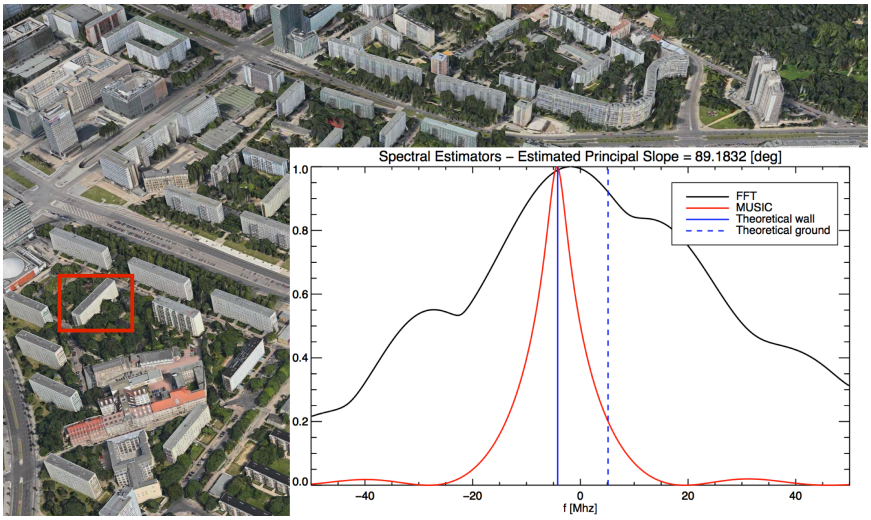

(a) vertical dominance

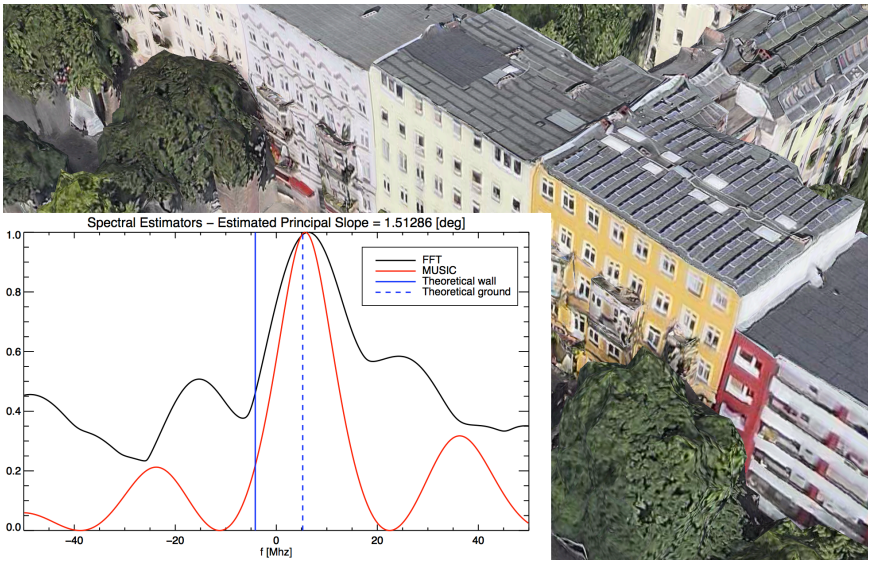

(b) horizontal dominance

Figure 5.11.: Estimation examples. (a) Exemplary estimation of vertical slope dominance. The southern-eastern part of the dataset is shown with a three-dimensional optical view (©Apple Inc.). The spectra of the building layover highlighted in red are over-imposed. In red, the MUSIC pseudo-spectrum is used to obtain the principal slope estimation, very close to 90 deg. A single contributor is estimated. In black, the maximum of periodogram is also shown. Frequencies corresponding to the vertical and the horizontal slopes are represented with a continuous and a dashed blue line, respectively. (b) Exemplary estimation of horizontal slope dominance. The spectra of the yellow building are over-imposed. The MUSIC pseudo-spectrum shows a principal slope estimation very close to 0 deg. Three layover contributors are estimated.

5.5. Discussion and conclusions

The subject of this chapter was the uncertainty assessment of complex terrains, focusing on urban areas with an investigation over the city of Berlin, Germany. In contrast with the previous chapters, the DEM was generated with higher resolution data, in order to assess the accuracy at the building level. The processing chain was reviewed and the major issues pointed out. The availability of an external LiDAR reference allows, also for this investigation, the assessment of the absolute error. LiDAR systems are generally the first choice for urban DEM generation. A single-baseline InSAR-DEM cannot be compared in terms of accuracy. Also optical systems allow the generation of urban DEMs with a much better accuracy. SAR cannot be related with those systems due to the geometrical distortions which strongly compromise the DEM accuracy. Nevertheless, the chapter analyzed the TanDEM-X potentials over urban areas and found for the test site an absolute error below 10 m. Even though the single building reconstruction resulted inaccurate, other urban studies can be performed, more in the global scale than in the local one. For instance, density studies or change detections could be feasible. An important advantage of the TanDEM-X mission is the global mapping, so that in principle high-resolution acquisitions can be commanded everywhere in the world. This is certainly not the case of ALS systems, which require to flight over the city with the proper instrumentation, being for instance an issue for problematic areas. Partially, this can be solved with optical satellite systems, but the limitation may be in this case the local weather, and again some area of the world may be difficult to map.

The uncertainty study demonstrated the following points:

1. An adaptive fringe filter is fundamental in the generation of urban DEMs.
2. The shape of the building depends on the number of components and their weight in the layover portion. For the most of the cases, elevation ramps are generated. This DEM shape is in common to layover generated in natural landscapes.
3. The measured RMSE is about 8 m for the complete model. This value is the highest among the dissertation's inspection. As for the investigation in Chapter 4, also in this case the error distributions are not Gaussian.
4. The major source of errors are building layovers.
5. A layover map can be generated on a building-by-building base by inspecting the geocoding stage of the InSAR processor. A novel detector has been implemented.
6. Layover decomposition is not feasible with a sole interferogram. Nevertheless, the principal layover component can be estimated. For the majority of the detected buildings, the principal component has been estimated as the vertical facade.

6. Summary

This dissertation showed several applications using digital elevation models generated with spaceborne bistatic interferometry. The attention has been posed on uncertainty instruments and methods with application to four test cases. Every chapter has been concluded with final remarks, as well as the papers in the appendix. For this reason, they will be not repeated here. Nevertheless, some major point can be stressed:

- It is fundamental, in an uncertainty study, to take into account for the time-varying dielectrical properties of the medium to image. For instance, it has been demonstrated how the accuracy is varying depending on the phenological stages for the paddy-rice mapping and depending on the snow type (changing during the day) for the subglacial volcano mapping.
- Accuracy is strictly related to terrain slope. Apart from the non-mappable layover and shadow slopes, a different accuracy level at different slopes has been reported. Even if not fully characterizing the error statistics, RMSE has been demonstrated to increase with the complexity of the scene. The RMSE measure for agricultural fields, moderate terrain and cities is below the meter, 4m and 8m, respectively. To be noticed, the TanDEM-X specifications have been accomplished for all the test sites, even though referring to the final fused, calibrated and mosaicked DEM and not to the single-pass DEM.
- A unique parameter describing the InSAR DEM accuracy is not existing and also not particularly meaningful due to the variety in the accuracy level inside the scene (e.g. different slopes and land covers). Global descriptors such as RMSE, CE90 and LE90 can be certainly employed to have an impression of the global quality. An additional novel parameter, just related to InSAR processing, q_{ratio}, has been introduced in the thesis context and shall be considered together with the height error derived from the interferometric coherence, which does not distinguish between areas affected by unwrapping errors and correctly unwrapped areas. Moreover, in case of urban DEMs, layover areas may show average coherence values but an inaccurate DEM at their positions. The detection of these areas has been developed on the building level.
- The obtained results open to potential applications using the TanDEM-X DEM as input. The accuracy obtained in the first investigation makes a rice yield estimation based on plant height a possible task. The second investigation opens to geophysical applications based on the volcano topography, such as flow predictions and heat source modelling. The third one showed how a fusion between different sources such as TanDEM-X and CartoSAT-1, may bring to an enhanced DEM due to the complementarity of their errors. Finally, the fourth investigation opens to urban monitoring applications, such as density controls or urbanization growth inspections. All these applications are possible because of the high accuracy level.

Bibliography

Albino, F., Smets, B., d'Oreye, N., and Kervyn, F. (2015). High-resolution TanDEM-X DEM: An accurate method to estimate lava flow volumes at Nyamulagira volcano (DR Congo). *Journal of Geophysical Research: Solid Earth*, 120(6):4189–4207.

Antropov, O., Rauste, Y., Häme, T., and Praks, J. (2015). TanDEM-X InSAR time series data in forest cover mapping in boreal zone. In *Proceedings of Fringe 2015*.

Askne, J., Fransson, J., Santoro, M., Soja, M., and Ulander, L. (2013). Model-based biomass estimation of a hemi-boreal forest from multitemporal TanDEM-X acquisitions. *Remote Sensing*, 5(11):5574–5597.

Baltsavias, E. (1999). Airborne laser scanning: basic relations and formulas. *ISPRS Journal of Photogrammetry and Remote Sensing*, 54(2):199–214.

Bamler, R. and Hartl, P. (1998). Synthetic aperture radar interferometry. *Inverse Problems*, 14(4):R1.

Bamler, R. and Schättler, B. (1993). *SAR geocoding: data and systems*, chapter SAR data acquisition and image formation, pages 53–102.

Bickel, D., Hensley, W., and Yocky, D. (1997). The effect of scattering from buildings on interferometric SAR measurements. In *Geoscience and Remote Sensing, 1997. IGARSS'97. Remote Sensing-A Scientific Vision for Sustainable Development., 1997 IEEE International*, volume 4, pages 1545–1547. IEEE.

Bolstad, P.and Stowe, T. (1994). An evaluation of DEM accuracy: elevation, slope, and aspect. *Photogrammetric Engineering and Remote Sensing*, 60(11):1327–1332.

Breit, H., Fritz, T., Balss, U., Lachaise, M., Niedermeier, A., and Vonavka, M. (2010). TerraSAR-X SAR processing and products. *Geoscience and Remote Sensing, IEEE Transactions on*, 48(2):727–740.

Breit, H., Lachaise, M., Balss, U., Rossi, C., Fritz, T., and Niedermeier, A. (2012). Bistatic and interferometric processing of TanDEM-X data. In *Synthetic Aperture Radar, 2012. EUSAR. 9th European Conference on*, pages 93–96. VDE.

Breit, H., Younis, M., Balss, U., Niedermeier, A., Grigorov, C., Hueso-Gonzalez, J., Krieger, G., Eineder, M., and Fritz, T. (2011). Bistatic synchronization and processing of TanDEM-X data. In *Geoscience and Remote Sensing Symposium (IGARSS), 2011 IEEE International*, pages 2424–2427. IEEE.

Capaldo, P., Crespi, M., Fratarcangeli, F., Nascetti, A., and Pieralice, F. (2011). High-resolution SAR radargrammetry: A first application with COSMO-SkyMed spotlight imagery. *Geoscience and Remote Sensing Letters, IEEE*, 8(6):1100–1104.

Carabajal, C. and Harding, D. (2005). ICESat validation of SRTM C-band digital elevation models. *Geophysical research letters*, 32(22).

Chai, T. and Draxler, R. R. (2014). Root mean square error (RMSE) or mean absolute error (MAE)?–arguments against avoiding RMSE in the literature. *Geoscientific Model Development*, 7(3):1247–1250.

Chang, K. and Tsai, B. (1991). The effect of DEM resolution on slope and aspect mapping. *Cartography and geographic information systems*, 18(1):69–77.

Cumming, I. G. and Wong, F. H. (2005). *Digital Processing of Synthetic Aperture Radar Data: Algorithms and Implementation*. Artech House remote sensing library. Artech House.

d'Angelo, P., Lehner, M., Krauss, T., Hoja, D., and Reinartz, P. (2008). Towards automated DEM generation from high resolution stereo satellite images. In *Proc. ISPRS Congr.*, pages 1137–1342.

d'Angelo, P. and Reinartz, P. (2011). Semiglobal matching results on the ISPRS stereo matching benchmark. In *ISPRS Hannover Workshop 2011: High-Resolution Earth Imaging for Geospatial Information*, pages 79–84.

Deledalle, C., Denis, L., and Tupin, F. (2011). NL-InSAR: Nonlocal interferogram estimation. *Geoscience and Remote Sensing, IEEE Transactions on*, 49(4):1441–1452.

Deo, R., Rossi, C., Eineder, M., Fritz, T., and Rao, Y. (2015). Framework for fusion of ascending and descending pass TanDEM-X raw DEMs. *Selected Topics in Applied Earth Observations and Remote Sensing, IEEE Journal of*, 8(7):3347–3355.

DigitalGlobe (2015). https://www.digitalglobe.com/products/stereo-imagery. Technical report.

Eineder, M. (2003a). Efficient simulation of SAR interferograms of large areas and of rugged terrain. *Geoscience and Remote Sensing, IEEE Transactions on*, 41(6):1415–1427.

Eineder, M. (2003b). Problems and solutions for InSAR digital elevation model generation of mountainous terrain. In *Proc. Fringe 2003 Workshop, Frascati, Italy*.

Erten, E., Rossi, C., and Yuzugullu, O. (2015). Polarization impact in TanDEM-X data over vertical-oriented vegetation: The paddy-rice case study. *Geoscience and Remote Sensing Letters, IEEE*, 12(7):1501–1505.

Farr, T. and al. (2007). The shuttle radar topography mission. *Reviews of geophysics*, 45(2).

Federal Geographic Data Committee, F. (1998). FGDC-STD-007.3-1998. *Geospatial Positioning Accuracy Standards, Part 3: National Standard for Spatial Data Accuracy*.

Fiedler, H., Boerner, E., Mittermayer, J., and Krieger, G. (2005). Total zero Doppler steering-a new method for minimizing the Doppler centroid. *Geoscience and Remote Sensing Letters, IEEE*, 2(2):141–145.

Fierz, C. and al. (2009). *The international classification for seasonal snow on the ground*. UNESCO/IHP Paris.

Flood, M. (2004). ASPRS guidelines: Vertical accuracy reporting for LiDAR data.

Franceschetti, G. and Lanari, R. (1999). *Synthetic aperture radar processing*. CRC press.

Gatelli, F., Guamieri, A., Parizzi, F., Pasquali, P., Prati, C., and Rocca, F. (1994). The wavenumber shift in SAR interferometry. *Geoscience and Remote Sensing, IEEE Transactions on*, 32(4):855–865.

Gernhardt, S. and Bamler, R. (2012). Deformation monitoring of single buildings using meter-resolution SAR data in PSI. *ISPRS Journal of Photogrammetry and Remote Sensing*, 73:68–79.

Ghiglia, D. and Pritt, M. (1998). *Two-dimensional phase unwrapping: theory, algorithms, and software*. Wiley New York.

Gini, F., Lombardini, F., and Montanari, M. (2002). Layover solution in multibaseline SAR interferometry. *Aerospace and Electronic Systems, IEEE Transactions on*, 38(4):1344–1356.

Gislason, S. and al. (2015). Environmental pressure from the 2014–15 eruption of Bardarbunga volcano, Iceland. *Geochem. Perspect. Lett*, 1:84–93.

Gorokhovich, Y. and Voustianiouk, A. (2006). Accuracy assessment of the processed SRTM-based elevation data by CGIAR using field data from USA and Thailand and its relation to the terrain characteristics. *Remote Sensing of Environment*, 104(4):409–415.

Gruber, A., Wessel, B., Martone, M., and Roth, A. (2015). The TanDEM-X DEM mosaicking: Fusion of multiple acquisitions using InSAR quality parameters. *Selected Topics in Applied Earth Observations and Remote Sensing, IEEE Journal of*, pages 1–11.

Guðmundsson, M., Höganadóttir, P., Kristinsson, A., and Guðbjörnsson, S. (2007). Geothermal activity in the subglacial Katla caldera, Iceland, 1999–2005, studied with radar altimetry. *Annals of Glaciology*, 45(1):66–72.

Guo, R. and Zhu, X. (2014). High-Rise Building Feature Extraction Using High Resolution Spotlight TanDEM-X Data. In *EUSAR 2014; 10th European Conference on Synthetic Aperture Radar; Proceedings of*, pages 1–4. VDE.

Hallikainen, M., Ulaby, F., and Abdelrazik, M. (1986). Dielectric properties of snow in the 3 to 37 GHz range. *Antennas and Propagation, IEEE Transactions on*, 34(11):1329–1340.

Ham, A. (2005). A standardized approach to phase unwrap detection removal and void fill of the Shuttle Radar Topography Mission (SRTM) data. *Proceeding of SRTM Data Validation and Applications Workshop*.

Hanssen, R. (2001). *Radar interferometry: data interpretation and error analysis*, volume 2. Springer Science & Business Media.

Heady, B., Kroenung, G., and Rodarmel, C. (2009). High resolution elevation data (HRE) specification overview. In *ASPRS/MAPPS 2009 Conference*.

Hellwich, O. and Ebner, H. (2000). Geocoding SAR interferograms by least squares adjustment. *ISPRS Journal of Photogrammetry and Remote Sensing*, 55(4):277 – 288.

Ishimaru, A. (1978). *Wave propagation and scattering in random media*, volume 2. Academic press New York.

Johnson, D. J., Sigmundsson, F., and Delaney, P. T. (2000). Comment on" volume of magma accumulation or withdrawal estimated from surface uplift or subsidence, with application to the 1960 collapse of kīlauea volcano" by pt delaney and df mctigue. *Bulletin of Volcanology*, 61(7):491–493.

JPL (2014). NASADEM announcement. https://earthdata.nasa.gov/community/community-data-system-programs/measures-projects/nasadem. Accessed: 2015-10-15.

Just, D. and Bamler, B. (1994). Phase statistics of interferograms with applications to synthetic aperture radar. *Appl. Opt.*, 33(20):4361–4368.

Kay, S. (1988). *Modern spectral estimation: theory and application*. Englewood Cliffs: Prentice Hall.

Kellndorfer, J., Walker, W., LaPoint, E., Kirsch, K., Bishop, J., and Fiske, G. (2010). Statistical fusion of Lidar, InSAR, and optical remote sensing data for forest stand height characterization: A regional-scale method based on LVIS, SRTM, Landsat ETM+, and ancillary data sets. *Journal of Geophysical Research: Biogeosciences (2005–2012)*, 115(G2).

Krieger, G., De Zan, F., Bachmann, M., Gonzalez, J., Cassola, M., and Zink, M. (2012). Unexpected height offsets in TanDEM-X: Explanation and correction. In *Geoscience and Remote Sensing Symposium (IGARSS), 2012 IEEE International*, pages 295–298. IEEE.

Krieger, G. et al. (2009). The Tandem-L mission proposal: Monitoring earth's dynamics with high resolution SAR interferometry. In *Radar Conference, 2009 IEEE*, pages 1–6. IEEE.

Krieger, G., Moreira, A., Fiedler, H., Hajnsek, I., Werner, M., Younis, M., and Zink, M. (2007). TanDEM-X: A satellite formation for high-resolution SAR interferometry. *Geoscience and Remote Sensing, IEEE Transactions on*, 45(11):3317–3341.

Kropatsch, W. and Strobl, D. (1990). The generation of SAR layover and shadow maps from digital elevation models. *Geoscience and Remote Sensing, IEEE Transactions on*, 28(1):98–107.

Kubanek, J., Westerhaus, M., Schenk, A., Aisyah, N., and Brotopuspito, K.and Heck, B. (2015). Volumetric change quantification of the 2010 Merapi eruption using TanDEM-X InSAR. *Remote Sensing of Environment*, 164:16–25.

Kugler, F., Schulze, D., Hajnsek, I., Pretzsch, H., and Papathanassiou, K. (2014). TanDEM-X Pol-InSAR performance for forest height estimation. *Geoscience and Remote Sensing, IEEE Transactions on*, 52(10):6404–6422.

Lachaise, M., Fritz, T., and Eineder, M. (2014). Dual-baseline phase unwrapping challenges in the TanDEM-X mission. In *EUSAR 2014; 10th European Conference on Synthetic Aperture Radar; Proceedings of*, pages 1–4. VDE.

Lancashire, P., Bleiholder, H., Boom, T., Langelüddeke, P., Stauss, R., Weber, E., and Witzenberger, A. (1991). A uniform decimal code for growth stages of crops and weeds. *Annals of Applied Biology*, 119(3):561–601.

Lee, S. and Fatoyinbo, T. (2015). TanDEM-X Pol-InSAR inversion for mangrove canopy height estimation. *Selected Topics in Applied Earth Observations and Remote Sensing, IEEE Journal of*, 8(7):3608–3618.

Li, Z., Zhu, C., and Gold, C. (2010). *Digital terrain modeling: principles and methodology*. CRC press.

Ludwig, R. and Schneider, P. (2006). Validation of digital elevation models from SRTM X-SAR for applications in hydrologic modeling. *ISPRS Journal of Photogrammetry and Remote Sensing*, 60(5):339–358.

Martone, M., Bräutigam, B., Rizzoli, P., Gonzalez, C., Bachmann, M., and Krieger, G. (2012). Coherence evaluation of TanDEM-X interferometric data. *ISPRS Journal of Photogrammetry and Remote Sensing*, 73:21–29.

Méric, S., Pottier, E., and Fayard, F. (2009). *Radargrammetric SAR image processing*. INTECH Open Access Publisher.

Miller, C. and Laflamme, R. (1958). The Digital Terrain Model - theory and application. *Photogrammetric Engineering & Remote Sensing*.

Pierce, L., Kellndorf, J., Walker, W., and Barros, O. (2006). Evaluation of the horizontal resolution of SRTM elevation data. *Photogrammetric Engineering & Remote Sensing*, 72(11):1235–1244.

Pike, R. and Rozema, W. (1975). Spectral analysis of landforms. *Annals of the Association of American Geographers*, 65(4):499–516.

Poland, M. (2014). Time-averaged discharge rate of subaerial lava at Kilauea Volcano, Hawaii, measured from TanDEM-X interferometry: Implications for magma supply and storage during 2011–2013. *Journal of Geophysical Research: Solid Earth*, 119(7):5464–5481.

Rabus, B., Eineder, M., Roth, A., and Bamler, R. (2003). The shuttle radar topography mission - a new class of digital elevation models acquired by spaceborne radar. *ISPRS Journal of Photogrammetry and Remote Sensing*, 57(4):241–262.

Richards, J. (2009). *Remote sensing with imaging radar*, volume 1. Springer.

Riel, B., Milillo, P., Simons, M., Lundgren, P., Kanamori, H., and Samsonov, S. (2015). The collapse of Bardarbunga caldera, Iceland. *Geophysical Journal International*, 202(1):446–453.

Rignot, E., Echelmeyer, K., and Krabill, W. (2001). Penetration depth of interferometric synthetic-aperture radar signals in snow and ice. *Geophysical Research Letters*, 28(18):3501–3504.

Rizzoli, P., Bräutigam, B., Kraus, T., Martone, M., and Krieger, G. (2012). Relative height error analysis of TanDEM-X elevation data. *ISPRS Journal of Photogrammetry and Remote Sensing*, 73:30–38.

Rodriguez, E., Morris, C., and Belz, J. (2006). A global assessment of the SRTM performance. *Photogrammetric Engineering & Remote Sensing*, 72(3):249–260.

Rossi, C. and Eineder, M. (2015). High-resolution InSAR building layovers detection and exploitation. *Geoscience and Remote Sensing, IEEE Transactions on*, 53(12):6457–6468.

Rossi, C., Eineder, M., Fritz, T., and Breit, H. (2010). TanDEM-X mission: raw DEM generation. In *Synthetic Aperture Radar (EUSAR), 2010 8th European Conference on*, pages 1–4. VDE.

Rossi, C., Eineder, M., Fritz, T., D'Angelo, P., and Reinartz, P. (2013). Quality assessment of TanDEM-X raw DEMs oriented to a fusion with CartoSAT-1 DEMs. In *Proc. 33rd EARSeL Symp., Matera, Italy*.

Rossi, C. and Erten, E. (2015). Paddy-rice monitoring using TanDEM-X. *Geoscience and Remote Sensing, IEEE Transactions on*, 53(2):900–910.

Rossi, C. and Gernhardt, S. (2013). Urban DEM generation, analysis and enhancements using TanDEM-X. *ISPRS Journal of Photogrammetry and Remote Sensing*, 85(0):120 – 131.

Rossi, C., Gonzalez, F. R., Fritz, T., Yague-Martinez, N., and Eineder, M. (2012). TanDEM-X calibrated raw DEM generation. *ISPRS Journal of Photogrammetry and Remote Sensing*, 73(0):12 – 20.

Rossi, C., Minet, C., Fritz, T., Eineder, M., and Bamler, R. (2016). Temporal monitoring of subglacial volcanoes with TanDEM-X - application to the 2014-2015 eruption within the Bardarbunga volcanic system, Iceland. *Remote sensing of the environment*, submitted.

Russell, K. and Congalton, G. (1998). *Assessing the Accuracy of Remotely Sensed Data*. Boca Raton, FL: CRC Press.

Sansosti, E., Berardino, P., Manunta, M., Serafino, F., and Fornaro, G. (2006). Geometrical SAR image registration. *Geoscience and Remote Sensing, IEEE Transactions on*, 44(10):2861–2870.

Schutz, B., Zwally, H., Shuman, C., Hancock, D., and DiMarzio, J. (2005). Overview of the ICESat mission. *Geophysical Research Letters*, 32(21).

Schwäbisch, M. (1998). A fast and efficient technique for SAR interferogram geocoding. In *Geoscience and Remote Sensing Symposium Proceedings, 1998. IGARSS '98. 1998 IEEE International*, volume 2, pages 1100–1102 vol.2.

Sigmundsson, F. et al. (2015). Segmented lateral dyke growth in a rifting event at Bardarbunga volcanic system, Iceland. *Nature*, (517):191–195.

Smith, B. and Sandwell, D. (2003). Accuracy and resolution of shuttle radar topography mission data. *Geophysical Research Letters*, 30(9).

Solberg, S., Astrup, R., Breidenbach, J., Nilsen, B., and Weydahl, D. (2013). Monitoring spruce volume and biomass with InSAR data from TanDEM-X. *Remote Sensing of Environment*, 139:60–67.

Stiles, W. and Ulaby, F. (1980). The active and passive microwave response to snow parameters: 1. wetness. *Journal of Geophysical Research: Oceans (1978–2012)*, 85(C2):1037–1044.

Stilla, U., Soergel, U., and Thoennessen, U. (2003). Potential and limits of InSAR data for building reconstruction in built-up areas. *ISPRS Journal of Photogrammetry and Remote Sensing*, 58:113 – 123.

Sun, G., Ranson, K., Kharuk, V., and Kovacs, K. (2003). Validation of surface height from shuttle radar topography mission using shuttle laser altimeter. *Remote Sensing of Environment*, 88(4):401–411.

Szeliski, R. (2010). *Computer vision: algorithms and applications*. Springer Science & Business Media.

Thiele, A., Cadario, E., Schulz, K., Thonnessen, U., and Soergel, U. (2007). Building recognition from multi-aspect high-resolution InSAR data in urban areas. *Geoscience and Remote Sensing, IEEE Transactions on*, 45(11):3583–3593.

Thiele, A., Wurth, M., Even, M., and Hinz, S. (2013). Extraction of building shape from TanDEM-X data. *Proc. Int. Archives Photogramm., Remote Sens. Spatial Inf. Sci*, 1:W1.

Toutin, T. (2002). Impact of terrain slope and aspect on radargrammetric DEM accuracy. *ISPRS Journal of Photogrammetry and Remote Sensing*, 57(3):228–240.

Touzi, R., Lopes, A., Bruniquel, J., and Vachon, P. (1999). Coherence estimation for SAR imagery. *Geoscience and Remote Sensing, IEEE Transactions on*, 37(1):135–149.

Vasile, G., Trouve, E., Lee, J., and Buzuloiu, V. (2006). Intensity-driven adaptive-neighborhood technique for polarimetric and interferometric SAR parameters estimation. *Geoscience and Remote Sensing, IEEE Transactions on*, 44(6):1609–1621.

Wechsler, S. (2003). Perceptions of digital elevation model uncertainty by DEM users. *URISA-WASHINGTON DC-*, 15(2):57–64.

Wechsler, S. and Kroll, C. (2006). Quantifying DEM uncertainty and its effect on topographic parameters. *Photogrammetric Engineering & Remote Sensing*, 72(9):1081–1090.

Wegmüller, U. and Werner, C. (1997). Retrieval of vegetation parameters with SAR interferometry. *Geoscience and Remote Sensing, IEEE Trans. on*, 35(1):18–24.

Wehr, A. and Lohr, U. (1999). Airborne laser scanning an introduction and overview. *ISPRS Journal of Photogrammetry and Remote Sensing*, 54(23):68 – 82.

Weih Jr., R. (2004). Modeling slope in geographic information system. *Journal of the Arkansas Academy of Science*, 58.

Wendleder, A., Wessel, B., Roth, A., Breunig, M., Martin, K., and Wagenbrenner, S. (2013). TanDEM-X water indication mask: Generation and first evaluation results. *International Journal of Applied Earth Observation and Geoinformation*, 6(1):171–179.

Wilkinson, A. (1998). Synthetic aperture radar interferometry: A model for the joint statistics in layover areas. In *Communications and Signal Processing, 1998. COMSIG'98. Proceedings of the 1998 South African Symposium on*, pages 333–338. IEEE.

Williams Jr, R., Hall, D., and Benson, C. (1991). Analysis of glacier facies using satellite techniques. *Journal of Glaciology*, 37(125):120–128.

Wright, J. (1977). Map makers are human comments on the subjective in maps. *Cartographica: The International Journal for Geographic Information and Geovisualization*, 14(1):08–25.

Yague-Martinez, N., Eineder, M., Brcic, R., Breit, H., and Fritz, T. (2010). TanDEM-X mission: SAR image coregistration aspects. In *Synthetic Aperture Radar (EUSAR), 2010 8th European Conference on*, pages 1–4. VDE.

Zandbergen, P. (2008). Positional accuracy of spatial data: Non-normal distributions and a critique of the national standard for spatial data accuracy. *Transactions in GIS*, 12(1):103–130.

Zebker, H., Villasenor, J., et al. (1992). Decorrelation in interferometric radar echoes. *Geoscience and Remote Sensing, IEEE Transactions on*, 30(5):950–959.

Zhou, Q.and Liu, X. (2004). Analysis of errors of derived slope and aspect related to DEM data properties. *Computers & Geosciences*, 30(4):369–378.

Zhu, X. and Bamler, R. (2010). Very high resolution spaceborne SAR tomography in urban environment. *Geoscience and Remote Sensing, IEEE Transactions on*, 48(12):4296–4308.

Appendix

A. Relevant publication as part of the thesis

A.1. TanDEM-X calibrated raw DEM generation

Rossi, C., Gonzalez, F. R., Fritz, T., Yague-Martinez, N., and Eineder, M., TanDEM-X calibrated raw DEM generation. *ISPRS Journal of Photogrammetry and Remote Sensing*, 73, 12-20, 2012.

ISPRS Journal of Photogrammetry and Remote Sensing 73 (2012) 12–20

Contents lists available at SciVerse ScienceDirect

ISPRS Journal of Photogrammetry and Remote Sensing

journal homepage: www.elsevier.com/locate/isprsjprs

TanDEM-X calibrated Raw DEM generation

Cristian Rossi *, Fernando Rodriguez Gonzalez, Thomas Fritz, Nestor Yague-Martinez, Michael Eineder

Remote Sensing Technology Institute, German Aerospace Center (DLR), D-82234 Oberpfaffenhofen, Germany

ARTICLE INFO

Article history:
Available online 2 July 2012

Keywords:
TanDEM-X
Raw DEM
InSAR processing
SAR stereo-radargrammetry
Absolute phase offset estimation
DEM calibration

ABSTRACT

The TanDEM-X mission successfully started on June 21st 2010 with the launch of the German radar satellite TDX, placed in orbit in close formation with the TerraSAR-X (TSX) satellite, and establishing the first spaceborne bistatic interferometer. The processing of SAR raw data to the Raw DEM is performed by one single processor, the Integrated TanDEM-X Processor (ITP). The quality of the Raw DEM is a fundamental parameter for the mission planning. In this paper, a novel quality indicator is derived. It is based on the comparison of the interferometric measure, the unwrapped phase, and the stereo-radargrammetric measure, the geometrical shifts computed in the coregistration stage. By stating the accuracy of the unwrapped phase, it constitutes a useful parameter for the determination of problematic scenes, which will be resubmitted to the dual baseline phase unwrapping processing chain for the mitigation of phase unwrapping errors. The stereo-radargrammetric measure is also operationally used for the Raw DEM absolute calibration through an accurate estimation of the absolute phase offset. This paper examines the interferometric algorithms implemented for the operational TanDEM-X Raw DEM generation, focusing particularly on its quality assessment and its calibration.

1. Introduction

TanDEM-X is a synthetic aperture radar (SAR) mission using two satellites flying in close formation with the generation of a global Digital Elevation Model (DEM) accomplishing the high accuracy HRTI-3 standards as primary objective. A 90% relative point-to-point height accuracy of 2 m is required for moderate terrain at 12 m posting. Moreover the mission has also important secondary objectives such as the generation of local DEMs following the higher standard accuracy HRTI-4, the support to applications based on Along Track Interferometry (ATI) and on PolInSAR and, more in general, to new SAR modes and techniques (Krieger et al., 2007). All of these goals, together with the complexity of the bistatic system and its synchronization, require a robust, flexible, stable and dedicated processor. The Integrated TanDEM-X Processor (ITP) is built to deal with the bistatic processing issues, providing as output a Raw DEM and the operational standard products from experimental modes (Breit et al., 2011).

The Raw DEM is the product of the interferometric chain embedded in ITP (Fritz et al., 2011): it is generated using as input the unwrapped phase, calibrated for a local factor to make it proportional to the real terrain height. Before entering in detail on the topics of the paper, the Raw DEM has to be clearly distinguished from the final calibrated *TanDEM-X DEM*, main output of the mission. A TanDEM-X bistatic acquisition may reach 300 s depending on the orbit and the actual terrain acquired, which means about 2000 km in along-track. A single processing over such long data take is thus operationally hardly possible and the data take is split in scenes of about 50 km along-track – the across-track extension is about 30 km – with a small overlap among them. The interferometric DEM retrieved from the single scene belonging to the bistatic acquisition is called *Raw DEM*. Unlike the TanDEM-X DEM, the Raw DEM could be affected by instrument phase drift or baseline errors, causing height tilts or biases (Hueso-Gonzalez et al., 2010). A calibration strategy making use of correction functions and ICESat data as Ground Control Points is implemented in the Mosaicking and Calibration Processor (MCP) (Wessel et al., 2011) for the generation of the global TanDEM-X DEM. Preliminary studies on the accuracy of the TanDEM-X DEM are described in (Gruber et al., 2012). Using an intermediate version of the TanDEM-X DEM, generated during the first coverage, an absolute accuracy below 1 m has been found for flat terrains by comparisons with GPS tracks, laser scanning DEM and ICESat points as ground truth. Thus, the absolute and relative accuracy requirements can clearly be fulfilled.

In the context of SAR interferometry, the coregistration processing step plays an important role. Due to the different viewing geometries, the active and the passive channel focused data are locally shifted in the two-dimensional slant range – azimuth domain. This local shift is proportional to the time delay between the active and the passive channel and consequently to the local height.

* Corresponding author.
E-mail address: cristian.rossi@dlr.de (C. Rossi).

0924-2716/$ - see front matter © 2012 International Society for Photogrammetry and Remote Sensing, Inc. (ISPRS) Published by Elsevier B.V.All rights reserved.
http://dx.doi.org/10.1016/j.isprsjprs.2012.05.014

Using this information it is in principle possible to generate DEMs following a *stereo-radargrammetric* technique, thus exploiting the distance transformation functions by projections on two antennas in a different spatial position (Leberl, 1990). Besides the geometrical shifts, one can use the unwrapped phase to retrieve the absolute ranging satellite-target. But whereas the geometrical shifts are absolute, i.e. reflecting the real geophysical delay, the unwrapped phase is usually referred to one point and what is missing to the absolute ranging is the so called *absolute phase offset*, which has to be estimated and added to the unwrapped phase before converting to height and geocoding it. Madsen (1995) firstly compared the stereo-radargrammetric and the interferometric measures for the absolute phase offset estimation with the *residual delay method*, foreseeing a resampling of the passive channel with a mapping matrix given by the unwrapped phase, in a way that the active and the resampled passive channels result in same delay. A discrepancy between them is an estimate of the absolute phase offset and is measured through a second coregistration. This method, tested also for the Shuttle Radar Topography Mission (SRTM) (Rabus et al., 2003), assumes that the coregistration accuracy is not sufficient for a direct comparison with the unwrapped phase. In Section 2 it is shown how the ITP coregistration algorithm retains a sufficient accuracy for the direct use of the coregistration shifts. Moreover, in the residual delay method, the phase offset estimate results biased in the presence of one or more phase unwrapping errors. In the proposed algorithm the larger portion of the DEM not affected by errors is detected and masked, providing thus a useful indicator to the TanDEM-X Ground Segment for a re-processing of scenes with a percentage of unwrapping errors extending to more than the 3% of the Raw DEM, as in TanDEM-X specifications (Krieger et al., 2007).

In Section 3 the Raw DEMs calibration within a data take is handled. As mentioned before, a TanDEM-X data take is split into several Raw DEMs with a small overlap between them. Since the calibration step implemented in MCP is data take dependent (Gruber et al., 2012), a continuity among Raw DEMs without offsets is mandatory. The phase offset calculated by ITP for each scene is used for two purposes. On the one hand, a phase offset chosen as the integer part modulo 2π of the estimate accomplishes the continuity requirement. On the other hand, the fractional part of the estimate is used as indicator of possible instrument inaccuracies.

Finally, in Section 4 exemplary results are shown.

2. Raw DEM generation

The processing steps requested for the generation of the two channels focused data are here only briefly introduced. A first fundamental operation is the synchronization pulse evaluation for the phase and timing corrections to be applied to the SAR data, followed by a bistatic focusing replica and the computation of all the focusing parameters (Bamler et al., 2007; Breit et al., 2011). This point is crucial as it defines the phase offsets and delays used in the interferometric processing chain. A geometrical analysis of the common ground coverage and a Doppler analysis are carried out prior to the SAR focusing step, performed adopting key modules of the TerraSAR Multimode SAR Processor (TMSP) (Breit et al., 2010).

2.1. Spectral filtering

The interferometric processing begins with the spectral filtering, necessary for the selection of the azimuth and range coherent spectral bands. The different viewing geometry of the TSX and the TDX satellites, as sketched in Fig. 1, yields a geometrical decorrelation (Gatelli et al., 1994), a loss of coherence, avoidable with the

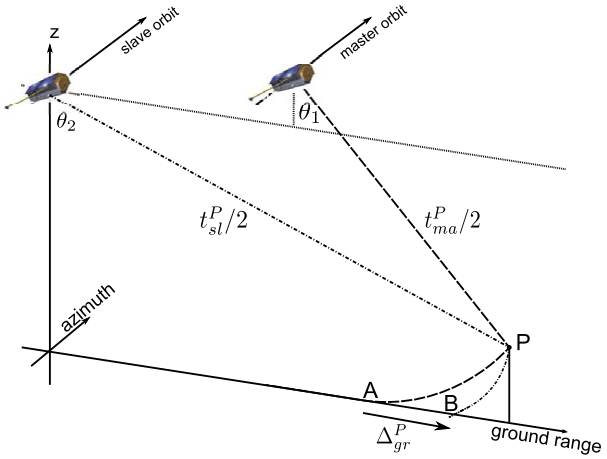

Fig. 1. Example of TanDEM-X configuration. The active channel sees the point P at the time t_{ma}^P and images it in ground range at a given reference height at the position A; the passive channel at B. The stereo-radargrammetric shift, in the ground range domain, is Δ_{gr}^P.

elimination of the not-coherent spectral bands. This operation increases the coregistration precision, as analyzed in the next subsections.

The maximum tolerable deviation of viewing angles is given by Prati and Rocca (1993):

$$\Delta\theta = \theta_2 - \theta_1 \leqslant 2\frac{f_{rg}}{f_0}\tan\left(\frac{\theta_1+\theta_2}{2}\right), \tag{1}$$

where f_0 is the central frequency of 9.65 GHz. Approximating the angles difference as $\Delta\theta \approx B_\perp/r_0$, where r_0 is the slant range, one can express the limit in terms of the perpendicular baseline $B_\perp$, the *critical baseline*, an important system parameter for the overall performances. In a typical TanDEM-X scenario, with a range bandwidth f_{rg} of 100 MHz and flat terrain, $B_\perp$ is varying between 5 and 16 km, for lo mean incidence angles $\theta = (\theta_1 + \theta_2)/2$ of respectively 20 and 50 degrees and an angle difference $\Delta\theta$ of 0.008 and 0.025 degrees. The critical baseline is much larger than the perpendicular baselines used for the DEM generation, smaller than 1 km.

2.2. Coregistration

Coregistration is an essential processing step for all the cases in which one has two images covering the same area and for which one wants to obtain a precise sample-wise overlap. In Fig. 1 an example of TanDEM configuration for a fixed azimuth time is shown. For a better understanding, the plot is represented in ground range domain, nevertheless the stereo-radargrammetric shifts computed in the processor are in slant range domain. The master satellite sees the point P with a look angle θ_1 at a range time t_{ma}^P, while the slave one sees it for (θ_2, t_{sl}^P). In the ground range domain at a given reference height, the point P is imaged at the position A for the master channel and at B for the slave one yielding a shift Δ_{gr}^P. The slant range stereo-radargrammetric shift computed in the processing for that point is:

$$\Delta^P = \left(\left(t_{sl}^P - t_{sl}^0\right) - \left(t_{ma}^P - t_{ma}^0\right)\right)\cdot f_{rg}^s, \tag{2}$$

where f_{rg}^s is the range sampling frequency and t_{ma}^0, t_{sl}^0 are the master and slave reference times respectively.

In ITP the azimuth and range shifts are computed for a set of patches arranged in a grid. A patch is composed by 1024 samples – 32 by 32 –, experimentally proven to be a good compromise between accuracy, for the expected coherence (Section 2.3.1), and computation time. The coregistration strategy is the following (Yague Martinez et al., 2010):

1. *Geometrical coregistration.* A geometrical computation of the azimuth and range shifts is firstly derived using orbit information and an external DEM.
2. *Cross-correlation.* The geometrical estimate is used as an a priori to maximize the patches overlap. Firstly, a coherent cross-correlation on the complex data is performed. A peak test of the correlation function is used to compute the quality of the operation: if the test is not passed, then an incoherent cross-correlation (on the amplitude) is performed. If the quality is still bad, for example in areas with a very low SNR, then the geometrical shifts are used.
3. *Outliers rejection.* An outlier elimination procedure of the resampling matrices based on the correlation coefficient and on the shift values is performed.

2.3. Absolute phase estimation

In contrast to a *radargrammetric DEM* retrieval, which is based on the shifts computed in the coregistration step and their geometrical transformation to a terrain height, a SAR interferometric technique is based on the exploitation of the complex interferogram. A critical stage of the interferometric chain is the absolute phase retrieval starting from the wrapped interferogram phase. This processing step is fundamental since the topographic phase ϕ_{top} is sensitive to the terrain height h through the relation:

$$\frac{\partial \phi_{top}}{\partial h} = \frac{2\pi B_{\perp}}{\lambda R_{ma} \sin\theta_1}, \tag{3}$$

where R_{ma} is the actual active channel slant range, i.e. $R^P_{ma} = t^P_{ma} c/2$. An error in this step would imply many distortions: height errors, displacements in line of sight and a stretching or a dilation of the DEM.

The TanDEM-X phase unwrapping strategy uses a dual-baseline approach. During the first mission year a complete coverage with an height of ambiguity of about 40–55 m is foreseen, while for the second year a smaller one, of about 35 m, will be used in order to obtain a higher accuracy at a cost of a more difficult phase unwrapping operation. The difficulties are mitigated with the approach described in (Lachaise et al., 2008), which is based on the use of the combined information from the two years.

The absolute topographic phase can be written for the point P in Fig. 1 as:

$$\phi^P_{top} = \phi^P_{unw} + \phi^P_{off}, \tag{4}$$

where ϕ^P_{unw} is the unwrapped phase resulting from the processing:

$$\phi^P_{unw} = \phi^P_0 + 2\pi k^P \tag{5}$$

and ϕ^P_{off} is what is missing to the unwrapped phase to make it equal to the absolute phase, in other words the *absolute phase offset*:

$$\phi^P_{off} = 2\pi q^P + \phi^P_N. \tag{6}$$

In Eqs. (5) and (6), k^P and q^P are integer constants, ϕ^P_0 is the wrapped interferogram phase and ϕ^P_N is the phase noise, considered as additive and varying among $[-\pi,\pi)$ (Just and Bamler, 1994). The absolute phase offset concept is linked to the fact that the phase unwrapping processing step is relative to one point, the *reference point*, for which k is zero. The first term in Eq. (6), the *integer part*, is constant over all the Raw DEM in the absence of phase unwrapping errors. For the reconstruction of the terrain height starting from the unwrapped phase ϕ_{unw}, as in Eq. (3), it is fundamental to estimate the terms $2\pi k$ and ϕ_N. Considering again the example in Fig. 1, the coregistration shift in Eq. (2) transformed to phase is:

$$\phi^P_{radgr} = 2\pi f_0 \left(\frac{\Delta^P}{\bar{f}^s_{rg}} + (t^0_{sl} - t^0_{ma}) \right) = 2\pi f_0 (t^P_{sl} - t^P_{ma}). \tag{7}$$

Rewriting Eq. (4) as:

$$\phi^P_{top} = 2\pi f_0 (t^P_{sl} - t^P_{ma}) + \phi^P_N, \tag{8}$$

it is clear how the stereo-radargrammetric and the interferometric measures yield the same quantity, the absolute ranging, except for the phase offset, which is estimated with a difference between the two measures:

$$\Delta\phi = \phi^P_{radgr} - \phi^P_{unw} = -\phi^P_{off}. \tag{9}$$

The algorithm implemented in ITP for the absolute phase offset retrieval is shown in Fig. 2. It is composed of four steps:

1. *Phase difference map generation.* As explained in Section 2.2, the stereo-radargrammetric shifts are computed for a set of scene patches, whereas the unwrapped phase is at the full interferogram resolution. It follows that the first step before evaluating the differences is a downsampling of ϕ_{unw} to the raster of ϕ_{radgr}.
2. *Noise reduction filter.* The global variance of the differences could be high due to the presence of patches for which an incoherent cross-correlation was performed, i.e. low coherence areas, affecting the stereo-radargrammetric phase, or to noise in the unwrapped phase caused by layover/shadow regions or general decorrelations. Therefore, when a histogram of the difference is built, it presents a wide main lobe. A filtering procedure over the phase difference map – the median filter is the easiest solution and it is the one operationally implemented – to shrink the histogram is then essential.
3. *Histogram search.* A possible phase unwrapping error creates a secondary lobe in the histogram. The taller the lobe is, the greater the area affected by the error. A peak detection is performed over the histogram of the filtered phases to detect possible phase unwrapping errors.
4. *Absolute phase offset retrieval.* The mean value over the main lobe of the histogram of the differences provides the absolute phase offset ϕ_{off}. In this computation only patches for which a coherent cross-correlation was performed are used. In case of a small number of coherent patches, less than the 10% of the total, also the incoherent ones are used.

In Section 4 a processing example of the algorithm is shown.

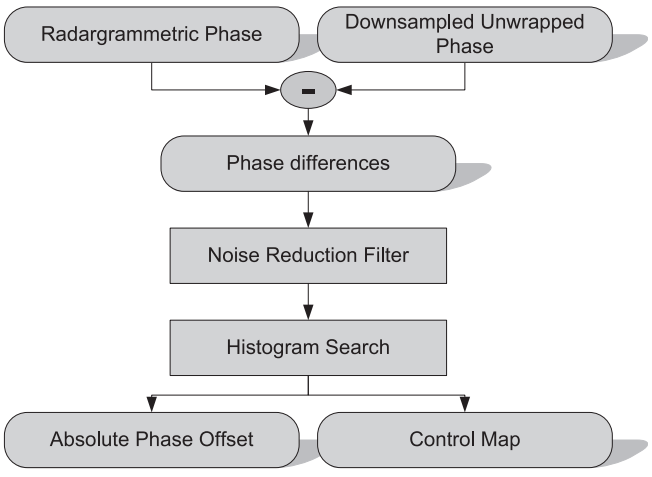

Fig. 2. Algorithm implemented for the retrieval of the absolute phase offset. The difference between the unwrapped phase and the stereo-radargrammetric estimates is used to derive the absolute phase offset and a control map.

2.3.1. Estimation accuracy

The accuracy of the absolute phase offset retrieval can be derived from Eq. (9), looking at the precision of the coregistration and the phase unwrapping processing steps.

In a nominal scenario, the cross-correlation coherent patches are usually above the 10% threshold. For these patches the accuracy was derived in (Bamler and Eineder, 2005) through a Cramer Rao Lower Bound (CRLB) analysis. It was stated that the shift accuracy depends on the coherence and is inversely proportional to the estimation window for the shift computation:

$$\sigma_{\Delta^P} = \sqrt{\frac{3}{2N}} \frac{\sqrt{1-\gamma_P^2}}{\pi\gamma_P} w_{rg}^{3/2}, \tag{10}$$

where N is the estimation window, composed by 1024 samples in ITP, γ is the interferometric coherence and w_{rg} is the range oversampling factor of 1.1 in ITP. The CRLB is shown in Fig. 3.

For an unambiguous phase offset estimation a shift estimation accuracy smaller than half of the wavelength (1.55 cm) is needed. Looking at Fig. 3 and considering a range resolution cell of 1.5 m, a standard deviation lower than 1/100 of a pixel is required, i.e. a coherence higher than 0.8. The CRLB is nevertheless a theoretical bound, valid for flat terrain or for smooth topography, whose topographic phase is perfectly demodulated from the data. Any residual artefact or not gaussian scattering degrades the accuracy. For the absolute phase offset estimation a considerable amount of patches is used (typically more than 10,000), strongly increasing the overall estimate precision by a $\sqrt{M}$ factor, where M is the number of coherent patches. It is then possible to conclude that the coregistration shift accuracy is not limiting the absolute phase offset estimation.

The other factor of the estimation, the unwrapped phase, could really limit the accuracy. Several error source could bias the estimate. Orbital errors are typically the main limiting errors, causing tilts or biases to the final DEM. The target of the TanDEM-X mission is a baseline accuracy of 1 mm, which means a vertical displacement of ±1.1 m for an error in the parallel baseline of $\Delta B_{\parallel}$ = ±1 mm and an height of ambiguity of 35 m (Krieger et al., 2007). An error in the perpendicular baseline has a less significant impact. Considering Eq. (3), such error yields a phase offset of about 0.2 radians, making a baseline inaccuracy unimportant for the integer part of the absolute phase offset (Section 3). Geometrical decorrelations, like layover and shadow, can cause also a phase jump of $k \cdot 2\pi$. In this case one single phase offset is not sufficient to ensure the correctness of the final global height. A number of offsets equal to the number of phase unwrapping errors, represented by different peaks in the histogram built with the phase differences, would be needed. The method described in Section 2.3 could be precisely used at this purpose in its histogram search step. Nonetheless, the TanDEM-X mission concept does not require this approach as it is built on two years with different baselines exactly for this purpose. In ITP the estimated errors are just marked.

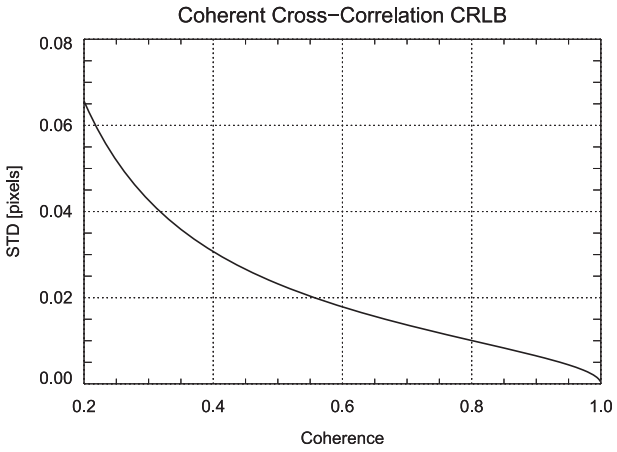

Fig. 3. Cramer-Rao lower bound for shift estimation using a coherent cross-correlation technique for the ITP processing configuration.

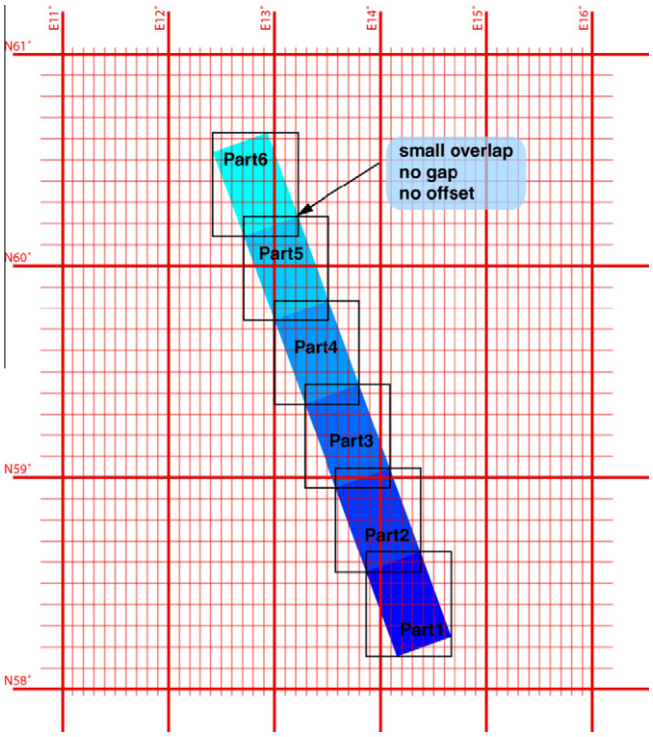

Fig. 4. Example of TanDEM-X data take and subdivision in raw DEMs. A typical raw DEM is 50 km long and 30 km wide. The Raw DEMs are represented in different blue shades with a squared box representing their extension in geographic coordinates.

2.4. Geocoding and quality maps generation

Once the absolute phase is estimated, the height can be easily retrieved with geometrical transformations. The approach operationally used is efficient as in one step it makes the conversion and locates the heights in geographical coordinates (*geocoding*) (Rossi et al., 2010). A set of maps assessing the quality of the Raw DEM is also generated: the *Height Error Map*, indicating for every Raw DEM pixel its standard error, the *Flag Mask*, flagging the problematic part of the scene as layover, shadow, water areas and phase unwrapping flags (cuts/residues), and the *Radargrammetric Control Map*, for a visual overview of the phase unwrapping errors.

The latter map is generated using the histogram computed for the absolute phase offset estimation. As described in Section 2.3, in presence of one of more phase unwrapping errors, the histogram is composed of several lobes. The radargrammetric control map is generated masking the lobes not used for the phase offset estimation, through a local minima search. A standard RGB color table is then imposed to the map, centered on the estimation value. Therefore by visually inspecting the map one can have a visual impression of the quality of the Raw DEM: when the map is mostly green the phase unwrapping operation worked well and the final Raw DEM is expected to be accurate. The presence of red/blue color is also meaningful, as the main lobe shape can be visually comprehended: a strong presence of these colors stands for a large estimate variance (wide lobe). Additionally the lobe structure can be also derived since the color map is linear. A map example is in Fig. 9.

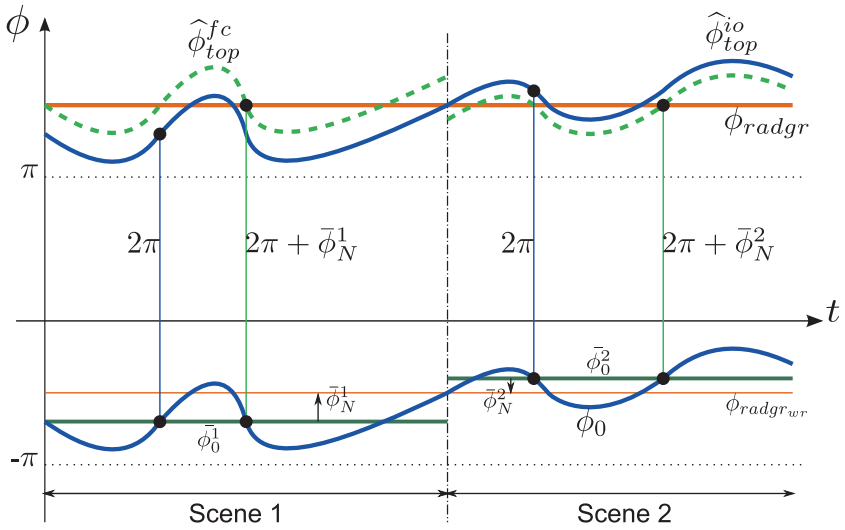

Fig. 5. Raw DEM calibration strategy, example with two raw DEMs with no overlap among them. The curves at the bottom of the plot represent the unwrapped phases whereas the upper ones the results with different calibration approaches.

Finally, a quality parameter, derived exploiting the comparison of the interferometric and the stereo-radargrammetric measurements, is derived. It is named q_{ratio}:

$$q_{ratio} = \frac{p_{tot} - p_{out}}{p_{tot}}, \tag{11}$$

where p_{tot} is the total number of pixels of the radargrammetric control map and p_{out} is the number of masked pixel outside the main lobe. The q_{ratio} is a novel and useful parameter for performance assessment as it gives to the ground segment the percentage of false heights to be corrected in a second stage.

3. Raw DEM calibration

In the first year of the operational stage of the mission, starting from December 12, 2010, over 12,000 data takes were acquired and split in more than 120,000 Raw DEMs. As outlined in Fig. 4, there is a small overlap between the Raw DEMs belonging to one data take. The Raw DEM calibration is performed following an *intra-data take* strategy, finalized to ensure height continuity among overlapping Raw DEMs. The global TanDEM-X DEM calibration strategy follows instead an *inter-data take* approach (Wessel et al., 2011; Gruber et al., 2012), making then the height continuity between Raw DEMs a strict requirement.

Assuming a lack of phase unwrapping errors in between Raw DEMs, an obvious choice for the absolute phase offset accomplishing the continuity requirement is its integer part:

$$\phi_{off_{int}} = \phi_{off} - \arctan\left(\frac{\sin(\phi_{off})}{\cos(\phi_{off})}\right). \tag{12}$$

A visual explanation for the calibration of two contiguous Raw DEMs is provided in Fig. 5. There is no overlap for a better understanding/visualization. The terms in Eqs. (4)–(8) are here pointed out:

- ϕ_{radgr}, in bold orange, is the reference phase derived from the coregistration shifts, representing the real topography with no errors in it.
- $\phi_{radgr_{wr}}$, in orange, is the "optimal" unwrapped phase. For simplicity here it is assumed that $k = 0$ (Eq. (5)), i.e. $\phi_{unw} = \phi_0$.
- ϕ_0, in bold blue, is the unwrapped phase, exaggeratedly noisy around a mean value in green, $\bar{\phi}^1_0$ for the first scene and $\bar{\phi}^2_0$ for the second one. The mean noise values are respectively $\bar{\phi}^1_N$, positive, and $\bar{\phi}^2_N$, negative.
- *Calibration Scene 1.* The approach described in Section 2.3 yields to an absolute phase offset estimate of $\hat{\phi}^1_{off} = 2\pi + \bar{\phi}^1_N > 2\pi$. Using the full value for the absolute phase retrieval, one derives the *fully calibrated* topographic phase $\hat{\phi}^{fc_1}_{top}$, in dashed green, whereas using only the integer its part computed as in Eq. (12), one derives the *integer only calibrated* topographic phase $\hat{\phi}^{io_1}_{top}$.
- *Calibration Scene 2.* The same considerations made for the scene 1 yield $\hat{\phi}^2_{off} = 2\pi + \bar{\phi}^2_N < 2\pi$, $\hat{\phi}^{fc_2}_{top}$ and $\hat{\phi}^{io_2}_{top}$.

From Fig. 5 and the above considerations it is clear how the fully calibrated absolute phase offset would bring a discontinuity between adjacent Raw DEMs, while the integer only correction in Eq. (12) provides an homogeneous result, without height discrepancies, proving its robustness to phase noise. Absolute height inaccuracies, coming from the integer only correction, could be present in the Raw DEM. Nevertheless, they will be corrected when generating the global TanDEM-X DEM, as the height is consistent among *intra-data take* Raw DEMs.

The fractional part of the phase offset:

$$\phi_{off_{frac}} = \arctan\left(\frac{\sin(\phi_{off})}{\cos(\phi_{off})}\right) \tag{13}$$

is the measurement of the inaccuracies described above. It is then a tool for the fine calibration of the satellite, as it is influenced by baseline inaccuracies, sync-link and electronic delays. Specifically, the latter are relevant in bistatic acquisitions where signals take different paths through the two instruments and small discrepancies yield shift measurements not related to the geometries. Also

Table 1
Main parameters of the Cordillera Central Mountains acquisition used as test site.

Central incidence angle	47°
Perpendicular baseline	140 m
Height of ambiguity	60 m
Average coherence	0.65
q_{ratio}	94.2%

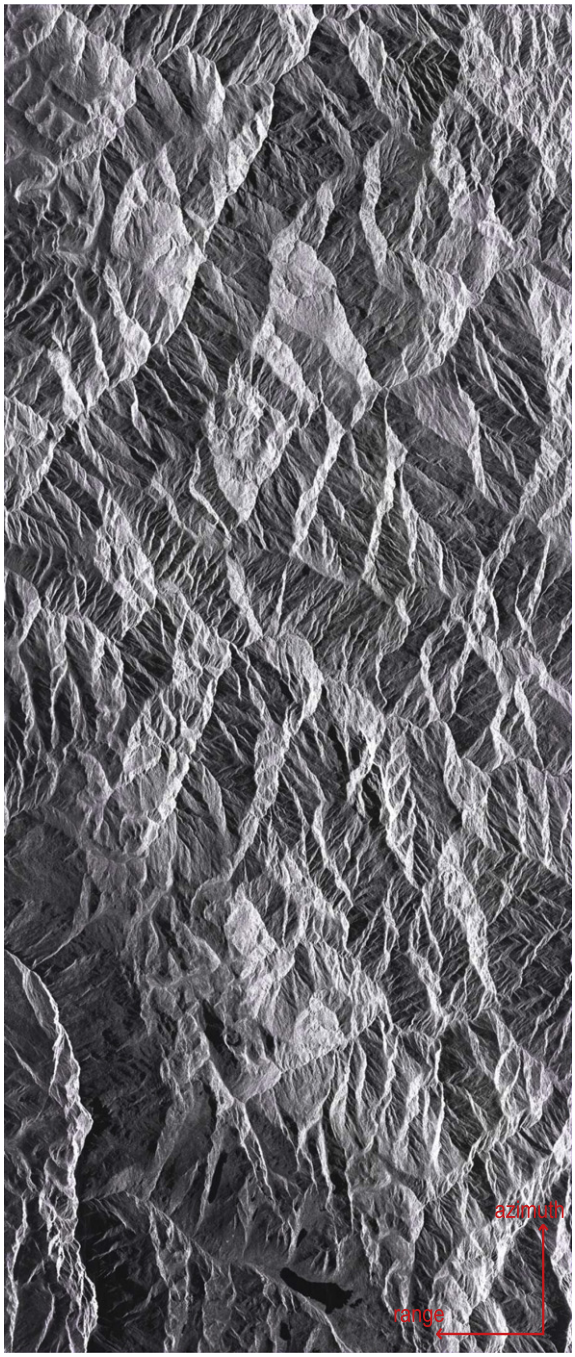

Fig. 6. SAR amplitude image of the master channel.

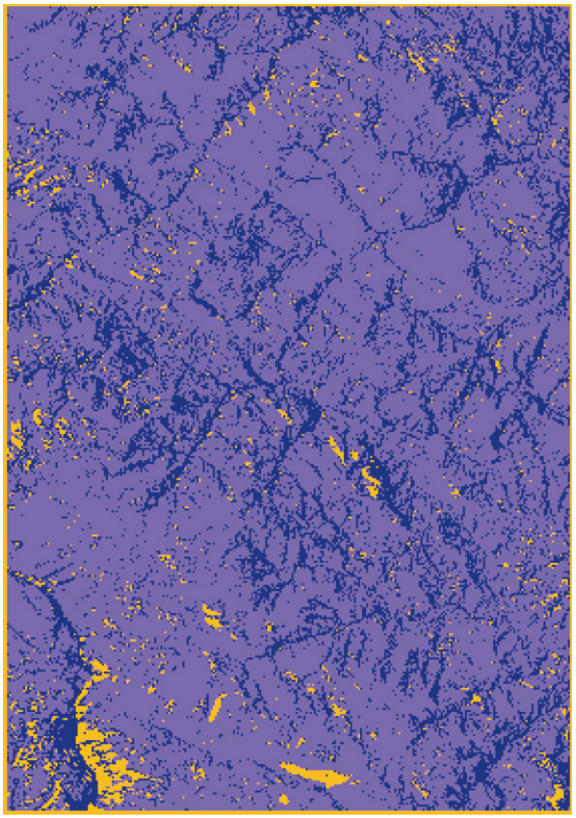

Fig. 7. ITP SAR coregistration map. The purple, blue and yellow colors represent respectively the estimate from coherent cross-correlation, incoherent cross-correlation and orbital information.

the phase offsets from the sync-link show up as deviations from the offsets simulated from reference data. These operationally provided offset from the ITP were successfully exploited for the fine instrument calibration during the Commissioning Phase and the early operational phase.

4. Processing example

An operational processing example helps to better understand the algorithms presented in Section 2. The considered acquisition was taken on April 11, 2011, over the Cordillera Central Mountains in Peru. The main parameters are outlined in Table 1.

The SAR amplitude image of the master channel is shown in Fig. 6. The scene is mountainous, composed of several peaks and valleys, presenting all the typical SAR geometric phenomena due to the side looking geometry: layover, shadow and foreshortening. The interferometric average coherence is 0.65 as it is a mean over all the scene, including the problematic areas affected by geometrical decorrelations.

The SAR coregistration processing step can be performed in three ways, as outlined in Section 2.2. In Fig. 7 the three different areas are represented in violet (coherent cross-correlation), blue (incoherent cross-correlation) and yellow (geometric registration). The percentage of the three methods is respectively 76%, 21% and 3%, or, expressing in number of patches, 86,000, 24,000 and 3300. As more than 10% of the patches – 11,000 patches – are coherent, only that kind are used for the absolute phase offset estimation. At a first sight, the incoherent estimates are located in the problematic areas and the geometric ones where the backscattering is very low. The stereo-radargrammetric shifts computed at this stage are shown in slant range coordinates in Fig. 8. They are the basis for the generation of the *radargrammetric DEM*. The parallax effect is clear through the range ramp, spanning about two pixels.

The processing continues with the interferogram generation and the phase unwrapping. The difference between the unwrapped phase and the stereo-radargrammetric one (Eq. (9)), generated exploiting Eq. (7) with the shifts in Fig. 8, is shown in Fig. 9. This map is the basis for the absolute phase offset estimation through its histogram exploitation (Fig. 10), as explained in Section 2.3. Although from the map it is possible to visually see two homogeneous areas different from the mean at the bottom left and right, in the histogram those regions are masked by noise. Moreover the standard deviation of the histogram is considerably high: 28.6 radians. From the difference's histogram it is thus not possible

Fig. 8. Stereo-radargrammetric shifts derived from the coregistration processing step. The color scale is saturated between −1 [pixel] (blue) and +1 [pixel] (white).

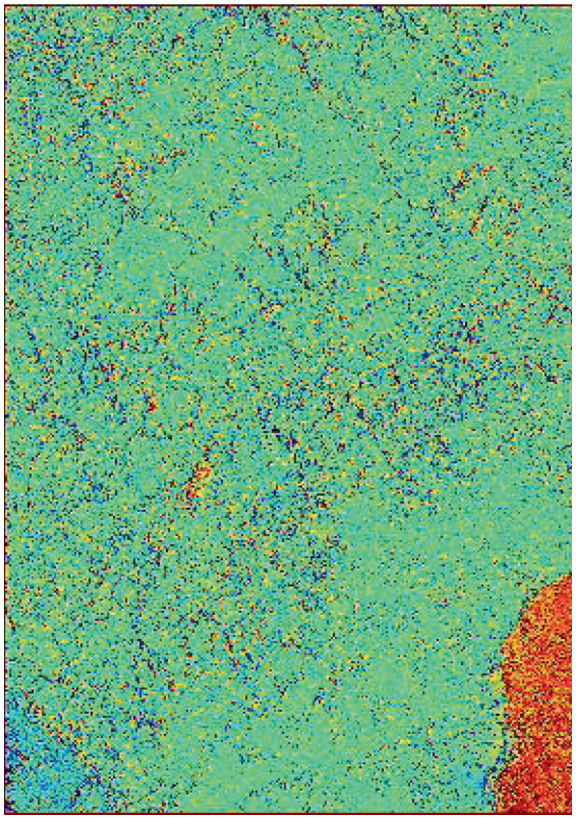

Fig. 9. Stereo-radargrammetric and unwrapped phase difference. The color scale is a linear RGB saturated between −200 and 0 radians.

to find any phase unwrapping error directly. The absolute phase offset could be estimated with the mean value of the differences matching with the 86,000 coherent patches, resulting in a value of −98.65 radians. When a median filtering of size 5×5 is iteratively applied for noise reduction, the histogram main lobe is highly compressed, reaching a variance of 2.24 rad. Even if the estimated absolute phase offset is only slightly varying from its originally estimated value (its integer part is not changing), the filtering operation allows the detection of two secondary peaks, whose underlying area is colored in yellow in Fig. 10. These small peaks correspond to the regions at the bottom left and bottom right affected by the PU errors, caused by the shadow area surrounding them. The peak detection is performed with a local minima/maxima search. For this purpose the raw histogram, having a bin spacing of $\pi/3$, cannot be directly used; a smoothed version of it is rather used for the estimation. Since the minimum possible distance between two errors is 2π, the boxcar average window size used for the smoothing must be chosen in a way that such error is still detectable, so that

$$w_f b_h \leqslant \pi, \tag{14}$$

where w_f is the filter size and b_h is the bin spacing; in the selected case $w_f = 3$.

The detection of false heights is visually represented in the radargrammetric control map in Fig. 11. Two local minima were found for $m_1 = -111.8$ and $m_2 = -87.7$ radians; values outside the range $[m_1, m_2]$ are masked in black. The q_{ratio}, computed as in Eq. (11), is 0.942, meaning that about the 6% of the scene has a wrong terrain height. Looking the blue and the red spots in Fig. 11, it is possible to see how these noisy estimates, lying at the extreme

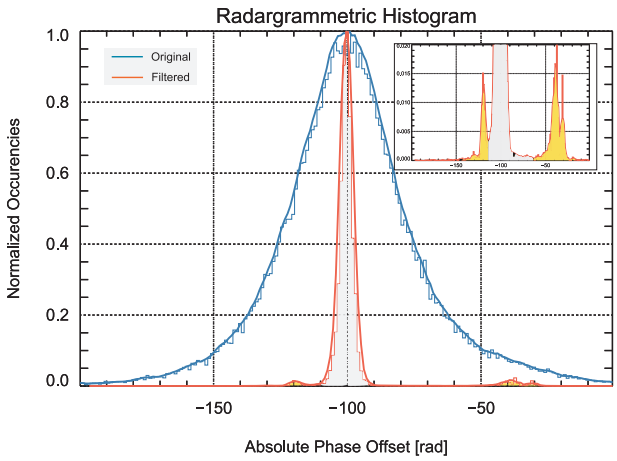

Fig. 10. Histogram of the phase difference (blue) and its filtered version (orange). In grey the area corresponding to main unwrapped region, in yellow the area corresponding to phase unwrapping errors. In the top left window, a zoom over the secondary peaks is highlighted.

parts of the main lobe of the histogram in Fig. 10, correspond in fact to regions for which incoherent or geometric methods were used in the coregistration operation, as shown in Fig. 7. Beside the two areas located at the south-west and sout-east of the acquisition, also some small regions are outside the main lobe range. Comparing this small black patches with the map in Fig. 7, it is noticeable their matching with geometrical coregistration shift estimates. It must be again pointed out that the radargrammetric

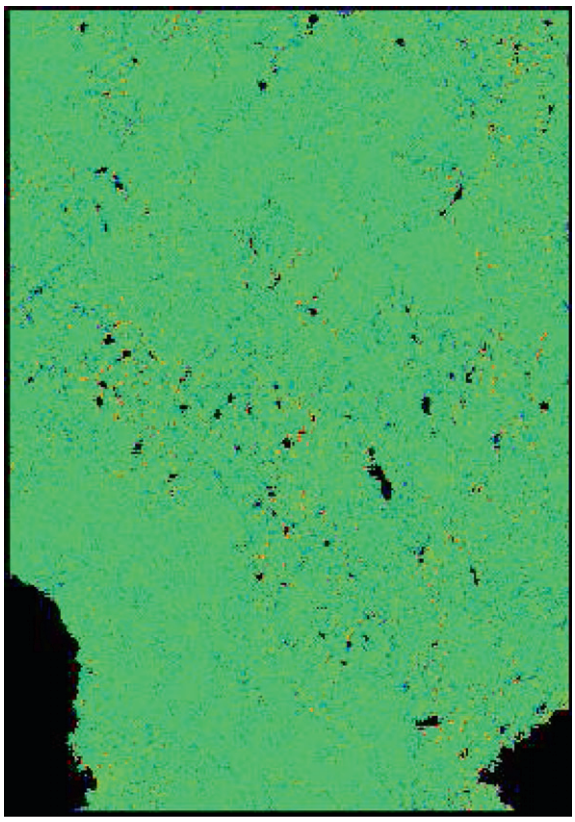

Fig. 11. *Radargrammetric control map*. The unmasked area has a RGB color scale saturated at the local minima of the histogram main lobe.

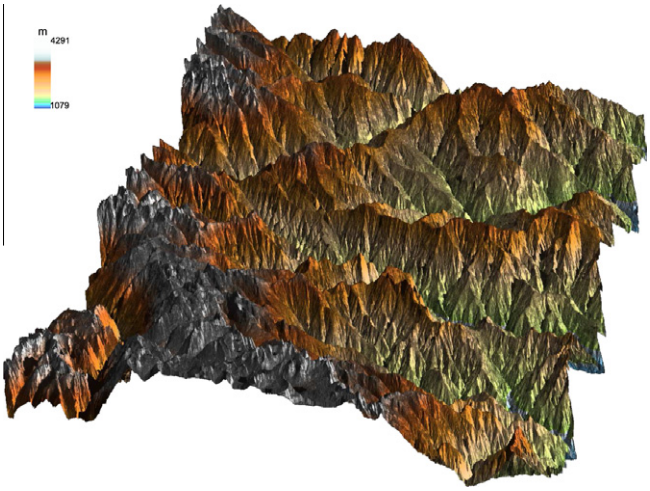

Fig. 12. Three dimensional view of the Raw DEM generated with the acquisition taken on the 11th April, 2011, over the Cordillera Central Mountains in Peru.

control map is a global map, representing the whole scene, while the portion of the scene used for the absolute offset estimation is only the one for which a coherent cross-correlation operation was used in the coregistration processing step.

The final Raw DEM is represented in a three dimensional view in Fig. 12. The bottom-left part, subject to the error, is also visibly noticeable. The Raw DEM statistics are in Table 2. The layover and shadow percentage are underestimated as the SRTM DEM was used for their calculation (Rossi et al., 2010). The PU regions is the count of the local maxima of the smoothed histogram.

Table 2
Raw DEM statistics. Layover and shadow are computed with a C-Band SRTM DEM.

Min height	986.29 m
Max height	4414.42 m
Mean height	2680.28 m
Mean coherence	0.65
Mean height error	2.76 m
Std height error	3.45 m
PU regions	6
q_{ratio}	0.942
Perc. layover	1%
Perc. shadow	1.1%
Perc. PU residues	3.7%
Perc. PU cuts	3.64%

5. Conclusions

The generation of the TanDEM-X Raw DEM follows an optimal, operationally efficient and accurate processing chain. The focusing and the interferometric chains are embedded in one single processor, the Integrated TanDEM-X Processor, installed in the central processing and archiving facilities (PAF) in DLR Oberpfaffenhofen, Germany. A novel quality parameter stating the goodness of the overall processing is derived. A quality analysis is fundamental for a possible (re-)planning or (re-)processing of the acquisitions, and its robustness is essential in the mission concept. In the ITP context, a quality analysis has to be carried out for the single portion, or scene, of the bistatic acquisition, and a natural technique is the comparison with some reference data. Another DEM could be used for the purpose. The SRTM DEM is, for example, used successfully for several operations in the processing chain, as for the geometrical registration of the channels. The major limitation to its use is the fact that it is not global. A second limitation is the time span between the two DEMs acquisition dates. The choice is then to look internally, to the geometrical parallaxes, to the stereo-radargrammetry, used for the coregistration of the two channels. With this information it is possible to build a reference DEM from the TanDEM acquisition itself and to compare it with the one created with the unwrapped phase. The accuracy of the comparison depends on the coregistration accuracy: it was demonstrated how in the TanDEM-X scenario the coregistration stage has a quality which allows the proposed approach. The comparison allows also the estimation of the absolute phase offset, necessary for the calibration of the Raw DEM. It was also demonstrated how an accurate estimation of the phase offset yields a strategy for the connection of the Raw DEMs inside a data take without height discrepancies among them. In summary, the stereo-radargrammetric measures computed in the interferometric processing are successfully used for the quality control of the instrument, the acquisitions, and the calibration of the TanDEM-X Raw DEMs.

The TanDEM-X project is partly funded by the German Federal Ministry for Economics and Technology (Foerderkennzeichen 50 EE 1035).

References

Bamler, R., Eineder, M., 2005. Accuracy of differential shift estimation by correlation and split-bandwidth interferometry for wideband and delta-k SAR systems. IEEE Geoscience and Remote Sensing Letters 2 (2), 151–155.

Bamler, R., Meyer, F., Liebhart, W., 2007. Processing of bistatic SAR data from quasi-stationary configurations. IEEE Transactions on Geoscience and Remote Sensing 45 (11), 3350–3358.

Breit, H., Fritz, T., Balss, U., Lachaise, M., Niedermeier, A., Vonavka, M., 2010. TerraSAR-X SAR processing and products. IEEE Transactions on Geoscience and Remote Sensing 48 (2), 727–740.

Breit, H., Younis, M., Balss, U., Niedermeier, A., Grigorov, C., Hueso-Gonzalez J., Krieger, G., Eineder, M., Fritz, T., 2011. Bistatic syncronyzation and processing of TanDEM-X data. In: Proceedings of IEEE International Conference on Geoscience

and Remote Sensing Symposium, IGARSS 2011, Vancouver, Canada, 24–29 July, pp. 2424–2427.
Fritz, T., Rossi, C., Yague Martinez, N., Rodriguez Gonzalez F., Lachaise, M., Breit, H., 2011. Interferometric processing of TanDEM-X data. In: Proceedings of IEEE International Conference on Geoscience and Remote Sensing Symposium, IGARSS 2011, Vancouver, Canada, 24–29 July, pp. 2428–2431.
Gatelli, F., Guarnieri, A.M., Parizzi, F., Pasquali, P., Prati, C., Rocca, F., 1994. The wavenumber shift in SAR interferometry. IEEE Transactions on Geoscience and Remote Sensing 32 (4), 855–865.
Gruber, A., Wessel, B., Huber, M., Roth, A., 2012. Operational TanDEM-X DEM calibration and first validation results. ISPRS Journal of Photogrammetry and Remote Sensing, this issue.
Hueso-Gonzalez, J., Bachmann, M., Krieger, G., Fiedler, H., 2010. Development of the TanDEM-X calibration concept: analysis of systematic errors. IEEE Transactions on Geoscience and Remote Sensing 48 (2), 716–726.
Just, D., Bamler, R., 1994. Phase statistics of interferograms with applications to synthetic aperture radar. Applied Optics 33 (20), 4361–4368.
Krieger, G., Moreira, A., Fiedler, H., Hajnsek, I., Werner, M., Younis, M., Zink, M., 2007. TanDEM-X: a satellite formation for high-resolution SAR interferometry. IEEE Transactions on Geoscience and Remote Sensing 45 (11), 3317–3341.
Lachaise, M., Fritz, T., Eineder, M., 2008. A new dual baseline phase unwrapping algorithm for the TanDEM-X mission. In: Proceedings of 7th European Conference on Synthetic Aperture Radar, EUSAR 2008, Friedrichshafen, Germany, 2–5 June (on CD-ROM).
Leberl, F., 1990. Radargrammetric Image Processing. Artech House, Norwood, USA.
Madsen, S.N., 1995. On absolute phases determination techniques in SAR interferometry. In: Proceedings of SPIE Algorithms for Synthetic Aperture Radar Imagery II, vol. 2487, Orlando, USA, 19–21 April, pp. 393–401.
Prati, C., Rocca, F., 1993. Improving slant-range resolution with multiple SAR surveys. IEEE Transactions on Aerospace and Electronic Systems 29 (1), 135–143.
Rabus, B., Eineder, M., Roth, A., Bamler, R., 2003. The Shuttle Radar Topography Mission (SRTM) – a new class of digital elevation models acquired by spaceborne radar. ISPRS Journal of Photogrammetry and Remote Sensing 57 (4), 241–262.
Rossi, C., Eineder, M., Fritz, T., Breit, H., 2010. TanDEM-X mission: raw DEM generation. In: Proceedings of 8th European Conference on Synthetic Aperture Radar, EUSAR 2010, Aachen, Germany, 7–10 June (on CD-ROM).
Wessel, B., Gruber, A., Wendleder, A., Huber, M., Breunig, M., Marchalk, U., Kosmann, D., Roth, A., 2011. Production chain towards first calibrated and mosaicked TanDEM-X DEMs. In: Proceedings of IEEE International Conference on Geoscience and Remote Sensing Symposium, IGARSS 2011, Vancouver, Canada, 24–29 July, pp. 2432–2435.
Yague Martinez, N., Eineder, M., Brcic, R., Breit, H., Fritz, T., 2010. TanDEM-X mission: SAR image coregistration aspects. In: Proceedings of 8th European Conference on Synthetic Aperture Radar, EUSAR 2010, Aachen, Germany, 7–10 June (on CD-ROM).

A.2. Paddy-rice monitoring using TanDEM-X

Rossi, C., and Erten, E., Paddy-rice monitoring using TanDEM-X. *IEEE Transactions on Geoscience and Remote Sensing*, 53(2), 900-910, 2015.

Paddy-Rice Monitoring Using TanDEM-X

Cristian Rossi and Esra Erten

***Abstract*—This paper evaluates the potential of spaceborne bistatic interferometric synthetic aperture radar images for the monitoring of biophysical variables in wetlands, with a special interest on paddy rice. The assessment is made during the rice cultivation period, from transplanting to harvesting time (May to October) for fields around Gala lake (Turkey), one of the largest and most productive paddy rice planting area in the country. Detailed ground truth measurements describing biophysical parameters are collected in a dedicated campaign. A stack of 16 dual-pol TanDEM-X images is used for the generation of 32 digital elevation models (DEMs) over the studied area. The quality of the data allows the use of the interferometric phase as a state variable capable to estimate crop heights for almost all the growing stages. The early vegetative rice stage, which is characterized by flooded fields, cannot be represented by the interferometric phase due to a low signal-to-noise ratio but can be easily detected by amplitude and interferometric coherence thresholding. A study on the impact of the polarization in the signal backscatter is also performed. An analysis of the differences between HH and VV DEMs shows the varying signal penetration for the two polarizations at different growing stages. The validation with reference data demonstrates the capability to establish a direct relationship between interferometric phase and rice growth. The very high coherence of TanDEM-X data yields elevation estimates with root-mean-square error in a decimetric level, supporting temporal change analysis on a field-by-field basis.**

***Index Terms*—Agriculture, digital elevation model (DEM), paddy-rice monitoring, polarimetry, synthetic aperture radar (SAR) interferometry, TanDEM-X.**

I. Introduction

REMOTE sensing is a mature technology for observation of natural environmental changes. In terms of agricultural monitoring applications, radar sensors differ from optical, multispectral, and thermal sensors. First, radar imaging provides a timely mapping of the scattering properties of biophysical variables, including night and all-weather condition monitoring. Second, the system not only measures amplitudes but also phases of the backscattered signal, yielding the joint derivation of absolute ranging and backscattering coefficients. Hence, for crop inspection applications, temporal synthetic aperture radar (SAR) images are an attractive instrument to exploit.

For more than 10 000 years, rice has been one of the most important products in the food market. Rice agriculture, which is considered a seasonal planting, is mainly possible in temperate climates. A rice growth cycle from panicle initiation to maturing, takes about 110–250 days. Throughout this cycle, roots and bottom part of the stem stay submerged in water for approximately 90 days. The rice growth cycle mainly consists of three stages: *vegetative*, *reproductive*, and *maturation*. In these phenological stages, rice plants exhibit distinct structural differences. These differences are described by using a scale called *Biologische Bundesanstalt, bundessortenamt und CHemische industrie* (BBCH) [1]. All growing stages can be associated with the BBCH scale, as shown in Table I. In response to the increasing demand of rice, monitoring of farming activities cannot be left only to farmers. Information on crop activities is also significant to governments for planning strategies. Specifically, observations with remote sensing technologies are urgent for developing countries. In this case, considering that rice fields are generally cultivated under cloudy and rainy weather, radar remote sensing is of particular interest in their monitoring.

TABLE I
BBCH Scale of Rice

Major Stage	BBCH Scale	Description
Vegetative	00	Germination
	10	Leafing
	20	Tillering
	30	Stem elongation
	40	Booting
Reproductive	50	Heading
	60	Flowering
	70	Fruiting
Maturation	80	Ripening
	90	Senescence

Accordingly, synthetic aperture radar (SAR) images have been already used for several campaigns for crop inspections [2]–[10]. Sun *et al.* [2] made an analysis to determine the most suitable combination of frequency, polarization and incidence angle for rice monitoring. The main outcome of the study is the definition of a relationship between the C-band backscatter coefficient and the *leaf area index* (LAI), provided also by [11]. Following this paper and exploiting the RADARSAT mission, several other researches on C-band rice monitoring are reported [3], [9]. These researches underline how temporal C-band backscatter depends on the biophysical stage of the crop. However, due to the limited information about biophysical parameters obtained from single channel SAR images, it is not easy to calculate some physical parameters as *height above ground*, *number of leafs*, and *leaf angle* directly from backscattering coefficients. The work in [12]–[16] underlined the potential of multiple polarimetric measurements in rice monitoring. These studies, employing a time series analysis,

Manuscript received January 10, 2014; revised March 26, 2014 and May 29, 2014; accepted June 9, 2014. Date of publication July 30, 2014; date of current version August 12, 2014.

C. Rossi is with the Remote Sensing Technology Institute, German Aerospace Center (DLR), D-82234 Oberpfaffenhofen, Germany (e-mail: cristian.rossi@dlr.de).

E. Erten is with the Department of Geomatics Engineering, Istanbul Technical University, Istanbul 34469, Turkey (e-mail: eerten@itu.edu.tr).

Color versions of one or more of the figures in this paper are available online at http://ieeexplore.ieee.org.

Digital Object Identifier 10.1109/TGRS.2014.2330377

reported the relationship between BBCH scale and polarimetric observables as *entropy*, *alpha*, ratio, and coherence between HH and VV polarized images.

Many possible measures of rice growth as canopy height, LAI, biomass, etc. are considered in the works cited aforementioned. Among them, canopy height is the most direct measurement and has direct relationship with growth rate, particularly in the vegetative stage. Sun *et al.* [2] and Inoue *et al.* [10] reported the correlation between canopy height and backscattering coefficients, although the scattering process is not a function depending only on crop height. In fact, an indirect relationship can be assessed. As the canopy gets higher, a double-bounce scattering mechanism generated by the interaction between the stems and the underlying water surface yields high reflections. This relationship is reported to vary among frequency bands [4], [17]. These works analyze the electromagnetic scattering, which is a function of intricate interrelations among physical parameters of rice. Moreover, as based on experimental data sets and locally selected thresholds, their accuracy may be insufficient for operational processors commanded to process various data sets.

Next to single-image backscattering information, interferometric phase information provides an additional support with the cost of two SAR images. From an agricultural application point of view, in the literature, interferometric phase information has been employed by exploiting the coherence as in [18]–[20]. In these works, most of the attention has been given on the accuracy of the interferometric phase in tandem data set. However, the European Remote Sensing (ERS) satellite data set with low resolution cannot tackle the physical-based spatial heterogeneity problem in paddy rice fields. The use of the *differential* interferometric phase, which is a direct function of temporal volume change, is also rare in paddy-rice monitoring literature. Instead, several studies have been reported for soil moisture modeling [21], glacier [22], seismic events [23], and urban area [24] volume changes. These previous volume studies emphasize that two aspects have to be considered in terms of monitoring applications. The first one is the potential penetration, causing an underestimation in volume deviations. The second one is the large temporal baselines, causing unreliable interferometric phase information. A promising SAR mission to attenuate these limitations is TanDEM-X [25], which allows to measure small phase center variations related to the changes in canopy height, since the relatively short X-band wavelength interacts mostly with upper sections of the crop. The objective of this paper is to examine the relationship between the crop height and the differential interferometric phase for paddy rice and to explore the new capabilities of TanDEM-X monitoring for assessment of crop growth. TanDEM-X is an innovative SAR concept, first in space making use of a bistatic configuration to generate high-resolution digital elevation model (DEM) accomplishing HRTI-3 accuracy requirements. The flexible commanding yields the acquisition of several DEMs over the same area in a short revisit time. In this paper, a stack of 16 dual-pol acquisitions over one of the largest and most productive paddy rice planting area in Turkey, around Gala lake, is analyzed. The differential interferometric phase is derived and used as a *state*

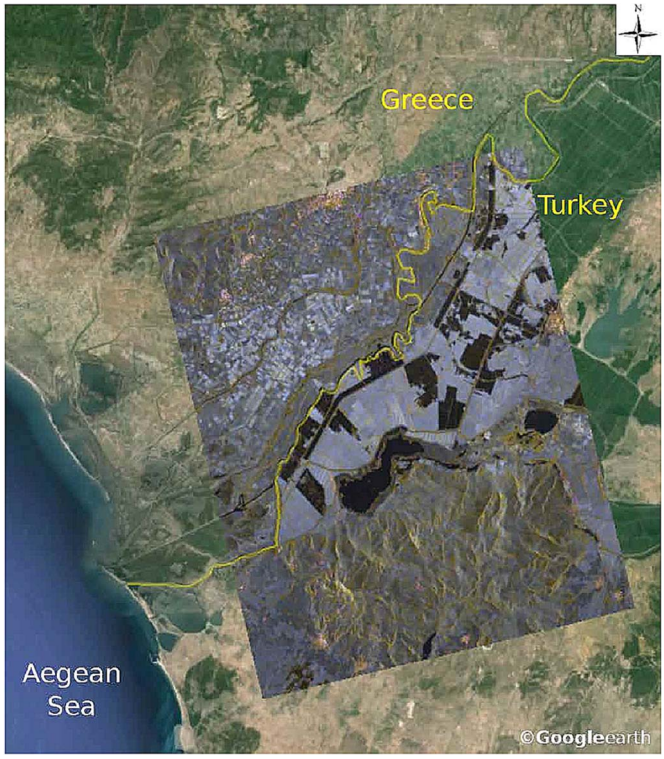

Fig. 1. RGB composite master amplitude acquired on the 12.05.2012, showing the location of the study area.

variable to describe the rice phenological stage. The limitations depicted above, i.e., the difficulties to relate a backscatter analysis with a derivation of crops height and the difficulties to establish operational schemes, are reduced by employing the bistatic system.

TanDEM-X data have been recently analyzed in [26] with outcomes strongly limited by the small baselines of the experimental acquisitions. Moreover, low signal-to-noise ratio (SNR) was an issue by producing low coherence in the growing stages. For the case under study, the TanDEM-X experimental data set has baselines well suitable for an interferometric analysis. To present the first TanDEM-X results with the aim of crop height monitoring, this paper is organized as follows. In Section II, the test site and the ground measurement campaign are described, leading to the problem formulation of temporal growth change. The next section is dedicated to the processing strategies employed for the derivation of change maps using the data stack. The extraction of crop heights without using external data is also outlined in here. The validation and establishment of a relationship between rice phenology and interferometric height is then presented. Section IV concludes this paper revisiting and synthesizing the aforementioned considerations.

II. Test Site and Ground Measurement Campaign

The lower course of the Maritsa River and surrounding areas, where it forms the border of Greece and Turkey, is a unique wetland environment consisting of lakes, rivers and agricultural fields (see Fig. 1). In the last 50 years, changes in topography due to debris flow and heavy rain affecting the regional ecosystem were measured. Recently, the region is controlled

Fig. 2. First line shows portions of agricultural fields acquired on the 30th of May, 2013, illustrating the differences in agricultural practice. The second line shows the temporal pictures of field 8.

TABLE II
MAIN PARAMETERS OF THE INTERFEROMETRIC DATA SET (HH CHANNEL)

acquisition date (DOY)		center incidence angle [deg]	perpendicular baseline [m]	height of ambiguity [m]	interferogram resolution [m]	standard error* [m]
12.05.2012	(133)	36.8	253.7	23.1	10.2	0.36
14.06.2012	(166)	36.8	242.3	24.2	10.3	0.38
06.07.2012	(188)	36.8	234.3	25.1	10.2	0.40
17.07.2012	(199)	36.8	227.2	25.8	10.2	0.41
28.07.2012	(210)	36.8	222.7	26.3	10.3	0.42
19.08.2012	(232)	36.8	213.4	27.4	10.2	0.43
10.09.2012	(254)	36.8	204.4	28.7	10.3	0.46
13.10.2012	(297)	36.8	187.1	31.3	10.3	0.50
26.11.2012	(331)	36.8	181.3	32.3	10.3	0.51
05.03.2013	(64)	36.8	112.0	52.8	10.4	0.83
16.03.2013	(75)	36.8	111.5	53.1	10.4	0.84
10.05.2013	(130)	36.8	139.7	42.1	10.4	0.67
21.05.2013	(141)	36.8	141.1	41.6	10.3	0.66
01.06.2013	(152)	36.8	146.6	40.2	10.3	0.63
23.06.2013	(174)	36.8	144.3	40.7	10.4	0.64
26.07.2013	(207)	36.8	111.6	52.8	10.3	0.84

by the government and made available for agricultural practice, mainly for paddy rice. Considering the regional risk of debris flow, agricultural fields have to be monitored, controlling, by this way, the effect of flow. For instance, if the seeding has been affected from flow and irrigation, farmers can do transplanting again before it is too late for seeding.

In order to better understand the microwave interaction with agricultural fields, the state organization Trakya Agricultural Research Institute collected detailed ground truth in eight fields with four independent samples per field during the growth cycle (May to October) of paddy rice in 2013. *Height above ground and water*, *number of plants per area*, *number of leaves per area*, *number of tillers per area*, *number of panicles per area*, *stem diameter*, *leaf width*, *leaf length*, and *leaf angle* were collected in the fieldwork. The fieldworks dates are illustrated in Fig. 2 with the pictures taken during these studies. To highlight the spatial variation in response to changes in agricultural practice, the first line in Fig. 2 shows the pictures taken from different fields on the same day. In this region, different fields are cultivated variously depending on the field owner decision. Despite their variety in cultivating, the phenological evolution (BBCH scale) of the monitored parcels is similar but shifted in time [see Fig. 3(a)]. Since their temporal trends are similar, in the second line of Fig. 2, temporal pictures simultaneously taken in the fieldworks are shown only for a single field (field 8). In the study area, the sowing method is direct seeding by broadcasting, implying random seeding instead of a regular straight-row one.

The phenological development of these fields shows a clear similar trend with the rice field monitored in Sevilla, Spain by [17]. However, it is important to underline that the differential slope indicating the step from the reproductive stage to the maturation stage is higher in the Sevilla campaign then in the Gala Lake one. In [17], a classification of BBCH scales is done based on a set of rules obtained from the Sevilla data set. Using the same decision tree may bring inaccuracies in other study areas.

Considering the interest in volume changes of agricultural fields, Fig. 3 shows the plots of the relationship between canopy height, BBCH scale and day of the year obtained during the field works. Most fields were homogeneous and crops reached maximum height after flowering. As Fig. 2 illustrates, when a crop reaches the flowering stage, it is fully developed with no gaps between plants. During the cultivation period, the monotonous relationship between canopy height and BBCH scale in Fig. 3(b) makes the elevation monitoring appealing. To be noticed, height sensitivity to crop development is particularly high up to about BBCH 60. After this stage, plant height exhibits just small changes. In Section I, it is outlined how backscattering coefficients of radar signal do not allow a direct detection of BBCH-stages due to lack of detectable physical changes in the phenology. Thus, in this paper, the earlier analysis based on backscattering coefficients is extended, and the differential interferometric phase is explored in terms of biophysical parameters in the next section.

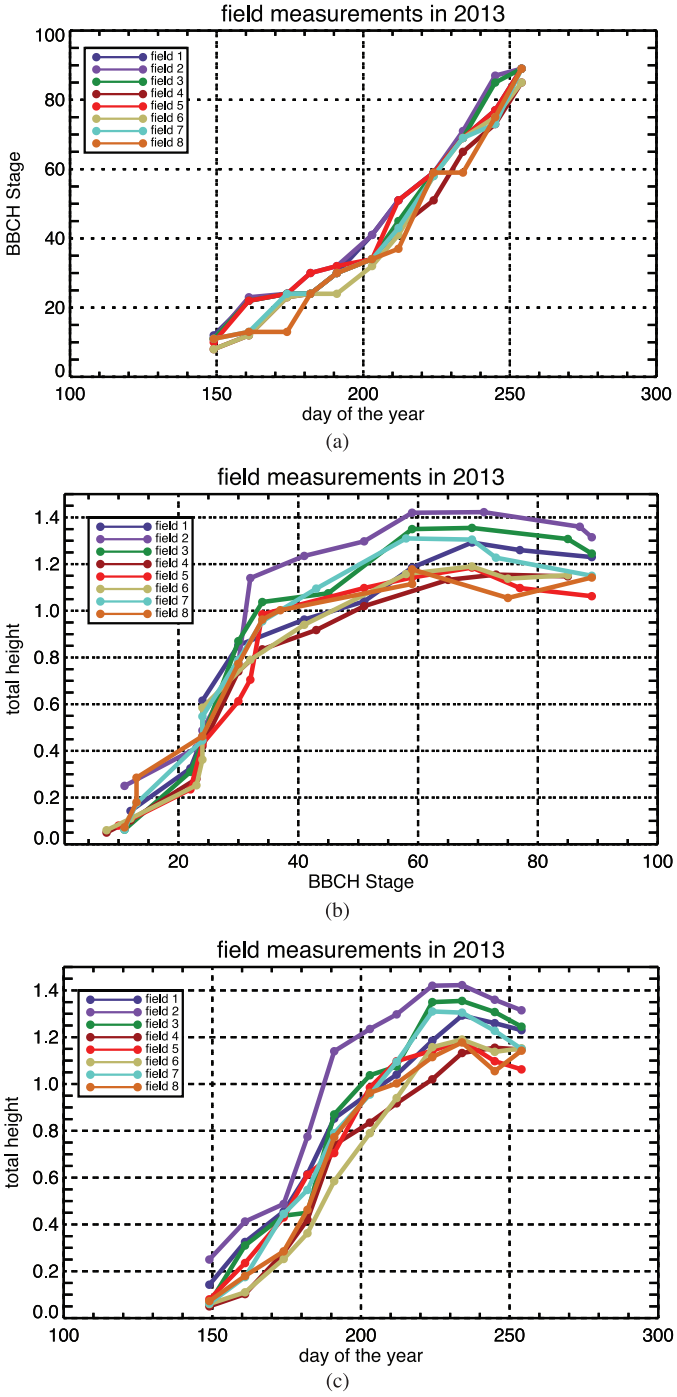

Fig. 3. Biophysical stage characterized by BBCH scale of the monitored eight fields as a function of day of year (a) and of height above the ground (b). The relationship between the day of the year and the canopy total height (c).

III. Processing Results and Validation

In the framework of the German Aerospace Center (DLR) project *XTILAND*1476, 16 dual-pol TanDEM-X acquisitions have been acquired over the Gala lake region in 2012 and 2013. Specifically, nine acquisitions have been commanded in 2012 and eight in 2013 at the same incidence angle. As shown in Table II, only the 2012 acquisitions are covering all the rice growing stages (May to October), whereas the 2013 acquisitions are missing the maturation stage (August to October). For this reason, although the GPS campaign has been conducted in

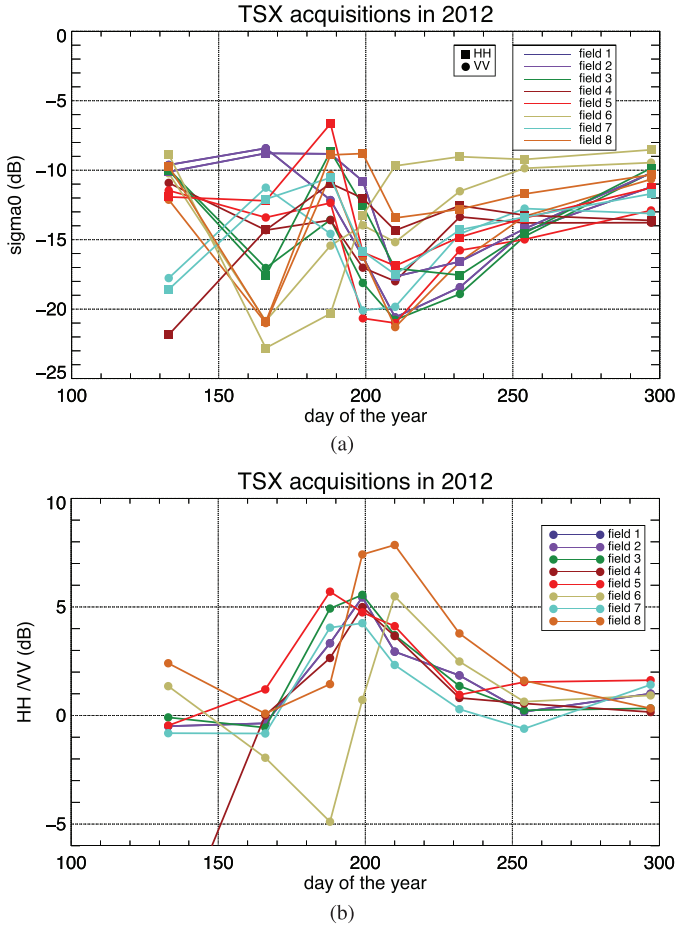

Fig. 4. (a) Measured backscattering coefficients in HH and VV polarization. (b) Polarimetric ratio $\sigma^0_{\mathrm{HH}}/\sigma^0_{\mathrm{VV}}$.

2013, the sole 2012 acquisitions are employed in the following analysis. An additional reason relies to the height sensitivity of the different bistatic configurations. Height of ambiguity (HoA), an important system parameter describing the elevation range of a phase cycle—smaller and more accurate the generated DEM—, ranges between about 20 and 30 m for the 2012 acquisitions and between about 40 and 50 m for the 2013 ones. To give a quantitative idea, assuming a Gaussian distributed phase error, a coherence value of 0.8 yields a standard error of 0.36 m for the 12.05.2012 processed configuration (HoA: 23.1 m) and a standard error of 0.84 m for the 26.07.2013 one (HoA: 52.8 m) [27].

The data stack is processed with the Integrated TanDEM-X Processor (ITP) at the DLR processing facilities [28]. ITP is the operational system employed in the TanDEM-X mission for the generation of the raw DEM given as input SAR raw data. The processor is commanded to generate HH and VV DEMs for a total of 32 DEMs, with an output raster of 6 m. As in Table II, the interferogram resolution is triggered to be around 10 m by multilooking the input coregistered data, yielding height errors at a coherence value of 0.8 specified in the last column of the table. Considering the purpose of tracking crop height in all the growing stages, the multilooking process is a necessary step to reduce the phase noise and the resulting standard error to a decimetric level. Due to the relatively smooth topography of the scenes, phase unwrapping is not an issue

(even for small height of ambiguities) and no unwrapping errors have been detected. To ensure a straightforward analysis, all the DEMs have been generated at the same output grid and have been equally calibrated jointly using Shuttle Radar Topography Mission (SRTM) and Ice, Cloud, and land Elevation Satellite (ICESat) data. For the following analysis, the HH channel has been chosen. Nevertheless, a study with the differences observed between the different polarizations is provided in the following section.

A. Dual-Polarization Study

Before studying the differential interferometric phase with the crop height estimation purpose, the temporal trend of backscattering coefficients represented by σ^0 is examined. The image intensity values for HH and VV polarizations are transformed to σ^0 according to [29] and plotted in Fig. 4(a). The different agricultural practices can be seen by comparing the various fields on the time line. As reported in [6], HH/VV ratio is an excellent indicator of rice phenological stages; thus, it is also plotted in Fig. 4(b). As expected, the temporal trend of the backscattering information is similar to the previous detailed work at X-band in [17]. The HH/VV ratio is sensitive to rice phenology due to both the attenuation depending on the incidence wave polarization and the dominance of the double-bounce interaction between stems and flooded ground.

An investigation of polarization-dependent penetration depths is meaningful for crop height monitoring. Over automatically selected fields (see next section), HH and VV polarized interferograms are transformed to surface height values. Their relationship, which is demonstrated by scatter plots of the observed HH and VV height values, is temporarily analyzed, as shown in Fig. 5. The temporal scatter plots exhibit a strong linear relationship between the observations. Nevertheless, slight elevation differences are measured depending on the phenological stage of the crop. Although the scatter plots in Fig. 5(a) and (d) show very little height discrepancies for different polarizations, the ones in Fig. 5(b) and (c) have higher differences. The BBCH scale of the crop is 78 and 95 on August 19 and September 10, respectively, indicating that the crop was extremely dry (see also Fig. 2). With such a dry vegetation layer, the X-band radar signal penetrates into the canopy with different penetration length depending on the polarization. This difference is related to the fact that HH signal penetrates more effectively into canopies than the VV does [30]. It can be noticed that rice canopy is mainly vertically oriented until the beginning of August, then the orientation becomes random after flowering stages (fruiting, ripening, and senescence), meaning that the effects of canopy orientation on the penetration depth can be ignored. Considering quantitative analysis, the correlation between the height measurements obtained from HH and VV polarized images is examined using linear regression. High temporal correlation values, such as $R = \{0.982, 0.984, 0.981, 0.987\}$, are almost the same and not changeable depending on the phenological stage of the canopy. However, the disturbance term, which is related to the differences between HH and VV observations, is changing depending on the phenological stage. The height differences obtained from

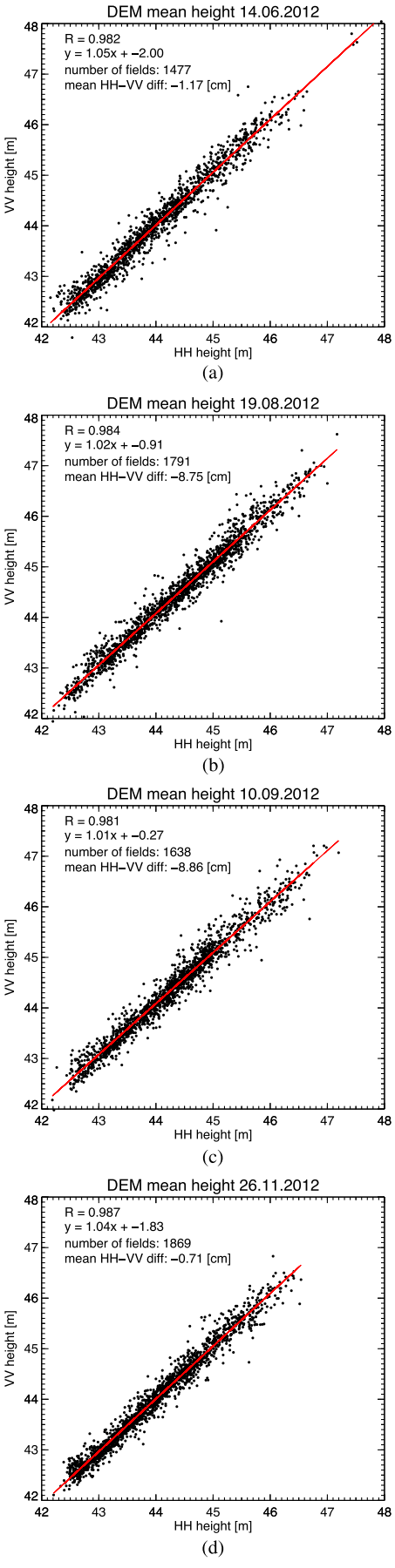

Fig. 5. Height measurements obtained by HH and VV polarized images over the selected agricultural fields for four different dates.

HH and VV polarized interferograms increase about 8 cm in maturation stages as expected from the aforementioned considerations. Additionally, over the detected agricultural fields, the average coherence for HH and VV polarized interferograms acquired on August 19 and on September 10 are analyzed. A standard deviation of 0.06 and 0.03 is obtained for VV and HH polarized interferometric coherences, respectively. This also proves that the HH polarized signal has the ability to more stably penetrate into the canopy when it is dry as the interior part of the rice plant provides a more stable return than the surface component.

B. Interferometric Phase Study

A strategy to evaluate the potential of the differential interferometric SAR data is assessed here and outlined in Fig. 6. The input coregistered complex data stack (CoSSC stack) is processed in ITP for both polarimetric channels. ITP is specially triggered to output an equally calibrated DEM stack by using external information. In particular, an SRTM DEM, calibrated with ICESat, is used in the absolute phase offset stage for all the DEMs in order to provide consistent outputs without discrepancies among them [28]. As seen in Section III-A, the two polarization channels yield the generation of very similar elevation profiles—ignoring the early vegetative stage—with centimeter inconsistencies in the maturation stage (dry season). Thus, just a single channel, HH, is chosen for the analysis.

The main scope of the interferometric investigation is the verification of rice stages by using temporal elevation data. To this aim, field segmentation is mandatory, reasonably assuming consistent growing within single fields. An important subproduct to exploit, generated during the interferometric processing, is the coherence. By describing the similarity of the coregistered complex master and slave data, the coherence is a considerable input for the analysis, supporting the segmentation algorithm. As described in Section II, flooded parcels of land characterize the early vegetative state. During this state, fields are covered by water and separated by a path network composed by soil or rare grass, as visible also in Fig. 8, representing the May 2012 acquisition. A gravel road network is also in the test site separating parcel groups. This natural segmentation is well visible by inspecting the interferometric coherence in Fig. 8(b), which is as good as inspecting the master channel amplitude in Fig. 8(a). This visibility relies on the water body electromagnetic spectrum. Nonmoving water behaves like a mirror, reflecting the incident signal wave in a specular direction, yielding a very low return to the SAR antenna. This phenomenon brings also a low interferometric coherence due to the consequent SNR decorrelation. Moreover, it is also known that a water body decorrelates within tens of milliseconds [31]. Although TanDEM-X is a bistatic mission built to avoid temporal decorrelations, the satellite formation brings small along-track time lags varying between 50 ms (equator) and 0 ms (poles). The global study performed in [32] demonstrated that from 10 ms, water decorrelates. In the studied test case, the mean measured time lag of about 30 ms overcomes the limit. Several investigations have been proposed about the derivation of water bodies from the joint use of amplitude and coherence [32], [33]. In this paper, the technique proposed by [32], operationally employed for the generation of water body mask as an auxiliary product of the official TanDEM-X DEM, is adopted. By analyzing 1700 randomly worldwide-distributed scenes, [32] established two thresholds that provided a correctness analysis well above 90%. Specifically, a threshold value of 40 for the amplitude digital number (corresponding to -18 dB in radar brightness and about -20 dB in Sigma-Nought for the studied case) and 0.23 for the coherence were selected. Three water mask confidence levels are then generated: 1) detection from coherence threshold; 2) detection from amplitude threshold; and 3) detection from both thresholds. The third level represents the highest confidence one. In this paper, this strategy is applied for scenes having flooded crops. In Fig. 8, the 12.05.2012 amplitude and coherence data show the flooded parcels for that date with low values. As visible, not all the fields were already flooded (see also Fig. 2). To better cover the test site, additional information is retrieved by using also the 21.05.2013 and 01.06.2013 acquisitions.

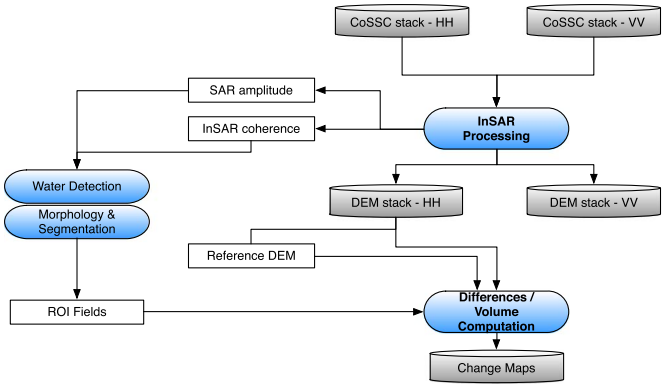

Fig. 6. Flowchart with the processing strategy employed for the analysis.

A potential issue in the detection relies in the presence of wind during the acquisition. For the Rayleigh criterion, a surface is regarded as specular if its vertical variation is smaller than about 5 mm for X-band at 36.8° [30]. Wind may induce waves with height well above this value, resulting in backscattered energy at the sensors. Thus, amplitude threshold can result too low for these cases and can generate misdetections. Nevertheless, water decorrelation yields low coherence and water results masked with the second confidence level [20]. In the study area, the highest confidence level is reached for all the detections indicating a proper threshold selection for both amplitude and coherence. Although not representing the studied scenario, false detections can arise due to volume decorrelation on forested areas or on geometrical decorrelation zones (radar shadow/layover). While a DEM is helpful to discard detection on slopes (i.e., on mountain shadows), a false color composite (FCC) using coherence, backscatter and differential backscatter has been demonstrated as useful to generate land cover maps to discard forest and urban settlements from the water mask [34].

Straight after the water detection, a binary morphological erosion with a 3-by-3 rectangular structuring element is performed to remove isolated artifacts and a binary shape fill is performed to remove possibly remaining holes within shapes. The final mask is then segmented and the fields numbered. A to-

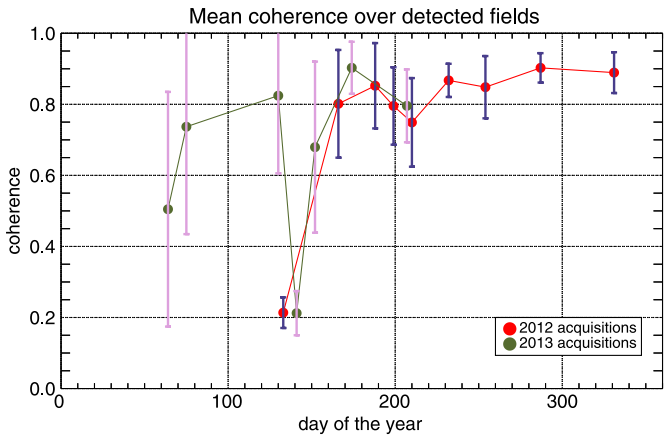

Fig. 7. (Red line) Mean coherence trend for the fields extracted by using the 12.05.2012 acquisition and (green line) by using the 21.05.2013 acquisition. The standard deviation is highlighted with error bars.

tal of more than 2000 fields are detected. The detection and the segmentation are performed in the geocoded domain, in order to easily compare them with ground truth data. To be noticed, geolocation errors hardly occur due to the precise calibration and the practically flat scenario. In this test site, segmentation errors may manifest due to the path length between fields (3–8 m). Considering the DEM spacing of 6 m and the resolution of about 10 m, paths span just 1–2 pixels, possibly creating false linking between regions. Nevertheless, the comparison between the segmentation and the ground truth for the eight fields chosen for the analysis reveals a good matching with an average completeness of 91%, defined as the ratio between the segmented field and the reference one. The remaining 9% may be attributed to the erosion procedure with a square element.

Fig. 7 shows the mean 2012 coherence values for detected flooded fields on 12.05.2012 (red points) and the mean 2013 values for fields flooded on 21.05.2013 (green points). The 2012 acquisitions, spanning the plant growing cycle, exhibit the good quality of the derived elevation for all the stages (June–September), excluding the early vegetative stage (May). A coherence of around 0.2 for the May acquisition (flooded field) yields unreliable elevation values. Moreover, this value results overestimated due to the estimation bias caused by the finite estimation support of 11 by 11 samples [35]. Accurate heights are instead generated for the later data. Coherence fluctuates around 0.8 for the June–July data with a decreasing trend mainly caused by the increasing HoA for similar field conditions (wet environment, fresh plants). This value increases for the following two acquisitions (August–September) as the field condition switches to dense vegetation, ideally behaving like a distributed scatterer. To be noticed, a coherence value of around 0.85 corresponds to better height accuracy than the one specified in Table II. The last two 2012 acquisitions are over the plant cycle, after the harvesting. Here, coherence around 0.9 indicates very accurate elevation values, as the field condition transformed to bare soil with a very rough surface, yielding high SNR. The last acquisition, November 2012, is taken as reference as it indicates the terrain height without water or rice plants. The 2013 acquisition is also shown in Fig. 7 for completeness. The first two data cover the early year period prior the plantation and have huge coherence variations,

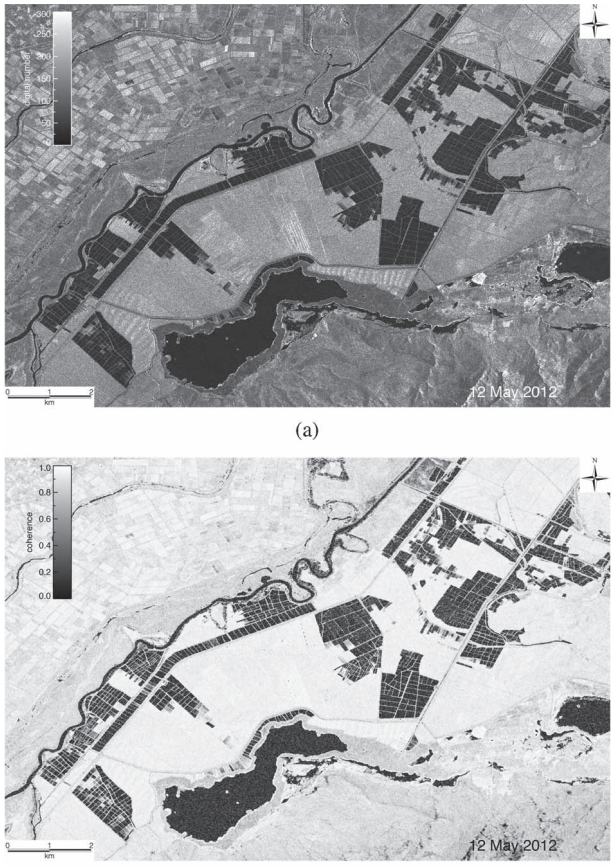

Fig. 8. (a) SAR master channel amplitude and (b) interferometric coherence of the 12.05.2012 TanDEM-X acquisition, used to extract field shapes.

also denoting poor elevation accuracy. The field detection is performed for the late May acquisition, showing a similar value and accuracy to the one used for the 2012 field extraction. The prior and following data provide a higher coherence with high variations, indicating nonhomogeneous conditions for the fields under analysis. The last two acquisitions, in the reproductive stage, follow the same trend of the one in 2012 (see Fig. 8).

Fig. 9 visually shows the plant growth of July 06, August 19 and September 10, 2012. The differences with the reference height of November 2012 are here represented with an overlay between the amplitude and the mean height difference for all the detected fields having an average coherence above 0.8 for both the analyzed and the reference acquisitions. Inspecting these maps, one could check the growing trend on a field-by-field basis. For instance, the July map in Fig. 9(a) shows a quite homogeneous result with plant heights around 70 cm. The August map in Fig. 9(b) reveals the growing of most of the plants, with doubled heights compared with Fig. 9(a). For some of the fields, the higher maturation level is reached about a month later, as visible in Fig. 9(c). In general, these maps can be used for the agricultural planning, in terms of production volume and outcomes.

Finally, to highlight the TanDEM-X capability in assessing the temporal crop growth, in Fig. 10 the mean height for the 2012 detected fields (flooded in Fig. 8) is shown in black and the standard deviation highlighted in purple. The reference temporal elevation is overplotted. Although a detailed

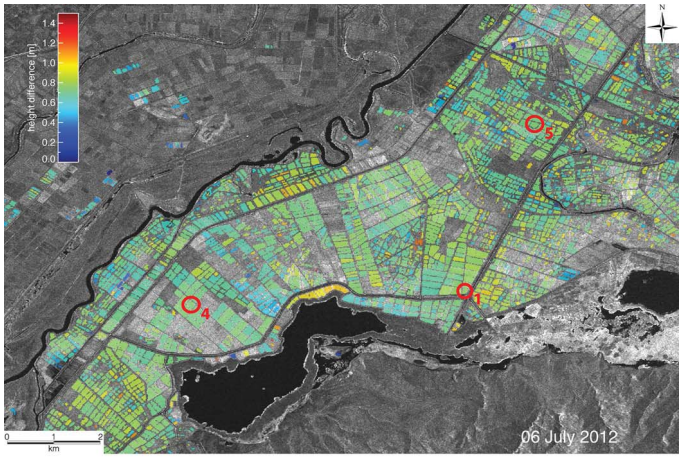

(a)

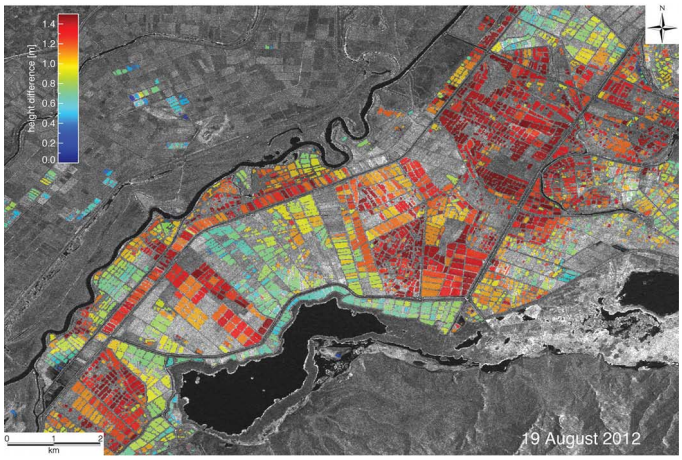

(b)

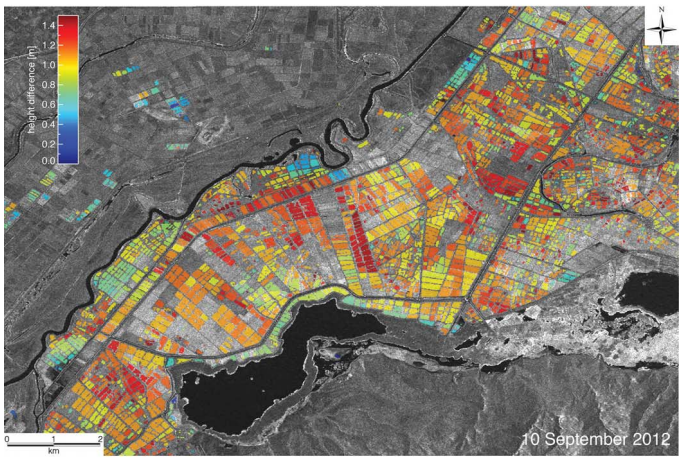

(c)

Fig. 9. Temporal 2012 height change analysis. The difference between the (06.07, 19.08, 10.09) acquisitions and the reference one in 26.11 is shown in the subfigures (a), (b), and (c), respectively. The changes are shown in a field by field basis, for fields having coherence higher than 0.8 for both the analyzed and reference acquisitions. The three fields under analysis in Section III-C are marked in (a). (a) 06.07.2012. (b) 19.08.2012. (c) 10.09.2012.

validation is provided in the next section, the mean trend already shows a good accordance with the reference. The height deviation for the late July acquisitions has to be linked to the different growing periods of the detected fields.

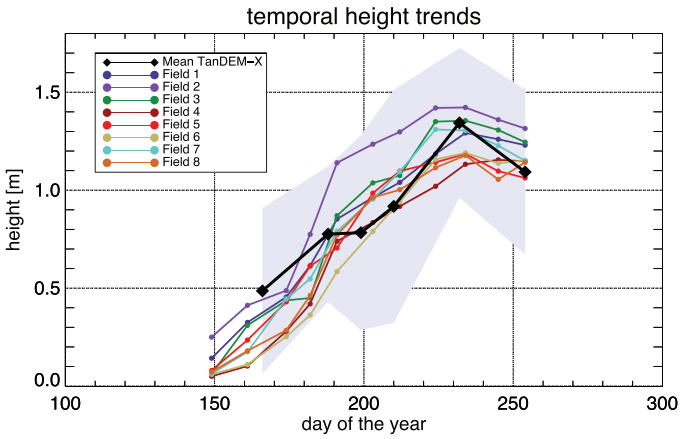

Fig. 10. (Black) Mean temporal TanDEM-X elevation trend for 2012 detected fields and (purple) corresponding standard deviation. The reference fields are overplotted with colors in the legend.

C. Relationship Between Canopy Height and Interferometric Phase

The analysis and the validation of the derived elevation with respect to the field measurements is assessed. Fig. 10 already provides a visual overview of the reference elevation data and the mean TanDEM-X trends. Here, three out of eight fields [marked in Fig. 9(a)] are studied in detail with the analysis depicted in Fig. 11. The results from the other fields are not shown since they perform very similar to the selected three fields.

Before entering in the analysis of the current data set, it is meaningful to predict the expected height for the vegetation in the general electromagnetic framework. It is well known that the interferometric phase is proportional to the height of the scattering phase center. The phase center location depends on the complex interaction of the microwave signal with the imaged surface. For canopies, it is usually below the top of the vegetation as the transmitted signal travels within the medium, penetrating into it [36]. The degree of penetration is characterized by the extinction coefficient, a parameter depending on the system wavelength and the effective dielectric constant of the imaged medium. In particular, extinction coefficient is inversely proportional to the wavelength and directly proportional to the imaginary part of the effective dielectric constant. This corresponds to an increased penetration depth for large wavelengths and for reduced moisture content in the medium. Considering the interferometric analysis, the smaller the extinction, the lower the scattering center. Consequently, the retrieved elevation will be equal or smaller depending on the actual effective dielectric constant of the canopy (and the ground), since in the proposed approach, the canopy height is retrieved with a difference between a plant growing phase and bare soil—the latter from a postharvest data take. In the following, the interpretation based on the current experiment is provided.

An important remark for the comparison between interferometric heights and ground truth data relies on the different years of the two data sources. As underlined beforehand, the sole 2012 TanDEM-X data fully covers the growing stages and is used for validation despite the campaign has been performed in 2013. In practice, validation inaccuracies could take place depending on the seeding date decided by the field owner. For

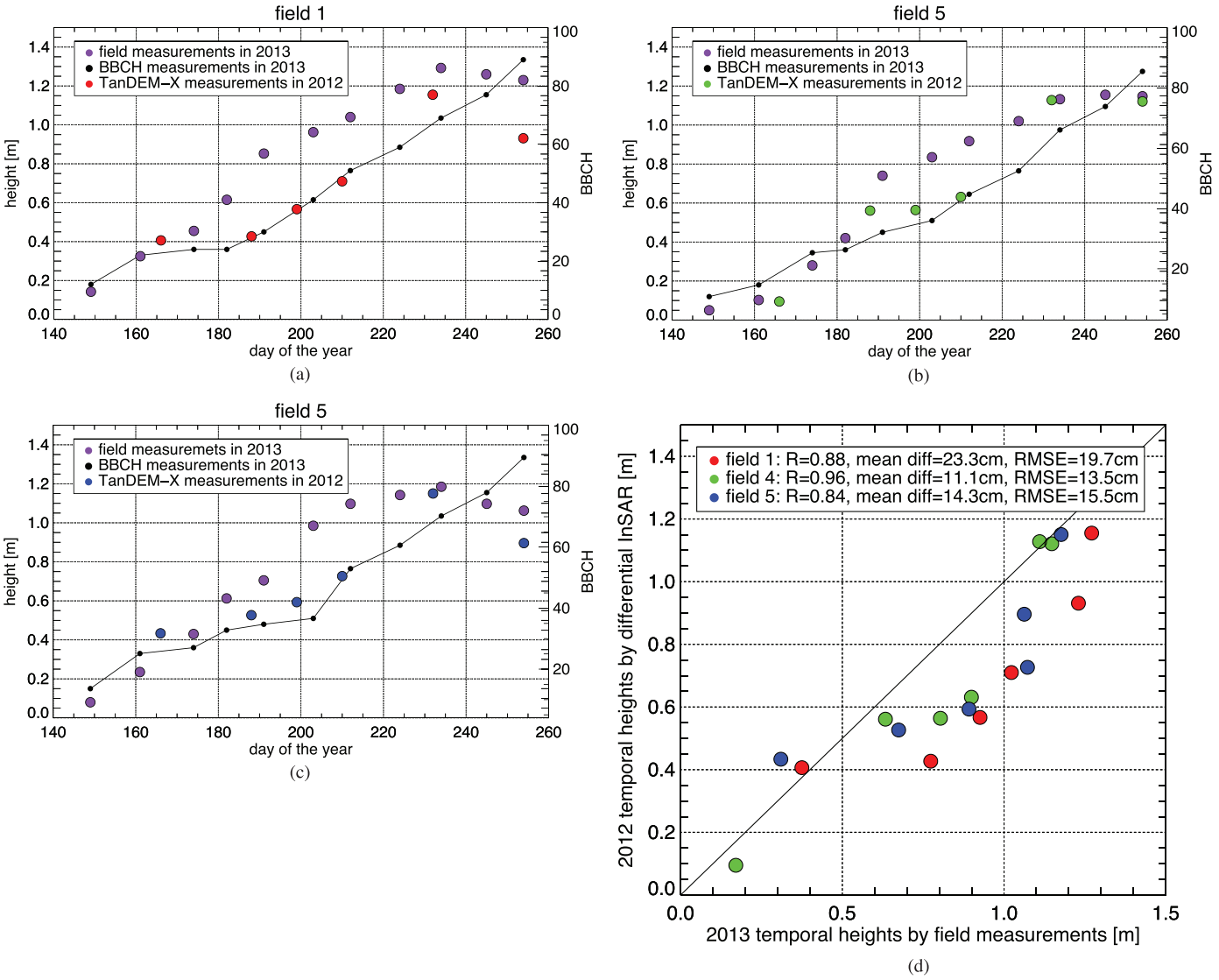

Fig. 11. Comparison of height measurements, superimposed over temporal BBCH scales, between the ground measurements (purple circles) held in 2013 and the one from bistatic interferometry [(a) red, (b) green, (d) blue circles] in 2012 over the three different fields shown in Fig. 9(a). (d) Corresponding scatter plot with quantitative analysis at the top. (a) Field1. (b) Field4. (c) Field5. (d) Scatter plot.

the fields under analysis, the seeding date discrepancy between the two years has been stated to be less than a week, thus strongly limiting this error source. A second inaccuracy source resides in changes in plant moisture variations between the two years, manifesting in a root-mean-square error increase due to the different penetration into the canopy.

The differential-InSAR-based and the field-measurement-based canopy height is shown in Fig. 11 along with the BBCH-scale measurement as reference. The 6 TanDEM-X measurements (June to September 2012) are not well spanned as the 11 ground measurements (June to September 2013) but show common peculiarities. As already reported in the previous section, the elevation trend is well detected by the interferometric measure for the late vegetative phase, reproductive and maturation stages. Instead, the early vegetative phase represented by the May 2012 acquisition yields strongly biased elevation values and is not considered in the following analysis.

The June acquisition corresponds to the central vegetative stage (tillering, Table I). In this phase, plants emerge from water (see the second and the third picture in the second row in Fig. 2). In the SAR resolution different cell phenomena, such as double scattering, water reflection, and surface reflections combine together. The interferometric elevation results underestimated, showing a mean difference with a reference data of 7.7 cm for all the eight fields under study. A singular exception is measured for the field 5 in Fig. 11(c), with an overestimation of about 10 cm, to be attributed to a lower coherence value and a higher phase noise. For this take, double bounces between growing vegetation and standing water should be the dominant part of the radar return. The aforementioned scattering phase center is located at the water elevation for the cardinal effect on corners—in this case, represented by quasi-vertical stems on calm water. However, the small measured height difference suggests the partial presence of the phenomenon due to the use of a short wavelength (3.1 cm) at a relatively high incidence angle (about 37°), yielding a limited penetration of the echo inside the fresh vegetated volume. For the three July measurements, the elevation is largely underestimated with a mean

difference of 26.5 cm. Also, this discrepancy, in the end of the vegetative stage and beginning of the reproduction (booting-heading, Table I), can be explained with the radar wave interaction with the inner part of fresh canopy (see fourth picture in the second row in Fig. 2). The August acquisition instead exhibits a generally good matching, with a mean underestimation of 4.8 cm. Being at the beginning of the maturation stage (fifth picture in the second row in Fig. 2), plants start to densely produce milky grains at their surface, which reflect the signal at X-band. The last considered acquisition, in September, falls at the end of the maturation (seventh picture in the second row in Fig. 2). The grain is dry and mature, with a maximum height slightly smaller than the previous stage. On this date, the interferometric elevations have become underestimated on average, with a mean difference of 16 cm. In principle, at this stage, plant elements are more randomly oriented and drier than in previous ones, hence making more similar the propagation for all polarizations. Nevertheless, a higher phase center is measured for the VV polarization, as shown in Fig. 5(c). The reason relies in the lower backscattering component from the volume, due to its drier condition, hence increasing the relative importance of the double-bounce contribution to the backscattered signal, which is located at the ground surface. Since the double-bounce contributes more to HH than to VV, the phase center is more close to the ground at HH than at VV, and hence, the higher phases at VV than at HH. Following this consideration, a more accurate elevation result can be generated using the VV channel.

For completeness, a best fit analysis in the form of $y = ax + b$ is used for calculating the offset between the two measurements. The corresponding scatter plot is in Fig. 11(d). Due to the growing height trend in time, this plot can be easily interpreted in a similar way of the others in Fig. 11. The generally underestimated InSAR tendency is more noticeable in the center portion of the plot, for the reproductive stage. As the data time sampling is not overlapping, a linear interpolation for the reference at the InSAR locations is performed, with possible errors coming from the nonlinearity of the plant growth attenuated by the fine reference sampling [see Fig. 11(a)–(c)]. The two sources become highly correlated, with a correlation coefficient R equal to 0.88, 0.96, and 0.84 for the three fields under analysis. The mean differences and root-mean-square errors are in the decimetric level. In detail, the mean differences between reference and InSAR result 23.3, 11.1, and 14.3 cm and the root-mean-square error 19.7, 13.5, and 15.5 cm. Although the scattering analysis and the quantitative evaluation performed on this section are useful to understand the overall process, the focus shall be on the centimeter accuracy of the system for this application, and its capability of temporarily tracking the elevation through most of all the growing stages of paddy rice fields.

IV. Conclusion

The outcomes presented in this paper underline that X-band differential bistatic interferometry, which is of great benefit in observing surface height changes, has a great potential in paddy rice elevation mapping and can provide inputs to production estimation in terms of volumetric changes. A test site widely employed for rice production in Turkey has been investigated with 16 dual-pol TanDEM-X acquisitions spanning two years and a dedicated ground campaign. The research demonstrates that for absolute ranging studies at X-band wave polarization is not particularly relevant—only small elevation discrepancies around 8 cm were measured in the dry season. Nevertheless, polarization is of fundamental importance for every other study on physical parameters. For instance, the HH/VV backscatter ratio, an instrument to classify the different phenological stages is presented in the paper as well. The ITP is employed for raw DEM generation and internal calibration with freely available references as SRTM and ICESat. Fields are then individually extracted in the interferometric processor without external references by searching for flooded areas during the rice early vegetative stages. This segmentation allows the elevation tracking on a field-by-field basis, being attractive for separated crop inspections. The absolute approach is then made differential with the objective of volumetric production assessment. Height differences with a digital terrain model, derived in this case from the data set itself employing a postharvest data take, yield the direct validation with ground truth measurements. The increasing temporal elevation trend is well derived by TanDEM-X, with a general underestimation, particularly in the reproductive rice stage due to the wave interaction with lower portions of the plant. The root-mean-square error is contained between a few centimeters and about 20 cm, depending on the actual phenological phase. Although plant elevations are tracked with a good accuracy for most of the plant growing phases, the main limitation relies on the inability to map plant heights at early growing stages due to the lack of coherence in the data. In conclusion, as already seen in other geophysical domains, this specific application strengthens the use of bistatic SAR interferometry for the tracking of dynamical earth elevation changes.

Acknowledgment

The authors would like to thank the anonymous reviewers for their helpful contributions to improve the overall paper quality, as well as the colleagues A. Parizzi and I. Hajnsek for the fruitful scientific discussions on the paper topics and H. Breit, T. Fritz, and F. Rodriguez-Gonzalez for the processing supervision in handling experimental data in an operational and systematic way. The *Rice and Wetlands monitoring in Turkey* project is performed by funding of The Scientific and Technological Research Council of Turkey (TUBITAK Project 113Y446). TanDEM-X SAR data were supplied by German Aerospace Center under the Project XTILAND1476.

References

[1] P. Lancashire *et al.*, "A uniform decimal code for growth stages of crops and weeds," *Ann. Appl. Biol.*, vol. 119, no. 3, pp. 561–601, Dec. 1991.

[2] S. Yun *et al.*, "Rice monitoring and production estimation using multitemporal RADARSAT," *Remote Sens. Environ.*, vol. 76, no. 3, pp. 310–325, Jun. 2001.

[3] M. Chakraborty, K. R. Manjunath, S. Panigrahy, N. Kundu, and J. S. Parihar, "Rice crop parameter retrieval using multi-temporal, multi-incidence angle RADARSAT SAR data," *ISPRS J. Photogramm. Remote Sens.*, vol. 59, no. 5, pp. 310–322, Aug. 2005.

[4] P. Patel, H. S. Srivastava, S. Panigrahy, and J. S. Parihar, "Comparative evaluation of the sensitivity of multi-polarized multi-frequency SAR backscatter to plant density," *Int. J. Remote Sens.*, vol. 27, no. 2, pp. 293–305, Jan. 2006.
[5] C. Wang *et al.*, "Characterizing L-band scattering of paddy rice in southeast China with radiative transfer model and multitemporal ALOS/PALSAR imagery," *IEEE Trans. Geosci. Remote Sens.*, vol. 47, no. 4, pp. 988–998, Apr. 2009.
[6] A. Bouvet, T. Le Toan, and N. Lam-Dao, "Monitoring of the rice cropping system in the Mekong delta using ENVISAT/ASAR dual polarization data," *IEEE Trans. Geosci. Remote Sens.*, vol. 47, no. 2, pp. 517–526, Feb. 2009.
[7] E. Erten, A. Reigber, L. Ferro-Famil, and O. Hellwich, "A new coherent similarity measure for temporal multi-channel scene characterization," *IEEE Trans. Geosci. Remote Sens.*, vol. 50, no. 7, pp. 2839–2851, Jul. 2011.
[8] H. S. Srivastava, P. Patel, Y. Sharma, and R. R. Navalgund, "Multi-frequency and multi-polarized SAR response to thin vegetation and scattered trees," *Current Sci.*, vol. 97, no. 3, pp. 425–429, Aug. 2009.
[9] I. Choudhury, M. Chakraborty, S. C. Santra, and J. S. Parihar, "Methodology to classify rice cultural types based on water regimes using multitemporal RADARSAT-1 data," *Int. J. Remote Sens.*, vol. 33, no. 13, pp. 4135–4160, Jul. 2012.
[10] Y. Inoue, E. Sakaiya, and C. Wang, "Capability of C-band backscattering coefficients from high-resolution satellite SAR sensors to assess biophysical variables in paddy rice," *Remote Sens. Environ.*, vol. 140, pp. 257–266, Jan. 2014.
[11] S. L. Durden, L. A. Morrissey, and G. P. Livingston, "Microwave backscatter and attenuation dependence on leaf area index for flooded rice fields," *IEEE Trans. Geosci. Remote Sens.*, vol. 33, no. 3, pp. 807–810, May 1995.
[12] J. M. Lopez-Sanchez, J. D. Ballester-Berman, V. D. Navarro-Sanchez, and F. Vicente-Guijalba, "Experimental validation of the interferometric coherence formulation in single-transmit mode," in *Proc. IEEE IGARSS*, 2012, pp. 3114–3117.
[13] J. M. Lopez-Sanchez and J. D. Ballester-Berman, "Potentials of polarimetric SAR interferometry for agriculture monitoring," *Radio Sci.*, vol. 44, no. 2, pp. RS2010-1–RS2010-20, Apr. 2009.
[14] J. M. Lopez-Sanchez, J. D. Ballester-Berman, and I. Hajnsek, "First results of rice monitoring practices in Spain by means of time series of TerraSAR-X dual-pol images," *IEEE J. Sel. Topics Appl. Earth Observ. Remote Sens.*, vol. 4, no. 2, pp. 412–422, Jun. 2011.
[15] J. M. Lopez-Sanchez, I. Hajnsek, and J. D. Ballester-Berman, "First demonstration of agriculture height retrieval with PolInSAR airborne data," *IEEE Geosci. Remote Sens. Lett.*, vol. 9, no. 2, pp. 242–246, Mar. 2012.
[16] J. M. Lopez-Sanchez, F. Vicente-Guijalba, J. D. Ballester-Berman, and S. R. Cloude, "Polarimetric response of rice fields at C-band: Analysis and phenology retrieval," *IEEE Trans. Geosci. Remote Sens.*, vol. 52, no. 5, pp. 2977–2993, May 2014.
[17] J. M. Lopez-Sanchez, S. R. Cloude, and J. D. Ballester-Berman, "Rice phenology monitoring by means of SAR polarimetry at X-band," *IEEE Trans. Geosci. Remote Sens.*, vol. 50, no. 7, pp. 2695–2709, Jul. 2012.
[18] U. Wegmüller and C. Werner, "Retrieval of vegetation parameters with SAR interferometry," *IEEE Trans. Geosci. Remote Sens.*, vol. 35, no. 1, pp. 18–24, Jan. 1997.
[19] M. E. Engdahl, M. Borgeaud, and M. Rast, "The use of ERS 1/2 TanDEM interferometric coherence in the estimation of agricultural crop heights," *IEEE Trans. Geosci. Remote Sens.*, vol. 39, no. 8, pp. 1799–1806, Aug. 2001.
[20] H. S. Srivastava, P. Patel, and R. R. Navalgund, "Application potentials of synthetic aperture radar interferometry for land-cover mapping and crop-height estimation," *Current Sci.*, vol. 91, no. 6, pp. 783–788, Sep. 2006.
[21] F. De Zan, A. Parizzi, P. Prats-Iraola, and P. López-Dekker, "A SAR interferometric model for soil moisture," *IEEE Trans. Geosci. Remote Sens.*, vol. 52, no. 1, pp. 418–425, Jan. 2014.
[22] E. Erten, "Glacier velocity estimation by means of a polarimetric similarity measure," *IEEE Trans. Geosci. Remote Sens.*, vol. 51, no. 6, pp. 3319–3327, Jun. 2013.
[23] E. Erten, A. Reigber, and O. Hellwich, "Generation of three-dimensional deformation maps from InSAR data using spectral diversity techniques," *ISPRS J. Photogramm. Remote Sens.*, vol. 65, no. 4, pp. 388–394, Jul. 2010.
[24] C. Rossi and S. Gernhardt, "Urban DEM generation, analysis and enhancements using TanDEM-X," *ISPRS J. Photogramm. Remote Sens.*, vol. 85, pp. 120–131, Nov. 2013.
[25] G. Krieger *et al.*, "TanDEM-X: A satellite formation for high-resolution SAR interferometry," *IEEE Trans. Geosci. Remote Sens.*, vol. 45, no. 11, pp. 3317–3341, Nov. 2007.
[26] J. M. Lopez-Sanchez, F. Vicente-Guijalba, and J. D. Ballester-Berman, "The problem of SNR in PolInSAR observations with TanDEM-X over rice fields," presented at the 4th TanDEM-X Science Team Meeting, Wessling, Germany, Jun. 12–14, 2013, DLR Oberpfaffenhofen, DLR Oberpfaffenhofen.
[27] D. Just and R. Bamler, "Phase statistics of interferograms with applications to synthetic aperture radar," *Appl. Opt.*, vol. 33, no. 20, pp. 4361–4368, Jul. 1994.
[28] C. Rossi, F. R. Gonzales, T. Fritz, N. Yague-Martinez, and M. Eineder, "TanDEM-X calibrated raw DEM generation," *ISPRS J. Photogramm. Remote Sens.*, vol. 73, pp. 12–20, Sep. 2012.
[29] H. Breit *et al.*, "TerraSAR-X SAR processing and products," *IEEE Trans. Geosci. Remote Sens.*, vol. 48, no. 2, pp. 727–740, Feb. 2010.
[30] F. M. Henderson and A. J. Lewis, *Principles and Applications in Imaging Radar*. New York, NY, USA: Wiley, 1998.
[31] R. Bamler and P. Hartl, "Synthetic aperture radar interferometry," *Inverse Probl.*, vol. 14, no. 4, pp. R1–R54, Aug. 1998.
[32] A. Wendleder *et al.*, "TanDEM-X water indication mask: Generation and first evaluation results," *IEEE J. Sel. Topics Appl. Earth Observ. Remote Sens.*, vol. 6, no. 1, pp. 171–179, Feb. 2013.
[33] G. Nico, M. Pappalepore, G. Pasquariello, A. Refice, and S. Samarelli, "Comparison of SAR amplitude vs. coherence flood detection methods-a GIS application," *Int. J. Remote Sens.*, vol. 21, no. 8, pp. 1619–1631, Jan. 2000.
[34] H. S. Srivastava *et al.*, "Potential applications of multi-parameteric Synthetic Aperture Radar (SAR) data in wetland inventory: A case study of Keoladeo National Park (A world heritage and Ramsar site), Bharatpur, India," in *Proc. Taal, 12th World Lake Conf.*, 2008, pp. 1862–1879.
[35] R. Touzi, A. Lopes, J. Bruniquel, and P. W. Vachon, "Coherence estimation for SAR imagery," *IEEE Trans. Geosci. Remote Sens.*, vol. 37, no. 1, pp. 135–149, Jan. 1999.
[36] K. Sarabandi and Y. C. Lin, "Simulation of interferometric SAR response for characterizing the scattering phase center statistics of forest canopies," *IEEE Trans. Geosci. Remote Sens.*, vol. 38, no. 1, pp. 115–125, Jan. 2000.

Cristian Rossi received the Laurea Magistrale (M.Sc.) degree in telecommunication engineering from Politecnico di Milano, Milan, Italy, in 2006. From 2006 to 2008, he was Project Engineer with Aresys s.r.l. (a Politecnico di Milano spin-off company). Since 2008, he has been with the SAR Signal Processing Department, Earth Observation Center, German Aerospace Center (DLR), Oberpfaffenhofen, Germany, where he works on the development of the Integrated TanDEM-X Processor and on novel interferometry algorithms for SAR missions. His research interests focus on urban remote sensing, multisource data fusion, digital elevation models, and Doppler shift estimation for ocean currents.

Esra Erten received the B.S. degree in geodesy and photogrammetry engineering and the M.S.E.E. degree in satellite communication and remote sensing from Istanbul Technical University (ITU), Istanbul, Turkey, in 2003 and 2005, respectively. She received the Ph.D. degree in computer vision and remote sensing from the Berlin University of Technology, Berlin, Germany, in 2010.

From April 2008 to June 2010, she was with the High-Frequency Institute, German Aerospace Center (DLR), Oberpfaffenhofen, Germany, where she worked on information theory for multichannel synthetic aperture radar (SAR) images. From 2010 to 2012, she was with the Chair of Earth Observation and Remote Sensing, Institute of Environmental Engineering, ETH Zurich, Zurich, Switzerland, where she worked on applied radar remote sensing for environmental parameter estimation. Currently, she is an Associate Professor with the Department of Geomatics Engineering, Faculty of Civil Engineering, ITU. Her research interests include information extraction and image understanding from SAR and optical images; in particular, information theory, multivariate statistics, polarimetry, interferometry, and hyperspectral imaging.

A.3. Polarization Impact in TanDEM-X Data Over Vertical-Oriented Vegetation: The Paddy-Rice Case Study

Erten, E., Rossi, C., Yuzugullu, O., **Polarization Impact in TanDEM-X Data Over Vertical-Oriented Vegetation: The Paddy-Rice Case Study**, *IEEE Geoscience and Remote Sensing Letters*, 12(7), 1501-1505, 2015.

Polarization Impact in TanDEM-X Data Over Vertical-Oriented Vegetation: The Paddy-Rice Case Study

Esra Erten, Cristian Rossi, and Onur Yüzügüllü

***Abstract*—It has been recently shown that the TanDEM-X mission is capable of tracking the plant growth of rice paddies. The precision of the elevation measure depends on the physical interaction between the synthetic aperture radar (SAR) signal and the canopy. In this letter, this interaction is studied by considering the signal polarization. In particular, the vertical and horizontal wave polarizations are compared, and their performance in the temporal mapping of the crop height is analyzed. The temporal elevation difference analysis shows a monotonically increasing trend within the reproductive stage of the canopy, with maximum height discrepancies between polarizations of about 9 cm. From an operational point of view of InSAR-based vegetation height measurements, this letter demonstrates that the oriented structure of the canopy shall be considered not only in polarimetric InSAR studies but also in the interpretation of bistatic spaceborne interferometric elevation models.**

***Index Terms*—Agriculture, copolar phase difference (CPD), polarimetry, synthetic aperture radar (SAR), TanDEM-X, X-Band.**

I. Introduction

THE canopy height is a primary structural characteristic for phenological stage studies, carbon storage, and biomass calculations. Because of its importance, canopy height estimation has been studied many times by making use of remote sensing technologies, particularly synthetic aperture radar (SAR). Related works can be gathered into two groups.

First, a considerable amount of research has been done by using radiative transfer theory (RTV). RTV is applied to calculate the radar backscattering that depends on the geometric and physical features of the canopy [1]–[3]. These studies indicate that backscattering is based on the canopy's physical attributes such as the leaf area index, the plant height, the stem width, the number of leaves, the leaf angle, and the leaf size. Due to the complicated electromagnetic interaction between radar waves and the vegetation canopy, it is not easy to develop the direct relationship of the backscattering with biophysical parameters. Thus, for estimating the canopy's physical parameters from SAR backscattering values, Monte Carlo simulations are required [2].

Second, interferometric phase information, which is a direct function of the canopy height, i.e., not an indirect function as backscattering information, provides an additional instrument to canopy studies with the sole cost of two SAR images [4], [5]. From an agricultural application's point of view, the interferometric phase for the operational canopy height calculation requires a particular system configuration. Since the plant is temporally growing, two acquisitions at different dates will provide very low coherence and no stable phase information. To overcome this limit, the acquisitions must be commanded at the same time. Among them, the TanDEM-X is the first spaceborne mission designed to globally acquire data in order to generate digital elevation models (DEMs) at High-Resolution Terrain Information 3 (HRTI-3) standards [6], [7].

An analysis of TanDEM-X capabilities in assessing canopy heights was performed in [8]. This study shows that TanDEM-X images have a great potential in mapping the canopy height through almost the entire plant growth. A relevant feature is the high resolution of the sensors, which brings the assessment on the field level. However, the strong variability in the location of the phase center through the canopy causes underestimations for the estimated height. This depends on the phenology of the crops and the system parameters (polarization, bandwidth, etc.). The objective of this study is to deeply analyze the capabilities and limitations of TanDEM-X monitoring by considering the wave polarization. The work in [8] showed the relationship between the crop height and the differential interferometric phase for paddy rice using the HH polarimetric channel. In this letter, the VV channel is also considered, and a comprehensive comparison between the two polarizations is presented. Observed height differences are theoretically related to the path of the wave through the canopy, which has to be considered when plants are in the reproductive stage. Recent work [9] has also studied the polarization-dependent height differences in TanDEM-X acquisitions for the assessment of snow depth.

This letter is organized as follows. In Section II, the study area and the data set are introduced. Additionally, the phenology of the crops on the acquisition dates is briefly described by making use of polarimetric features. Section III analyzes the estimated crop heights for both polarizations. Section IV concludes this letter with the main outcomes.

Manuscript received December 16, 2014; revised February 18, 2015; accepted March 3, 2015. Date of publication March 19, 2015; date of current version June 5, 2015. This work was supported by the Scientific and Technological Research Council of Turkey (TUBITAK) under Project 113Y446.

E. Erten is with the Department of Geomatics Engineering, Istanbul Technical University, 34469 Istanbul, Turkey.

C. Rossi is with the Remote Sensing Technology Institute, German Aerospace Center, 82234 Wessling, Germany.

O. Yüzügüllü is with the Institute of Environmental Engineering, Swiss Federal Institute of Technology (ETH) Zurich, 8093 Zurich, Switzerland.

Color versions of one or more of the figures in this paper are available online at http://ieeexplore.ieee.org.

Digital Object Identifier 10.1109/LGRS.2015.2410339

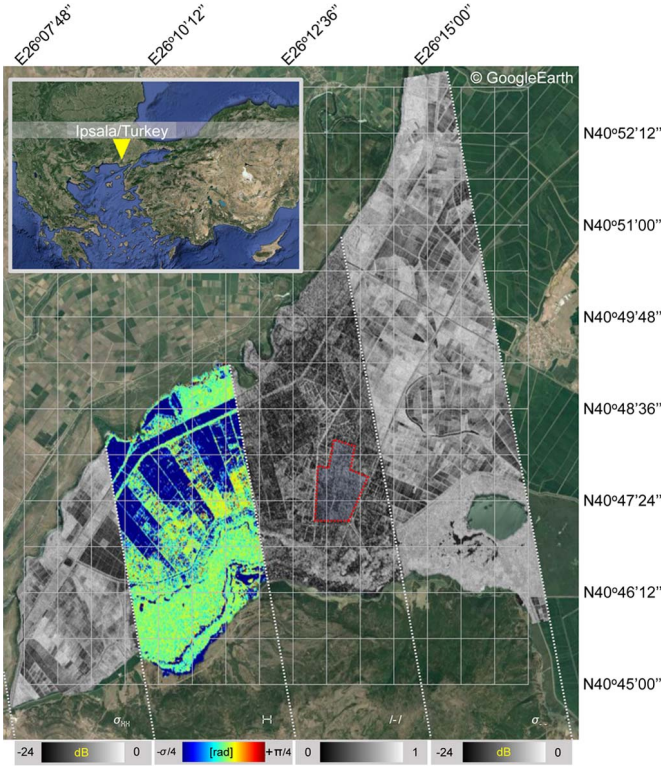

Fig. 1. Agricultural study area in Ipsala, Turkey. The copolar images acquired on June 21, 2014 in the HH and VV polarizations, and their coherence and phase difference measurements are placed over the Google Earth image. The selected fields for the study are highlighted by the red dashed line.

II. Study Area and Complex Image Analysis

The study area is a unique wetland environment consisting of lakes, rivers, and agricultural rice fields, which are visually detectable on the Google Earth image given in Fig. 1. In this region, which is located in Ipsala, Turkey, the agricultural practices of paddies are owner dependent, i.e., with time shifts between seeding days among neighbor agricultural fields. Nevertheless, fields are generally flooded and seeded during late May and are harvested in early October. In the study area, the sowing method is direct seeding by broadcasting, implying random seeding instead of regular straight-row seeding. To give an overview of a spatial distribution and heterogeneity in the sowing procedure of the agricultural fields, the backscattering images acquired on June 21, 2014 in the HH and VV polarizations, and their coherence and phase difference measurements are placed over the Google Earth image in Fig. 1. Differences in polarimetric observations among the agricultural fields can be detected.

Interferometric SAR (InSAR)-based vegetation height measurements were analyzed using a stack of nine HH and VV dual-polarization TanDEM-X images acquired through the cultivation period of 2012, with an incidence angle of 37°. Some relevant properties of the images are given in Fig. 2. For each observation point, the vertical error bar indicates the height of ambiguity that is inversely proportional to the baseline, whereas the horizontal error bar shows the unreliability of the HH interferometric observations with the equality $1-|\gamma|$, where $|\gamma|$ represents the mean coherence value. These coherence values are obtained by averaging the estimates over the 50 neighbor

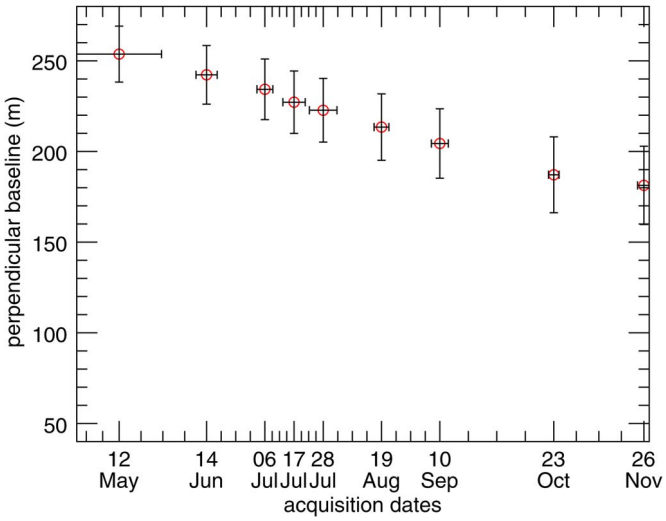

Fig. 2. Perpendicular baselines of TanDEM-X and TerraSAR-X acquisitions with respect to the acquisition dates. For each acquisition date, the vertical error bar indicates the height of ambiguity, whereas the horizontal error bar shows the unreliability of the HH interferometric acquisitions due to the coherence values, i.e., the smaller $1-|\gamma|$ is, the better accuracy is achieved.

agricultural fields highlighted in Fig. 1, which are analyzed in the following sections.

Once coherence maps, interferograms, and DEMs have been generated with the interferometric TanDEM-X processor [7], the next step is to identify the phenological stages of the canopy during the acquisitions. Here, it is necessary to remind that this letter contains a concise presentation of the height measurement differences based on phenological stages and polarimetric acquisitions. It is not intended to give an in-depth description of the bistatic interferometric processing but merely the characterization of elevation measurements considering the polarization (see [7] and [8] for detailed information about the process of a bistatic interferometric configuration).

To identify the phenological stages of the fields, polarimetric features such as *copolar backscattering values and their ratio, the copolar phase difference (CPD)*, and *entropy* are analyzed among the 50 selected agricultural fields. First, four polarimetric features, which are obtained from the polarimetric acquisition vector $k=[S_{\mathrm{HH}}\, S_{\mathrm{VV}}]$ for the whole canopy, are expressed by the following:

$$\begin{aligned}
\sigma_{\mathrm{HH}} &= 10\log_{10}\left\langle \left| S_{\mathrm{HH}} S_{\mathrm{HH}}^{*} \right| \right\rangle \quad [\mathrm{dB}] \\
\sigma_{\mathrm{VV}} &= 10\log_{10}\left\langle \left| S_{\mathrm{VV}} S_{\mathrm{VV}}^{*} \right| \right\rangle \quad [\mathrm{dB}] \\
\varphi &= \tan^{-1}\left(\frac{\left\langle S_{\mathrm{HH}} S_{\mathrm{VV}}^{*} \right\rangle}{\sqrt{\left\langle |S_{\mathrm{HH}}|^{2} \right\rangle \left\langle |S_{\mathrm{VV}}|^{2} \right\rangle}} \right) \quad [\mathrm{rad}] \\
R_{\mathrm{HH,VV}} &= 10\log_{10}\left(\frac{\left\langle |S_{\mathrm{HH}}|^{2} \right\rangle}{\left\langle |S_{\mathrm{VV}}|^{2} \right\rangle} \right) \quad [\mathrm{dB}]
\end{aligned} \tag{1}$$

where σ_{HH} and σ_{VV} are the backscattering coefficients for the HH and VV channels, respectively, φ is the CPD, and $R_{\mathrm{HH,VV}}$ is the backscattering ratio. Fig. 3 shows the plots of the polarimetric features for all of the monitored fields, in which each field is shown by a different color. To tackle the heterogeneity inside the fields, K-means clustering was applied before assigning a value for each field, as detailed in [10].

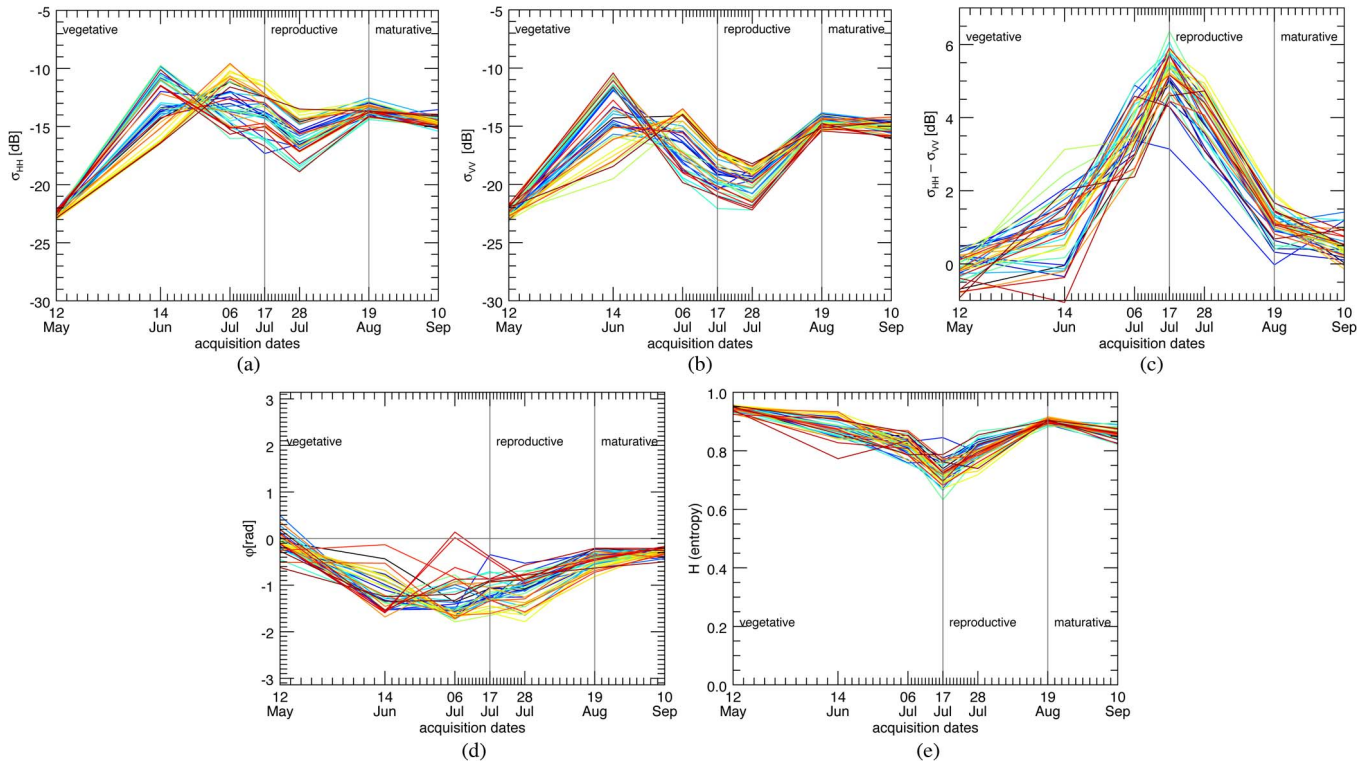

Fig. 3. Observed polarimetric features such as (a) σ_{HH}, (b) σ_{VV}, (c) $\sigma_{\mathrm{HH}}-\sigma_{\mathrm{VV}}$, (d) CPD, and (e) entropy through the entire cultivation period for 50 randomly selected neighbor paddy-rice fields. Each agricultural field appears in a different color. The plotted transition dates are estimated from time-series analysis.

The temporal behavior of the backscattering intensity, i.e., *sigma nought*, during the cultivation period is shown with the HH and VV polarizations in Fig. 3(a) and (b), respectively. Considering the low values of σ_{HH} and σ_{VV}, we can infer that the fields are flooded in the beginning of May. Then, when the paddy elevation starts to be over the water level, the total backscattering coefficient increases, indicating the existence of unfolded leaves and the beginning of leaf development. The overall backscatter level is particularly high at this stage due to the strong presence of signal double bounces. A loss is then perceived by the cause of tillering, followed by panicle initiation. Here, the appearance of two distinct peaks corresponds to different grow rates for the chosen fields as a result of different agricultural practices (see also [8]). Whenever the canopy becomes tall enough and the panicle initiation starts, a decrease in the backscattering is observed for both channels due to higher absorption. It is to be noted that the VV channel [see Fig. 3(b)] exhibits a higher loss than the HH channel [see Fig. 3(a)], with the decay reaching almost the flooded field level of early May. The different extinction for the two polarizations in the presence of thin, fresh, and vertical structures is well noticeable here. Later on, the backscattering coefficients increase until the end of the reproductive stage (August 19). No evident discrepancy between the polarizations is any more visible.

The ratio between the two backscattering coefficients is plotted in Fig. 3(c). By considering this temporal aspect and the previous works in [1], [11], and [12], it is possible to assign the three main phenological stages of the canopy on the acquisition dates (*vegetation, reproductive, maturation*), as highlighted over the figures. In the study area, the reproductive stage started on July 17 for most of the fields, and the transition from the reproductive stage to the maturation stage began in late August. The assigned transition dates from the vegetative stage to the reproductive stage, which is one of the most critical events in a plant life, can be also proved by taking into account the temporal trend of the CPDs of the TanDEM-X acquisitions shown in Fig. 3(d). In the presence of standing water, straight after transplanting, the measured copolar phase φ is around zero. This little depolarization implies, by definition, a smooth surface. The development of the standing erect canopy over the water surface then yields double-bounce scattering. This phenomenon causes a negative CPD. As the plant development continues further, the scattering becomes more homogeneous, and the vertical component diminishes. This yields a phase difference increase that is measured until the beginning of the maturation stage, which is around August 19 and the following harvesting. Due to the increased field homogeneity, the CPD variance gets lower as well. It may be noticed here that the differences in the seeding practice among the fields have resulted in different growth rates, which cause a high variance in the CPD values through the fields in the vegetative and reproductive stages. However, as the canopy becomes more mature, i.e., before harvesting, the path difference among the fields converges to null, and all the other polarimetric features of the agricultural fields turn out to be homogeneous.

Finally, the polarimetric decomposition proposed in [13] has been applied to evaluate the entropy parameter. This analysis provides information about temporal existing scattering mechanisms (a maximum of two) through the cultivation. The analysis of entropy given in Fig. 3(e) supports the assigned phenological step dates by the polarimetric features. Entropy, which characterizes the degree of randomness of the scattering, makes its minimum on July 17, when the double bounce dominates other scattering types. Later, as the paddy continues to grow,

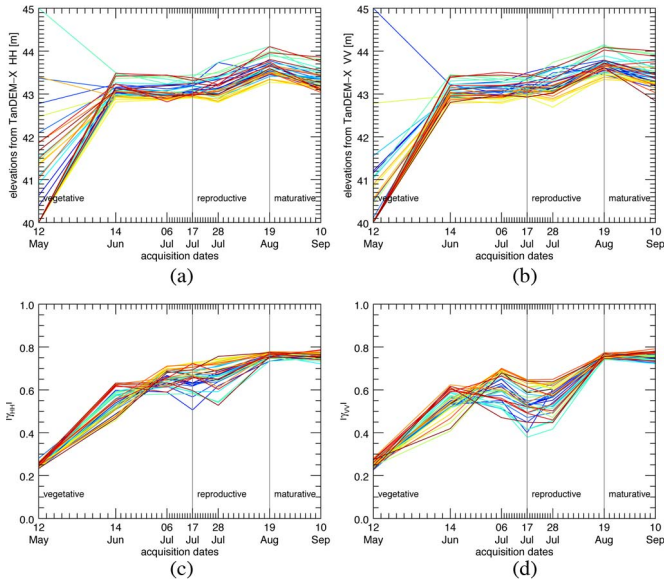

Fig. 4. Inventory of topographic surface changes. The value of multitemporal elevation measurements from the TanDEM-X HH and VV channels are shown in (a) and (b), respectively, and their reliability information is based on their coherence values shown in (c) and (d), respectively. The plotted transition dates are estimated from the time-series analysis.

the increase in randomness is observed again due to the higher intensiveness of the canopy. Here, it should be noticed that the high entropy at the beginning of the time series is due to the random process of the system noise, not to the presence of more than one dominant scattering. The flooded fields in May exhibit backscatter values that are very close to the system's noise-equivalent sigma zero, which is about -23 dB for the beam under study.

III. DEM Analysis

The features shown in the previous section demonstrate the possibility of estimating the phenological stage of the fields from copolarimetric TanDEM-X signatures where no ground measurements exist. In order to analyze the potential of height measurements using copolarimetric TanDEM-X data, these features will be useful in characterizing the height differences obtained from the HH- and VV-polarized interferograms. The analysis in the previous section has been performed for the monostatic channel of the TanDEM-X acquisition; in this section, the bistatic channel is used to generate the canopy elevation model.

The bistatic HH-polarized TanDEM-X data have been shown to be capable of tracking elevation changes at the decimetric level [8]. This study is expanded to explore the suitability of the VV polarization. To conduct this study, in Fig. 4, the elevation estimations are analyzed for the same fields shown in Fig. 3. Both the HH-polarized [see Fig. 4(a)] and VV-polarized [see Fig. 4(b)] TanDEM-X data give very similar temporal trends, with a maximum slope gradient in the reproductive stage. Although the height gradients of the agricultural fields coincide with the phenological stages of the canopy, the mean elevations on the acquisition on May 12 are found to be random for both polarizations. This result agrees with the mean coherence value ($\sim$0.25) and the mean sigma-nought value (~ -23 dB) on that acquisition day, indicating flooded fields.

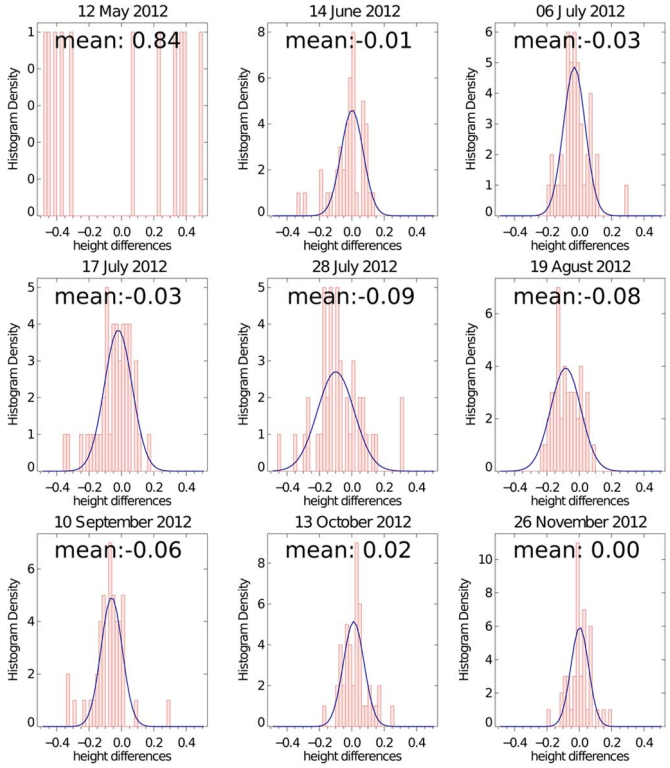

Fig. 5. Temporal histograms of the difference between the elevation measurements from the HH- and VV-polarized TanDEM-X images among the neighbor paddy fields. A Gaussian fit (blue line) is superimposed.

The sensitivity of the TanDEM-X acquisitions is assessed through the visual and qualitative comparison of the temporal CPD [see Fig. 3(d)] and the interferometric coherence values of the TanDEM-X measurements at the HH and VV acquisitions (see Fig. 4(c) and (d), respectively).

An evident visual divergence is for the late vegetative stage and the early reproductive stage (around July 17). Here, the HH elevation accuracy is larger than the VV elevation accuracy, as the coherence values are higher. The standard deviation is also smaller for the horizontal polarization. Thus, when considering assessing the crop elevation with bistatic data for the central growing stage, it seems meaningful to privilege the HH channel. By inspecting the CPD and considering the analysis in the previous section, it results in the VV channel yielding higher phase centers and therefore better modeling the top of the canopy. A choice is then difficult; a quantitative evaluation is provided in the following. On the contrary, the two other stages perform similarly, i.e., the early vegetative stage has very low coherence and poor elevation estimates for both channels, whereas the late reproductive and maturation stages perform well.

To make the polarization dissimilarity, i.e., distributing from the end of the vegetative stage to the beginning of the maturation stage, clearer, the probability density functions (pdfs) in terms of the histogram of the elevation differences are temporally plotted in Fig. 5. The histograms of the elevation differences from the HH- and VV-polarized acquisitions were established among the selected fields for each acquisition day. On one hand, for the flooded fields, the copolar elevation difference measurement is uniformly distributed because of the unreliable phase information. On the other hand, for the other acquisitions, the elevation differences are closer to the Gaussian

TABLE I
SAMPLE AND GAUSSIAN-FIT STATISTICS OF THE DIFFERENCE BETWEEN THE HH AND VV ELEVATIONS

Dates	sample statistics		Gaussian-fit statistics	
	mean (m)	std (m)	center (m)	std (m)
12 May	0.84	2.04	-	-
14 Jun.	-0.01	0.23	0.00	0.07
06 Jul.	-0.03	0.08	-0.03	0.07
17 Jul.	-0.03	0.11	-0.02	0.09
28 Jul.	-0.09	0.19	-0.10	0.11
19 Agu.	-0.08	0.07	-0.08	0.09
10 Sep.	-0.05	0.10	-0.04	0.07
23 Oct.	0.02	0.07	0.01	0.05
26 Nov.	0.00	0.06	0.00	0.04

distribution, with the mean and the variance strongly dependent on the radar parameters and the canopy properties.

It is interesting to see the effect of the extinction coefficient in the vertical channel through almost all the phenological stages. The temporal mean difference measurements monotonically increase until the acquisition date of July 28. After, they monotonically decrease until the paddy rice starts to collapse and lose its height and, hence, the vertical structure. Similar results are reported in [14] for another vertical-structured canopy maize with indoor experiments. For the pdf obtained from the agricultural fields acquired on November 26 when the fields were already harvested, there is almost ($\sim$ the millimeter level) no difference between the polarimetric TanDEM-X measurements.

In this pdf-based analysis, the estimate of the sample mean elevation differences is not the only interest. A consistency analysis among the neighbor paddy fields is also important, and it is given in Table I. The sample standard deviations for each acquisition date show the variability of the outcomes for each phenological stage. The values are nearly stable through the maturation stage, but in the vegetative and reproductive stages, they are relatively high also considering the differences in the growing rate. As reported in Table I, a Gaussian-fit analysis is superimposed for each acquisition date histogram. Temporal Gaussian standard deviations are in accordance with the signature of the sample standard deviations. The horizontal polarization yields DEMs with lower crop heights, i.e., up to about 10-cm differences. The vertical polarization yields higher elevation models, i.e., close to the true top canopy elevation [8]. As aforementioned, the horizontal polarization provides, on average, more accurate elevation results for the central growing stage. Stepping back to the polarization choice, if the objective is the determination of the crop elevation, the local field coherence can be the final trigger.

IV. CONCLUSION

The analysis showed in this letter has been intended to provide knowledge about the use of dual-polarization TanDEM-X data for paddy-rice monitoring, which is in extension to the work in [8], by completely considering the wave polarization. Our results clearly indicate that, according to the phenological stage of the canopy, there are differences between the height measurements of the TanDEM-X HH and VV channels. These differences in the height of the scattering phase center depend on the different attenuations of the polarized channels, reaching 10 cm in the reproductive stage. This discrepancy has to be considered in the operational applications in which the canopy height is used as a state variable, e.g., for indirect yield estimation and biomass calculation methods. In these works, the plant height factor is served as a state variable to specify the morphological characterization, and its accuracy in the centimeter level is important, particularly for large-scale agricultural fields.

Although the entire analysis is only given for paddy rice, the results can be generalized for the canopies having a vertical structure and a similar dielectric constant behavior as paddy rice. Typical polarimetric features as the backscatter ratio, the CPD, entropy, etc., are also studied in the test case and demonstrated well in accordance with previous studies.

ACKNOWLEDGMENT

The authors would like to thank the German Aerospace Center (DLR) for providing the TanDEM-X data set.

REFERENCES

[1] A. Bouvet, T. Le Toan, and N. Lam-Dao, "Monitoring of the rice cropping system in the Mekong delta using ENVISAT/ASAR dual polarization data," *IEEE Trans. Geosci. Remote Sens.*, vol. 47, no. 2, pp. 517–526, Feb. 2009.

[2] Y. Inoue, E. Sakaiya, and C. Wang, "Capability of C-band backscattering coefficients from high-resolution satellite SAR sensors to assess biophysical variables in paddy rice," *Remote Sens. Environ.*, vol. 140, pp. 257–266, Jan. 2014.

[3] V. Kalogirou, P. Ferrazzoli, A. Deulla Vecchia, and M. Foumelis, "On the SAR backscatter of burned forests: A model-based study in C-band, over burned pine canopies," *IEEE Trans. Geosci. Remote Sens.*, vol. 52, no. 10, pp. 6205–6215, Oct. 2014.

[4] M. E. Engdahl, M. Borgeaud, and M. Rast, "The use of ERS 1/2 Tandem interferometric coherence in the estimation of agricultural crop heights," *IEEE Trans. Geosci. Remote Sens.*, vol. 39, no. 8, pp. 1799–1806, Aug. 2001.

[5] X. Blaes and P. Defourny, "Retrieving crop parameters based on Tandem ERS 1/2 interferometric coherence images," *Remote Sens. Environ.*, vol. 88, no. 4, pp. 374–385, Dec. 2003.

[6] G. Krieger *et al.*, "TanDEM-X: A satellite formation for high-resolution SAR interferometry," *IEEE Trans. Geosci. Remote Sens.*, vol. 45, no. 11, pp. 3317–3341, Nov. 2007.

[7] C. Rossi, F. R. Gonzales, T. Fritz, N. Yague-Martinez, and M. Eineder, "TanDEM-X calibrated raw DEM generation," *ISPRS J. Photogramm. Remote Sens.*, vol. 73, pp. 12–20, Sep. 2012.

[8] C. Rossi and E. Erten, "Paddy-rice monitoring using TanDEM-X," *IEEE Trans. Geosci. Remote Sens.*, vol. 53, no. 2, pp. 900–909, Feb. 2015.

[9] S. Leinss, G. Parrella, and I. Hajnsek, "Snow height determination by polarimetric phase differences in X-band SAR data," *IEEE J. Sel. Topics Appl. Observ. Remote Sens.*, vol. 7, no. 9, pp. 3794–3810, Sep. 2014.

[10] O. Yüzügüllü, E. Erten, and I. Hajnsek, "Rice growth monitoring by means of X-band co-polar SAR: Feature clustering and BBCH scale," *IEEE Geosci. Remote Sens. Lett.*, vol. 12, no. 6, pp. 1218–1222, Jun. 2015.

[11] J. M. Lopez-Sanchez, J. D. Ballester-Berman, and I. Hajnsek, "First results of rice monitoring practices in Spain by means of time series of TerraSAR-X dual-pol images," *IEEE J. Sel. Topics Appl. Earth Observ. Remote Sens.*, vol. 4, no. 2, pp. 412–422, Jun. 2011.

[12] J. M. Lopez-Sanchez, S. R. Cloude, and J. D. Ballester-Berman, "Rice phenology monitoring by means of SAR polarimetry at X-band," *IEEE Trans. Geosci. Remote Sens.*, vol. 50, no. 7, pp. 2695–2709, Jul. 2012.

[13] S. R. Cloude, "The dual polarization entropy/alpha decomposition: A PALSAR case study," in *Proc. 3rd PolInSAR Workshop*, Frascati, Italy, 2007, pp. 1–6.

[14] J. M. Lopez-Sanchez, J. Fortuny-Guasch, and J. D. Ballester-Berman, "Indoor wide-band polarimetric measurements on maize plants: A study of the differential extinction coefficient," *IEEE Trans. Geosci. Remote Sens.*, vol. 4, no. 44, pp. 758–767, Apr. 2006.

A.4. Quality assessment of TanDEM-X raw DEMs oriented to a fusion with CartoSAT-1 DEMs

Rossi, C., Eineder, M., Fritz, T., D'Angelo, P., and Reinartz, P., **Quality assessment of TanDEM-X raw DEMs oriented to a fusion with CartoSAT-1 DEMs**, *Proc. 33rd EARSeL Symp.*, Matera, Italy, 2013.

Towards Horizon 2020

Rosa Lasaponara, Editor
EARSeL, 2013

Quality Assessment of TanDEM-X Raw DEMs Oriented to a Fusion with CartoSAT-1 DEMs

Cristian Rossi, Michael Eineder, Thomas Fritz, Pablo D'Angelo and Peter Reinartz

German Aerospace Center (DLR), Remote Sensing Technology Institute (IMF), Oberpfaffenhofen, Germany; cristian.rossi@dlr.de

Abstract. This paper addresses a quality assessment of TanDEM-X standard raw DEMs, with a resolution of 12 meters, for two different terrain configurations: urban areas and moderate topography. The analysis is performed in the geospatial domain. Beside TanDEM-X, the same analysis is also carried out for CartoSAT-1 and LiDAR DEMs. The latter one is used as a reference. Nevertheless, the focus is centered on TanDEM-X, whose geometric limitations and their impacts on the DEM are analyzed here in detail. How the DEM appears in layover, shadow and phase unwrapping error areas is one of the objectives of the paper. The chosen test site is around Terrassa/Barcelona (Spain), offering all kinds of terrain variations. The final scope of the analysis is to learn about the potentials and the limitations of the two systems, radar (TanDEM-X) and optical (CartoSAT-1), in a way to optimally fuse them and to create an enhanced DEM. A simple fusion processing chain, based on a weighted average depending on the quality of the DEMs adapted to the local geometry, is tested. First results show that in urban areas the improvements are limited, mainly due to the previously analyzed geometrical issues, whereas in moderate terrain areas the enhancement is significant, with a drop in the RMSE of about 25% for TanDEM-X and 30% for CartoSAT-1.

Keywords. TanDEM-X, raw DEM, CartoSAT-1, DEM fusion.

1. Introduction

The TanDEM-X satellite has been launched about three years ago, in June 2010. Since that date, the mission has been scheduled to acquire data finalized to the generation of a global DEM following the HRTI-3 standards [1]. The TanDEM-X global DEM is generated by mosaicking and calibrating individual raw DEMs [2], having an average extension of 30 by 50 kilometers. At the Oberpfaffenhofen (Germany) processing facilities, the raw DEM production rate is particularly high (more than 500 raw DEMs per day). This large rate is made possible by using optimal algorithms in the raw DEM processing chain, embedded in a single processor named Integrated TanDEM-X Processor (ITP) [3].

The quality of the mosaicked DEM is continuously monitored [4]. In this paper, we investigate at the source of the errors looking at the quality of a standard raw DEM, having a resolution of about 12 meters. An assessment for a special case has been already performed in [5]. A height standard deviation of 6 meters has been reported for a high resolution urban DEM with 2.5 meters raster. In general, the quality of raw DEMs depends on many factors. First, the particular Synthetic Aperture Radar (SAR) geometry has a big impact in the DEM. Layover and shadow issues are intrinsic to the side-looking SAR geometry. The layover phenomenon occurs when the terrain slope exceeds the radar look angle causing a superposition, in a single resolution cell, of contributions coming from other areas. Shadow occurs when a region is not illuminated by the radar. The raw DEM profile for these areas is derived in [5]. Second, focusing and interferometric processing errors may manifest in the raw DEM in several forms. The interfer-

ometric coherence is an instrument for measuring these errors: it is simply the degree of correlation between the two images used for the raw DEM generation. Many inaccuracies can be included in this measure [1]. Nevertheless, it does not take into account errors manifesting after the interferogram generation in the processing chain. Phase unwrapping inaccuracies are the biggest issues not considered in the coherence. They manifest in the raw DEM in height gradients proportional to the system height of ambiguity, an important parameter which triggers the performances. A way to detect these errors has been proposed in [6]. It makes use of the radargrammetric measurements employed in the coregistration processing stage as absolute reference.

The TanDEM-X mission is designed to mitigate raw DEM errors making use of a combination of several raw DEMs for the affected areas, in a *dual-baseline* approach [7]. In Sec. 2, we focus on the single-baseline raw DEM, investigating the discrepancies between TanDEM-X and a LiDAR reference in the geospatial domain. A CartoSAT-1 DEM processed at a 5 meters raster [8] is also analyzed. The chosen test site is around Terrassa/Barcelona (Spain), offering all kinds of terrain variations. Two DEM portions with different topography are studied. In Sec. 3, a simple DEM fusion based on the TanDEM-X and CartoSAT-1 geometrical proprieties is proposed and analyzed. The paper is concluded in Sec. 4 with a brief summary and an overview of future activities.

2. Quality assessment of TanDEM-X and CartoSAT-1 DEMs

The study is performed over the first two DEM patches used for the ISPRS benchmarking in [8]. The acquisition dates of the data used for the DEMs generation are November 2011 (TanDEM-X), February 2008 (CatoSAT-1) and November 2007 (LiDAR). The following assessment is based on the geometrical characteristics of the input DEMs, using approaches similar to the ones in [9]. For the analysis, the DEMs have been projected to the same grid (UTM, 10 meters raster). Nevertheless, it has to be noticed that the input resolution differs. TanDEM-X has the poorest resolution, of about 12 meters, whereas CartoSAT-1 and LiDAR have a comparable one of 2.5 and 2 meters respectively.

2.1. Terrassa, urban landscape

The first considered patch is over an urban area surrounded by smooth landscape. DEMs and relative geospatial maps are shown in Fig. 1. The first row contains the elevation models. The area, composed by a dense urban zone (northern part) and an industrial zone (center part), lies at the border of the TanDEM-X acquisition: the raw DEM does not fully cover the portion. A visual inspection of the DEMs and the geospatial maps shows how CartoSAT-1 has a better mapping of buildings compared to TanDEM-X, which results noisier. Moreover, buildings in TanDEM-X appear slightly shifted (wrongly geolocated), as visible from the error map in the fourth column. This is due to the layover mapping in the geocoding processing stage of TanDEM-X raw DEMs. In layover regions the raw DEM profile has been demonstrated to be a simple height ramp [5]. The buildings height and dimensions result generally underestimated and enlarged, respectively. Buildings lying in the vertical direction have a larger error [5]. The industrial area, composed by large structures, results better represented, with a comparable number of detected structures as in the reference.

Regarding CartoSAT-1, its urban mapping is over-performing the SAR sensor. Here, geometrical issues are less conspicuous. Occlusions may occur and small houses may be wrongly represented, but their effect in the DEM is less noticeable than the overall noise noticed for

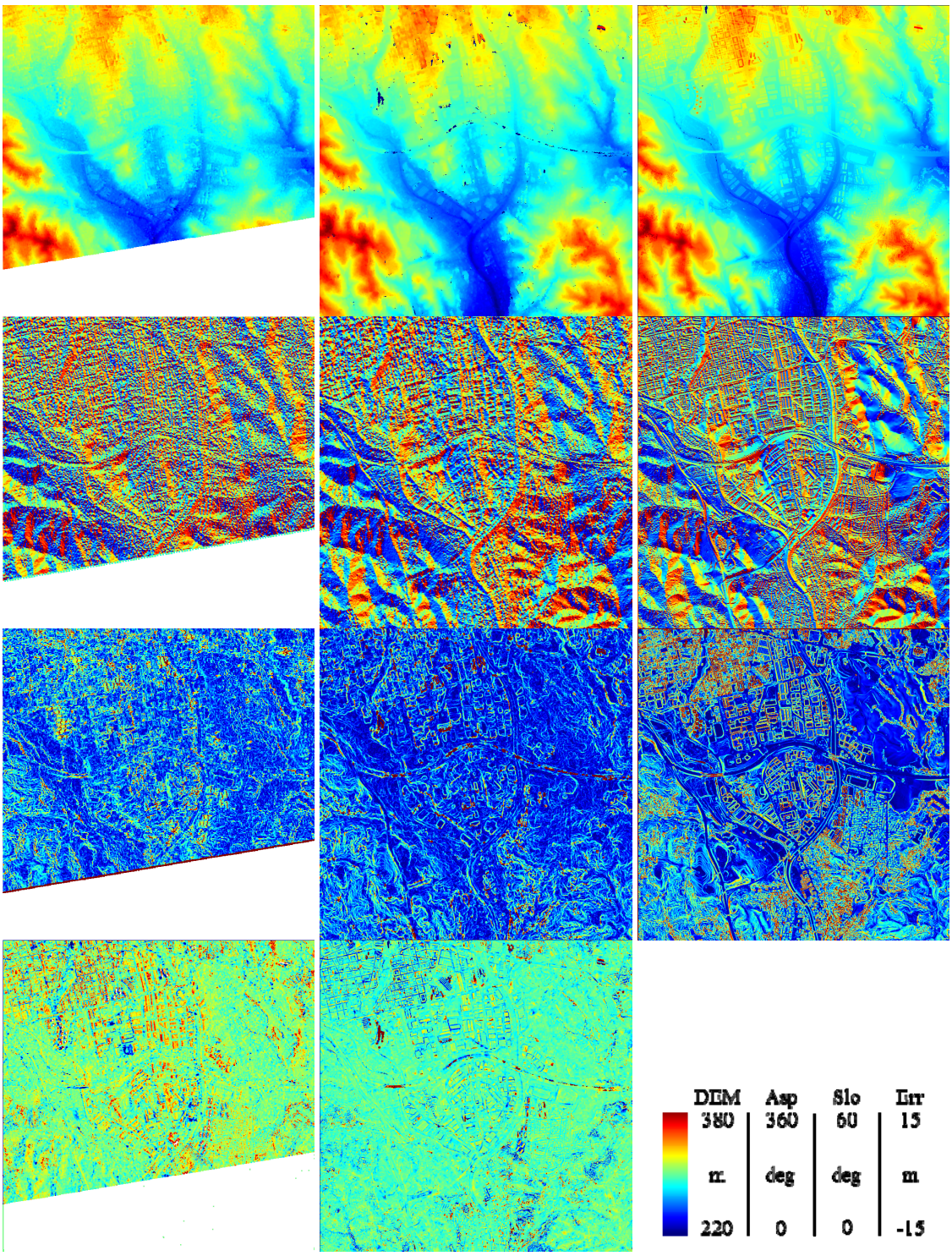

Figure 1: Terrassa geospatial maps for TanDEM-X (left column), CartSAT-1 (center column) and LiDAR (right column). The DEM portion, the aspect map, the slope map and the DEM difference with LiDAR are represented in the rows (first to fourth). The color scaling of the maps is at the bottom-right.

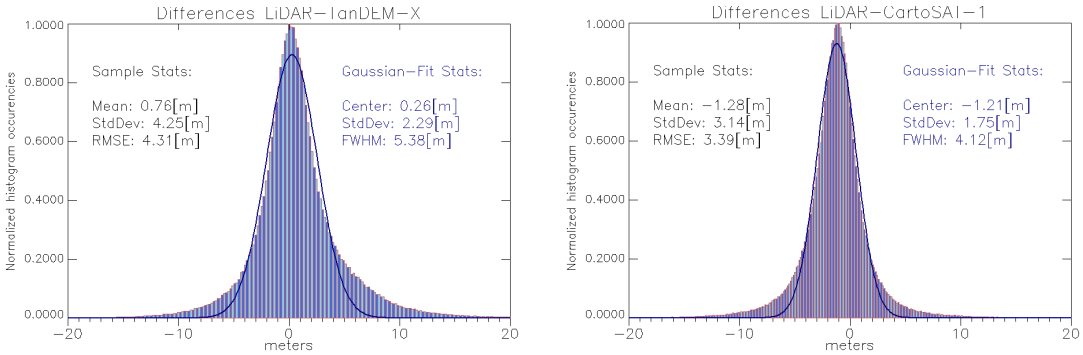

Figure 2: Terrassa test site: absolute differences between reference and TanDEM-X (left) and CartoSAT-1 (right) histograms.

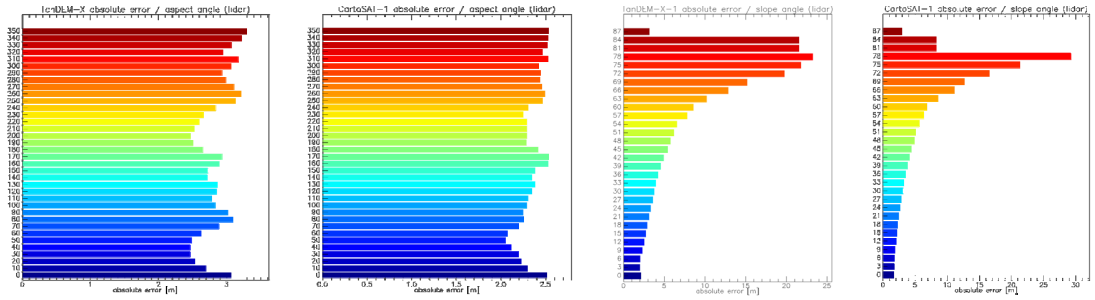

Figure 3: Terrassa test site: absolute error dependency for TanDEM-X aspect and slope (first and third) and CartoSAT-1 aspect and slope (second and fourth).

TanDEM-X. Only increasing the SAR resolution, i.e. adopting spotlight acquisitions, the results may be comparable. A contrast between the two DEMs is the presence of invalid pixels. In the CartoSAT-1 DEM, they are marked as dark blue points (Fig. 1, second column, first row). They are mainly located in the dense urban area, at the edge of some houses and on the main road. A skyscraper area at the north-west is fully invalidated. Contrariwise, in the TanDEM-X raw DEM there are only valid pixels: a DEM solution is always found from the interferometric phase. The solution may be inaccurate for low coherence areas: a map relating the standard height error to the measured coherence, called Height Error Map (HEM), is an ITP output [10]. Nevertheless, in case of urban areas, HEM is not fully matching the real standard error. This is due to layover zones, having high coherence when in both of the acquisitions the same layover component dominates – i.e. when the scattering of the wall fully dominates over the scattering of the roof or the ground, all contained in the same resolution cell.

In Fig. 2 the differences between the LiDAR reference and the studied DEMs are represented. Globally, CartoSAT-1 has better sample statistics, with a root mean square error drop of about 20% when compared to TanDEM-X. Regarding the absolute calibration, CartSAT-1 has more height overestimations whereas TanDEM-X has more underestimations, as previously explained (see also Fig. 1, fourth row). The calibration is a key issue for the interferometric reconstruction. In fact, a mis-calibration not only yields a global offset, but also geolocation errors [6]. This is not the case for the optical matching algorithms.

In Fig. 3 the dependency of the errors with aspect and slope is represented. The slope dependency is similar for both of the cases, with higher errors for higher slopes. The aspect dependency slightly differs for north-east degrees, where TanDEM-X has higher errors due to shadowing.

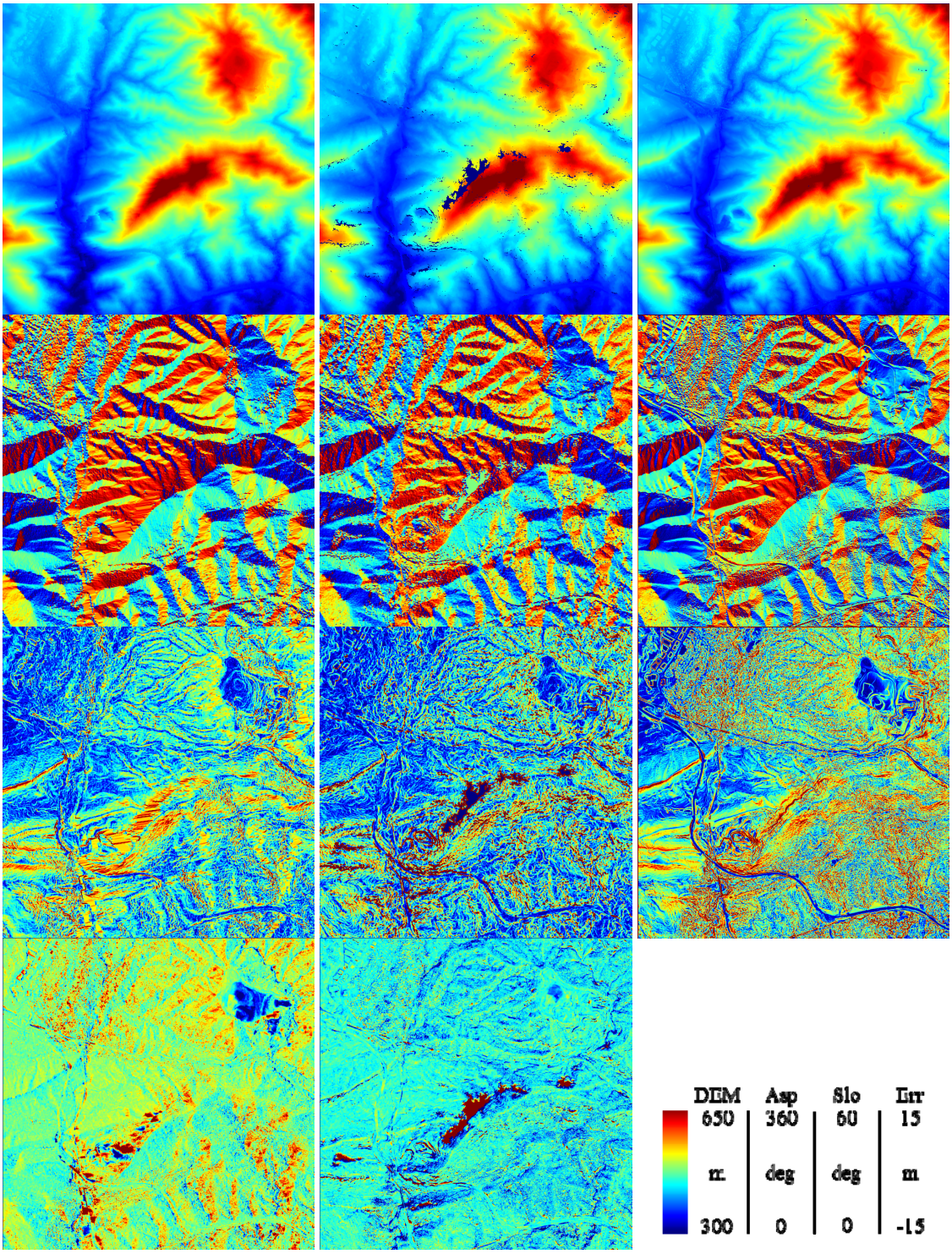

Figure 4: Vacarisses geospatial maps for TanDEM-X (left column), CartSAT-1 (center column) and LiDAR (right column). The DEM portion, the aspect map, the slope map and the DEM difference with LiDAR are represented in the rows (first to fourth). The color scaling of the maps is at the bottom-right.

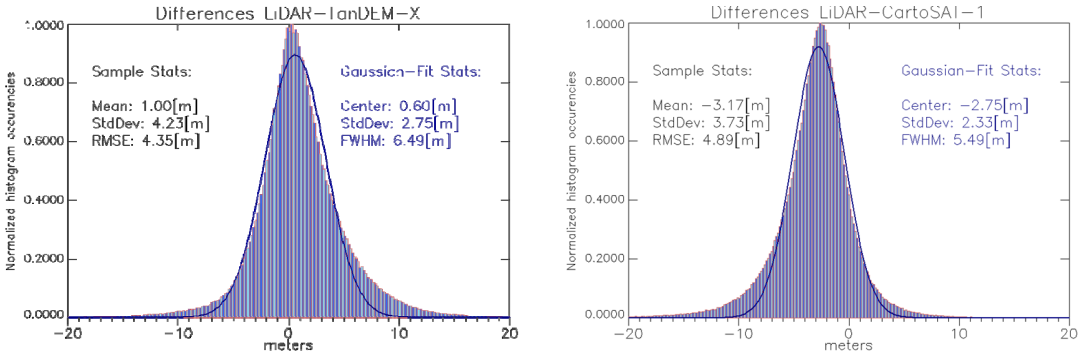

Figure 5: Valcarisses test site: absolute differences between reference and TanDEM-X (left) and CartoSAT-1 (right) histograms.

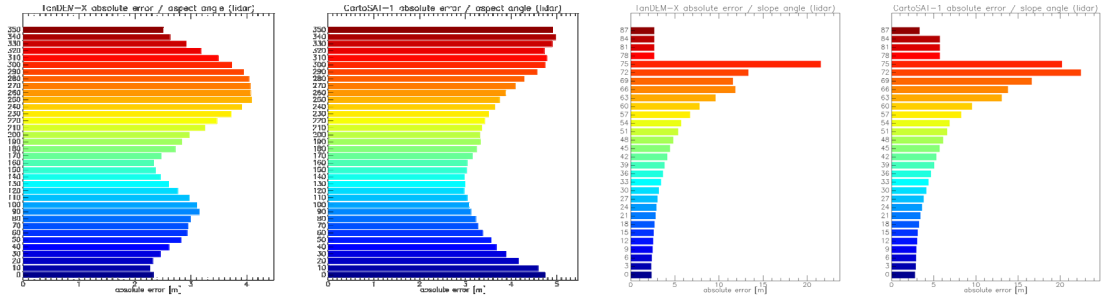

Figure 6: Valcarisses test site: absolute error dependency for TanDEM-X aspect and slope (first and third) and CartoSAT-1 aspect and slope (second and fourth).

2.2. Valcarisses, moderate terrain

The second test site for the benchmarking is composed by moderate terrain. The first row of Fig. 4 shows the DEMs. The patch is composed by a hill (center scene), an accumulation area (north-east), and an industrial area (north-west). The assessment follows the same strategy as in Sec. 2.1. A visual comparison of the elevation models does not reveal significant discrepancies as for the urban case. This is quantitatively demonstrated with the error histogram in Fig. 5. For this patch, TanDEM-X has a better RMSE, with a 10% drop compared to CartoSAT-1. As for the previous case, TanDEM-X underestimates the heights – due to layover areas – whereas CartoSAT-1 overestimates them, especially for high quotes. The absolute error is larger for CartoSAT-1. The accumulation area plays a role in the error particularly for TanDEM-X (Fig. 4, fourth row), having a 4 years temporal baseline with the reference, while CartoSAT-1 is much closer (4 months).

The western side of the hill is rather steep, with slopes larger than 60 degrees (Fig. 4, third column, third row). In this area there is the biggest concentration of CartoSAT-1 invalids. Since the western side is the one facing towards the SAR sensor, layover occurs for TanDEM-X. As for the previous patch, a height ramp is generated in layover zones (visible also in the aspect map of Fig. 4, first column, second row). In this case, the height error is proportional to topographic modulations around the height slope.

Interesting considerations can be made looking at Fig. 6. The error dependency with the slope is similar to the previous case – larger error for steeper terrain –. Instead, the dependency with the aspect shows a complementarity between TanDEM-X and CartoSAT-1. In particular, the TanDEM-X histogram results bimodal, with larger errors around two peaks, localized around the shadow aspect (first peak, easterly aspect) and the layover one (second and large peak, westerly aspect). Car-

toSAT-1 has instead larger errors for northerly aspect. Both of the sensors achieve the best performance for southerly aspect.

3. A quick DEM fusion approach

The two DEM sources can be combined in order to obtain an enhanced version of the elevation model. Several studies have been already performed (i.e. [12]). The DEM fusion basically relies on understanding of the source of errors of the input map to fuse. As already pointed out, the TanDEM-X HEM is a powerful map to exploit at the purpose. DEM samples with a large HEM should be discarded. They can be on water areas, shadow zones or dense forested areas where volume decorrelation occurs. Other samples to be discarded are the ones where phase unwrapping errors occur. They can be easily detected with a large threshold on the height difference between the two DEMs. The discrepancy is large as proportional to multiples of the height of ambiguity, having typical ranges of 40-60 meters for the mission. Invalid samples of the CartoSAT-1 DEM will be replaced by TanDEM-X, assuring that the replacement does not include phase unwrapping errors by checking the difference with a replacement by interpolation. Any other sample should be mixed following quality criteria. According to the considerations in Sec. 2, the complementarity of the sensors with respect to the aspect angle is an exploitable criterion. The dependency with the slope angle is less effective, since the sensors behave at the same manner. Nevertheless, training curves triggering the DEM sample weights are built. The first step is the absolute calibration of CartoSAT-1 to TanDEM-X, having a more accurate calibration. The complete algorithm is the following (CS stands for CartoSAT-1 DEM and TD for TanDEM-X raw DEM):

DEM fusion algorithm

1. Absolutely calibrate CS to the mean TD height
2. Replace CS invalid by linear interpolation
3. Check the difference between the filled invalid and TD. If (|difference| < HoA-***th1***), then use TD value
4. For every other sample, check the difference: d1 = |CS-TD|. If (d1> HoA-***th1***), then use CS sample, otherwise go to point 5.
5. Check the HEM value for the current sample. If larger than ***th2***, then use CS sample, otherwise go to point 6.
6. Perform a weighted average of the two DEM samples, depending on the current slope and aspect for both of the sensors and also on HEM for TD. In the average, CS and TD have a total weight depending on the scene to map. Moreover, the slope, aspect and HEM weights have also a different impact in the average.

This simple algorithm is based on the use of thresholds and weights. The set of parameters employed for the Valcarisses benchmarking site is in Tab. 1. The aspect training curves are shown in Fig. 7. In Fig. 8 and Fig. 9 the results of the fusion are represented. The fused DEM results more accurate than the input DEMs (Fig. 5), with a better absolute calibration and a drop of the RMSE of about the 25% when compared to TanDEM-X and 30% when compared to CartoSAT-1. In contrast, the fusion result for the first benchmarking site, with the urban area of Terrassa, provides a smaller improvement, with a RMSE drop of 27% when compared to TanDEM-X and 7% for CartoSAT-1. The set of parameters for the first site are the same of the ones in Tab.1, except for the total weights, set to 75% for CartoSAT-1 and 25% for TanDEM-X due to the issues considered in Sec. 2.1. Nevertheless, large DEM problems as invalids or phase unwrapping errors are solved.

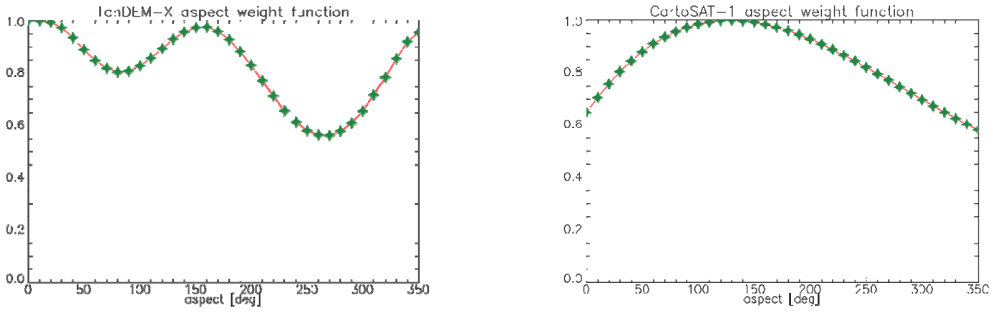

Figure 7: Aspect weight for TanDEM-X (left) and CartoSAT-1 (right)

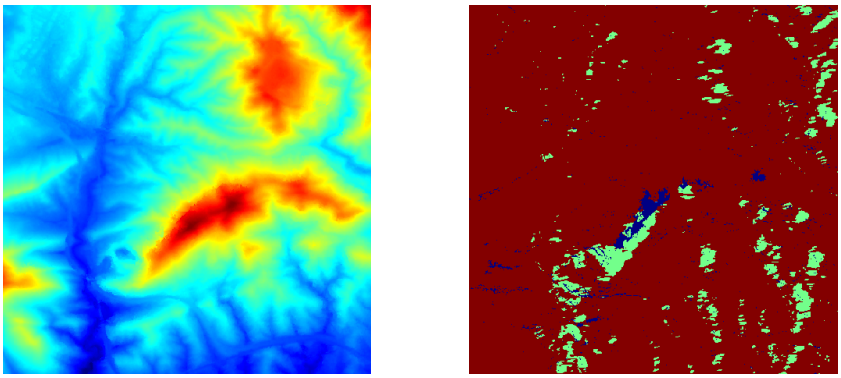

Figure 8: Valcarisses test site: fusion result (left) and fusion map (right). The colors in the map stand for weighted average (red), only CS/HEM threshold (green), only TD/CS invalid (dark blue), CS interpolation/CS invalid (light blue), only CS/TD phase unwrapping error (yellow).

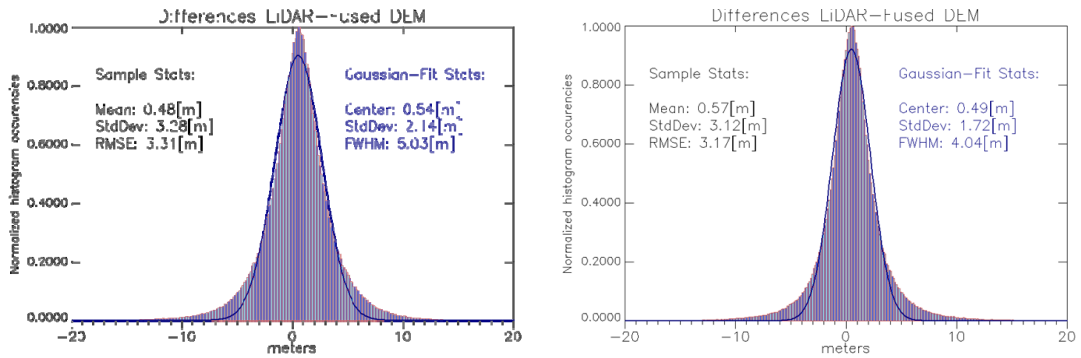

Figure 9: Histogram of the differences between reference and fused DEM for Valcarisses (left) and Terrassa (right).

Table 1. Parameters used for the DEM fusion (Valcarisses).

Parameter	**Value**	**Parameter**	**Value**
HoA	45m	CS aspect weight	60%
th1	10m	CS slope weight	40%
th2	2.5m	TD HEM weight	60%
total CS weight	50%	TD aspect weight	30%
total TD weight	50%	TD slope weight	10%

4. Conclusions

A first study on the quality of standard TanDEM-X raw DEMs and CartoSAT-1 DEMs oriented to their fusion has been proposed. The analysis has been carried out in the geospatial domain. For urban areas, the higher resolution of CartoSAT-1 and the lack of geometrical issues as layover let its globally better mapping when compared to TanDEM-X. Contrariwise, for moderate terrain the two sensors results comparable, with a slightly better mapping accuracy for TanDEM-X. Accordingly, the fusion results significantly improve the performances for non-urban areas, whereas for municipal zones the improvements are almost only for TanDEM-X. Future studies rely on more complex fusion algorithms and the exploitation of the spectral domain for the analysis.

References

[1] Krieger, G., Moreira, A., Fiedler, H., Hajnsek, I., Werner, M., Younis, M., Zink, M., 2007. TanDEM-X: A Satellite Formation for High-Resolution SAR Interferometry. IEEE Transactions on Geoscience and Remote Sensing 45 (11), 3317-3341.

[2] Gruber, A., Wessel, B., Huber,M., Roth, A., 2012. Operational TanDEM-X DEM Calibration and First Validation Results. ISPRS Journal of Photogrammetry and Remote Sensing 73, 39-49.

[3] Fritz, T., Rossi, C., Yague Martinez, N., Rodriguez Gonzalez F., Lachaise, M., Breit, H., 2011. Interferometric Processing of TanDEM-X Data. In: Proceedings of IEEE International Conference on Geoscience and Remote Sensing Symposium, IGARSS 2011, Vancouver, Canada, 24-29 July, pp. 2428-2431.

[4] Brautigam, B., Rizzoli, P., Martone, M., Bachmann, M., Kraus, T., Krieger, G., 2012. InSAR and DEM quality monitoring of TanDEM-X. In: Proceedings of IEEE International Conference on Geoscience and Remote Sensing Symposium, IGARSS 2012, Munich, Germany, 22-27 July, pp.5570-5573.

[5] Rossi, C., Gernhardt, S., Urban DEM generation, analysis and enhancements using TanDEM-X. ISPRS Journal of Photogrammetry and Remote Sensing (under review).

[6] Rossi, C., Rodriguez Gonzalez, F., Fritz, T., Yague Martinez, N., Eineder, M., 2012. TanDEM-X calibrated Raw DEM generation. ISPRS Journal of Photogrammetry and Remote Sensing 73, 12-20.

[7] Lachaise, M., Balss, U., Fritz, T., Breit, H., 2012. The Dual Baseline Interferometric Chain for the TanDEM-X Mission. In: Proceedings of IEEE International Conference on Geoscience and Remote Sensing Symposium, IGARSS 2012, Munich, Germany, 22-27 July, pp.5562-5565.

[8] d'Angelo, P., Reinartz, P., 2011. Semiglobal matching results on the ISPRS stereo matching benchmark. In: ISPRS Hannover Workshop 2011: High-Resolution Earth Imaging for Geospatial Information.

[9] Toutin, T., 2002. Impact of terrain slope and aspect on radargrammetric DEM accuracy, ISPRS Journal of Photogrammetry and Remote Sensing 57, 228-240.

[10] Rossi, C., Eineder, M., Fritz, T., Breit, H., 2010. TanDEM-X Mission: Raw DEM Generation. In: Proceedings of 8th European Conference on Synthetic Aperture Radar, EUSAR 2010, Aachen, Germany, 7-10 June, (on CD-ROM).

[11] Hoja, D., Reinartz, P., Schroeder, M., 2006. Comparison of DEM generation and combination methods using high resolution optical stereo imagery and interferometric SAR data. In: Proceedings of the ISPRS Commission I Symposium "From Sensors to Imagery", pp. 1682-1777.

A.5. Urban DEM generation, analysis and enhancements using TanDEM-X

Rossi, C., and Gernhardt, S., Urban DEM generation, analysis and enhancements using TanDEM-X. *ISPRS Journal of Photogrammetry and Remote Sensing*, 85, 120-131, 2013.

ISPRS Journal of Photogrammetry and Remote Sensing 85 (2013) 120–131

Contents lists available at ScienceDirect

ISPRS Journal of Photogrammetry and Remote Sensing

journal homepage: www.elsevier.com/locate/isprsjprs

Urban DEM generation, analysis and enhancements using TanDEM-X

Cristian Rossi [a,*], Stefan Gernhardt [b]

[a] Remote Sensing Technology Institute, German Aerospace Center (DLR), Oberpfaffenhofen, Germany
[b] Chair of Remote Sensing Technology, Technische Universität München, Munich, Germany

ARTICLE INFO

Article history:
Received 15 November 2012
Received in revised form 30 July 2013
Accepted 23 August 2013
Available online 26 September 2013

Keywords:
TanDEM-X
Urban DEM
InSAR processing
PSI-DEM
DEM fusion

ABSTRACT

This paper analyzes the potential of the TanDEM-X mission for the generation of urban Digital Elevation Models (DEMs). The high resolution of the sensors and the absence of temporal decorrelation are exploited. The interferometric chain and the problems encountered for correct mapping of urban areas are analyzed first. The operational Integrated TanDEM-X Processor (ITP) algorithms are taken as reference. The ITP main product is called the raw DEM. Whereas the ITP coregistration stage is demonstrated to be robust enough, large improvements in the raw DEM such as fewer percentages of phase unwrapping errors, can be obtained by using adaptive fringe filters instead of the conventional ones in the interferogram generation stage. The shape of the raw DEM in the layover area is also shown and determined to be regular for buildings with vertical walls. Generally, in the presence of layover, the raw DEM exhibits a height ramp, resulting in a height underestimation for the affected structure. Examples provided confirm the theoretical background. The focus is centered on high resolution DEMs produced using spotlight acquisitions. In particular, a raw DEM over Berlin (Germany) with a 2.5 m raster is generated and validated. For this purpose, ITP is modified in its interferogram generation stage by adopting the Intensity Driven Adaptive Neighbourhood (IDAN) algorithm. The height Root Mean Square Error (RMSE) between the raw DEM and a reference is about 8 m for the two classes defining the urban DEM: structures and non-structures. The result can be further improved for the structure class using a DEM generated with Persistent Scatterer Interferometry. A DEM fusion is thus proposed and a drop of about 20% in the RMSE is reported.

1. Introduction

The mapping of urban areas is important for many management applications, such as urban development monitoring, urban climate studies and renewable energy surveys. Airborne data are widely used for this purpose in the generation of Digital Elevation Models (DEMs). LiDAR (Light Detection And Ranging) is a mature technology for obtaining DEMs in an urbanized environment (Wehr and Lohr, 1999; Haala and Brenner, 1999). Through the exploitation of digital photogrammetry, stereoscopic photographs are also employed (Smith and Smith, 1996; Abanmy et al., 1995). Investigations on airborne Synthetic Aperture Radar (SAR) data using an experimental millimeterwave interferometric system have been conducted recently (Schmitt et al., 2011). In contrast, spaceborne SAR is not heavily exploited, largely due to the lack of suitable data. In fact, an essential prerequisite for the successful exploitation of SAR data for urban reconstruction is a resolution capable of mapping the desired target (Soergel et al., 2006). For instance, the popular SRTM SAR mission, providing a DEM with a resolution of 30 m at best, has been demonstrated unsuitable for accurate mapping of metropolitan areas (Gamba et al., 2002). A second prerequisite, but no less important, is the absence of temporal decorrelation between the two SAR acquisitions. A bistatic interferometric system satisfies this prerequisite. When using a monostatic configuration, also called repeat-pass interferometry, one is faced with several limitations. Temporal decorrelation (Zebker and Villasenor, 1992) makes the SAR measure unusable when the phase center of the scatterer changes between the acquisitions. This phenomenon is very common in vegetated areas. Even if not affecting buildings in general, it is fundamental to avoid this effect for the overall accuracy of urban DEMs that usually include vegetated areas. A secondary limitation that plays also a role for short temporal baselines is the atmospheric phase screen (APS) present in a single image. Studies with repeat-pass configurations have been performed for urban DEMs generated with two TerraSAR-X repeat-pass acquisitions. A global accuracy of 10 m (RMSE) was reported (Sefercik et al., 2012). Nevertheless, they are locally affected by atmospheric artefacts yielding false elevation values. In this case, the use of several repeat-pass acquisitions and the

* Corresponding author. Tel.: +49 8153282167.
E-mail address: cristian.rossi@dlr.de (C. Rossi).

0924-2716/$ - see front matter © 2013 International Society for Photogrammetry and Remote Sensing, Inc. (ISPRS) Published by Elsevier B.V. All rights reserved.
http://dx.doi.org/10.1016/j.isprsjprs.2013.08.006

Persistent Scatterer Interferometry (PSI) technique can attenuate and locally solve the decorrelation problem (Perissin and Rocca, 2006).

The primary objective of the TanDEM-X mission is the generation of a global DEM following the high standard accuracy HRTI-3 (Krieger et al., 2007). The X-band sensors employed for the mission allow an accurate mapping of buildings, hence satisfying the first prerequisite for successful urban reconstruction. Additionally, the mission constitutes the first bistatic SAR interferometer in space, enabling a precise surface reconstruction free of atmospheric and temporal decorrelations by a single-pass acquisition, thus satisfying the second prerequisite. To accomplish the spatial resolution requirement of 12 m, stripmap data is used. Nevertheless, this resolution does not assure an accurate mapping of dense metropolitan areas, where the separation between buildings is smaller than the spatial resolution. Instead, semi-urban and industrial areas are mapped accurately, with a DEM interferometric standard error reported to be below one meter for the test case in (Rossi et al., 2011). The mission foresees however experimental spotlight acquisitions to generate higher resolution DEMs following the HRTI-4 standards with a spatial resolution of 6 m. With this resolution, a denser urban mapping is feasible.

The non-linearity of urban structures yields several limitations in interferometric SAR city modelling. In Section 2, the typical processing issues in the Integrated TanDEM-X Processor (ITP) are outlined. The urban geometry and the implications for coregistration, phase unwrapping and geocoding processing stages are analyzed here. The DEM profile for buildings with vertical walls is theoretically derived in this section. In Section 3, an analysis of a high resolution urban DEM of Berlin (Germany) is carried out. The DEM, generated with a raster of 2.5 m, is produced from a single-pass spotlight TanDEM-X acquisition. To obtain the statistics reported in Section 3.4 at this fine raster, ITP is modified by decreasing the standard independent number of looks in the interferometric processing and by adopting an adaptive algorithm for the multi-look processing stage. An enhanced version is then generated by a fusion with a DEM obtained by PSI (Gernhardt and Bamler, 2012). The evaluation of the DEMs and the comparison study with respect to a reference is provided. The paper is concluded in Section 4 with a brief summary and an overview of future activities.

2. High resolution urban DEM generation

The main goal of the TanDEM-X mission is the generation of a global DEM, thus including all cities in the world. The processing of SAR raw data for the generation of the *raw DEM* is performed by one single processor, the Integrated TanDEM-X Processor (ITP) (Breit et al., 2011), not elaborated in this paper. The global *TanDEM-X DEM* is generated afterwards by mosaicking the raw DEMs (Gruber et al., 2012). ITP is configured in every single processing stage to provide a raw DEM close to the HRTI-3 standards (relative point-to-point height accuracy of 2 m for moderate terrain with slopes less than 20° in a 1° by 1° cell (NIMA, 2010)). In the processing facilities, the time required for the generation of a standard raw DEM (50 by 30 km) from the raw data is about 15 min. This optimization is conducted according to (Fritz et al., 2011; Rossi et al., 2012). An example of an operational raw DEM at 12 m resolution over Berlin is shown in Fig. 1. An evaluation of an urban operational raw DEM over Munich (Germany) is provided in (Rossi et al., 2012).

In this paper the focus is on high resolution raw DEMs, for building reconstruction purposes. In this case, ITP processing at DLR may be modified in order to generate solutions adapted for urban mapping. In the next subsection the main modifications and the urban limitations to the interferometric chain are introduced.

2.1. Spectral shift filtering and coregistration

The spectral shift stage can be switched off in case of purely urban areas. The statistical base which justifies it, namely distributed scattering, is generally not valid for municipal zones (Gatelli et al., 1994). Moreover, the geometrical configuration of the TanDEM-X mission is built such that the small gain from spectral shift filtering is only 3–5%. Nevertheless, this processing step is always enabled, also in this paper, to obtain a better accuracy for mixed scene configurations (rural, urban).

The coregistration procedure exploited in ITP is designed in order to leave misalignments well below the pixel level (Martinez et al., 2010). It is based on a multi-step correlation algorithm for windows with a configurable size and separation. For every window, two radargrammetric shifts, one for the azimuth and one for the range directions, are computed. This set of shifts is then used for resampling of the slave channel in the master channel geometry. In the spotlight case, the window size is set to about 35 m in azimuth and to 19 m in the range direction (32 by 32 pixels). The separation between windows is 70 and 30 m, respectively. Trade-offs between window size and desired accuracy were already predicted for the coherent case (Bamler and Eineder, 2005; Erten et al., 2010). Due to different statistics they are however not valid for urban scenarios. In the urban case, several scatterers

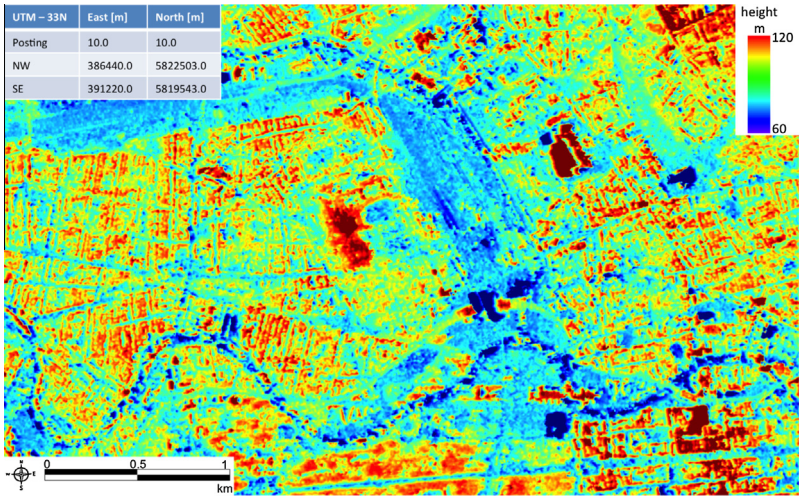

Fig. 1. TanDEM-X operational raw DEM over a central area of Berlin (Germany). The DEM is in UTM projection (zone 33N, corner coordinates at the top-left).

inside the coregistration window may impact in the determination of the single shift. If the scatterers lie at different ground heights, a coregistration mismatch and a consequent loss of coherence is produced. In Fig. 2 an example of mismatch generated by the discrepancy Δd between two radargrammetric shifts is shown ($\Delta d = dP1 - dP2$). It is assumed that the scatterers $P1$ and $P2$ belong to the same coregistration window W and dominate over all the other scatterers in the window. For a better understanding, the plot is represented in ground range domain. Nevertheless, the radargrammetric shifts computed in the processor are in slant range domain. The discrepancy Δd can be computed geometrically (Leberl, 1990).

The coregistration error produced by the mismatch Δd yields a coherence loss ξ_c (Just and Bamler, 1994):

$$\xi_c = 1 - sinc(\Delta d). \quad (1)$$

A simulation is performed to evaluate the coherence loss for a standard TanDEM-X scenario with a height ambiguity of 40 m. The result for different height discrepancies in a coregistration window cell is given in Fig. 3. Due to the relatively small baselines of the helix formation of TanDEM-X the loss is unimportant (a coherence of about 0.05 for a height discrepancy of 100 m). Therefore, the standard ITP coregistration approach will not be modified for the urban raw DEM generation.

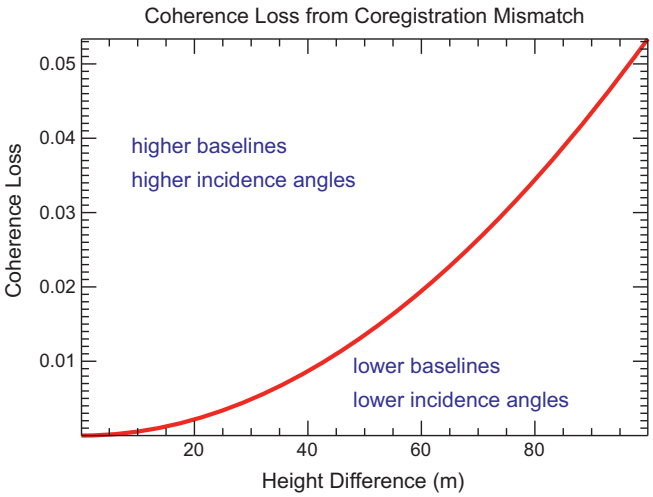

Fig. 3. Coherence loss caused by a coregistration mismatch generated by two scatterers with different heights in the same coregistration window for a TanDEM-X scenario with a height ambiguity of 40 m and an incidence angle of 37°. A different SAR geometry would shift the curve into the upper (higher baselines and/or angles) or lower region (lower baselines and/or angles) of the plot.

2.2. Interferogram generation

The interferogram generation determines the raw DEM resolution Ω_r through the independent number of looks used in the processing:

$$\Omega_r = \frac{n_{az}\delta_{az}^{gr} + n_{rg}\delta_{rg}^{gr}}{2}, \quad (2)$$

where n_{az} and n_{rg} are the azimuth and range independent number of looks and δ_{az}^{gr} and δ_{rg}^{gr} represent the single SAR pixel azimuth and range ground resolution. The estimation of the independent number of range looks is made considering the common bandwidth after the spectral filtering: $n_{rg} = n_{rg}^{ML} * f_{bdw}/f_{rsf}$, where n_{rg}^{ML} is the number of range looks used for multi-looking processing, f_{bdw} is the common range bandwidth and f_{rsf} is the total range bandwidth.

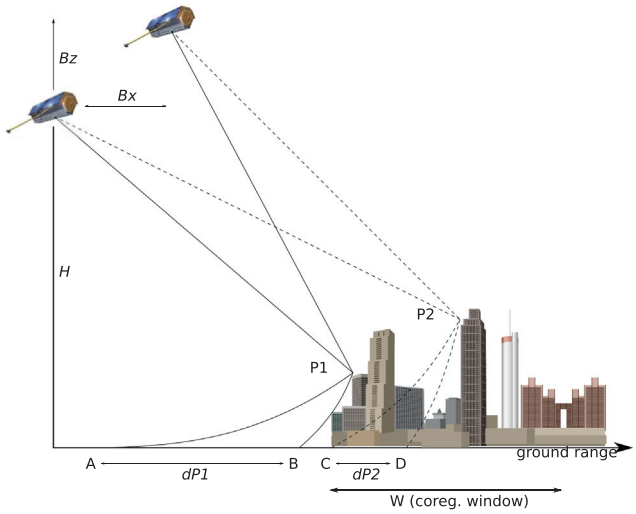

Fig. 2. Coregistration mismatch geometry at a fixed azimuth time. The scaling does not represent the real geometry and is exaggerated for better comprehension. The scatterers $P1$ and $P2$, belonging to the same coregistration window W, generate the radargrammetric shifts on the ground $dP1$ and $dP2$, respectively. H is the master satellite's height and B_x and B_z are the horizontal and the vertical baselines, respectively.

The estimation for the azimuth dimension is similarly made considering the ratio between the processed azimuth bandwidth and total bandwidth (pulse repetition frequency).

For urban modelling purposes, the fast performing moving average window algorithm employed to reduce the phase noise in the ITP multilook stage can be changed. In particular, adaptive algorithms making use of amplitude statistics to fuse pixels with the same characteristics are analyzed here. The algorithm in (Vasile et al., 2004), named Intensity Driven Adaptive Neighborhood (IDAN), connecting consecutive pixels by a region growing technique, and the one in (Deledalle et al., 2011), named Non-Local InSAR (NL-InSAR), connecting non-consecutive pixels inside a search window, can be used for this purpose. The need to employ adaptive methods is obvious looking at Figs. 4 and 5, showing portions of the operationally and adaptively processed raw DEMs for a high resolution spotlight acquisition over Las Vegas acquired on the 25th September, 2011. The interferometric phase is processed to obtain a resolution Ω_r of 3.65 m (Eq. 2). The main geometrical and processing parameters for this test case are in Table 1. The NL-InSAR algorithm is used for the multilooking and the coherence estimation. The phase noise mitigation is evident comparing the two raw DEM portions. The height variance of the flat roof of the four buildings – about 5000 DEM samples – in the middle of the area is 4.72 m for the operational ITP software case and 0.68 m for the experimental one carried out by us. The improvement is large also for the phase unwrapping stage, necessary in this case due to the topography present in the scene. The combined use of the adaptively multilooked phase and the associated coherence dramatically increases the phase unwrapping quality ratio q_r. This ratio expresses the percentage of the scene not affected by phase unwrapping errors (Rossi et al., 2012). Whereas in the operational scenario q_r is 76%, meaning that about one quarter of the scene is affected by phase unwrapping errors, the experimental processing run yields a q_r of 99.9%, implying that the adaptive processing almost totally solved the phase unwrapping issue for this test case. The false heights in the operational scenario are caused by the very low coherent road at center-left of the scene (Fig. 6). The interferometric phase of the road is extremely noisy, creating several branch cuts. In the phase unwrapping stage, the two sides of the road remain unconnected, creating a height discrepancy between them of one phase cycle (35 m). In this test case, this issue is solved

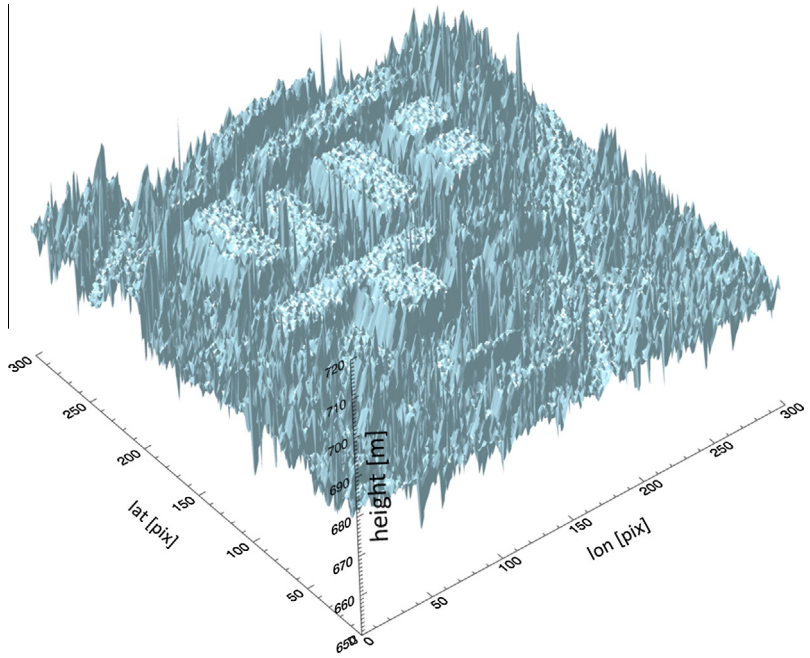

Fig. 4. Three dimensional shaded visualization of the raw DEM over Las Vegas for an industrial area generated using operational algorithms. The raw DEM sampling is 1.66 m, the patch extent is 500 by 500 m, the height variance of the four roofs is 4.72 m.

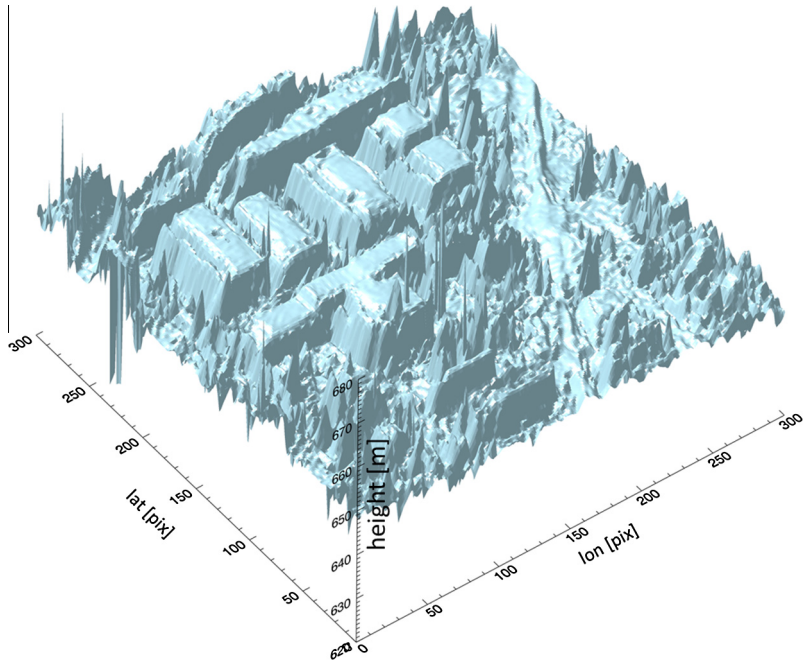

Fig. 5. Three dimensional shaded visualization of the raw DEM over Las Vegas for an industrial area experimentally generated using the NL-InSAR technique. The raw DEM sampling is 1.66 m, the patch extent is 500 by 500 m. The height variance of the four roofs is 0.68 m.

by employing the NL-InSAR algorithm, as shown in the *radargrammetric control maps* (Rossi et al., 2012) in Figs. 7 and 8. Hence, the combined use of the enhanced phase and coherence yields a reduction of false heights generated by the phase unwrapping stage. Further examples are provided in Section 3.

The noise mitigation adaptive algorithms can also be used to force a very high resolution and a fine DEM sample interval. In Section 3 the raw DEM of Berlin is generated at a grid posting of 2.5 m.

2.3. How does a building appear in a TanDEM-X raw DEM?

SAR is a side-looking sensor and is affected by geometrical issues such as layover and shadow. Layover occurs when the terrain slope exceeds the radar look angle causing a superposition, in a single resolution cell, of contributions coming from other areas. Shadow occurs when a region is not illuminated by the radar. In the case of buildings with vertical walls, layover and shadow

Table 1
Main parameters of the Las Vegas spotlight test site.

Range bandwidth	300 MHz
PRF	8200 Hz
Center incidence angle (master)	36°
Effective baseline	169.95 m
Height of ambiguity	+33.5 m
SSC pixel spacing (range)	0.45 m
SSC pixel spacing (azimuth)	0.87 m
Spectral shift filtering	Enabled
Multi-look algorithm	NL-InSAR
Total number of looks	25
Interferogram resolution	3.65 m
Mean coherence	0.76

always occur. A simple situation is sketched in Fig. 9. A large flat roof building is considered for study here (Fig. 8.2).

Fig. 9.1 shows the noise-free theoretical trend of the flattened unwrapped phase (red). The interferogram is considered flattened to better understand the phase profile, which is proportional only to topographic variations. An incidence angle of about 45 °C is considered. Below the trend, layover, shadow and normal mapping are marked in green, orange and blue, respectively. For this simple example, the layover part is a superposition of three different height contributions: ground, wall and roof. In particular, at a fixed azimuth time, an interferogram layover pixel may be modelled as the sum of three complex exponentials:

$$I(t_{rg}) = s_M(t_{rg}) s_S(t_{rg})^* = k_0 \exp\left(j\frac{4\pi}{\lambda}(\Delta R_{ground})\right) + k_0 \exp\left(j\frac{4\pi}{\lambda}(\Delta R_{wall})\right) + k_0 \exp\left(j\frac{4\pi}{\lambda}(\Delta R_{roof})\right) \quad (3)$$

where s_M and s_S are the complex focused pixels for the master and the slave channel at range time t_{rg}, k_0 is a complex constant, λ the sensor wavelength and ΔR is the slant range difference between the master and the slave channel. In this simplified model, the same complex constant is assigned for the three layover contributions, meaning an equal isotropic scattering mechanism. In real data this hypothesis is hardly true, multiple bounces may occur and one layover component may dominate over the others (Thiele et al., 2010). Considering the model in Eq. (3), the unwrapped flattened phase exhibits a peak at the beginning of the layover area, then a downward trend is noticeable. This is due to the decreasing wall height for increasing slant range distances, whereas the ground and roof heights remain constant. For the validity of this trend, the slave satellite is assumed to be the closer to the building, or, in other words, the height of ambiguity is assumed positive. The positive layover peak takes place when no phase unwrapping errors occur, i.e. the building has a height less than half the height of ambiguity. In areas not subject to layover and shadow, the phase is proportional to the single scatterer height. In the shadow area the phase is indeed not predictable as it is dominated by random noise.

Now, the question to be answered is: how does the building appear in the TanDEM-X raw DEM? The generation of the raw DEM from the unwrapped phase involves two steps: phase to height conversion and mapping from slant-range coordinates to geographic coordinates (*geocoding*). It should be noted that a plausible building reconstruction is not possible using just one single-pass acquisition. In fact, the raw DEM generation in layover areas is an ill-posed problem (for the simple case in Fig. 9 there are three unknown heights for a known phase value). In the literature, solutions to this specific SAR problem, based on the use of several acquisitions, started to appear more than ten years ago (Reigber and Moreira, 2000) under the name of *SAR tomography*.

Fig. 6. Master channel amplitude of the high resolution spotlight acquisition acquired over Las Vegas on the 25th September, 2011.

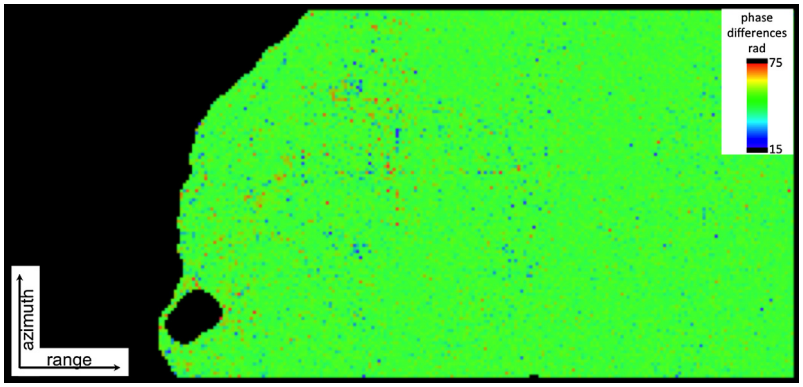

Fig. 7. Radargrammetric control map for the raw DEM operationally processed. The black area corresponds to phase unwrapping errors, spanning 24% of the scene.

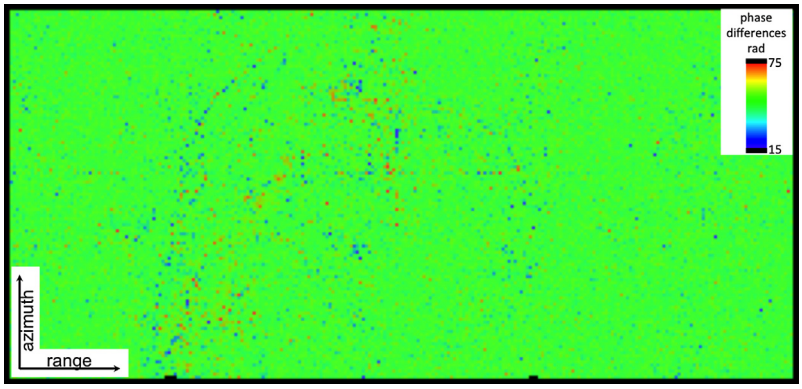

Fig. 8. Radargrammetric control map for the raw DEM processed experimentally.

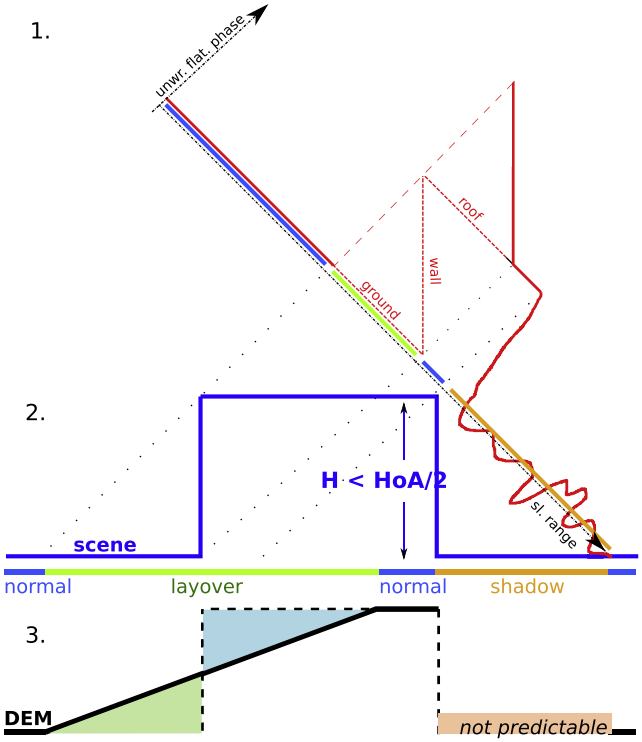

Fig. 9. Theoretical phase trend for a flat roof building and corresponding DEM. 1. Unwrapped phase trend. The interferometric phase is flattened. 2. Scene to map. The rectangular profile represents a building whose height does not exceed half the Height of Ambiguity (HoA) 3. Resulting TanDEM-X raw DEM.

Nevertheless, in the operational TanDEM-X processor, a raw DEM is automatically generated for urban areas (without *invalid* samples), even in the presence of the ill-posed problem: one of the purposes of this paper is to demonstrate its shape. The employed geocoding algorithm is the one proposed by (Schwaebisch, 1998). In fact, it is not only a geocoding algorithm as it includes the phase to height conversion. The starting point of the technique is the DEM grid and the unwrapped phase map is exploited by inverse geolocation and simulation (Rossi et al., 2010). The layover points are automatically discarded by the processing as they do not satisfy a convergence criterion between the simulated and processed unwrapped phase. As a result, a ramp connecting the layover boundaries is created (Fig. 9.3). For a single building the following issues can be addressed:

Geolocation error. A building is *enlarged* to a size depending on the layover extension, as the vertical wall is mapped as a slope. This results in incorrect geolocation. Moreover, the terrain height adjacent to the building is overestimated (green area of Fig. 9.3). The layover extension depends on the incidence angle: the steeper the angle, the greater is the geolocation error and the smaller is the shadow area, whose DEM profile cannot be predicted.

Building height underestimation. The height of the layover part of the building is underestimated, as shown in the blue area of Fig. 9.3.

Building size and orientation. The size and the orientation of a building have an impact on its height accuracy. In particular, a building oriented along the azimuth direction has a larger number of pixels affected by layover compared to one oriented along the range direction, resulting in a larger height error. Larger buildings, as shown in Fig. 4, have several pixels correctly mapped, thus increasing their height accuracy (assuming absence of errors for the mapping outside the layover area). The resolution of the sensor plays also a role on the number of the correctly mapped pixels for large buildings: the higher the resolution, the larger the mapping of pixels not subjected to layover or shadow, the better the final building height accuracy.

3. Analysis of the DEM and enhancements

3.1. High resolution TanDEM-X raw DEM generation

The test site chosen for the analysis is Berlin (Germany). The bistatic spotlight acquisition was acquired on the 4th of January, 2012. The satellites had a normal baseline of about 110 m yielding a height of ambiguity of 65 m, the incidence angle at the center of the scene is 41.8°. The geometrical and processing parameters are given in Table 2.

The upper part of Fig. 10 shows the raw DEM, generated at a raster of 2.5 m using the IDAN algorithm (Section 2.2) for the interferogram generation and the coherence computation. In the lower part of the figure a visual comparison for the boxed area between four different DEMs is provided. Whereas a quantitative analysis is provided in the next section, a qualitative one is given below.

Available and processed DEMs. The spotlight acquisition on the 4th of January is used for the generation of the high resolution raw DEM. Besides the experimentally processed raw DEM (with adaptive filtering), an equal resolution raw DEM is generated with operational algorithms. A standard resolution raw DEM of 12 m is generated from a stripmap acquisition, acquired on August 11th, 2011, having a normal baseline of 135 m and a height of ambiguity of +50 m. The center scene incidence angle

Table 2
Processing parameters for the Berlin spotlight test site.

Range bandwidth	300 MHz
PRF	8200 Hz
Center incidence angle (master)	41.8°
Effective baseline	108.1 m
Height of ambiguity	+65.4 m
SSC pixel spacing (range)	0.45 m
SSC pixel spacing (azimuth)	0.86 m
Spectral shift filtering	Enabled
Multi-look algorithm	IDAN
Total number of looks	20
Interferogram resolution	2.72 m
Mean coherence	0.69

Table 3
Input data acquisition dates and availability.

Input data	Acquisition date	Availability
DLR SRTM X-SAR	23-02-2000	Public
Spotlight TDM SSC	04-01-2012	TDM science users
Stripmap TDM SSC	11-08-2011	TDM science users
LiDAR	January–March 2009	Internal

is 41degr. In addition, a DLR SRTM X-SAR DEM with 30 m resolution and a LiDAR DEM at 1 m raster are available (see Table 3). The latter is also used as ground truth.

Building ramp. The ramp on the side of the building facing the satellites, explained in Section 2.3, is quite evident throughout the raw DEM in Fig. 10. The left side of the buildings is affected by layover. Buildings appear wrongly geolocated due to this issue. Buildings oriented in azimuth are more subject to this phenomenon.

Local phase unwrapping errors. Phase unwrapping issues may manifest themselves in the DEM at two scales: a large error, like the one in Fig. 7, and a local or micro-error, not detectable with the radargrammetric map. These second ones can be caused by shadow/noise and appear in the DEM as holes (dark blue color in Fig. 10) or spikes (dark red). Their deviation from the real height is a multiple of the height of ambiguity. A smoother phase and an enhanced coherence, obtained by using adaptive fringe filters (Section 2.2), have been demonstrated to reduce these errors. An example is shown in the lower part of Fig. 10. The rectangular building at the upper-left part of the image is the German parliament building. The building is not present at all, replaced by a *hole* instead, in the operational raw DEM (second from the left and Fig. 1). When increasing the resolution, the building appears (third DEM portion), even though micro-errors are present, like its upper-left part. Only the use of a filter mitigates the errors. The parliament building is only one example, dozens are noticeable when comparing filtered and unfiltered DEMs.

Vegetated areas. Tree heights are underestimated, as visible comparing TanDEM-X to LiDAR for the park at the southern part of the German parliament building.

DEM evolution. The first DEM section, DLR SRTM X-SAR, has been added just to show the gain in detail when increasing the sensor resolution (left to right).

3.2. DEM generation from Persistent Scatterer Interferometry

The purpose of the next two sections is to show how the integration of Persistent Scatter Interferometry (Perissin and Rocca, 2006) can improve the TanDEM-X raw DEM at the buildings location. For this purpose, a geocoded PS point cloud over Berlin, generated as in (Gernhardt and Bamler, 2012), is used as input for the generation of the so called *PSI-DEM*. The PSI-DEM is a rasterized version of the point cloud with some particular solution for treating the buildings. The straightforward solution of using the maximum height value of all the PSs within each cell of the PSI-DEM cannot be applied here, as the uncertainty in elevation estimates of the PS would lead to a biased result (Zhu and Bamler, 2010). Thus, the more robust median height value is used for each cell. However, a good solution cannot be obtained by this operator if façade PS are included. Consequently, these points have to be separated at first. To this end, a classification based on a Principal Component Analysis (PCA) is conducted. PCA identifies points that are mainly aligned vertically. The two main components of the PCA create a vertical plane in a Cartesian coordinate system. In addition, statistical parameters like local point density, local variance of height values and distance to the plane obtained by the PCA are evaluated and allow a refinement of the classification. After the separation of façade and roof/ground PS, both point clouds are converted to rasterized DEMs using the median operator for the cells of the roof/ground PS data and the maximum value for the cells of the façade PS data. In a final step, the holes of the roof/ground PSI-DEM are filled by information of the façade PSI-DEM, if data is available. Finally, the results are revised by morphological operations to fill isolated holes and to remove isolated cells, because buildings are assumed to appear as closed surface formations in the DEM.

3.3. DEM fusion

The main objective of an integration of a PSI-DEM and a TanDEM-X raw DEM is to solve the general building height underestimation problem. Assuming that TanDEM-X is underestimating the heights at the building locations, the simplest solution is to use it just to fill the invalid values of the PSI-DEM. A section of the Berlin raw DEM in which the PSI information is integrated in TanDEM-X is shown in Fig. 11. To visually better understand the improvements, a 3D model of the parliament of Germany, already investigated in Section 3.1, is shown in Fig. 12. The height slope explained in Section 2.3 is quite evident at the front façade of the structure (Fig. 12a). Moreover, a second ramp, caused by a height jump (internal atrium), is visible in the right part of the building from this perspective. A precise DSM reconstruction from LiDAR data can be seen in Fig. 12c. The fused DEM TanDEM-X - PSI is shown in Fig. 12b. The improvement in comparison to the sole TanDEM-X DEM is noticeable. At the building location the height slope is no longer present. The remaining slope next to the front façade is due to the fact that the PSI-DEM is not defined for the ground area adjacent to the parliament. The overall shape of the building also better fits with the reference. For this section, the absolute error for TanDEM-X is 4.17 ± 12.8 m and for the fused DEM is 0.87 ± 9.66 m. The improvements can be visually recognized comparing Figs. 13 and 14, representing the height differences for the whole tile between reference and TanDEM-X and between reference and fused DEM, respectively. Whereas in Fig. 13 the "ramp effect" appears evident at the building locations, in Fig. 14 this effect appears strongly mitigated, with remaining errors at the ground area next to the façades, where no PSI data is available. Further evident discrepancies emerge at the water channel and for structures not present in the reference DEM (an example is highlighted in Fig. 13). A quantitative analysis of the errors for the complete tile is provided in the next subsection.

3.4. Results analysis

Even though the relative TanDEM-X height accuracy requirements are successfully accomplished (Rizzoli et al., 2012), they

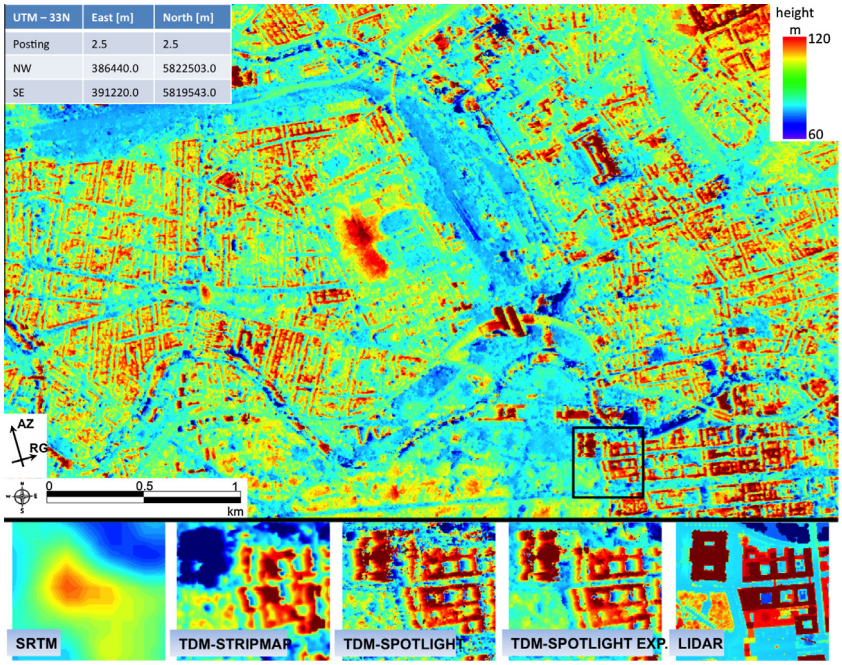

Fig. 10. Experimental 2.5 m resolution TanDEM-X DEM of Berlin, Germany (top). In the lower part, a visual comparison of the highlighted portion is shown for DLR SRTM X-SAR DEM, operational TanDEM-X raw DEM, experimental high-resolution TanDEM-X raw DEM, experimental filtered high-resolution TanDEM-X raw DEM and LiDAR DEM (left to right). The DEMs are in UTM projection (coordinates at the top-left). The SAR angles are shown at the bottom-left.

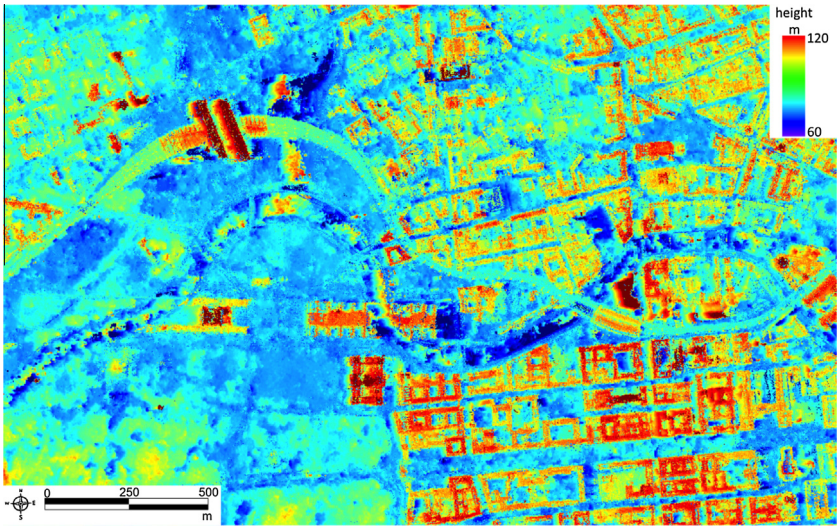

Fig. 11. Section of the Berlin raw DEM with the PSI information integrated. The color scale is the same as Fig. 10.

are too coarsely defined for urban areas. The cell of one degree square used for the DEM height error specification is too large for an accurate analysis over a single city. Considering that PSs mainly appear at building locations in the scene (Schunert and Soergel, 2012), the PSI-DEM validity map can also be seen as a segmentation map between structures (valid inside PS cells) and non-structures (invalid/outside PS cells). Using this knowledge, and the reference DEM, three histograms representing the height differences for the whole tile are analyzed.

First, the error for non-structures (i.e. roads, vegetation) is shown in Fig. 15. The sample mean and standard deviation are 0.32 and 7.64 m, respectively, and the Root Mean Square Error (RMSE) 7.65 m. A Gaussian fit is superimposed. The Gaussian standard deviation and Full Width at Half Maximum (FWHM) are 6.22 and 14.64 m, respectively. Whereas the mean is centered around zero, meaning that the TanDEM-X raw DEM is well calibrated, the histogram appears bimodal. The first narrow lobe corresponds in fact to the ground areas next to every building for which TanDEM-X overestimates the heights, as explained in Section 2.3. The mean overestimation is around 2 m.

Second, the error between the reference and TanDEM-X, considering the structures, is shown in Fig. 16. The histogram has statistics comparable with the previous one, with a slightly smaller Gaussian standard deviation. It is centered at around 4 m. The TanDEM-X building mis-calibration, as sketched in Fig. 9, is thus demonstrated to be around four meters for the test case. For other scenarios, this value may change depending on the current incidence angle, which triggers the height slope at the building layover

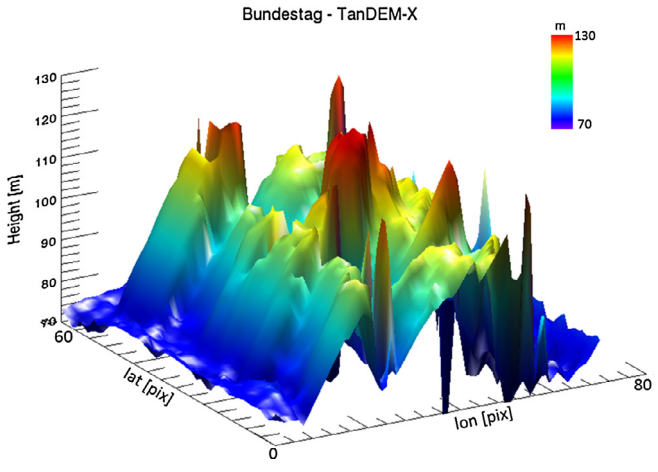

(a) TanDEM-X.

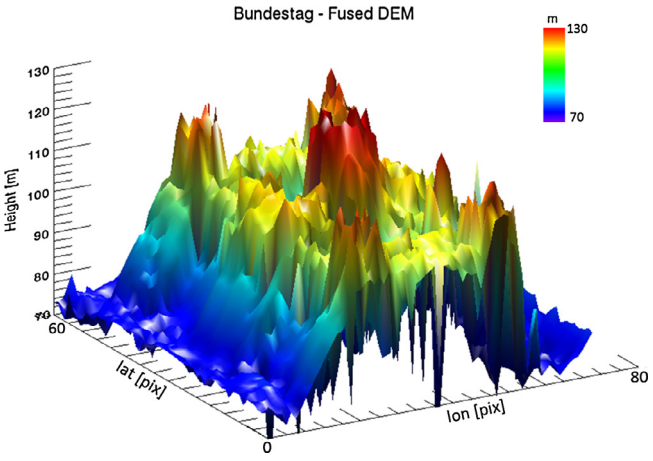

(b) TanDEM-X/PSI fused DEM.

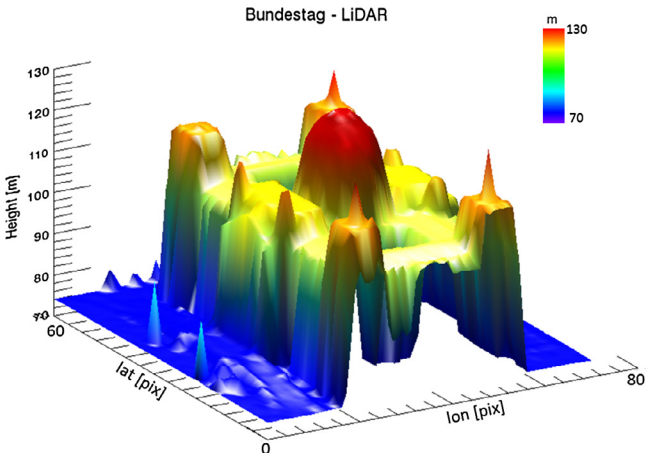

(c) LiDAR

Fig. 12. 3D model of the German parliament as seen by TanDEM-X (a), Fused DEM (b) and LiDAR (c). The model extent is 150 (northing) by 200 (easting) meters. Using LiDAR as reference, the absolute error for TanDEM-X is 4.17 ± 12.8 m and for the Fused DEM is 0.87 ± 9.66 m.

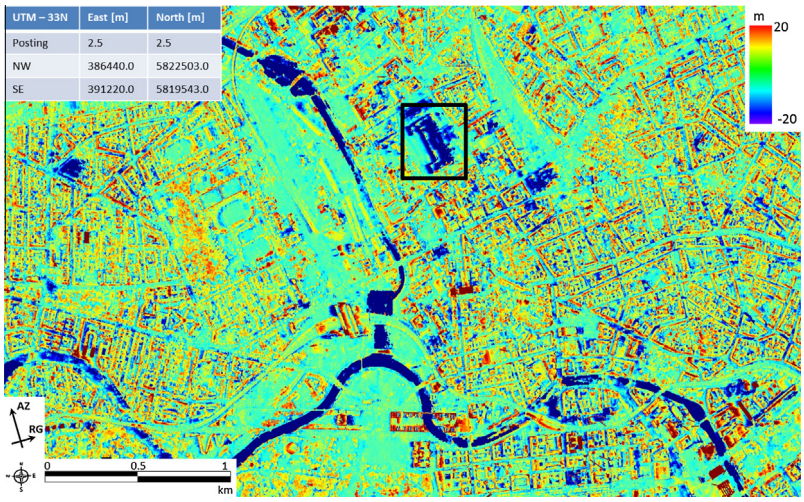

Fig. 13. Height difference map between the reference and the TanDEM-X raw DEM. The highlighted portion is a new building, not present in the reference DEM.

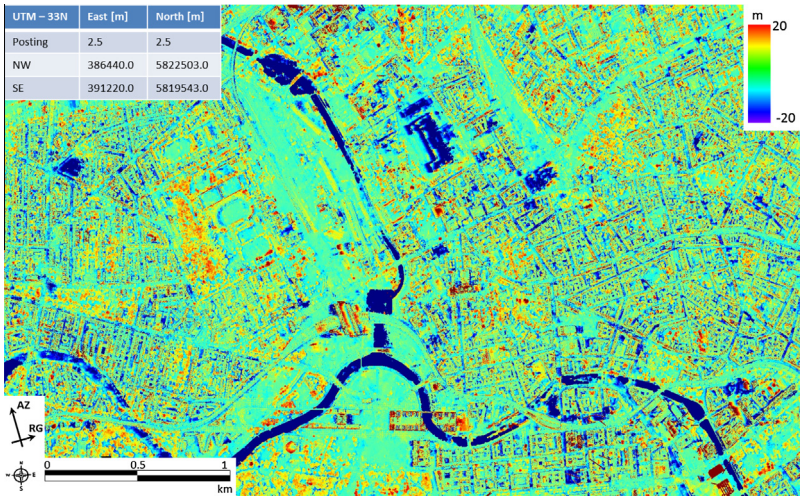

Fig. 14. Height difference map between the reference and the fused DEM.

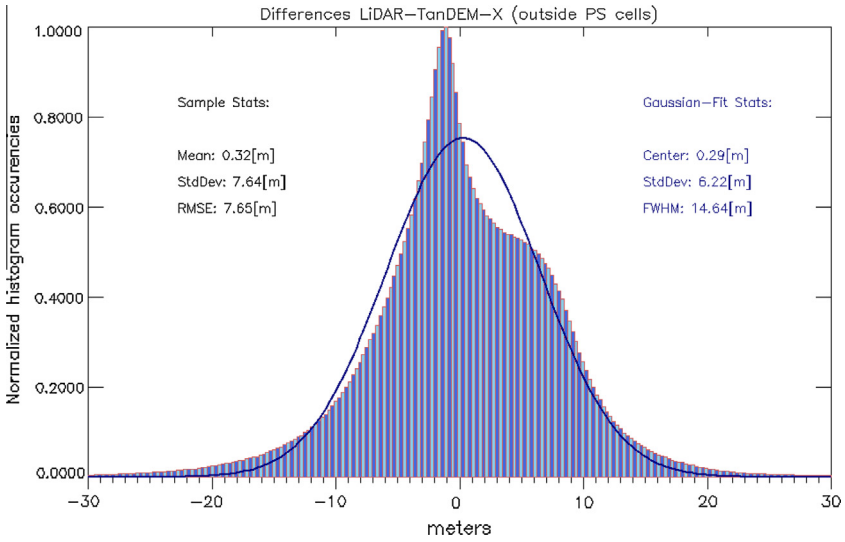

Fig. 15. Normalized histogram of the difference between reference and TanDEM-X DEMs for non-structure areas. The sample mean, standard deviation and RMSE are 0.32, 7.64 and 7.65 m, respectively. A Gaussian fit (blue line) provides a mean, standard deviation and a full width at half maximum (FWHM) of 0.29, 6.22 and 14.64 m, respectively. (For interpretation of the references to color in this figure legend, the reader is referred to the web version of this article.)

positions. The small peak, highlighted in Fig. 16, is caused by local occlusions.

Third, the building layover issue is highly mitigated when integrating PSI with the TanDEM-X raw DEM. The error of the fused DEM at the structure locations is now centered around zero (Fig. 17). The histogram is also narrower when compared with the previous ones, with a halved FWHM. The standard deviation is around 3 m. There are some residual non-linearities, resulting in taller tails when comparing with Gaussian distributions. These errors, which increase the sample statistics values, have different origins. Inspections of the locations of DEM disparities revealed large differences appearing very often at façade positions. Most likely, this is an indication for the occurrence of the following errors. At first, residual geocoding errors of the PS height point cloud will bias the location of façade PS. In consequence, the PSI-DEM will deviate especially at these cells from a reference (like a LiDAR DEM) and the differences will be large, i.e., the error corresponds to the height difference between ground and roof of the respective building. Secondly, the restricted elevation estimation accuracy of the PSI technique might cause an erroneous geolocation in horizontal position. Consequently, these PS are evaluated in height in a neighboring cell during the PS-DEM creation causing local deviations from the reference. The magnitude of these errors in the height of the PS-DEM cannot be predicted, whereas the occurrence also depends on the resolution, i.e., the cell size of the DEM. Last, the reference DEM might include structures that are not included in the PS data due to the different measurement techniques. For example, house roofs are very well recorded by ALS sensors (small footprint and high point density), whereas PSs only appear at corners or ridges (typical prerequisite: triple reflections) of a minimum extent. For example, for a signal-to-clutter ratio of 2.0, a side length of the corner reflector of 8 cm is required. By experience it is known that PS mainly appear at façade position and the distribution on roofs is very sparse. Accordingly, the roof is not represented completely in the PS-DEM. In consequence, deviations between both DEMs will occur at the magnitude of the individual building height. A more detailed analysis will be conducted in the future.

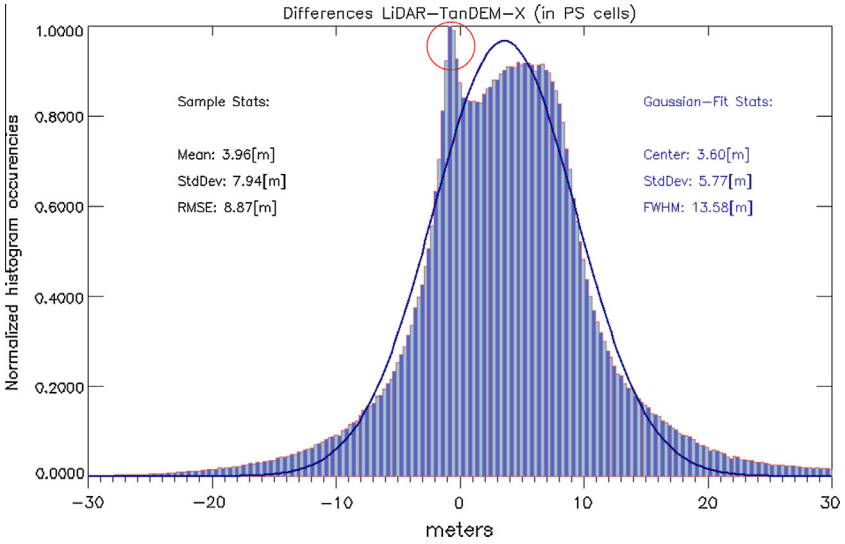

Fig. 16. Normalized histogram of the difference between reference and TanDEM-X DEMs for structure areas. The sample mean, standard deviation and RMSE are 3.95, 7.94 and 8.87 m, respectively. A Gaussian fit (blue line) provides a mean, standard deviation and a full width at half maximum (FWHM) of 3.60, 5.77 and 13.58 m, respectively. (For interpretation of the references to color in this figure legend, the reader is referred to the web version of this article.)

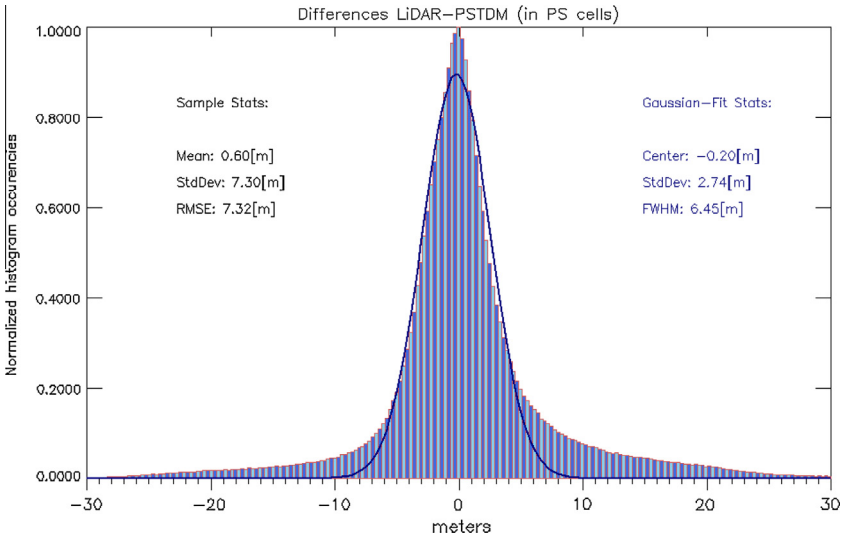

Fig. 17. Normalized histogram of the difference between reference and fused DEMs for structure areas. The sample mean, standard deviation and RMSE are 0.60, 7.30 and 7.32 m, respectively. A Gaussian fit (blue line) provides a mean, standard deviation and a full width at half maximum (FWHM) of −0.20, 2.74 and 6.45 m, respectively. (For interpretation of the references to color in this figure legend, the reader is referred to the web version of this article.)

Nevertheless, the improvements obtained compared to the sole use of TanDEM-X are noticeable.

4. Conclusions

This paper shows the potential of TanDEM-X in the mapping of urban areas, globally acquired by the mission. A first analysis of experimental high resolution urban raw DEMs was provided. The quality of the phase has been enhanced using SAR amplitude statistics by adaptive multilooking techniques (IDAN). The enhanced phase, together with the enhanced coherence, yields a smaller number of phase unwrapping errors. Moreover, they allow the generation of raw DEMs having a fine resolution of a few meters. It is demonstrated how layover affects the shape of the raw DEM creating height ramps at the building locations. The direct consequence is a global building height underestimation. For the chosen test site, the mean underestimation is around 4 m. This error was strongly mitigated by introducing PS results into the raw DEM, increasing the global accuracy of the fused DEM. Nevertheless, the ground area located next to the building is subject to the remaining errors of the TanDEM-X raw DEM (height slope) as no height information is available from the PSI-DEM due to the lack of PS on bare ground. A further improvement, planned as future research, is to fuse tomographic results with TanDEM-X data. In any case, the urban raw DEMs generated by the TanDEM-X mission allow the mapping of single buildings with a great amount of detail, representing valuable information in all applications requiring municipal mapping.

Acknowledgements

The authors would like to thank the anonymous reviewers for their helpful contribution as well as R. Brcic, M. Eineder, T. Fritz,

X. Zhu (DLR) and E. Erten (ITU) for the fruitful discussions on the paper topics. The TanDEM-X project is partly funded by the German Federal Ministry for Economics and Technology (Föerderkennzeichen 50 EE 1035).

References

Abanmy, F., Khamees, H., Scarpace, F., Vonderohe, A., 1995. An evaluation of DEM and ortho-photo generation on OrthoMAX. In: Proceedings of ACSM/ASPRS Annual Convention and Exposition, Charlotte, NC, 27 February–3 March, pp. 489–487.

Bamler, R., Eineder, M., 2005. Accuracy of differential shift estimation by correlation and split-bandwidth interferometry for wideband and delta-k SAR systems. IEEE Geoscience and Remote Sensing Letters 2 (2), 151–155.

Breit, H., Younis, M., Balss, U., Niedermeier, A., Grigorov, C., Hueso-Gonzalez, J., Krieger, G., Eineder, M., Fritz, T., 2011. Bistatic syncronyzation and processing of TanDEM-X Data. In: Proceedings of IEEE International Conference on Geoscience and Remote Sensing Symposium, IGARSS 2011, 24–29 July. Vancouver, Canada, pp. 2424–2427.

Deledalle, C.A., Denis, L., Tupin, F., 2011. NL-InSAR: nonlocal interferogram estimation. IEEE Transactions on Geoscience and Remote Sensing 49 (4), 1441–1452.

Erten, E., Reigber, A., Hellwich, O., 2010. Generation of three-dimensional deformation maps from InSAR data using spectral diversity techniques. ISPRS Journal of Photogrammetry and Remote Sensing 65 (4), 388–394.

Fritz, T., Rossi, C., Yague Martinez, N., Rodriguez Gonzalez, F., Lachaise, M., Breit, H., 2011. Interferometric processing of TanDEM-X Data. In: Proceedings of IEEE International Conference on Geoscience and Remote Sensing Symposium, IGARSS 2011, 24–29 July. Vancouver, Canada, pp. 2428–2431.

Gamba, P., DellAcqua, F., Houshmand, B., 2002. SRTM data characterization in urban areas. ISPRS Commission III Symposium on Photogrammetric Computer Vision 34 (Part 3B), 55–58.

Gatelli, F., Guarnieri, A.M., Parizzi, F., Pasquali, P., Prati, C., Rocca, F., 1994. The wavenumber shift in SAR interferometry. IEEE Transactions on Geoscience and Remote Sensing 32 (4), 855–865.

Gernhardt, S., Bamler, R., 2012. Deformation monitoring of single buildings using meter-resolution SAR data in PSI. ISPRS Journal of Photogrammetry and Remote Sensing 73 (1), 68–79.

Gruber, A., Wessel, B., Huber, M., Roth, A., 2012. Operational TanDEM-X DEM calibration and first validation results. ISPRS Journal of Photogrammetry and Remote Sensing 73 (1), 39–49.

Haala, N., Brenner, C., 1999. Extraction of buildings and trees in urban environments. ISPRS Journal of Photogrammetry and Remote Sensing 54 (23), 130–137.

Just, D., Bamler, R., 1994. Phase statistics of interferograms with applications to synthetic aperture radar. Applied Optics 33 (20), 4361–4368.

Krieger, G., Moreira, A., Fiedler, H., Hajnsek, I., Werner, M., Younis, M., Zink, M., 2007. TanDEM-X: a satellite formation for high-resolution SAR interferometry. IEEE Transactions on Geoscience and Remote Sensing 45 (11), 3317–3341.

Leberl, F., 1990. Radargrammetric image processing. Artech House, Norwood, MA.

Yague Martinez, N., Eineder, M., Brcic, R., Breit, H., Fritz, T., 2010. TanDEM-X mission: SAR image coregistration aspects. In: Proceedings of 8th European Conference on Synthetic Aperture Radar, EUSAR 2010, Aachen, Germany, 7–10 June, 4 p. (on CD-ROM).

National Imagery and Mapping Agency (NIMA), 2010. High Resolution Terrain Information (HRTI): Performance Specification, MIL-PRF-89048.

Perissin, D., Rocca, F., 2006. High-accuracy urban DEM using permanent scatterers. IEEE Transactions on Geoscience and Remote Sensing 44 (11), 3338–3347.

Reigber, A., Moreira, A., 2000. First demonstration of airborne SAR tomography using multibaseline L-band data. IEEE Transactions on Geoscience and Remote Sensing 38 (5), 2142–2152.

Rizzoli, P., Braeutigam, B., Kraus, T., Martone, M., Krieger, G., 2012. Relative height error analysis of TanDEM-X elevation data. ISPRS Journal of Photogrammetry and Remote Sensing 73 (1), 30–38.

Rossi, C., Eineder, M., Fritz, T., Breit, H., 2010. TanDEM-X mission: raw DEM generation. In: Proceedings of 8th European Conference on Synthetic Aperture Radar, EUSAR 2010, Aachen, Germany, 7–10 June, 4 p. (on CD-ROM).

Rossi, C., Fritz, T., Breit, H., Eineder, M., 2011. First urban TanDEM-X RawDEMs analysis. In: Proceedings of Joint Urban Remote Sensing Event, JURSE 2011, Munich, Germany, 11–13 April, pp. 65–68.

Rossi, C., Fritz, T., Eineder, M., Erten, E., Zhu, X.X., Gernhardt, S., 2012. Towards an urban DEM generation with satellite SAR interferometry. International Archives of Photogrammetry Remote, Sensing and Spatial Information Sciences 39 (Part B7), 73–78.

Rossi, C., Rodriguez Gonzalez, F., Fritz, T., Yague Martinez, N., Einieder, M., 2012. TanDEM-X calibrated raw DEM generation. ISPRS Journal of Photogrammetry and Remote Sensing 73 (1), 12–20.

Schmitt, M., Magnard, C., Brehm, T., Stilla, U., 2011. Towards airborne single pass decimeter resolution SAR interferometry over urban areas. In: Photogrammetric Image Analysis. Lecture Notes in Computer Science, vol. 6952. Heidelberg, Berlin, pp. 197–208.

Schunert, A., Soergel, U., 2012. Grouping of Persistent Scatterers in high-resolution SAR data of urban scenes. ISPRS Journal of Photogrammetry and Remote Sensing 73 (1), 80–88.

Schwaebisch, M., 1998. A fast and efficient technique for SAR interferogram geocoding. In: Proceedings of IEEE International Conference on Geoscience and Remote Sensing Symposium, IGARSS 1998, Seattle, USA, 6–10 July, pp. 1100–1102.

Sefercik, U.G., Schunert, A., Soergel, U., Watanabe, K., 2012. Validation of DEMs derived from high resolution SAR data: a case study on Barcelona. ISPRS Annals of Photogrammetry Remote Sensing and Spatial Information Sciences 1 (Part 7), 49–54.

Smith, J.S., Smith, D.G., 1996. Operational experiences of digital photogrammetric systems. International Archives of Photogrammetry Remote Sensing and Spatial Information Sciences 31 (Part B2), 357–362.

Soergel, U., Thoennessen, U., Brenner, A., Stilla, U., 2006. High-resolution SAR data: new opportunities and challenges for the analysis of urban areas. IEE Proceedings on Radar, Sonar and Navigation 153 (3), 294–300.

Thiele, A., Wegner, JD., Soergel, U., 2010. Building reconstruction from multi-aspect InSAR data. In: Radar Remote Sensing of Urban Areas. Springer, pp. 187–214.

Vasile, G., Trouve, E., Ciuc, M., Buzuloiu, V., 2004. General adaptive-neighborhood technique for improving synthetic aperture radar interferometric coherence estimation. Journal of the Optical Society of America A 21 (8), 1455–1464.

Wehr, A., Lohr, U., 1999. Airborne laser scanning an introduction and overview. ISPRS Journal of Photogrammetry and Remote Sensing 54 (23), 68–82.

Zebker, H.A., Villasenor, J., 1992. Decorrelation in interferometric radar echoes. IEEE Transactions on Geoscience and Remote Sensing 30 (5), 950–959.

Zhu, X., Bamler, R., 2010. Very high resolution spaceborne SAR tomography in urban environment. IEEE Transactions on Geoscience and Remote Sensing 48 (12), 4296–4308.

A.6. High-resolution InSAR building layovers detection and exploitation

Rossi, C., and Eineder, M., High-resolution InSAR building layovers detection and exploitation. *IEEE Transactions on Geoscience and Remote Sensing*, 53(12), 6457-6468, 2015.

High-Resolution InSAR Building Layovers Detection and Exploitation

Cristian Rossi and Michael Eineder, *Senior Member, IEEE*

***Abstract*—Layover affects the quality of urban interferometric synthetic aperture radar (InSAR) digital elevation models. Moreover, it is generally difficult to interpret because of the superposition of several contributions in a single SAR pixel. In this paper, a novel technique for the extraction of building layovers is first presented. It makes use of the geocoding stage embedded in the InSAR processor. It is shown that building layovers create a regular pattern in the mapping counter, a map describing the number of occurrences of a SAR pixel in the elevation model. Its exploitation yields a generation of a layover map without the use of external supports. The integration in the processor with a limited additional computational load and the capability to isolate layover signatures are additional benefits. Layover patches are then individually analyzed toward a better understanding of the complex urban signal return. A spectral estimation framework is employed to assess the slopes superimposed in the patches. Fringe-frequency estimation is involved. A set of simulations made for a nonparametric (fast Fourier transform) and a parametric (multiple signal classification) technique is performed prior to testing on real data. It is demonstrated that in X-band, for a single interferogram, just one layover contributor, when it dominates over the others, can be extracted with a sufficient accuracy. The algorithms are tested on a TanDEM-X spotlight acquisition over Berlin (Germany).**

***Index Terms*—Fringe-frequency estimation, geocoding, interferometric SAR (InSAR), layover detection, layover scattering decomposition, super-resolution, urban mapping.**

I. Introduction

An URBAN area is probably the most complex terrain to map with synthetic aperture radar (SAR) sensors. Geometrical distortions such as layover and shadow [1] always occur due to the SAR side looking viewing geometry on the frequent metropolitan slope discontinuities. Besides distortions, multiple scattering phenomena and building overlays make data interpretation difficult [2]–[4]. In this context, a height map generation is quite a challenging issue. Optical and LiDAR remote sensing technologies are widely used for this purpose [5], [6]. Next to them, urban reconstruction with SAR data is attractive, considering the increasing number of civil missions. For instance, inherent sensor proprieties such as night and atmosphere-free vision and data globalization may overcome optical and LiDAR limitations. In general, a surface model is a demanding product for many management applications and several studies have been reported in the recent years employing interferometric SAR (InSAR). They can be grouped in two research branches. Multibaselines techniques use a stack of SAR images over a specific area to derive the elevation information. Contrariwise, single-baseline techniques exploit the sole interferometric phase generated with two acquisitions. Within the first branch, tomographic algorithms have been applied to SAR (TomoSAR) with reconstruction accuracy depending on the number of images that has been used, the signal-to-noise ratio (SNR), and the baseline distribution [7], [8]. In the interesting parameter range of TomoSAR, the achievable height accuracy is on the order of a meter. In the tomographic approach, layover patches are not predetected, but the number of layover components are estimated in a pixel-wise fashion for a set of candidate pixels [9]. Within the second branch, in [10] a stochastic framework has been established to jointly retrieve a building classification and a height map. A mean root-mean-square error (RMSE) of 2.5 m has been reported for 19 buildings. Layover is estimated from the surface model itself and used to correct the classification map, but not the layover height. First studies about large-scale single-baseline polarimetric InSAR (PolInSAR) building height estimation have been presented in [11]. RMSE over 140 reference building was reported to be around 3 m. In [12], the TanDEM-X mission, in a single-baseline configuration, has been stated capable to generate a high-resolution surface model on a raster of 2.5 m over urban areas with a RMSE of about 8 m for the complete model. In addition, here, layover elevations are neither detected nor corrected. In short, the single-baseline reconstruction accuracy is severely limited in layover zones, where multiple facets are mapped in a single SAR resolution cell. For this reason, a precise identification of those areas is of fundamental importance for a proper digital elevation model (DEM) quality assessment. Additional applications for which the layover map is a useful support are urban object simulation, detection and analysis [13], [14] and change detection aimed at disaster management [15].

Precise layover detection usually requires an accurate input DEM. In particular, the elevation model has to be reprojected in SAR coordinates (slant range, azimuth) and the distance between satellite and model cell to be computed. A change of sign in the derivative of the distance function for iso-azimuth lines identifies the beginning of the layover area [16]. With this method, a right layover map can be generated for urban areas only when a sufficiently accurate DEM over the area is available (e.g., a LiDAR one). To be noticed, the DEM generated employing one SAR interferogram cannot be used for the purpose as not accurate enough on building layover positions

Manuscript received October 2, 2014; revised February 20, 2014; accepted May 30, 2015.

The authors are with the Remote Sensing Technology Institute, German Aerospace Center (DLR), D-82234 Oberpfaffenhofen, Germany (e-mail: cristian.rossi@dlr.de; michael.eineder@dlr.de).

Color versions of one or more of the figures in this paper are available online at http://ieeexplore.ieee.org.

Digital Object Identifier 10.1109/TGRS.2015.2440913

[12]. As an alternative, without a reference DEM, the particular layover phase trend [17] can be exploited. Preliminary studies on the layover detection exploiting the interferometric single-baseline wrapped phase have been performed [18]. In this paper, a novel technique to detect building layovers is introduced. The InSAR layover model is described in Section II. Layover geocoding, i.e., how layover pixels appear in the generated DEM, is analyzed in Section III. These two sections provide the theoretical background for the detection method presented in Section IV. The absence of building model hypothesis and the low computational cost are considerable aspects of the proposed algorithm.

The second part of this paper deals with the exploitation of the detected patches. In practice, building layover is composed of several contributors. At least two contributors superimpose in the layover area. Each contributor lies on a terrain slope (e.g., ground slope, wall slope, or roof slope). Once layover patches are detected, slope estimation can be carried out through a frequency analysis, reminding that the interferometric phase is proportional to terrain slopes [19]. In the SAR community, the fringe-frequency estimation is a well-known topic. The single frequency estimation is often linked to the phase unwrapping problem [20], whereas the multiple estimation to the tomographic framework [7]. As aforementioned, the latter case exploits a multibaseline data stack to provide the layover decomposition. In this paper, the estimation is instead performed in the spatial domain, looking for the number of slopes included in a building layover patch. In Section V, this problem is studied in detail with simulations and tested on real data. The focus is on the particular urban case, considering the periodogram and the conventional multiple signal classification (MUSIC) algorithm as references.

To introduce the problem, a clear example of single layover contributor dominance is shown in Fig. 1, a high-resolution spotlight interferometric data take [21] over Las Vegas, USA, acquired with TanDEM-X. In Fig. 1(a), the master channel amplitude is shown with the slant range coordinate in vertical direction, to highlight skyscraper layovers with a human-eye perspective. These high-rise constructions are well visible in the SAR amplitude as their layover signal is mainly dominated by their facades. Due to the typical skyscraper structure, i.e., extending in the vertical more than in the horizontal dimension, at the side-looking SAR geometry, roof features are superimposed just in a small layover portion and not in the full layover area. Closely inspecting the layover return, it is possible to detect structural features that behave as corner reflectors (e.g., window eaves). These features have a stronger backscatter than ground scatterers, thus making facade layover contributors dominate over others. The impact in the TanDEM-X interferogram is represented in Fig. 1(b). At skyscraper locations, a regular fringe pattern is well visible. The range fringe frequency corresponds to a vertical terrain, meaning that layover range cells are fully characterized by scatterers at the building facade, despite the superposition with ground scatterers. By counting the number of fringes and considering the height of ambiguity of 33 m, it is even possible to provide an estimate of the local skyscraper height. Whereas for high-rise buildings, layover detection seems to be at least a visually manageable task,

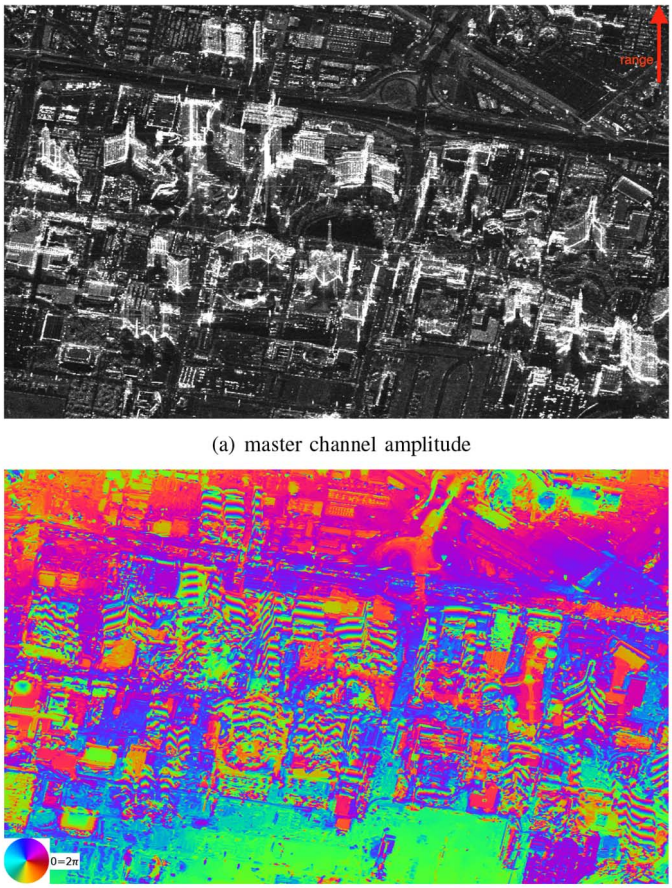

(a) master channel amplitude

(b) flattened interferogram

Fig. 1. Las Vegas *The Strip* as imaged by a spotlight TanDEM-X take. (a) Skyscraper layovers show a facade dominance in the amplitude signal. (b) The flattened interferogram at the skyscraper locations presents a regular fringe pattern.

this is not the case for regular buildings. Mixed contributions do not provide a clear fringe pattern. Rooftops may be fully included in the layover patch depending on the incidence angle, and structures as chimneys and antennas mix up with facade structures yielding a difficult interpretation. Tilted roof slopes may superimpose with the vertical and the horizontal slope. These considerations enclose the two main objectives of this paper. First, the definition of an algorithm to automatically detect layover zones, in order to identify low accuracy portions of an urban interferometric DEM. Second, the exploitation on a building-by-building base, in order to interpret the signal return and provide layover decomposition.

II. InSAR model

The simplest building shape is a rectangular cuboid, with the ground, roof, and wall represented by the lower and higher horizontal and the vertical segments, respectively, as in Fig. 2. In the layover area, the signal return is a superposition of these contributions. In the interferometric framework, for the master satellite, the slant range distance R_0 between the satellite and the three layover scatterers is not varying by definition. On the contrary, three different distances are measured between slave satellite and points on ground (R_1), wall (R_2), and roof (R_3).

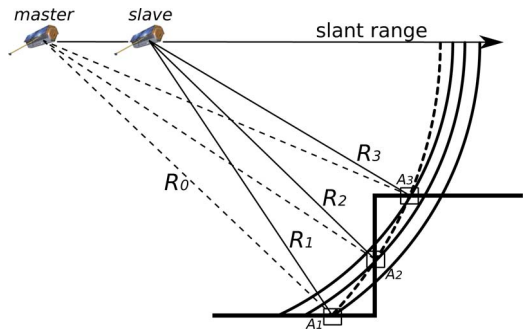

Fig. 2. Interferometric signal model for a building layover pixel. R_1 is the slant range distance between the satellite and the ground scatterer A_1, similarly for the wall scatterer (R_2, A_2) and the roof scatterer (R_3,A_3). R_0 is the master distance between the satellite and the three scatterers.

Thus, master s_m and slave s_s focused signal at the range r and azimuth x in the layover area are [22]

$$s_m(r,x) = \sum_{i=1}^{3} A_i(r,x)\exp\{-j2kR_0(r,x)\}$$
$$s_s(r,x) = \sum_{i=1}^{3} A_i(r,x)\exp\{-j2kR_i(r,x)\} \quad (1)$$

where k is the wavenumber, and A_i is a complex variable, including the bidimensional system impulse response and the local backscatter, which are assumed equal in both geometries.[1]

The interferometric phase is the argument of a sum of nine complex terms

$$\begin{aligned}\phi(r,x) &= \arg\left(s_m(r,x)s_s^*(r,x)\right)\\ &= \arg\left(\sum_{i=1}^{3}\left[\left(A_i^*\sum_{j=1}^{3}A_j\right)\right.\right.\\ &\quad\left.\left.\cdot\exp\{-j2k\left(R_i(r,x)-R_0(r,x)\right)\}\right]\right).\end{aligned} \quad (2)$$

The analytic derivation of (2) without further approximations is not bringing to a compact expression. Instead, simulations and test on real data have been conducted [24]. Equation (2) is plotted in Fig. 3 assuming A_i as a real constant for simplicity. The factors A_i are considered as weights to the exponential terms, i.e., they represent the impact of the single layover components in the signal. The interferometric phase is a decreasing function for increasing slant ranges in case of positive height of ambiguity. A noticeable phase gradient is at the layover beginning, with a singular exception for total ground dominance ($A_2 = A_3 = 0$). Total wall dominance ($A_1 = A_3 = 0$) yields the highest gradient. Mixed weights produce phase jumps with spreads depending on the actual backscattering configuration. The absolute phase layover trend is nonlinear, with the exception of single component dominance.

[1]Backscattering variations are measured in case of different ambient conditions, different system parameters or target changes. For small baselines, in an urban scenario, slight changes may be expected for the ground contribution, particularly in a dual-pass interferometric configuration. In a single-pass configuration, very little changes or no changes are expected [23].

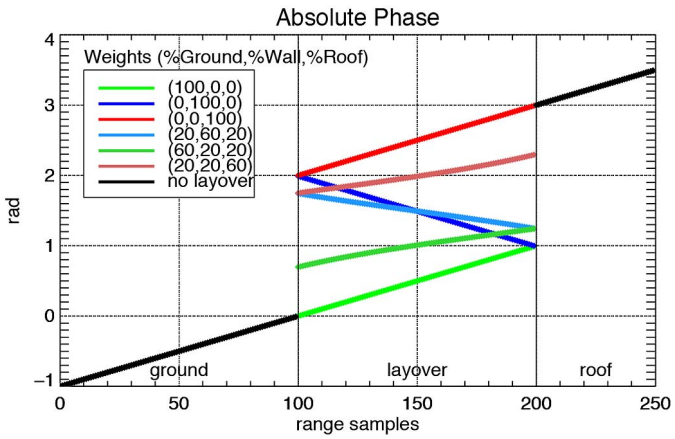

Fig. 3. Noise-free absolute phase simulation of a step function considering various exponential weights for the different segments composing the function. Ground, wall and roof represent the lower horizontal, the vertical and the higher horizontal segments, respectively. In the layover area, six cases are considered with different colors.

The range spectrum of the interferogram $I(f_r)$ can be derived by Fourier-transforming (2) in the range dimension

$$\begin{aligned}I(f_r) &= \sum_{i=1}^{3}\left[S_m(f_r) * S_s^*(-f_r)\right]\\ &\simeq \sum_{i=1}^{3}\left[R_{ii}(f_r-\Delta f_{r_i}) + C_{\mathrm{in}}(f_r-\Delta f_{r_i})\right.\\ &\quad\left. + C_{\mathrm{im}}(f_r-\Delta f_{r_i})\right], \quad \begin{cases} n\neq m\neq i \\ (n,m)\in[1,2,3]\end{cases}\end{aligned} \quad (3)$$

where $R_{ii}(f_r)$ is the autocorrelation of the ith layover scatterer spectrum and $C_{\mathrm{in}}(f_r)$ and $C_{\mathrm{im}}(f_r)$ are the cross correlations between the ith and the nth and the mth spectra, respectively. The spectra are bandpass filtered by the end-to-end SAR transfer function, approximated by a rectangular window [22], and shifted by Δf_r. System noise has not been considered in (1)–(3). Considering Gaussian noise, its impact is to add to (3) a broad triangular pattern centered on zero. Δf_r is proportional to the terrain slope α, according to [25]

$$\Delta f_{r_i} = -\frac{f_0\Delta\theta}{\tan(\theta-\alpha_i)} = -\frac{f_0\Delta\theta}{\tan(\theta_{\mathrm{inc}_i})} \quad (4)$$

where $\Delta\theta = B_n/R_0$, being B_n the normal baseline between the satellites, f_0 the carrier frequency, θ the master looking angle and θ_{inc} the local incidence angle. Equation (4) is valid also for the high-resolution urban scenario, although in principle, it was derived for distributed scattering, and it is currently the base of the spectral shift filtering operation in every InSAR processor [26]. High-resolution urban scenes are characterized by a set of coherent scatterers lying on planar surfaces, e.g., on a facade. These scatterers, having a stable phase, geometrically provide a set of differential paths, which is proportional to the slope, in which the scatterers are located, according to (4). An explicit example is in given Fig. 1(b), where the sequence of skyscraper window eaves at the vertical slope yields an interferometric phase with a clear fringe frequency. The same consideration

can be addressed for roof scatterers. Their radiometric pattern, hence their impact in the interferogram spectrum in (3), depends on their physical structure and cannot be uniquely defined. For instance, ground scattering may be locally a distributed one.

Thus, for the simple building model in Fig. 2, the frequency corresponding to the ground Δf_{ground} is equal to the roof one Δf_{roof} since they both have zero slope. A relationship between the flat ground and wall frequencies can be established considering the 90° separation

$$\theta_{\text{inc}}^{\text{ground}} = -\left(\frac{\pi}{2} - \theta_{\text{inc}}^{\text{wall}}\right). \tag{5}$$

In the frequency domain, (5) corresponds to a negative frequency for the ground/roof and a positive one for the wall (in the sign convention of (4)). Consequently

$$\begin{aligned}\Delta f_{\text{ground}} &= -\frac{f_0 \Delta\theta}{\tan(\theta_{\text{inc}})} \\ \Delta f_{\text{wall}} &= -\frac{f_0 \Delta\theta}{\tan\left(\theta_{\text{inc}} - \frac{\pi}{2}\right)} = f_0 \Delta\theta \tan(\theta_{inc}) \\ &= -\Delta f_{\text{ground}} \tan^2(\theta_{inc}).\end{aligned} \tag{6}$$

Equation (6) reveals that for this kind of analysis, it is important not to demodulate the interferogram for the flat Earth component, i.e., for Δf_{ground}. The estimation of the frequencies and the corresponding terrain slopes is described in Section V.

III. Layover Geocoding

The geocoding stage is usually the last stage of an InSAR processor. The absolute phase is converted here in surface elevation and georeferenced on a specific datum. Several methods were proposed (e.g., [27] and [28]). The geometric principle of this operation is simple. A SAR sensor images a point on Earth at a particular range. All the points located on a circle with a ray centered at the sensor position are imaged at the same range, thus yielding infinite solutions. In an InSAR framework, this ambiguity is solved by imaging the same point with a second sensor. The unwrapped InSAR phase defines hyperbolas having equal range differences between the sensors. Consequently, on the Doppler plane, a point on Earth is located at the intersection between an *iso-range-difference* hyperbola and a *iso-range* circle. This relationship yields the generation of a digital interferometric elevation model. An example of flat-Earth mapping is shown in Fig. 4(a).

This basic geometrical relationship can be also exploited for the layover case. As shown in Fig. 3, building layovers generally generate high absolute phase gradients at their beginning and their end. In Fig. 4(b), the focus is on the mapping of such a trend, in case of total vertical dominance. In this circumstance, the mapping of the SAR domain in the cartographic one is sparse, i.e., with a variable distance between mapped points. As effect, a DEM derived with a bilinear interpolation between points presents artificial ramps. In this example, the derived DEM points are shown in blue. The generated elevation points from the absolute phase are in red. The height of the elevation points, and consequentially the artificial model slopes, depends on the layover contributors weighting in the returned signal. A

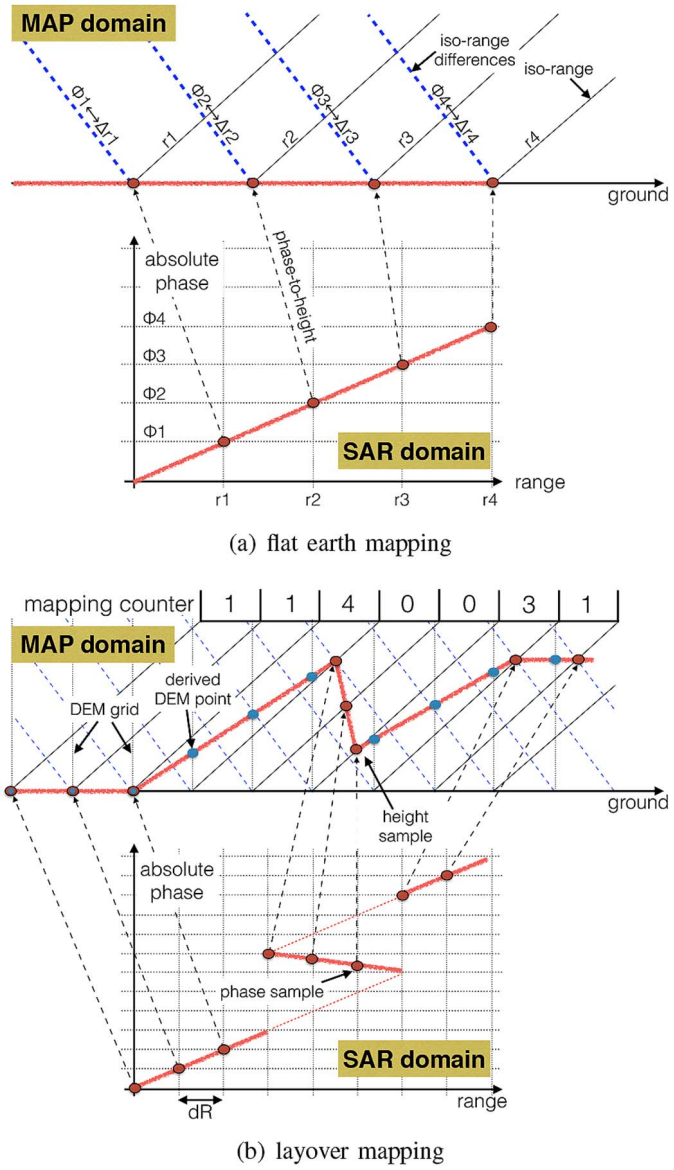

Fig. 4. SAR absolute phase mapping in a geographic domain. (a) Flat Earth mapping. Geographic points are determined at the intersection between iso-range circles and iso-range-differences hyperbolas, here drawn as straight lines. (b) Layover mapping. A phase gradient yields an elevation model ramp when employing a bilinear interpolation for the derivation of DEM points.

real example of interferometric urban elevation model with the highlighted effect is in Fig. 5(a). All the buildings imaged in this portion present the layover artifact, as highlighted for one of them with a red circle. A range section of the corresponding absolute phase is in Fig. 5(b). The real trend fits well with the simulated one in Fig. 3. A detailed study on the model accuracy is in [12]. Evidently, accuracy is limited at layover locations.

IV. Layover Detection

A. Algorithm

The derivation of the layover portion directly from the interferometric phase, e.g., searching for a high-phase gradient and subsequent phase slope, may be difficult due to phase noise superimposed to signal. The proposed procedure exploits

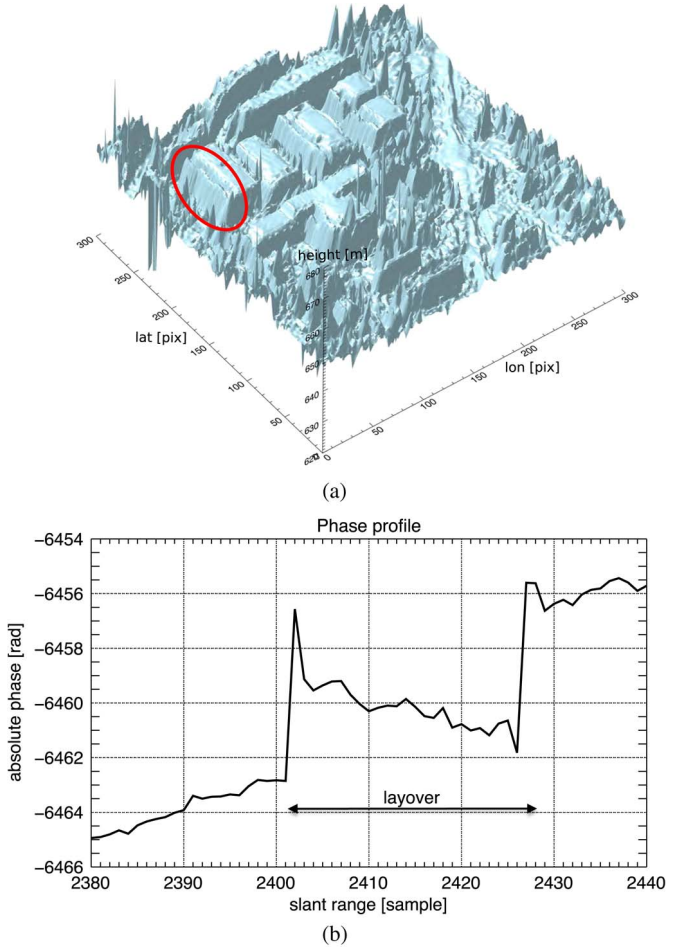

Fig. 5. (a) Three-dimensional interferometric elevation model portion over Las Vegas generated with spotlight TanDEM-X data. Layover ramps are marked for a building with a red circle. (b) Range section of the InSAR absolute phase for the highlighted building. (a) Elevation model. (b) absolute phase.

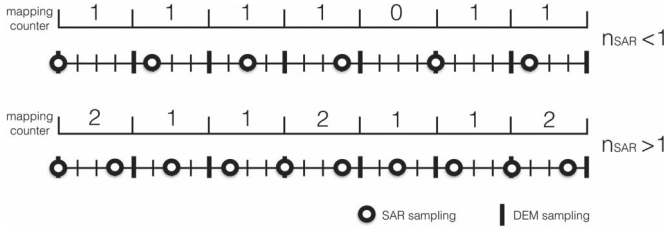

Fig. 6. Mapping counter measured in presence of a nonzero fractional part $\langle n_{\mathrm{SAR}} \rangle$ and an integer part equal to 1. At the top, $n_{\mathrm{SAR}} < 1$ yields a regularity of *no-mapping* pixels. At the bottom, $n_{\mathrm{SAR}} > 1$ yields a regularity of *multiple-mapping* pixels. The SAR sampling in the DEM raster is showed below the mapping counter.

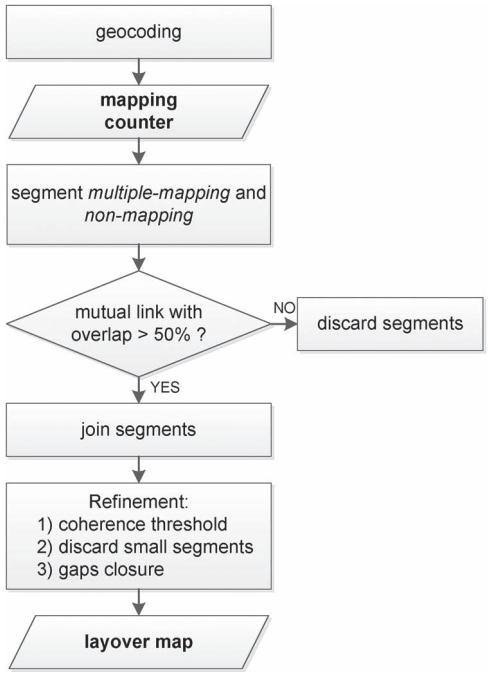

Fig. 7. Block scheme for the proposed building layover detector.

instead the geocoding algorithm described in the previous section and, in particular, a subproduct generated for the purpose and named *mapping counter*. The mapping counter is a map, in slant range coordinates, whose samples m_c describe the number of occurrences of a SAR interferogram pixel in the produced DEM. For a flat terrain, the SAR mapping on the DEM raster depends on the DEM posting and the subsampling used in the interferometric processing. In particular, the number of SAR pixels contributing to a DEM cell is

$$n_{\mathrm{SAR}} = \frac{1}{2}\left(\frac{\Delta^{\mathrm{LON}}_{\mathrm{DEM}}}{\Delta^{gr_{rg}}_{\mathrm{InSAR}}}\frac{\Delta^{\mathrm{LAT}}_{\mathrm{DEM}}}{\Delta^{az}_{\mathrm{InSAR}}}\right) \tag{7}$$

where $\Delta^{\mathrm{LON}}_{\mathrm{DEM}}$ and $\Delta^{\mathrm{LAT}}_{\mathrm{DEM}}$ represent the DEM posting for the northing and easting direction, and $\Delta^{gr_{rg}}_{\mathrm{InSAR}}$ and $\Delta^{az}_{\mathrm{InSAR}}$ the interferogram sampling in ground-range and azimuth dimensions, respectively. For an ideally flat terrain and noiseless interferogram, in case of $n_{\mathrm{SAR}} = 1$, every SAR pixel is used just once, and the mapping counter is a unit matrix. A divergence with this condition is an indicator of slopes. In the general case, the interferometric DEM exhibits slopes when the mapping counter pixel m_c differs from the integer part of n_{SAR}. Any terrain slope, also not in layover, impacts in the homogeneity of the mapping counter. Consequently, the detection of building layovers by inspecting the mapping counter results is more accurate in case of flat or locally flat terrains. To be remarked, the counter records integer values whereas n_{SAR} has usually a nonzero fractional part $\langle n_{\mathrm{SAR}} \rangle$. Thus, even for flat terrain, a discrepancy is recorded with a pattern depending on the ratio between the SAR and the DEM grids. Fig. 6 depicts the discrepancy measured in the mapping counter considering a nonzero fractional part and an integer part equal to 1. In the figure, the fractional part is negative and positive for the upper and lower example, respectively. It is then relevant, for the effectiveness of the algorithm, to set the interferometric processor in order to have $\langle n_{\mathrm{SAR}} \rangle$ close to zero.

The block scheme of the proposed algorithm is in Fig. 7. The mapping counter shown at the top of Fig. 4(b) (here $n_{\mathrm{SAR}} = 1$) can be taken as reference. A high-phase gradient creates a *multiple-mapping* region, i.e., $m_c > n_{\mathrm{SAR}}$. A straightforward technique to extract layovers is then used to detect pixels accomplishing this condition for every slant range line of the mapping counter. This constraint identifies the beginning of

a slope, or, in our case, a building layover zone. The following mapping counter pixels shall accomplish the condition $m_c < n_{\mathrm{SAR}}$. The detection implies a segmentation of the two regions and a mutual-link search. Flexibility in the mutual link must be introduced as phase noise, or a particular contributor weighting set, may disjoint them. Thus, a minimum overlap is set to 50% to increase the detection rate. This flexibility experimentally doubled layover detections (see next section). A set of refinements finalizes the layover map. If the building is large, then the nonmapping region must be enclosed in between two multiple-mapping regions by cause of the phase gradient at the end of the layover zone (see Fig. 3). In contrary, if the building is totally under the layover effect, then also its shadow area can accomplish the condition $m_c < n_{\mathrm{SAR}}$, thus falsely enlarging the estimated layover patch. In the latter case, the interferometric coherence is exploited in order to define the layover ending point through a threshold, approximating the coherence estimation bias value when the true coherence is zero [29]

$$t_0 = \frac{1}{2}\sqrt{\frac{\pi}{N_c}} \tag{8}$$

where N_c is the number of resolution cells used to estimate the coherence. Pixels having coherence lower than t_0 are considered as shadow pixels. Noisy areas may generate high-phase gradients and consequently wrong detections in the mapping counter. An efficient phase reduction algorithm (e.g., an adaptive multilooking technique) should be used to attenuate artifacts. Nevertheless, small false detections, as isolated layover coming from trees adjacent to buildings, can always be discarded considering the minimum spatial support of a standard building in the SAR interferogram. Finally, every detected building layover patch is made consistent by closing remaining gaps.

B. Example

The layover detection algorithm is tested for an interferometric TanDEM-X scenario. A bistatic spotlight acquisition taken on the January 4, 2012 over the city of Berlin (Germany) is chosen. The satellites had a normal baseline of about 110 m yielding a height of ambiguity of 65 m. The geometrical and processing parameters are in Table I. The same data set was used in [12] to test the TanDEM-X DEM generation capabilities over urban areas. As this paper's purpose is to work on a building-by-building base, the spotlight mode is of fundamental importance due to the high-resolution capable to isolate building signatures. Moreover, the bistatic configuration is, as well, favorable to circumvent false detection resulting from temporal decorrelation.

The detection of layover zones starts with the generation of the mapping counter. For a correct analysis of the map, the number of SAR pixels in the interferogram contributing to a DEM cell must be computed. The ground range and azimuth interferogram sampling are $\Delta^{gr_{rg}}_{\mathrm{InSAR}} = 2.03$ m and $\Delta^{az}_{\mathrm{InSAR}} = 2.60$ m, respectively. The TanDEM-X processing [30] is set to generate a DEM with longitude and latitude postings of $\Delta^{\mathrm{LON}}_{\mathrm{DEM}} = 2.16$ m and $\Delta^{\mathrm{LAT}}_{\mathrm{DEM}} = 2.37$ m. According to (7), n_{SAR} results 0.9877. Thus, following the guidelines in Section III, building layover is defined for mapping counter range segments composed of samples with values larger than one (tagged as *multiple mapping*). In Fig. 8 the mapping counter of the full acquisition is shown at the top left. In this case, no filtering is applied since the interferometric phase is generated using an adaptive-multilooking algorithm (IDAN) to strongly reduce speckle [31]. The map is quantized on three levels: a null value, in black, a unit value, in gray, and higher values in white. These last values, representing multiple mappings, are extracted and shown in the center-left map. In addition to this paper purposes, they can be used to estimate the building orientation in case of rectangular shapes. A regularity of diagonal multiple mappings is visible. This is the consequence of a nonzero fractional part $\langle n_{\mathrm{SAR}} \rangle$ and will be automatically discarded in the layover map refinement. At the bottom left, the $m_c < n_{\mathrm{SAR}}$ patches (tagged as *nonmapping* as $m_c = 0$) are extracted and coded in white. Mainly representing building shapes, they contain the larger part of the desired information. The refinement described in the previous section yields a detection of single building layovers. The result is the layover map shown at the bottom right. No *a priori* assumptions have been made about building shapes. The SAR amplitude of the master channel is also shown on top right to highlight the difficulties encountered by algorithms based only on simple amplitude and coherence thresholds (e.g., the layover portion of a building may be smaller than the full building patch). As a final remark, the additional processing time required for the generation of the layover map in the interferometric chain (from focused data to DEM) is negligible. This algorithm can be then easily integrated in an InSAR processor straight after the geocoding stage.

TABLE I
MAIN PARAMETER OF THE INTERFEROMETRIC SCENARIO UNDER TEST

parameter	value
range bandwidth f_s	300 Mhz
PRF	8200 Hz
center incidence angle (master)	41.8 deg
height of ambiguity	+65.4 m
data pixel spacing (range, azimuth)	0.45, 0.86 m
multi-look algorithm	IDAN
total number of looks	20
interferogram resolution	2.72 m
mean coherence	0.69
ground frequency Δf_{ground}	5.26 MHz
wall frequency Δf_{wall}	-4.14 MHz

V. FRINGE-FREQUENCY ESTIMATION

Once building layovers are extracted, they can be further analyzed by inspecting their spectral properties, in order to find the physical slopes superimposed in every detected patch. The frequencies characterizing the building layover spectrum in (3) can be estimated and the related ground slopes can be then derived by inverting (4)

$$\alpha = \arctan\left(\frac{f_{rg}\tan\theta + f_0\Delta\theta}{f_{rg} - f_0\Delta\theta\tan\theta}\right). \tag{9}$$

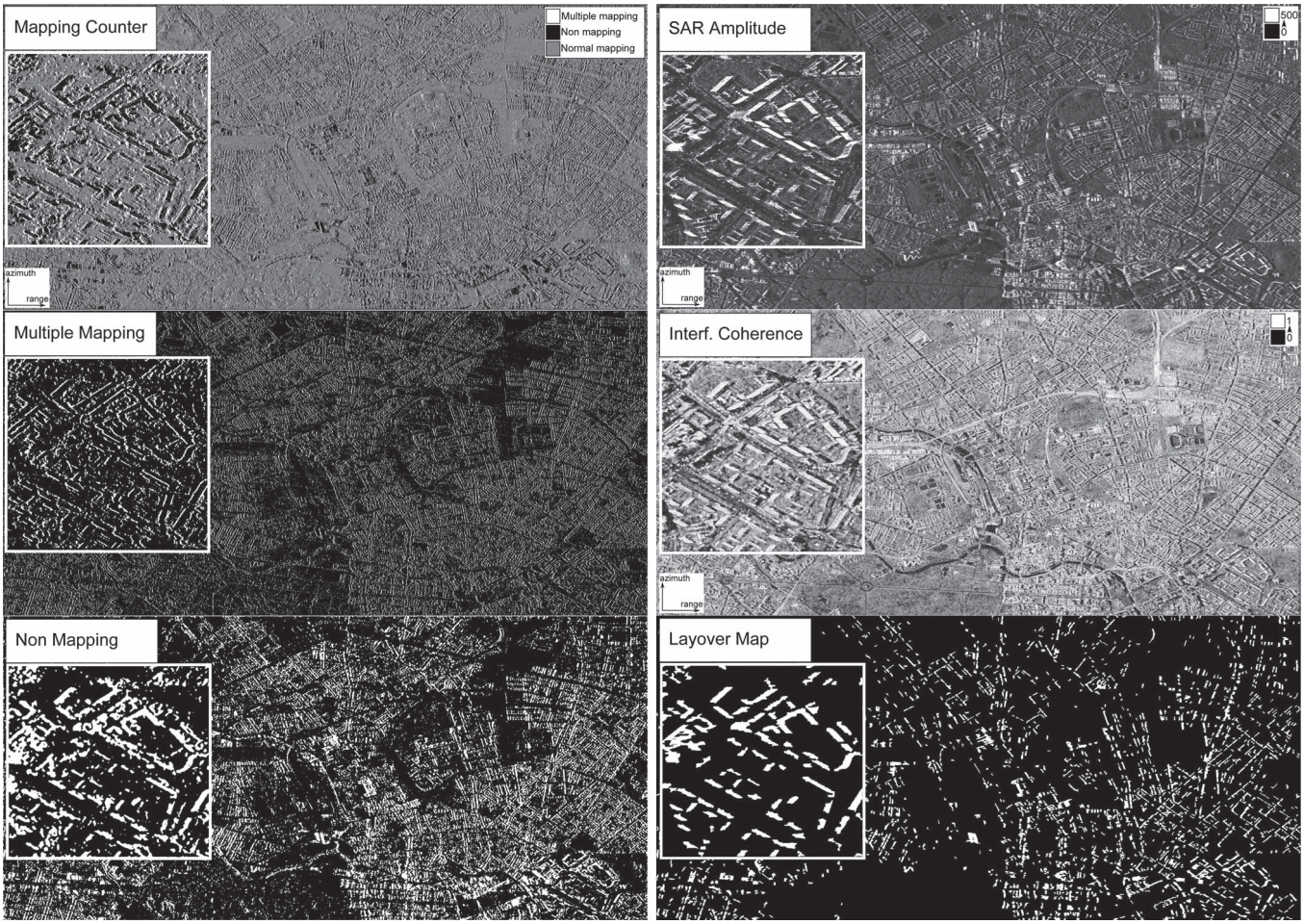

Fig. 8. Visual representation of the layover detection processing steps. (Top left) Mapping counter. $n_{\mathrm{SAR}} = 0.99$. In black the *nonmapping* areas having value $m_c = 0$, in gray the normal mapping areas having value $m_c = 1$ and in white the *multiple mapping* areas having value $m_c > 1$ are represented. (Middle left) *Multiple mapping* areas extracted from the mapping counter are in white. (Bottom left) *Nonmapping* area extracted from the mapping counter are in white. (Top right) SAR amplitude of the master channel in SAR coordinates. (Middle right) Interferometric coherence. (Bottom right) Final building layover map. The detected and segmented buildings are white coded. For all the figures the highlighted portion is a zoom of the south-east part of the map.

The number of layover contributors per building is also assessed during the estimation, assuming the building composed by planar facets. Ideally, approximating (2) at the first order, i.e., $\phi(r,x) \simeq \phi'_r dr + \phi'_x dx$, and solving for the local backscatter, layover heights can be determined by making use of the SAR phase-to-height conversion [22]. In the following, it is shown that the complete layover decomposition is impracticable with a sole interferogram because of the very small range layover support. Nevertheless, the dominant signal in the building layover can be extracted with a certain accuracy depending on the estimation technique, the number of layover range and azimuth pixels and the local SNR ratio.

A. Simulations

Two classical methods are analyzed in this paper: fast Fourier transform (FFT) (or *periodogram analysis*) and *conventional MUSIC*. The latter is a parametric method that fits with the interferogram model in (2). As both of the algorithms are very common and widely used in the spectral estimation framework, they will not be described in this paper. Details on the methods can be found in several dedicated books, e.g., [32] and [33].

The estimation is performed for every detected building layover, in the slant range domain. Each slant range line is assumed as an independent realization of the same process. This assumption implies a building modeled by planar surfaces, the same for every range line. To be noticed, with this assumption building orientation does not impact the estimation. The sole repercussion lies in the estimation of nonvertical and nonhorizontal slopes (e.g., gabled roofs): the estimated roof slope is the slope projected in the range direction and not the real one.

A complexity comes from the varying range support. Indeed, the realization dimensions, i.e., the number of range samples for every azimuth line, may vary depending on the building structure. In contrast, a standard frequency estimation usually assumes a constant size for each realization and then averages over the estimates. This issue is circumvented by assigning a specific weight for every realization, depending on its size. Larger realizations have larger weights. A minimum size is also defined. Realizations smaller than the minimum size are discarded. In the FFT algorithm, the set of range spectra of a building patch is computed over a defined frequency support, so that a simple weighted average is straightforward. In the MUSIC algorithm, the correlation matrix is estimated with a spatial

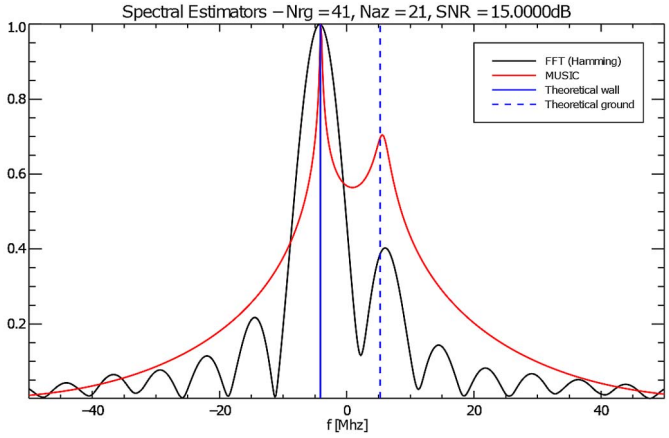

Fig. 9. Simulated spectrum (black) and pseudospectrum (red) for a bitonal signal. The simulated frequencies represent the wall frequency (blue) and ground frequency (dashed blue). The range spatial support is 41 samples. Spectra are averaged over an azimuth spatial support of 21 samples. SNR is set to 15 dB.

smoothing method [34] in order to use all the samples of valid realizations. The realization weight is then set as proportional to the number of smoothings per building range line: the larger the realization, the larger the number of smoothings, the larger the weight.

The scope of the following analysis is to demonstrate the potentials and the limits of the two algorithms for the particular case of the cuboid building model. A primary objective is the definition of the minimum realization size $n_{\text{lay}}^{\min}$ for an accurate slope estimation for the TerraSAR-X/TanDEM-X high-resolution spotlight case. For this purpose, a simulation of a sum of two sinusoids with frequencies Δf_{ground} and Δf_{wall} is performed. The model in (2) is approximated at the first order with a complex sum of two tones with frequencies Δf_{wall} and Δf_{ground} with real valued amplitudes. Amplitudes determine the backscatter of the wall and the ground/roof. SNR is defined by adding white Gaussian noise. Parameters of the simulations are given in Table I.

An unlimited number of different combinations can be simulated. A strong tone mixed up with a weak one is chosen as representing many cases analyzed in the next section. An exemplary simulation result is in Fig. 9. Here, one could visually evaluate the better MUSIC performance when compared with FFT in case of dominance of one frequency (in this case the wall one), providing two clear peaks at the frequency locations. Theoretically, considering the FFT resolution, the periodogram detection of two tones with equal weights requires a number of samples larger than

$$n_{\text{lay}}^{\min} > \frac{f_s}{|\Delta f_{\text{ground}} - \Delta f_{\text{wall}}|} \tag{10}$$

equal to 31 samples in our test case. A simulation is performed to evaluate the minimum range support at four different SNR levels (0,5,10,15 dB) for the two algorithms. In Fig. 10 the estimated absolute errors $|\widehat{\Delta f}_{\text{wall}} - \Delta f_{\text{wall}}|$ and $|\widehat{\Delta f}_{\text{ground}} - \Delta f_{\text{ground}}|$ are plotted for the four cases using a fixed azimuth support of 21 samples and 1000 simulation

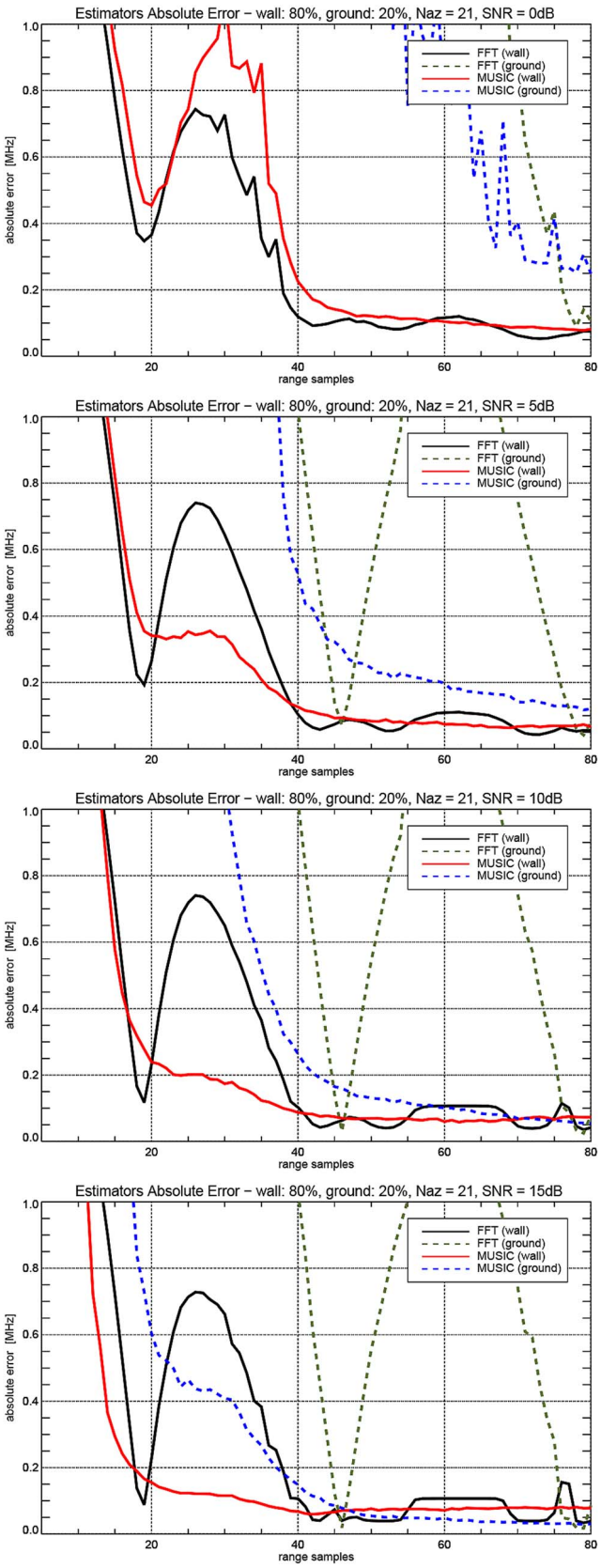

Fig. 10. Fringe-frequency absolute error for varying range support for FFT and MUSIC algorithms. Wall frequency is dominant in the simulation with a 80% weight (black and blue lines for FFT and MUSIC, respectively). Ground frequency has a 20% weight (dashed green and blue lines for FFT and MUSIC, respectively). SNR is set to 0, 5, 10, and 15 dB (top to bottom). 21 azimuth samples are considered in averaging the estimates. 1000 simulations per range sample are performed.

TABLE II
MINIMUM RANGE SUPPORT $n_{\text{lay}}^{\min}$ FOR A 80% WALL WEIGHT AND A 20% GROUND WEIGHT

	wall [a]	ground/roof [a]
MUSIC$\vert_{SNR=15dB}$	12/14/17	18/32/37
MUSIC$\vert_{SNR=10dB}$	14/17/23	32/37/43
MUSIC$\vert_{SNR=5dB}$	15/18/35	38/42/60
MUSIC$\vert_{SNR=0dB}$	35[b]/37/41	62[b]/75[b]/–

[a] Support for an absolute error of $0.8/0.4/0.2$ MHz.
[b] The curve is not monotonous. This value refers to the worst case.

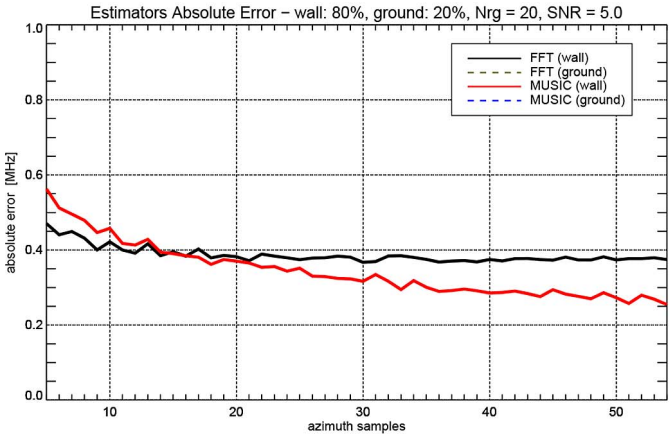

(a) azimuth support

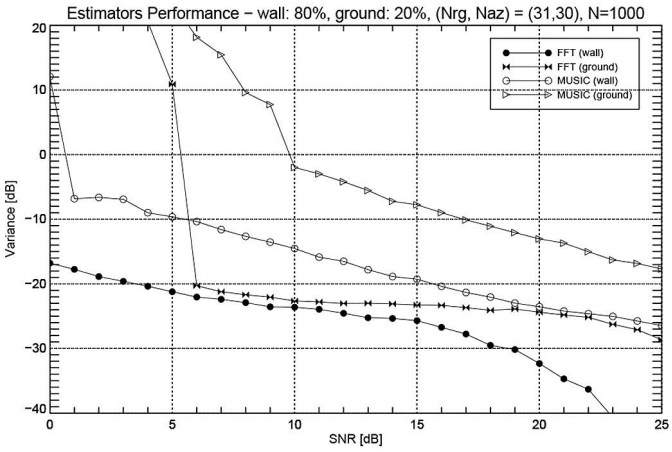

(b) estimator stability

Fig. 11. (a) Fringe-frequency absolute error for varying azimuth support for FFT and MUSIC algorithms. The range support is fixed to 20 samples. Wall frequency is dominant in the simulation with an 80% weight (black and blue lines for FFT and MUSIC, respectively). Ground frequency (20% weight) is out of the plot. SNR is 5 dB. 1000 simulations per azimuth sample are performed. (b) Estimators stability—variance of the absolute error—at varying SNR for FFT and MUSIC algorithms.

runs for each range sample under test. It is not surprising to see how MUSIC outperforms FFT in terms of accuracy, particularly for the low weighted frequency. Generally, MUSIC has a strong dependence on SNR: for very low SNR values, FFT tends to outperform MUSIC. Nevertheless, the general superior performance in the detection recommends the use of MUSIC. In Table II, the MUSIC minimum support for three different accuracy levels is summarized.

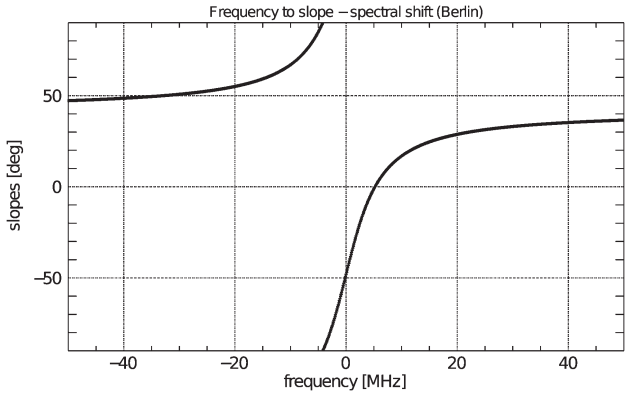

Fig. 12. Nonlinear relationship between ground slope and frequencies considering the data set used for the validation.

The azimuth support is used to average the frequency estimates. The impact in the absolute error is not as dramatic as the range support: in Fig. 11(a) a simulation at 5 dB reveals a decay of 0.2 MHz for 20 azimuth samples for MUSIC, whereas the impact in the FFT is not relevant. Finally, a study on the estimator's stability at varying SNRs confirms the consideration made above: MUSIC is less stable at low SNRs. For both of the tones, FFT provides a smaller estimation variance [Fig. 11(b)].

B. Principal Slope Estimation

The previous analysis, summarized in Table II, remarked that frequency estimation of a multitonal signal requires quite a large spatial support, considering building layovers. Layovers extend for a number of pixels depending on the building height and the incidence angle. Smaller incidence angles and higher constructions provide larger supports. By definition, resolution increases the number of layover pixels. Additionally, the problem is also nonlinear, considering (4). In Fig. 12, the relationship between slopes and frequencies is depicted considering the system parameters in Table I. The estimation accuracy at different slopes varies significantly. For instance, a deviation of 0.4 MHz in the frequency estimation for 90° yields an error of about 2°, whereas the same inaccuracy for 35° brings an estimation error of only 0.07°.

For all these reasons, proper layover decomposition and backscatter estimation is not feasible with a sole interferogram. Considering the simulations, the main layover component, when dominating over others, can be estimated with about 15 samples. Accurate secondary component estimation requires about a double number of samples, which makes a complete decomposition feasible only for high-rise and isolated buildings at X-band. Thus, only for the strongest component, i.e., the one with a higher backscatter, a single slope is estimated and denoted *principal slope*.

Since MUSIC provides frequency locations, but not an estimate of signal backscatter, a further estimation technique is required to detect the dominant frequency. First of all, the number of components is required as MUSIC input. For that, the Minimum Description Length (MDL) [32] has been chosen as selection technique. Considering the particular case, a maximum number of three components are considered. After that, if a single contributor is detected, then obviously, it is

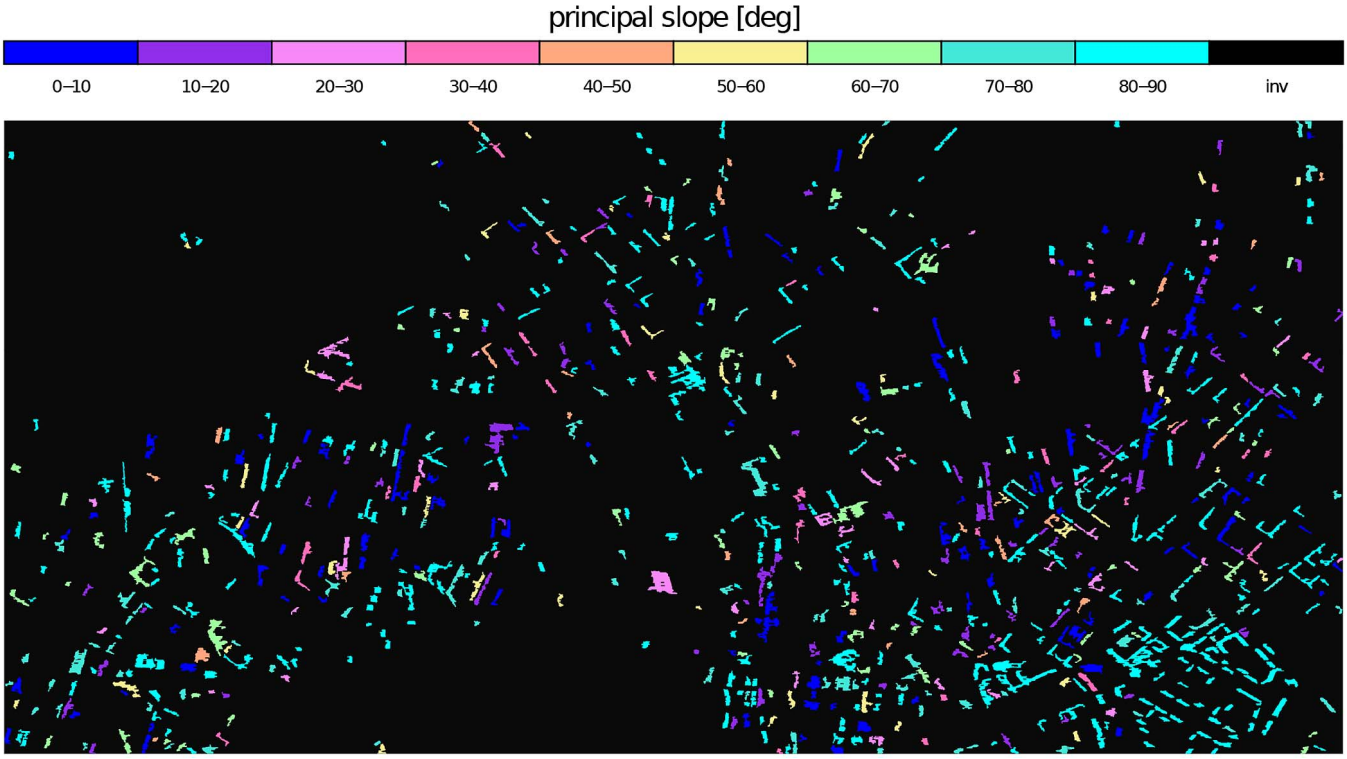

Fig. 13. Principal slope for the detected building layovers. A segmentation on the detected map and a conventional MUSIC algorithm is used to estimate the dominant frequency for layovers having a minimum range and azimuth support of 15 and 10 samples. Color scale is at the top.

the dominant one; otherwise, the dominant one is estimated by inverting the MUSIC model [33, p. 460].

C. Example

The frequency estimation framework is exploited to derive the principal slope of the layover portions. The test site is the same employed in Section IV-B. The principal slope, derived as in (9) by employing the conventional MUSIC algorithm, is shown in Fig. 13. Estimated slopes are regularly quantized in nine classes. Considering the performed simulations, the fringe frequency is estimated for layover patches having a minimum range and azimuth support of 15 and 10 samples, respectively. Discarded buildings can be visually recognized by comparing Fig. 13 and the bottom-right map in Fig. 8. The covariance matrix order is adaptively chosen depending on the actual range support. In particular, the order is defined as the minimum common support exceeding the minimum valid realization of 15 samples. The model order is estimated in the processing by adopting the MDL algorithm and fixing three tones as upper bound. In Fig. 14 the model order, i.e., the estimated number of layover components, is shown for the nine slope classes.

An analysis of the result indicates that for about 60% of the analyzed buildings (in total 866) wall has the dominance in the signal return. Flat roofs (or ground) dominate for about 25% and other slopes, as tilted roofs, for the remaining 15%. A first consideration is about the generally larger wall support at the acquisition incidence angle (Table I) considering the buildings conformation of the city under analysis. In fact, excluding wall portions not visible by the radar due to local occlusion (e.g., trees or close buildings), the wall is generally totally included in the portion, whereas roofs are only summing up for a section of the total layover support. A second consideration is about the balconies-windows configuration, which creates a set of strong reflectors at the vertical slope. For these configurations, the facade layover contribution dominates over the others. An example is provided in Fig. 15. The mentioned buildings conformation is evident for this portion, representing the southern-eastern part of the derived map and already taken as reference in Fig. 8. The derived spectrum and pseudospectrum for a benchmark structure are plotted at the bottom of the figure. A first-degree model is detected. The conventional MUSIC algorithm estimates a principal slope close to 90°. On the contrary, the FFT result is not accurately detecting the wall frequency. Generally, FFT results are much more sensible to local backscattering variations.

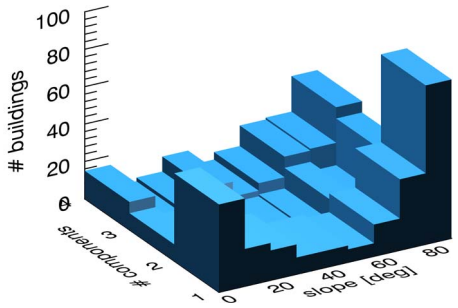

Fig. 14. Two-dimensional histogram of the estimated slopes and number of layover components. Axis represent the number of building layovers (z), the number of components (y) and the estimated principal slope (x).

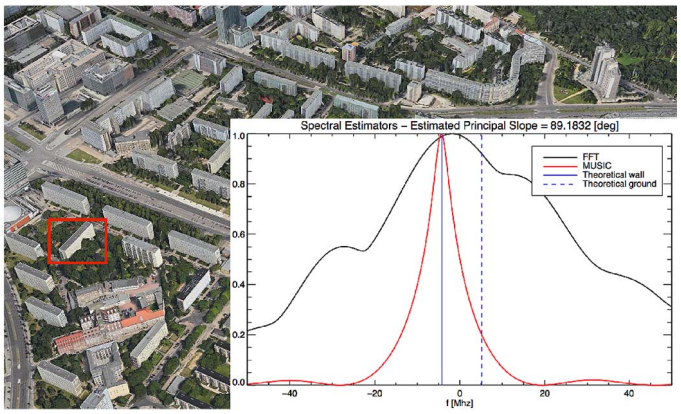

Fig. 15. Exemplary estimation of vertical slope dominance. The southern-eastern part of the data set is shown with a 3-D optical view (Apple Inc.). The spectra of the building layover highlighted in red are overimposed. In red, the MUSIC pseudospectrum is used to obtain the principal slope estimation, very close to 90°. A single contributor is estimated. In black, the maximum of periodogram is also shown. Frequencies corresponding to the vertical and the horizontal slopes are represented with a continuous and a dashed blue line, respectively.

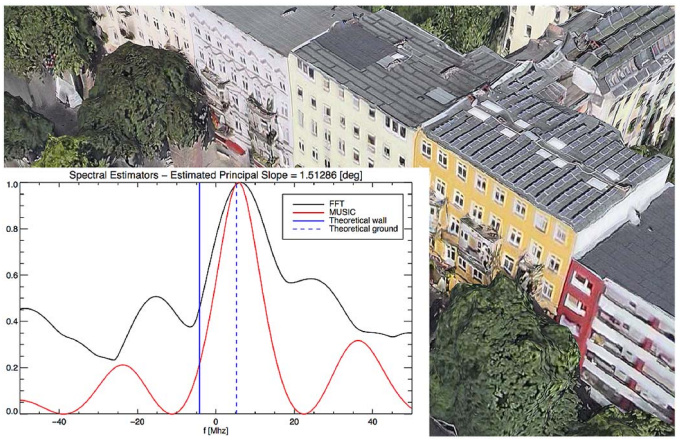

Fig. 16. Exemplary estimation of horizontal slope dominance. The buildings under analysis are shown with a 3-D optical view (Apple Inc.). The spectra of the yellow building are overimposed. In red, the MUSIC pseudospectrum is used to obtain the principal slope estimation, very close to 0°. Three layover contributors are estimated. In black, the maximum of periodogram is also shown. Frequencies corresponding to the vertical and the horizontal slopes are represented with a continuous and a dashed blue line, respectively.

Strong reflectors at the roof tops make the roof slope dominate. An example is in Fig. 16. The orange and the connected yellow building are belonging to a single layover patch. The adjacent red building is instead differently segmented due to a low coherence area that disjoins it. The horizontal slope is found as dominant, because of the set of solar panels and chimneys on the flat roof. The spectra here are more complex: in the layover patch also adjacent trees superimpose, and the vertical slope is not estimated. The other two slopes are not accurately estimated, once again demonstrating the inability to completely reconstruct the layover signal with a single interferogram. Nevertheless, the principal component provides useful information, e.g., the facet, in which strong scatterers are lying. This information is not easy to retrieve by inspecting the single amplitude, coherence and absolute phase. On the whole, it has been experimentally verified that when various scatterers at a specific facet exhibit a high backscattered signal return, their facet slope is measured and a single slope is estimated. Fig. 14 demonstrates that for the majority of the detected layovers a single contributor is estimated.

VI. Conclusion

The mapping of urban areas with SAR sensors is of increasing attractiveness due to the increment of high-resolution data available. With new missions, as TanDEM-X, and expected future ones, urban SAR research is growing in a field dominated nowadays by optical or LiDAR sensors. In this context, this paper presents an algorithm for the detection of the layover portion of buildings. The focus is on the interferometric processor, and, in particular, on the geocoding stage. The particular layover absolute phase trend is exploited in the mapping matrices in a way to precisely identify layovers. The attractive points of the algorithm are the absence of *a priori* hypotheses and the lack of external high-resolution DEMs in input. These detections are also useful for an accuracy evaluation of InSAR-generated urban DEMs.

Spectral estimation is then considered in this paper as an additional instrument toward a better understanding of the physical phenomena behind the layover scattering decomposition. A super-resolution algorithm, MUSIC, is employed to derive the fringe frequencies characterizing the layover portion. Due to the limited estimation support, only the dominant frequency is found to be reliable information. The nonlinear relationship with slopes is employed to derive a *principal slope* map. A bistatic interferometric scenario is tested. It is found that for the layover's majority the facade contribution is the prevailing one due to the presence of targets with a high backscattered signal return at the vertical slope. Moreover, the number of layover contributors is assessed prior to the spectral estimation. It has been estimated that the signal return is dominated by a single contribution for the majority of the layovers.

The layover map application range is certainly wider than the one delineated in this paper. First, a change detection of the derived parameters (shape, slopes) for different temporal acquisition may support damage assessment applications. Second, geographical building orientation can be easily derived. Third, the result can be related to a persistent scatterer interferometry quality precheck. Fourth, the principal slope map and the estimation of the number of components can be an instrument for electromagnetic and simulation studies. Finally, as the scenario considered is the interferometric bistatic one, which main purpose is the generation of a DEM, the derived estimates can be used to improve the elevation model in the detected positions.

References

[1] G. Schreier, "Geometrical properties of SAR images," in *SAR Geocoding: Data and Systems*. Karlsruhe, Germany: Wichmann, 1993, pp. 103–134.

[2] U. Stilla, U. Soergel, and U. Thoennessen, "Potential and limits of InSAR data for building reconstruction in built-up areas," *ISPRS J. Photogramm. Remote Sens.*, vol. 58, no. 1/2, pp. 113–123, Jun. 2003.

[3] M. Quartulli and M. Datcu, "Stochastic geometrical modeling for built-up area understanding from a single SAR intensity image with meter resolution," *IEEE Trans. Geosci. Remote Sens.*, vol. 42, no. 9, pp. 1996–2003, Sep. 2004.
[4] U. Soergel, U. Thoennessen, A. Brenner, and U. Stilla, "High-resolution SAR data: New opportunities and challenges for the analysis of urban areas," *Proc. Inst. Elect. Eng.—Radar, Sonar Navig.*, vol. 153, no. 3, pp. 294–300, Jun. 2006.
[5] F. Rottensteiner and C. Briese, "A new method for building extraction in urban areas from high-resolution LIDAR data," *Int. Arch. Photogramm. Remote Sens. Spatial Inf. Sci.*, vol. 34, no. 3/A, pp. 295–301, 2002.
[6] M. Crespi *et al.*, "Radiometric quality and DSM generation analysis of CartoSat-1 stereo imagery," in *Proc. Int. Arch. Photogramm., Remote Sens. Spatial Inf. Sci.*, 2008, vol. 37, pp. 1349–1355.
[7] X. X. Zhu and R. Bamler, "Very high resolution spaceborne SAR tomography in urban environment," *IEEE Trans. Geosci. Remote Sens.*, vol. 48, no. 12, pp. 4296–4308, Dec. 2010.
[8] S. Duque, C. Rossi, and T. Fritz, "Single-pass tomography with alternating bistatic TanDEM-X data," *IEEE Geosci. Remote Sens. Lett.*, vol. 12, no. 2, pp. 409–413, Feb. 2015.
[9] A. Pauciullo, D. Reale, A. De Maio, and G. Fornaro, "Detection of double scatterers in SAR tomography," *IEEE Trans. Geosci. Remote Sens.*, vol. 50, no. 9, pp. 3567–3586, Sep. 2012.
[10] C. Tison, F. Tupin, and H. Maitre, "A fusion scheme for joint retrieval of urban height map and classification from high-resolution interferometric SAR images," *IEEE Trans. Geosci. Remote Sens.*, vol. 45, no. 2, pp. 496–505, Feb. 2007.
[11] E. Colin-Koeniguer and N. Trouv, "Performance of building height estimation using high-resolution PolInSAR images," *IEEE Trans. Geosci. Remote Sens.*, vol. 52, no. 9, pp. 5870–5879, Sep. 2014.
[12] C. Rossi and S. Gernhardt, "Urban DEM generation, analysis and enhancements using TanDEM-X," *ISPRS J. Photogramm. Remote Sens.*, vol. 85, pp. 120–131, Nov. 2013.
[13] D. Brunner, G. Lemoine, L. Bruzzone, and H. Greidanus, "Building height retrieval from VHR SAR imagery based on an iterative simulation and matching technique," *IEEE Trans. Geosci. Remote Sens.*, vol. 48, no. 3, pp. 1487–1504, Mar. 2010.
[14] J. Tao, S. Auer, G. Palubinskas, P. Reinartz, and R. Bamler, "Automatic SAR simulation technique for object identification in complex urban scenarios," *IEEE J. Sel. Topics Appl. Earth Observ. Remote Sens.*, vol. 7, no. 3, pp. 994–1003, Mar. 2014.
[15] R. Cossu, F. Dell'Acqua, D. Polli, and G. Rogolino, "SAR-Based seismic damage assessment in urban areas: Scaling down resolution, scaling up computational performance," *IEEE J. Sel. Topics Appl. Earth Observ. Remote Sens.*, vol. 5, no. 4, pp. 1110–1117, Aug. 2012.
[16] W. Kropatsch and D. Strobl, "The generation of SAR layover and shadow maps from digital elevation models," *IEEE Trans. Geosci. Remote Sens.*, vol. 28, no. 1, pp. 98–107, Jan. 1990.
[17] A. Thiele, J. Wegner, and U. Soergel, "Building reconstruction from multi-aspect InSAR data," in *Radar Remote Sensing of Urban Areas* ser. ser. Remote Sensing and Digital Image Processing, vol. 15, U. Soergel, Ed. Dordretch, The Netherlands: Springer-Verlag, 2010, pp. 187–214.
[18] A. Thiele, M. M. Wurth, M. Even, and S. Hinz, "Extraction of builidng shape from TanDEM-X data," in *Proc. ISPRS*, 2013, vol. XL-1/W1, pp. 345–350.
[19] A. Monti Guarnieri, "SAR interferometry and statistical topography," *IEEE Trans. Geosci. Remote Sens.*, vol. 40, no. 12, pp. 2567–2581, Dec. 2002.
[20] U. Spagnolini, "2-D phase unwrapping and instantaneous frequency estimation," *IEEE Trans. Geosci. Remote Sens.*, vol. 33, no. 3, pp. 579–589, May 1995.
[21] M. Eineder, N. Adam, R. Bamler, N. Yague-Martinez, and H. Breit, "Spaceborne spotlight SAR interferometry with TerraSAR-X," *IEEE Trans. Geosci. Remote Sens.*, vol. 47, no. 5, pp. 1524–1535, May 2009.
[22] R. Bamler and P. Hartl, "Synthetic aperture radar interferometry," *Inv. Probl.*, vol. 14, no. 4, pp. R1–R54, Aug. 1998.
[23] D. Perissin and F. Rocca, "High-accuracy urban DEM using permanent scatterers," *IEEE Trans. Geosci. Remote Sens.*, vol. 44, no. 11, pp. 3338–3347, Nov. 2006.
[24] A. Thiele, E. Cadario, K. Schulz, U. Thonnessen, and U. Soergel, "Building recognition from multi-aspect high-resolution InSAR data in urban areas," *IEEE Trans. Geosci. Remote Sens.*, vol. 45, no. 11, pp. 3583–3593, Nov. 2007.
[25] C. Prati and F. Rocca, "Limits to the resolution of elevation maps from stereo SAR images," *Int. J. Remote Sens.*, vol. 11, no. 12, pp. 2215–2235, Dec. 1990.
[26] F. Gatelli *et al.*, "The wavenumber shift in SAR interferometry," *IEEE Trans. Geosci. Remote Sens.*, vol. 32, no. 4, pp. 855–865, Jul. 1994.
[27] O. Hellwich and H. Ebner, "Geocoding SAR interferograms by least squares adjustment," *ISPRS J. Photogramm. Remote Sens.*, vol. 55, no. 4, pp. 277–288, Nov. 2000.
[28] M. Schwabisch, "A fast and efficient technique for SAR interferogram geocoding," in *Proc. IEEE IGARSS*, Jul. 1998, vol. 2, pp. 1100–1102.
[29] C. Oliver and S. Quegan, *Understanding Synthetic Aperture Radar Images*. Stevenage, U.K.: SciTech, 2004.
[30] C. Rossi, F. R. Gonzalez, T. Fritz, N. Yague-Martinez, and M. Eineder, "TanDEM-X calibrated raw DEM generation," *ISPRS J. Photogramm. Remote Sens.*, vol. 73, pp. 12–20, Sep. 2012.
[31] G. Vasile, E. Trouve, J.-S. Lee, and V. Buzuloiu, "Intensity-driven adaptive-neighborhood technique for polarimetric and interferometric SAR parameters estimation," *IEEE Trans. Geosci. Remote Sens.*, vol. 44, no. 6, pp. 1609–1621, Jun. 2006.
[32] S. Kay, *Modern Spectral Estimation: Theory and Application*. Englewood Cliffs, NJ, USA: Prentice-Hall, 1988.
[33] M. H. Hayes, *Statistical Digital Signal Processing and Modeling*. Hoboken, NJ, USA: Wiley, 1996, p. 460.
[34] T.-J. Shan, M. Wax, and T. Kailath, "On spatial smoothing for direction-of-arrival estimation of coherent signals," *IEEE Trans. Acoust., Speech, Signal Process.*, vol. 33, no. 4, pp. 806–811, Aug. 1985.

Cristian Rossi received the Laurea Magistrale (M.Sc.) degree in telecommunication engineering from Politecnico di Milano, Milan, Italy, in 2006.

From 2006 to 2008, he was with Aresys, Milan, Italy. Since 2008, he has been with the SAR Signal Processing Department, Earth Observation Center, German Aerospace Center (DLR), Oberpfaffenhofen, Germany, where he works on the development of the integrated TanDEM-X processor and on novel interferometry algorithms for synthetic aperture radar missions. His research interests include urban remote sensing, multisource data fusion, digital elevation models, and environmental parameter estimation.

Michael Eineder (SM'01) is a specialist for synthetic aperture radar (SAR). He has been with the German Aerospace Center (DLR) since 1990, where he is currently heading the SAR Signal Processing Department of DLR's Remote Sensing Technology Institute. He has worked on a series of international SAR missions including the recent German missions TerraSAR-X and TanDEM-X. Since 2006, he has been a Part-Time Lecturer of remote sensing with the Technische Universitaet Muenchen (TUM), and since 2013, he has been a TUM Honorary Professor. His research interests encompass SAR, InSAR, and SAR imaging geodesy.